

THE ASSOCIATION OF TALL EYEWALL CONVECTION
WITH TROPICAL CYCLONE INTENSIFICATION

by

Owen A. Kelley
A Dissertation
Submitted to the
Graduate Faculty
of
George Mason University
in Partial Fulfillment of
The Requirements for the Degree
of
Doctor of Philosophy
Computational Sciences and Informatics

Committee:

<u>Michael E. Summers</u>	Dr. Michael Summers, Dissertation Director
<u>Jeffrey Halverson</u>	Dr. Jeffrey Halverson, Committee Member
<u>Menas Kafatos</u>	Dr. Menas Kafatos, Committee Member
<u>James Beall</u>	Dr. James Beall, Committee Member
<u>Dimitrios Papaconstantopoulos</u>	Dr. Dimitrios Papaconstantopoulos, Department Chairperson
<u>Peter Becker</u>	Dr. Peter Becker, Associate Dean for Graduate Studies, College of Science
<u>Vikas Chandhoke</u>	Dr. Vikas Chandhoke, Dean, College of Science

Date: March 5, 2008

Spring Semester 2008
George Mason University
Fairfax, VA

The Association of Tall Eyewall Convection
with Tropical Cyclone Intensification

A dissertation submitted in partial fulfillment of the requirements for the degree of
Doctor of Philosophy at George Mason University

By

Owen A. Kelley
Master of Science
George Mason University, 1997
Bachelor of Arts
St. John's College, 1993

Director: Michael Summers, Professor
Department of Physics and Astronomy

Spring Semester 2008
George Mason University
Fairfax, VA

Copyright 2008 Owen A. Kelley

ACKNOWLEDGEMENTS

Over the past four years, a number of people have discussed with me the ideas in this dissertation. They include Tom Bell, Natalie Blades, Craig Bohren, Scott Braun, Daniel Cecil, Jeff Halverson, Bart Kelley, Genevieve Demos Kelley, John Kwiatkowski, Chris Landsea, Chuntao Liu, David Marks, Daniel Melendez, Mike McCumber, Bob Meneghini, Bill Olson, Dave Silberstein, Joanne Simpson, Erich Stocker, John Stout, and Ed Zipser. The above mentioned people do not necessarily agree with the conclusions of this dissertation, nor are they responsible for any errors. Section 3.9 contains unpublished research from a collaboration with John Stout. The TRMM Science Data and Information System (TSDIS) provided computational facilities.

The dissertation was strengthened by suggestions from my adviser Michael Summers and my dissertation committee, which includes Jim Beall, Jeff Halverson, and Menas Kafatos.

Various organizations and individuals provided the data used in this dissertation. NASA/JAXA/NICT provided TRMM data. Many TRMM subsets were downloaded from the JAXA Tropical Cyclone Database. NCDC provided ground radar data. The National Hurricane Center (NHC) and the Joint Typhoon Warning Center (JTWC) provided world-wide best track wind intensity estimates. Scott Braun provided output from his simulation of Hurricane Bonnie (1998). Mark DeMaria provided his database of intensity predictors from the Statistical Hurricane Intensity Prediction Scheme (SHIPS). Klaus Hoinka provided the tropopause climatology. NLDN data provided by Nicholas Demetriades of Vailsala Thunderstorm. GOES data provided by Ray Zehr. NOAA provided radiosonde profiles (<http://raob.fsl.noaa.gov>).

Looking back ten years, several courses at George Mason University and at the University of Maryland prepared me to conduct atmospheric research. Those courses were taught by Michael Summers, John Wallin, Daniel Carr, Clifton Sutton, Bob Atlas, and Eugenia Kalnay. During the same period, I developed my research skills at the Naval Research Laboratory (NRL). At NRL, my work was directed by Michael Picone, Daniel Melendez, Robert Meier, Ken Dymond, and Bob McCoy.

Looking back further, I am grateful to my parents for giving me a sense of curiosity about the world and a full measure of tenacity.

TABLE OF CONTENTS

	Page
List of tables.....	vii
List of figures.....	ix
List of abbreviations	xii
List of symbols.....	xv
Abstract.....	xx
 1. Introduction.....	 1
 2. Literature review.....	 13
2.1. Tall convective cells in tropical cyclone eyewalls	13
2.1.1. History of tall eyewall cell observations.....	13
2.1.2. Tall eyewall cells as a mixture of air and water.....	17
2.1.3. Discussion of CAPE in tall eyewall cells	19
2.1.4. Updraft speed in tall eyewall cells	21
2.1.5. Surface rain rate of tall eyewall cells.....	22
2.1.6. Other properties of tall eyewall cells	22
2.1.7. Tropical climatological freezing height.....	23
2.1.8. Tropical cyclone wind intensity.....	24
2.2. The thermodynamic importance of water in the atmosphere	25
2.3. Satellite observations.....	29
2.3.1. Techniques for observing precipitation	29
2.3.2. Revisit time	36
2.4. Ground-based observations	39
2.5. Radar reflectivity.....	44
2.5.1. Mathematical derivation of radar reflectivity	48
2.5.2. Calculating the precipitation rate from radar reflectivity	55
2.5.3. Hydrometeor fall speed.....	57
2.6. Future instrumentation	62
2.7. Dynamics of tall convection.....	63
2.7.1. Parcel theory of convective updrafts.....	63

2.7.2.	Vertical distribution of temperature and pressure.....	66
2.7.3.	Mathematical derivation of vertical CAPE.....	71
2.7.4.	Circulation set up by a tall convective cell	77
2.8.	Dynamics of tropical cyclones	80
2.8.1.	Gradient wind balance	81
2.8.2.	Dissipative forces.....	82
2.8.3.	Eye subsidence.....	83
2.8.4.	The eye's thermal anomaly and wind intensity	86
2.8.5.	Energy conversion ratios.....	94
2.8.6.	Eyewall vorticity stretching.....	98
2.9.	Wave motion	99
2.9.1.	Static stability and inertial stability.....	101
2.9.2.	Gravity waves	103
2.9.3.	Rossby radius of deformation	106
2.9.4.	Rossby waves.....	111
2.10.	Maximum potential intensity of a tropical cyclone.....	112
2.11.	Factors affecting the actual intensity of a tropical cyclone	119
3.	Correlation examined with satellite observations.....	133
3.1.	Preparatory calculations	134
3.2.	Height calculation.....	139
3.3.	Case selection	145
3.4.	Choosing a radar reflectivity threshold	148
3.5.	Choosing a radar height threshold.....	152
3.6.	Choosing thresholds for other instruments.....	156
3.7.	Association with current tropical cyclone intensification	164
3.8.	Predicting future tropical cyclone intensification	171
3.9.	Extremely tall cells and tropical cyclones.....	176
3.9.1.	Locating extremely tall cells.....	178
3.9.2.	External properties of extremely tall cells	180
3.9.3.	Internal properties of extremely tall cells	182
3.9.4.	Discussion	190
4.	Correlation examined with ground-based observations.....	194
4.1.	Calculating height, area, and eyewall location.....	197
4.2.	The agreement between coincident satellite and ground radar observations	202

4.3. Time-azimuth plots.....	207
4.4. Case study of one tropical cyclone.....	209
4.5. Selection of cases for further analysis.....	211
4.6. Statistical summary of cases.....	212
4.7. Predicting tropical cyclone intensification.....	218
5. Causation examined with theory and models	228
5.1. Indicator vs. cause	228
5.2. A burst of tall eyewall cells as a cause of intensification:	
thermodynamic upper limit.....	230
5.2.1. Addition of energy by a burst of tall eyewall cells	231
5.2.2. Eye heating rate.....	234
5.2.3. Intensity change	238
5.3. Free parameters in the thermodynamic upper limit.....	240
5.4. Verifying the thermodynamic upper limit using observations of latent	
heating	244
5.5. Tall eyewall cells as causes of intensification: catching them in the act	
of warming the eye.....	249
5.5.1. Kinematics and dynamics of a simulated tall eyewall cell	251
5.5.2. Eye warming and wind intensification	255
5.6. Tall eyewall cells as indicators of intensification	259
5.7. Future work.....	266
6. Conclusions.....	275
Appendix.....	279
References.....	290

LIST OF TABLES

Table	Page
2.1. The Saffir-Simpson tropical cyclone disaster potential scale	25
2.2. Reflectivity (dBZ) to precipitation (mm/h) relationship for convective precipitation observed by the TRMM Precipitation Radar	56
2.3. The 28 C saturated adiabat at specified altitudes, plus the background profile at 20 km	58
2.4. Maximum updraft speed and minimum ascent time for a given value of CAPE under the assumption of no entrainment constant buoyancy, and an isothermal 205 K troposphere.	74
2.5. Maximum updraft speed as affected by a simple estimate of drag and entrainment.	76
2.6. The relationship between eye temperature anomaly and surface pressure drop based on the hydrostatic equation	91
2.7. TRMM precipitation-related instrument properties	124
2.8. TRMM precipitation-related instrument properties (continued)	125
2.9. Algorithms that generate TRMM standard products for various TRMM satellite instruments	126
2.10. WSR-88D instrument properties	127
2.11. Estimates of eyewall updrafts in the vicinity of 4 m/s	128
2.12. Estimates of eyewall updrafts of 10 to 40 m/s	129
2.13. Heavy convective rain rates	130
2.14. Duration of bursts of tall convective cells and concurrent change in intensity	131
2.15. Observations of the vertical profile of the eye's thermal anomaly	132
3.1. Tropical cyclones and TRMM Precipitation Radar overflights of tropical cyclones by ocean basin for 1998 through 2006	147
3.2. Tall eyewall convection vs. tropical cyclone wind intensification	169
3.3. Independent observations related to tall eyewall cells and intensification	170
3.4. Association of intensification with various predictors	173
3.5. Convective cells identified by the maximum height of their 20 dBZ radar reflectivity during July to October in 1998 to 2005	193
4.1. Tropical cyclone eyewalls with tall eyewall convection (20 dBZ \geq 14.5 km) observed near simultaneously by the TRMM Precipitation Radar and one or more WSR-88D ground radars	206

4.2.	Intensity change (knots) in two sets of WSR-88D observation periods, sorted for use with the sign test.....	216
4.3.	Intensity change (knots) in two sets of WSR-88D observation periods taking into account a possible 6 kt error in the estimation of wind intensity.....	218
4.4.	TRMM vs. WSR-88D.....	220
4.5.	WSR-88D observation periods	221
5.1.	Input parameters for estimating eye heating.....	237
5.2.	Estimates of eye heating	237
5.3.	Multiple linear regression to forecast intensity change from the present to 12 hours in the future for TRMM Precipitation Radar overflights of North Atlantic tropical cyclones from 1998 to 2003	261
5.4.	Percent variance explained in TRMM Precipitation Radar overflights of Atlantic tropical cyclones from 1998 to 2003.....	263
5.5.	Examples of eye subsidence warming	267
5.6.	Energy conversion ratios in atmospheric convection	268
5.7.	North Atlantic TRMM overflights of tropical cyclones in 1998 to 2003 with SHIPS predictor values available	269

LIST OF FIGURES

Figure	Page
1.1. Tall convective cells outside of tropical cyclones	3
1.2. Photographs of the inner core	7
2.1. An early radar observation of a tall eyewall cell	14
2.2. The TRMM satellite.....	32
2.3. A vertical cross section of an idealized hurricane showing the outline of the eyewall clouds and the outline of clouds of convective cells outside of the eyewall	34
2.4. 3D observations of tropical cyclone eyewalls by the TRMM Precipitation Radar	35
2.5. The average number of days between times that the TRMM Precipitation Radar observes a particular point on the Earth's surface as a function of degrees of latitude from the Equator.....	38
2.6. A WSR-88D ground radar	40
2.7. Vertical cross section of a typical ground radar volume scan	42
2.8. Schematic diagrams of convective cells dynamics.....	77
2.9. Schematic diagram showing a cross section through the center of a tropical cyclone.....	79
2.10. Schematic diagram showing possible forms of eye subsidence	84
2.11. Emanuel's Maximum Potential Intensity (MPI) theory	113
2.12. Variations of temperature with height in the tropical troposphere	121
2.13. Hydrometer size and its effects on fall speed	122
2.14. Tropical cyclone wind intensity and the eye's upper tropospheric thermal anomaly.....	123
3.1. Schematic diagram of the observation geometry of instruments on the TRMM satellite.....	135
3.2. Diagrams for calculating the height of a Precipitation Radar observation	141
3.3. The cumulative distribution function (CDF) of radar reflectivity	149
3.4. Latitude dependence of the 20 dBZ height of tropical cyclone eyewalls from 1998 to 2006.....	153
3.5. Schematic diagram of a tall convective cell	155
3.6. The Cumulative Distribution Function (CDFs) for non-radar observations of 126 overflights of intensifying tropical cyclones (red) and 143 overflights of non-intensifying tropical cyclones (blue).....	157
3.7. Multi-instrument TRMM overflights of tropical cyclone eyewalls.....	159

3.8.	Ice scattering by very large ice particles in Hurricane Erin observed by the TRMM Microwave Imager on 07 Oct 2002 (TRMM orbit #27905) off the coast of Georgia	162
3.9.	Tropical cyclone overflights segregated into three populations of size n based on the maximum height h of their eyewall's 20 dBZ signal	164
3.10.	Hurricane Carlotta at 1055 UT on 20 June 2000, at 14.66°N, 101.02°W.	
3.11.	The locations of convective cells with a 20 dBZ signal at least 17 km high during July through October of 1998 to 2005	181
3.12.	The observed distribution of θ_e (K) including heat of fusion	190
4.1.	Schematic diagram of the observation geometry of a weather radar on the ground	198
4.2.	Ground radar coverage in the southeast U.S. and 2004 tropical cyclone tracks	204
4.3.	Time-azimuth plots of the eyewall of Hurricane Georges on 25 September 1998	211
4.4.	Statistical distributions of satellite and ground radar observations of tall eyewall cells	214
4.5.	Comparison of Hurricane Alex's (2004) eyewall observed nearly simultaneously by the TRMM Precipitation Radar and two WSR-88D ground radars	222
4.6.	Comparison of Hurricane Claudette's (2003) eyewall observed nearly simultaneously by the TRMM Precipitation Radar and two WSR-88D ground radars	223
4.7.	Time-azimuth plots for intensifying tropical cyclones	224
4.8.	Time-azimuth plots for non-intensifying tropical cyclones	225
4.9.	Time-azimuth plots for non-intensifying tropical cyclones (continued)	226
4.10.	Evolution of a convective cell in Hurricane George's (1998) eyewall	227
5.1.	Two ways of looking at tall cells	229
5.2.	A schematic representation of a tropical cyclone whose eye is being warmed by a tall eyewall cell	232
5.3.	Variations in the maximum possible intensity change by changing the rain rate and horizontal area of tall eyewall cells	241
5.4.	Variations in the maximum possible intensity change by altering (1) the efficiency with which the eyewall latent heating is converted into eye warming and (2) the duration of the burst of tall eyewall cells	241
5.5.	Variations in the maximum possible intensity change caused by changes in the size of the inner radius of the eyewall	243
5.6.	The distribution of eyewall average rain rates observed by the TRMM Precipitation Radar in 1998 to 2003	271
5.7.	Subsidence heating from a tall eyewall cell observed in a simulation of Hurricane Bonnie 1080 minutes (18 hours) after the beginning of the simulation at a height of 14.9 km	272
5.8.	Same as Figure 5.7 except at a height of 10.9 km	273

5.9. Vertical profiles of updraft velocity and temperature for the simulated tall eyewall cell shown in Figures 5.7 and 5.8	274
--	-----

LIST OF ABBREVIATIONS

AMS	American Meteorological Society
CAPE	Convectively Available Potential Energy ($\text{J/kg}=\text{m}^2/\text{s}^2$)
CDF	Cumulative distribution function, the integral of the probability density function
dBZ	The logarithmic unit of radar reflectivity
GPM	Global Precipitation Measuring Mission, the NASA / JAXA experimental weather satellite scheduled for launch in 2013
HDF	Hierarchical data format, the file format used in the TRMM data archive
HRD	Hurricane Research Division, the civilian tropical cyclone research group within the U. S. National Weather Service
JAXA	Japan Aerospace Exploration Agency, the Japanese counterpart to NASA
LIS	TRMM Lightning Imaging Sensor
micron (μ)	An abbreviation for micrometer, $1\text{e-}6$ meters
NOAA	National Oceanic and Atmospheric Administration, the U.S. federal agency that contains the NHC, HRD, and NWS.
NHC	National Hurricane Center, the civilian operational tropical cyclone forecasting center within the National Weather Service
NWS	National Weather Service, the organization within the U.S. government that issues the official weather forecasts
PCT	Polarization corrected brightness temperature
PR	TRMM Precipitation Radar
p., pp.	Page and pages
TMI	TRMM Microwave Imager
TRMM	Tropical Rainfall Measuring Mission, the NASA / JAXA experimental weather satellite launched in 1997

UT	Universal Time. Universal time is within a few seconds of the time at zero degrees longitude [<i>Langley</i> , 1999].
VIRS	TRMM Visible and Infrared Scanner
WSR-88D	Weather Service Radar – 1988 Doppler, the designation of the current generation of operational weather radars used by the National Weather Service

<u>Variable</u>	<u>Units and their abbreviation</u>
Acceleration (a)	m/s^2
Angular frequency (ω)	1/s or radian/second
Area (A)	m^2 , $\text{km}^2 = 1\text{e}6 \text{ m}^2$
Column density	kg/m^2
Density (ρ)	kg/m^3
Energy (E)	Joule (J) = N m = $\text{kg m}^2 / \text{s}^2$
Energy flux	$\text{W} / \text{m}^2 = \text{J} / \text{s m}^2$
Force	Newton (N) = $\text{kg m} / \text{s}^2$
Frequency (f)	Gigahertz (GHz) = $1\text{e}6 \text{ Hz} = 1\text{e}6 \text{ cycles per second}$
Heat	J
Heat capacity (c)	J / K
Length	meter (m), kilometer (km), centimeter (cm) = $1\text{e}-2 \text{ m}$, millimeter (mm) = $1\text{e}-3 \text{ m}$, micron or micrometer $\mu = 1\text{e}-6 \text{ m}$
Mass (m)	kilogram (kg), gram (g)
Period (T)	s or second/cycle
Power (P)	watt (W) = $\text{J} / \text{s} = \text{kg m}^2 / \text{s}^3$, milliwatt (mW) = $1\text{e}-3 \text{ W}$
Precipitation rate (R)	mm/h, the millimeter depth of liquid water that would accumulate in 1 hour on a horizontal surface if the precipitation rate were constant for 1 hour
Pressure (p)	millibar (mbar) = 1 hPa = 100 Pa, Pascal (Pa) = $\text{N} / \text{m}^2 = \text{kg} / \text{m s}^2$
Radar reflectivity (Z)	dBZ (See section 2.5)
Specific enthalpy (k)	J / kg
Specific heat capacity (c)	J / K kg

Speed (v)	m/s, knots (kt) = 0.52 m/s
Temperature (T)	degrees Kelvin (K) = 273.16+C [<i>Wallace and Hobbs</i> , 2006, p. 468], Celsius (C), Fahrenheit (F)=1.8C+32
Time (t)	second (s), hour (h), day (d)
Volume (V)	m ³ , km ³ = 1e9 m ³ , cm ³ = 1e-6 m ³
Wavelength (λ)	m or meter/cycle
Wavenumber (k)	1/m or radian/meter

LIST OF SYMBOLS

Γ Gamma. The lapse rate Γ (K/km) is the observed rate at which temperature decreases with increasing altitude. The adiabatic lapse rate for saturated air Γ_s in the lower troposphere is approximately 5 to 6 K/km [Bohren and Albrecht, 1998, p. 292]. The dry adiabatic lapse rate Γ_d is 10 K/km in the lower troposphere [Bohren and Albrecht, 1998, p. 109] and varies little with altitude in the troposphere because gravity and the molecular mass of air is nearly constant [CRC, 2004, p. 14–23, Figure 3; Bohren and Albrecht, 1998, equation 3.46]. The dry adiabatic lapse rate is defined as $\Gamma_d = g / c_p$. At the surface, this equation gives a value of

$$\Gamma_{d, \text{surface}} = \frac{9.81 \text{ m/s}^2}{1004 \text{ J/K kg}} = 9.8 \text{ K/km}.$$

ε Epsilon. Thermodynamic efficiency (unitless).

ζ Zeta. Relative vorticity (radian/second or 1/s).

η Eta. Total vorticity (radian/second or 1/s), the sum of planetary vorticity f and relative vorticity ζ .

λ Lambda. Wavelength (m or meter/cycle).

μ Mu. Population mean.

ρ Rho. Atmospheric density (kg/m³).

ρ_0 Atmospheric density at the Earth's surface. In general, density can be calculated from more frequently measured quantities using a form of the ideal gas law [Wallace and Hobbs, 2006, p. 3]:

$$\rho = \frac{p}{R T}$$

Where p is pressure (Pa), R is the gas constant (J/K kg), and T is temperature (K). In fair weather at the tropical ocean's surface during tropical cyclone season ($p = 1010$ mbar; $q = 20$ g/kg; $R = 289$ J/K kg; $T=28^\circ\text{C}=301\text{K}$), the air density is 1.16 kg/m³. Under the eye of a tropical cyclone the pressure is ~5% lower ($p \approx 950$ mbar), so the surface density is also correspondingly 5% lower, 1.09 kg/m³.

σ	Sigma. Population standard deviation.
τ	Tau. Optical depth, the fraction of energy lost per unit distance that a beam of energy travels through a media.
A	Area in m^2 or km^2
C, c	(1) A constant of proportionality. (2) Heat capacity, the energy that must be added to an object or a unit mass to increase its temperature by 1 K in the absence of a phase change. Units are J/K, J/K kg, or J / K g. (3) The speed of light, $3.00\text{e}8$ m/s [<i>Wallace and Hobbs</i> , 2006, p. 467].
c_p	Specific heat capacity of dry air at constant pressure (1004 J/K kg) [<i>Wallace and Hobbs</i> , 2006, p. 467]
e	Base of the natural logarithm, 2.71828...
E	Energy (J)
F	(1) Flux, the rate that energy passes through a surface ($\text{J} / \text{s} \text{m}^2 = \text{watt} / \text{m}^2$). (2) Force (N).
f	(1) Coriolis parameter, $2 \Omega \sin \text{latitude}$, where Ω is the earth's angular velocity of rotation, 2π radians / (24×60^2 seconds) = $7.272\text{e-}5$ rad/s. At latitudes where tropical cyclones typically exist, f ranges from $3.764\text{e-}5$ 1/s at 15°N to $8.342\text{e-}5$ 1/s at 35°N . The coriolis parameter is sometimes referred to as the "planetary vorticity." (2) frequency (1/s or cycle/second). $f = 1/T, f = 2\pi w$.
g	Acceleration due to gravity, 9.8 m/s^2 . Equal to $G m_e / r^2$, where the universal gravitation constant G is $6.673\text{e-}11 \text{ N m}^2/\text{kg}^2$ [<i>Serway and Jewett</i> , 2004, p. 391], the mass of the Earth m_e is $5.97\text{e}24$ kg [<i>Wallace and Hobbs</i> , 2006, p. 469], and the average radius of the Earth r_e is 6371 km. At the Earth's surface, $g = 9.81 \text{ m/s}^2$, and at a 20 km altitude, $g = 9.75 \text{ m/s}^2$, so a value of 9.8 m/s^2 is used through out the dissertation.
H, h	Heating rate (J/s, K/day, or K/h)
k	(1) Scattering coefficient. (2) Specific enthalpy (J/kg). (3) Wavenumber (1/m or radian/meter).
L_f	Latent heat of fusion of water ($0.334\text{e}3$ J/g) [<i>Wallace and Hobbs</i> , 2006, p. 468]
\ln	Natural log, which is a logarithm to the base e, i.e., $\ln x = \log_e x = \log_{2.71828...} x$
\log	Logarithm to the base 10, i.e., $\log x = \log_{10} x$

L_v	Latent heat of vaporization of water (2.5e3 J/g) [<i>Wallace and Hobbs</i> , 2006, p. 468]
m	(1) Column mass (kg/m ²). (2) Mass (kg). (3) Sample mean, i.e., the observed mean of a sample from a population. (4) Sample median, i.e., the observed median of a sample.
N	Brunt-Vaisala frequency N averages 0.0115 radian/second in the troposphere [<i>Lane and Reeder</i> , 2001, p. 2427], which corresponds to buoyant oscillations with periods of approximately 9 minutes. Often the units of N are stated as 1/s.
N^2	Static stability, which equals the square of the Brunt-Vaisala frequency [section 2.9.1; <i>Montgomery and Enagonio</i> , 1998, p. 3177].
P	Power, the rate of energy transfer (J/s=watt)
p	Pressure, units of millibar (mbar) or hectopascal (hPa). 1 mbar = 1 hPa.
q	Specific humidity, the ratio of the mass of water vapor to the total mass of water vapor and dry air in a unit volume. Specific humidity is within a few percent of the more often reported value of water vapor mixing ratio (w). See the definition of w for units and variables used in calculating q [<i>Djuric</i> , 1994, p. 71]: $q = 0.622 \frac{p_{\text{vapor}}}{p} = \frac{R}{R_{\text{vapor}}} \frac{p_{\text{vapor}}}{p} \approx w$
r	Radius or distance between two points
R, R_d	(1) Precipitation rate, usually reported in mm/h but occasionally in inches per hour. 25.4 mm/h = 1 inch per hour. (2) Rossby radius of deformation [section 2.9.3, p. 106]. (3) The gas constant for dry air (R_d) is 287 J/K kg [<i>Wallace and Hobbs</i> , 2006, p. 467]. The gas constant for moist air (R) typically 287–289 J/K/kg in the lower troposphere and near R_d in the upper troposphere. R can be calculated as a thousand times (1000 g/kg) the universal gas constant R^* (8.3143 J/K mole) divided the molecular mass m of moist air (mole/g). The molecular mass of moist air can be calculated from the specific humidity q (g water / kg air+water) and from the molecular masses of dry air m_{dry} (28.97 g/mole) and water vapor m_{vapor} (18.97 g/mole) [<i>Wallace and Hobbs</i> , 2006, p. 65]: $m = \frac{q}{1000} m_{\text{vapor}} + \left(1 - \frac{q}{1000}\right) m_{\text{dry}}$ $R = 1000 \frac{R^*}{m}$
r_{earth}	Average radius of the earth, 6371 km. This quantity can be calculated from the equatorial and polar radii of the Earth, which are 6378.1 km and 6356.6

km [CRC, 2004, p. 14–3]. The mean radius of an ellipsoid, such as the Earth, can be calculated as the radius of a sphere with volume equal to that of the ellipsoid, $\frac{4}{3} \pi r^3 = \frac{4}{3} \pi abc$ [CRC, 1991, p. 112]. The mean radius works out to $r_{mean}=6371$ km using $r_{mean} = \sqrt[3]{r_{eq}^2 r_{pole}}$.

s Sample standard deviation, i.e., the observed standard deviation of a population. *s* is calculated as the square root of sample variance. Sample variance for a collection of *n* measurements of variable *x* with sample mean *m* is the following [Bhattacharyya and Johnson, 1977, p. 35]:

$$\frac{\sum (x - m)^2}{n - 1}$$

t (1) Duration of an event (seconds). (2) The statistic of the t-test.

T (1) Temperature (K). (2) Period of a wave (s or second/cycle). $T = 1/f$, $T = 2\pi / w$.

T_b Brightness temperature (K)

v Velocity, generally in m/s for calculations, but sometimes reported in knots (kt). 1 m/s = 1.94 kt = 2.24 mph = 3.6 km per hour

v_{sound} Speed of sound is from 340 m/s to 295 m/s between the surface and the lapse rate tropopause according to the U.S. standard atmosphere, which describes mid-latitude conditions [CRC, 2004, p. 14–20 to 14–21]. Houghton [1986, p. 106] gives the following formula for calculating the speed of sound: $v_{sound} = \sqrt{\gamma p \rho}$. The ratio of the specific heat capacity at constant pressure to the specific heat capacity at constant volume is $\gamma=1.4$ [Houghton, 1986, p.224]. Using this formula, at the Earth's surface, $v_{sound} = \sqrt{1.4 (1013e2 \text{ Pa}) (1.17 \text{ kg/m}^3)} = 348 \text{ m/s}$ based on the tropical values in Table 2.3 (p. 58). At a 15 km latitude, $v_{sound} = \sqrt{1.4 (130e2 \text{ Pa}) (0.22 \text{ kg/m}^3)} = 287 \text{ m/s}$.

w (1) Angular frequency (radians/second or 1/s). (2) Water vapor mixing ratio, the ratio of the mass of water vapor to the mass of dry air in a unit volume. Normally reported in units of grams of water per kg of air (i.e., g/kg). Must be converted to units of kg/kg for use in some calculations. Calculated in units of kg/kg from the water vapor pressure p_{vapor} , total atmospheric pressure *p*, and the ratio of gas constants for moist air and water vapor, R/R_{vapor} [Djuric, 1994, p. 71]:

$$w = 0.622 \frac{p_{vapor}}{p - p_{vapor}} = \frac{R}{R_{vapor}} \frac{p_{vapor}}{p - p_{vapor}}$$

Z	(1) Radar reflectivity (dBZ). (2) A value in the standard normal distribution.
z	Altitude in meters for calculations, but often reported in km
z_0	Scale height of atmospheric density in the troposphere (7 km) [<i>Wallace and Hobbs</i> , 2006, p. 9]

ABSTRACT

THE ASSOCIATION OF TALL EYEWALL CONVECTION WITH TROPICAL CYCLONE INTENSIFICATION

Owen A. Kelley, Ph.D.

George Mason University, 2008

Dissertation Director: Michael Summers

Despite decades of research, operational weather agencies still find it difficult to predict change in the intensity of a tropical cyclone's surface wind. This dissertation examines whether precipitation cells in a tropical cyclone eyewall provide information about change in wind intensity. Nine years of tropical cyclone overflights are studied with the first radar in space capable of resolving the detailed three-dimensional structure of precipitation. This radar is the Precipitation Radar on the Tropical Rainfall Measuring Mission (TRMM) satellite. With a single satellite overflight, the presence or absence of a tall eyewall cell correctly identifies whether or not intensification is occurring 62% of the time (166 out of 269 overflights). The empirical association of tall eyewall cells and wind intensification is also examined in a decade of tropical cyclones near landfall observed with the WSR-88D ground radars along the U.S. coast. With at least a 3 hour period of continuous ground radar observation, the frequent occurrence of tall eyewall

cells (at least 1 in 3 volume scans) correctly identifies whether or not wind intensification is occurring 83% of the time (24 out of 29 observation periods). These results suggest that the near-continuous nature of ground radar data compensates for the ground radar's coarser vertical resolution compared with the TRMM satellite radar. Physical mechanisms for the observed association are discussed. Based on an upper bound calculation, the energy released during a 9 hour long burst of tall eyewall cells could warm a tropical cyclone's eye by at most 4 K if the eye's radius were small (20 km). If the eye's radius were large (40 km), the same cells could warm the eye by at most 1 K. These upper bounds are based on the amount of latent heat released by the burst of tall cells. From the upper bound to the eye warming, an upper bound can be estimated for the maximum wind intensification that might be caused by the tall eyewall cells.

1.

Introduction

This dissertation examines to what extent tall rain cells in a tropical cyclone's eyewall is associated with increases in a tropical cyclone's surface wind intensity. The dissertation presents empirical evidence and physical mechanisms related to this idea.

This work may enhance our understanding of tropical cyclones and might assist with making forecasts of tropical cyclone wind intensity. Despite decades of research, operational weather agencies still find it difficult to predict changes in tropical cyclone winds [*Rogers et al.*, 2006; *USWRP*, 2000; *Heymsfield et al.*, 2001; *DeMaria and Kaplan*, 1999; *DeMaria and Gross*, 2003]. These winds threaten life and property when a cyclone approaches land [*Rappaport*, 2000]. The dissertation is related to earlier research on tall precipitation cells by Dr. Joanne Simpson [*Malkus*, 1959]. For this dissertation, 50,000 lines of software are written to convert the coordinates of satellite and ground-based data, to locate the eyewall region, to calculate summary statistics from the observations, and to visualize the observations at various intermediate steps. To examine combinations of variables not available in observations, the output from a high-resolution tropical cyclone simulation is analyzed. Various theoretical concepts are used

from radar engineering, statistics, atmospheric physics, and atmospheric thermodynamics.

When first considering this topic, several questions naturally arise: why not directly measure wind change instead of inferring it from the tropical cyclone's structure, why examine precipitation instead of clouds, why focus on the height of convection, why limit the study to the tropical cyclone's eyewall, and why has this study not been conducted before? A tropical cyclone's current wind intensity is difficult to measure accurately in realtime or even to estimate during post-analysis as is discussed at the beginning of chapter 4. Even if measurement were easy, predicting future winds from current winds would still be difficult. For this reason, it is reasonable to try instead to infer the change in wind intensity from tropical cyclone structure, as is done in this dissertation. *Smith* [2000] emphasizes the connection between tropical cyclone structure and wind intensity:

Because of the recognized importance of moist convection in hurricane dynamics, it is possible that any major improvement in intensity forecasts will depend, inter alia, on improvements in the representation of convection in hurricane models. In turn, such improvements will require improvements in our understanding of convection in hurricanes.

Moving on to the next question, one reason why precipitation is a helpful quantity to measure is that steady precipitation implies a steady addition of energy into the tropical cyclone in the form of latent heat that is released as water vapor condenses. In contrast, persistent clouds do not imply constant energy being added. A good reason to look at the radar-observed height of precipitation cells is that this height is not currently being used to make operational tropical cyclone forecasts. The reason for limiting the study to the

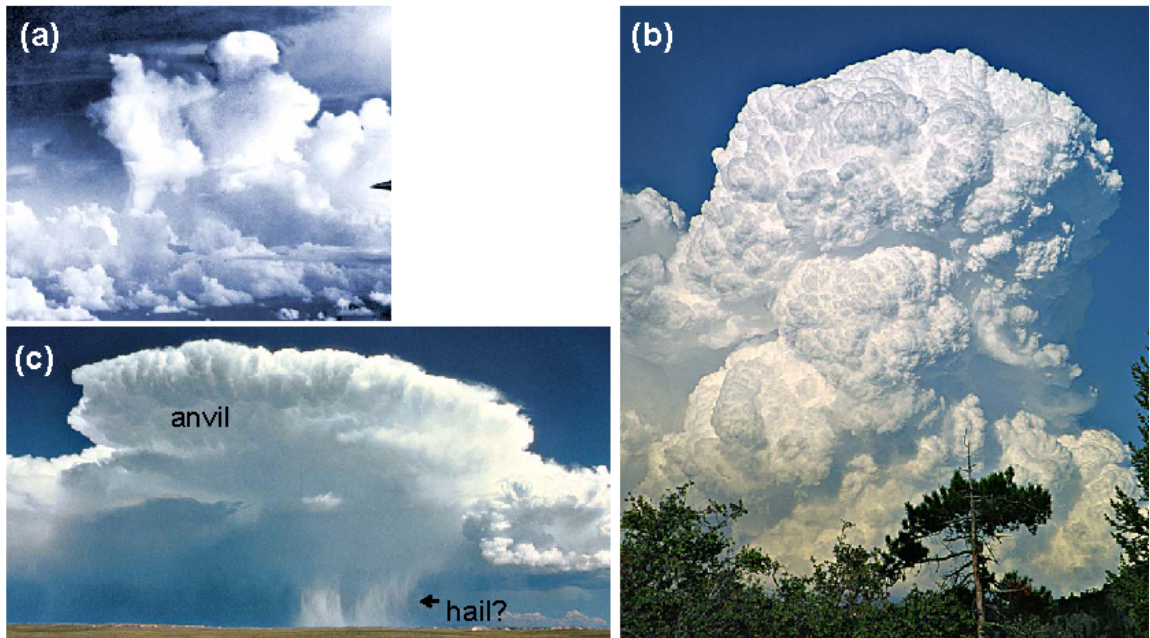


Figure 1.1. Tall convective cells outside of tropical cyclones. (a) Figure 5.40c from *Malkus and Riehl* [1964, p. 143]. The cell in the middle of the photo is 12 km tall. This photo was taken at 0672 UT in August of 1957 on leg 1 of flight 3 around 20°N latitude and 170°E longitude, west of Hawaii. (b) An isolated "young" tower forming over land. (c) A mature, large convective cell, displaying upper level outflow in the form of an "anvil" cloud. Panels b and c are from the UCAR Digital Image Library, where they are titled "towering cumulus cloud" (image DI-168) and "mature cumulonimbus" (image DI-104) at <http://www.fin.ucar.edu/ucardil/>. The date and location of panels b and c are unknown.

eyewall is primarily a practical one. The only precipitation radar in space has a narrow field of view (only 215 km across), which means that, on occasion, the entire eyewall is observed but the rainbands that extend up to 1000 km away from the tropical cyclone's center are never observed all at once. This study was not performed years ago because the first and only precipitation radar in space was launched in 1997 and it required nine years to collect a sufficiently large sample of tropical cyclone observations to calculate robust statistics on eyewall convection.

This dissertation continues a line of reasoning about tall precipitation cells that Joanne Simpson (formerly named Joanne Malkus) and Herbert Riehl began in the 1950s.

In 1958, they had the theoretical insight that a few tall cells are the upward leg of the general circulation of the atmosphere [*Riehl and Malkus*, 1958]. More specifically, Riehl and Malkus proposed that the majority of air transported upward near the Equator was transported inside of just 1000 to 3000 convective cells at any given time that were tall enough to approach the tropical tropopause (a ~15 km altitude). In contrast, the vast majority of clouds over the tropical ocean are non-precipitating and are short: they do not even reach the freezing level (a ~5 km altitude). *Wylie et al.* [2005] find that about half (47%) of the Earth is covered with low-level dense clouds, while *Alcala et al.* [2002] find that only 0.01% of the Tropics is covered with convective cells that overshoot the tropopause.

Compact storms are often called "convective cells," in part because they can be visually distinct from surrounding clouds, as shown in Figure 1.1. The term "cell" can be applied even if the storm cloud touches adjacent clouds because a convective cell is defined as a region of low-level inflow, mid-level updraft, and upper-level outflow. For example, a hurricane's eyewall is composed of convective cells bunched together so that a satellite photo shows an arc of convection rather than distinct cells (Figure 1.2). Whether isolated or bunched together, convective cells tend to form with a particular scale of approximately 10 km across horizontally [*Ray*, 1986, pp. 23, 332] and they last approximately 30 to 60 minutes [*Emanuel*, 1994, pp. 231–233; *Hendricks et al.*, 2004]. Tropical cyclones and other long-lived storms often appear to be an aggregate of convective cells plus the various non-precipitating cloud remnants from earlier

convective cells. This cellular structure exists in mesoscale convective systems (MCS) and mid-latitude squall lines [*Doswell*, 2001, p. 4].

A nickname for tall cell is "hot tower," and it is worth considering the physical reason for this nickname [*Anthes*, 2003]. For each gram of water vapor that condenses to form cloud droplets, enough latent heat is released to warm a cubic meter of air at the Earth's surface approximately 2.5 degrees Celsius. The variables used in this calculation are the specific latent heat of water (2500 J per gram of water), the specific heat of air at constant pressure (1004 J/K kg), the density of liquid water (1 g/cm³), and the density of air at the Earth's surface (~1 kg/m³) [*Wallace and Hobbs*, 2006]. Air warmed by even a fraction of a degree Celsius becomes less dense than its surroundings, which causes it to move upward due to its buoyancy (section 2.7). The circulation of mass and energy due to buoyancy is called "convection." A tall cell is called a "hot tower" because latent heat is released inside the cell.

Only one year after proposing that tall eyewall cells were important to the general circulation, *Malkus* [1959] proposed that a few tall undilute convective cells in a tropical cyclone eyewall were responsible for maintaining the tropical cyclone's circulation. This proposal became known as the "hot tower hypothesis" [*Anthes*, 2003]. The circulation is composed of air spiraling inward at the surface, moving up in the eyewall, and spiraling outward in the upper troposphere. This circulation is shown in blue in Figure 2.9 (p. 79).

From the 1960s to the 1990s, most scientists shifted their research away from tropical cyclone hot towers because other "gears" of a tropical cyclone's machinery appeared to provide more information about wind intensity. Tropical cyclone eyewalls

were simulated as symmetric rings because the discrete cells that compose the ring were considered an unimportant detail [*Emanuel*, 2002, pp. 80–81; *Camp and Montgomery*, 2001]. In these models, the eyewall appears as a featureless ring as is sometimes seen in real life (Figure 1.2a and 1.2b). The models make no allowance for an occasional occurrence of tall cells in the eyewall. During these decades, what captured scientists' imaginations were questions external to the tropical cyclone such as figuring out how much latent heat was transferred from ocean to atmosphere [*Craig and Gray*, 1996], not the later release of that latent heat in the eyewall.

Ironically, during the 1970s and 1980s, operational forecasters developed a very successful technique for predicting tropical cyclone wind intensity based on exactly the property of the tropical cyclones that was de-emphasized by researchers during those decades: the details of the non-symmetric eyewall cloud cover [*Dvorak*, 1975; *Velden et al.*, 2006; *Holland*, 1997, pp. 2533–2534].

During the same decades, some observational studies reported that the symmetric ring of convective cells was sometimes interrupted by spectacular episodes of a few tall convective cells. For example, *Lyons and Keen* [1994] talk about "explosive outbreaks" that produce "a radically different dynamical and microphysical environment" in intensifying tropical cyclones vs. steady tropical cyclones. Occasionally, tropical cyclone photos show a tall cell in the eyewall (Figures 1.2d and 1.2e). These events led to renewed interest in eyewall convective cells [*Wang and Wu*, 2004], but progress was hampered by lack of observations [*Reasor et al.*, 2000]. There was no archive of observations that could show how often tall eyewall cells were forming. Decades after

starting this avenue of research, Joanne Simpson championed the development of a satellite that would help to overcome this lack of data: the Tropical Rainfall Measuring Mission (TRMM) satellite launched in 1997 [Tao and Adler, 2003, chapters 13–15].

Today, with a decade of data archived from the TRMM satellite and from the latest generation of NOAA ground radars, this dissertation can conduct a survey of the height, horizontal size, and frequency of tall eyewall cells in many tropical cyclones. The

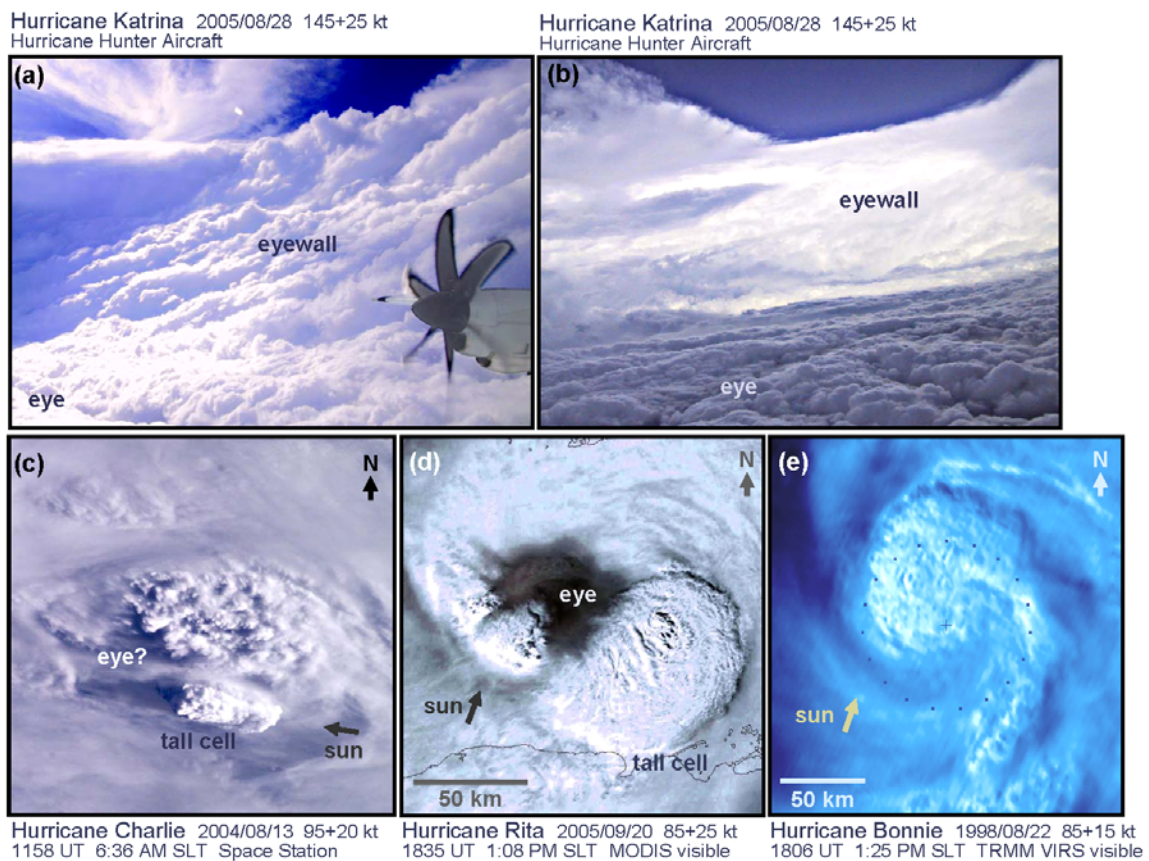


Figure 1.2. Photographs of the hurricane inner core. The photo captions give the name of the storm, the date in yyyy/mm/dd format, the NHC best track estimate of the current wind intensity and the change in wind intensity between six hour before and after the time of observation, the universal time (UT) of the observation, the solar local time (SLT) of the observation which is UT minus the longitude divided by 15 degrees per hour, and the source of the photograph. The photos are described in further detail at the end of chapter 1.

dissertation finds that tall eyewall cells are relatively common: 26% of the time (69 out of 269 TRMM satellite overflights) the eyewall contains at least one tall cell (Table 3.2, p. 169).

It is important to understand the terms in the dissertation's title because they are used throughout the text. "Tropical cyclone" is the name for warm-core systems throughout the Tropics. "Hurricane" specifically refers to a tropical cyclone that forms in the Atlantic ocean and East Pacific Ocean. "Typhoon" refers to a tropical cyclone that form in the West Pacific Ocean. Everywhere, the storms can be called by the generic name of "tropical cyclone" [*Wallace and Hobbs*, 2002, p. 336]. Answers to many questions about tropical cyclones can be found on the Frequently Asked Questions page maintained by Chris Landsea on the National Hurricane Center's (NHC) web site: <http://www.nhc.noaa.gov> .

When a convective cell is called "tall," this dissertation means that the region inside of the cell that contains precipitation extends above a fixed height threshold. Precipitation is falling drops of liquid water or ice particles. Chapter 3 analyzes TRMM data to come up with such a height threshold. Some texts use the counter-intuitive term "deep convection" instead of "tall convection" [*Emanuel*, 1994, chapter 14].

The most precise definition of a tropical cyclone's intensity is the maximum wind speed that exists anywhere at a height of 10 meters and that is sustained for a one-minute period [*Franklin et al.*, 2000; *NOAA*, 2007, p. 1–31]. Sustained surface winds are related to the damage done by a tropical cyclone that comes ashore [*Simpson et al.*, 2003, chapters 7 and 8; *Simpson*, 1973; *Rappaport*, 2000]. Obviously, the actual intensity of a

tropical cyclone can never be known because it would be impossible to measure the wind speed continuously at all locations under it. During the majority of a tropical cyclone's life when it is over ocean, surface winds are not measured anywhere. Instead, the surface winds are inferred from infrared cloud-top measurements, predicted in numerical simulations, or extrapolated from wind speeds observed by aircraft flying near a 3 km altitude.

Wind intensity is not the sole determinant of the damage caused by a tropical cyclone. On the coast, the greatest damage is done by a tropical cyclone's storm "surge," in which the ocean floods up to several kilometers inland [*Rappaport*, 2000]. Storm surge is largely determined by the shape of the coast and the shape of the seabed, although the surface wind intensity does also influence the height of the surge [*As-Salek*, 1998]. Further inland, the greatest damage and largest number of fatalities are often due to river flooding from the tropical cyclone's rainfall [*Negri et al.*, 1999; *Rappaport*, 2000]. The rain accumulation is influenced by the background humidity and instability of air in front of the tropical cyclone and by how long the tropical cyclone hovers over one location [*Houston et al.*, 1999; *Bosart and Dean*, 1991]. The surface wind intensity is very indirectly related to the total accumulation of surface precipitation [*Lonfat et al.*, 2004]. Even direct wind damage is not exactly proportional to wind intensity because other factors affect wind damage. These factors include the size of the tropical cyclone (which influences the duration of the high winds) and the speed of wind gusts under 1 minute in duration [*Powell et al.*, 1996; *Krayer and Marshall*, 1992]. *Pielke and Landsea* [1998] show that the damage varies approximately as the fourth power of the wind

speed. Despite the difficulties in measuring tropical cyclone intensity and despite the loose connection between wind speed and damage, tropical cyclone intensity is the most frequently used method for communicating to the public the damage potential.

A recent report asks, “Given the amount of effort that has been expended to observe, analyze, and predict tropical cyclone intensity change, why has so little progress been made?” [USWRP, 2000] Another recent study states a similar sentiment: “Intensity forecasts have little skill and have shown only slight improvement in the past 20 years” [Heymsfield *et al.*, 2001; DeMaria and Kaplan, 1999]. DeMaria and Gross [2003] show that the average 24-hour wind intensity forecasts issued by the National Hurricane Center had errors of approximately 15 knots around 1990 and only slightly lower errors of about 12 knots around the year 2000 [p. 122]. This error is equivalent to almost a full tropical cyclone "category" since each of the five categories on the Saffir-Simpson intensity scale cover about a 20 knot interval [Table 2.1, p. 25; Simpson, 1974].

Much of the dissertation examines specialized observations of tropical cyclone eyewalls, but to have a better sense of what the eyewall looks like, Figure 1.2 provides several photos. Figure 1.2a shows the gentle slope of the eyewall in the absence of tall eyewall cells. Figure 1.2b shows low-level eye clouds in shadow in the foreground due to the sun being blocked by the side of the eyewall behind the photo. Photos a and b were taken from a Hurricane Hunter Aircraft at a ~3 km altitude on the morning of 27 August 2005 in the middle of the eye of category 5 Hurricane Katrina. The eye's sea level pressure observed by a dropsonde at this time was 907 mbar, which is well below

the 920 mbar upper limit for a category 5 tropical cyclone (section 2.1.8). The photos can be downloaded from <http://www.hurricanehunters.com> .

In Figure 1.2c, a tall eyewall cell seen jutting out from the rest of the cloud cover in the neighborhood of the tropical cyclone's eyewall. As sometimes occurs, the cloud cover is obscuring the exactly location of the eye. It is not possible to tell from the photograph whether or not the tall cell is in the eyewall. At this time, Hurricane Charlie (2004) was undergoing rapid intensification near landfall. This photo was taken by an astronaut on the International Space Station, is centered on 24.7°N and 82.9°W, and was downloaded from <http://eol.jsc.naa.gov> as photo number ISS009-E-18184.

Figure 1.2d shows Hurricane Rita (2005) with two tall eyewall cells, as observed by the MODIS visible channels on NASA's Aqua satellite. The photo has 250 meter horizontal resolution and was contrast enhanced by the author after downloading Rita.A2005263.1835.250m.jpg from the MODIS rapid response web site <http://rapidfire.sci.gsfc.nasa.gov> . In Figure 1.2e, the ocean surface in the eye of Hurricane Bonnie (1998) is completely obscured by high-level clouds. The eye location is marked with a "+" in the middle of the photo, based on simultaneous radar observations. The ring of blue dots indicates the 50 km radius from the center of the eye. The radar observations reveal that the eyewall was a little closer to the eye than 50 km. The upper-level outflow seen in the northwest portion of the eyewall in Figure 1.2e is due to the tall cells observed by the TRMM Precipitation Radar. A 3D representation of the precipitation in these cells is shown in Figure 2.4a (p. 35).

The data used in this study are introduced in sections 2.3 through 2.5 and described in detail in sections 3.1 and 4.1. The data analysis method is described in sections 3.3 through 3.8 and sections 4.2 through 4.7. The primary focus of the dissertation is analyzing observations of tall eyewall cells. However, the dissertation does examine some simulated tall cells in section 5.5.

2.

Literature Review

2.1 Tall convective cells in tropical cyclone eyewalls

2.1.1. History of tall eyewall cell observations

This section first reviews the history of observations of tall cells in tropical cyclone eyewalls and then reviews our limited knowledge of the properties of these cells. The term "convective cell" was popularized as a result of the 1940s Thunderstorm Project, the first major field campaign to study continental storms with radar [*Doswell*, 2001, p. 4].

In 1958, during an early tropical cyclone research flight [*Dorst*, 2007], an aircraft radar observed tall convection in the eyewall of Hurricane Daisy [*Jordan et al.*, 1960].

This radar observation led to the theory that tall cells in a tropical cyclone eyewall were important to maintaining the tropical cyclone's surface winds [*Malkus*, 1960]. As can be seen in Figure 2.1, this early observation was blurry and the radar reflectivity measurement was merely qualitative.

In 1961, the first weather satellite to fly with an infrared instrument during hurricane season saw tall eyewall convection inside of Hurricane Anna, the first tropical cyclone of the season [Bandeem *et al.*, 1963]. The satellite was spin stabilized, which caused it to point earthward during only one portion of each orbit. This satellite was part of the series of weather satellites called Television Infrared Observation Satellites (TIROS). Some of the coldest 11 micron infrared temperatures observed during the first few years of TIROS operation occurred in Hurricane Anna (1961) on July 21 during a period of intensification from category 1 to category 3. These very cold temperatures

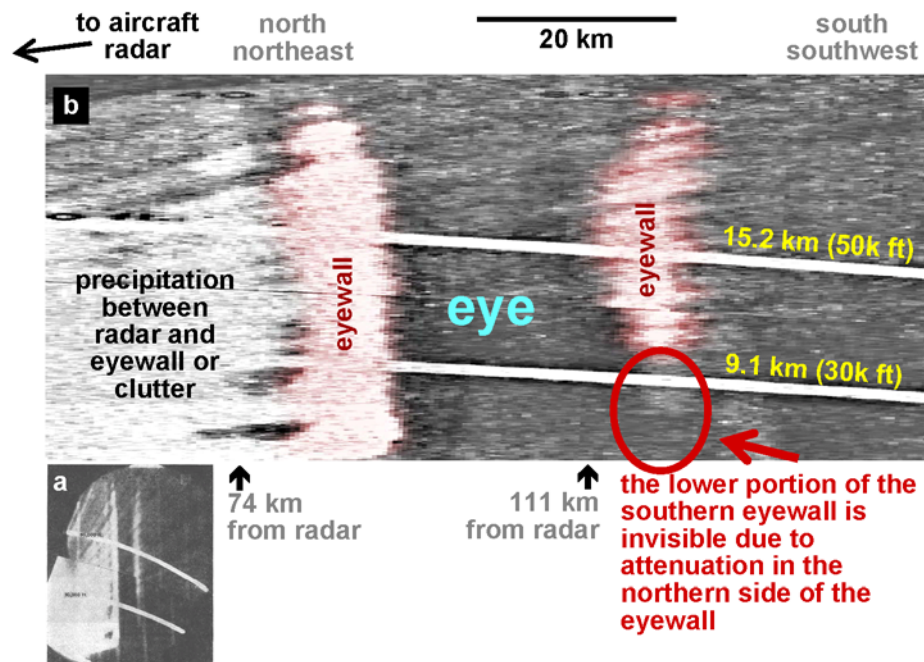


Figure 2.1. An early radar observation of a tall eyewall cell. (a) A vertical cross section of the eyewall of Hurricane Daisy (1958) from Figure 4 of *Jordan et al.* [1960]. The aircraft observations of Hurricane Daisy were the first radar observations of tall convective cells in hurricane eyewalls [*Simpson et al.*, 1998; *Malkus*, 1960]. (b) A contrast-enhanced version of the same figure.

(201 to 207 K \pm 5 K) were attributed to anvils of cumulonimbus clouds tall enough to reach the 16 km high tropical tropopause [*Bandeen et al.*, 1963; See also *Fujita and Arnold*, 1963; *Tepper*, 1963]. This cold temperature is more impressive because the infrared instrument's footprint was 68 km, which is so large that the average temperature of the entire eyewall must have been 201–207 K.

As discussed later in this dissertation, some of the recent advances in eyewall observation have come from aircraft or from dropsondes released by aircraft [cf., *Eastin et al.*, 2005, parts 1 and 2; *Halverson et al.*, 2006]. Recent satellite studies focus on sequences of tall cells rather than on individual cells (Table 2.14, p. 131). A sequence of tall cells in one portion of the eyewall is called a "convective burst."

As listed in Table 3.4 (p. 173), previous studies show an empirical association between wind intensification and infrared cloud observations of the inner core of a tropical cyclone (the eyewall plus the inner rain bands). The six hour running average of infrared brightness temperature within 2 degrees of the cyclone's center can explain 37% to 59% of the variance in the wind intensity change according to *Steranka et al.* [1986]. These percentages may be overestimates because both *Steranka et al.*'s wind values and wind-predictor variable are both calculated from infrared observations.

West [1998, Ph.D.] finds that 20% of the variance of wind intensity 24 hours in the future can be explained with a single snapshot of the entire tropical cyclone using multi-channel passive microwave observations. These observations detect both precipitation and clouds.

The advantage of the radar technique described in this dissertation is that it requires fewer observations than the microwave and infrared techniques. Only one radar snapshot of just the eyewall is needed.

Predicting wind intensification from lightning observations remains little more than a plausible theoretical idea despite some enthusiastic advocates. The limiting factor is that eyewalls have so little lightning that the lightning can fall below the detectable limit of some lightning sensors. Lightning is rare in most eyewalls (<1 flash per minute in the entire eyewall) when compared to a 10 kilometer across mid-latitude storm cell that typically has 1 to 12 flashes per minute [*Ushio et al.*, 2001]. *Lyons and Keen* [1994] promote the idea of using eyewall lightning to predict tropical cyclone wind intensification:

Satellite[-observed] supercells are known to have predictive value with respect to further tropical storm intensification. Thus, the same prognostic value is likely to be true for their associated lightning bursts. Lightning bursts may mark the more intense supercells and, in turn, discriminate those supercell bearing [tropical] storms that have a relatively higher probability of rapid intensification.

Significant lightning occurs in the eyewall much less frequently than does wind intensification. *Molinari et al.* [1999] report that lightning occurs in about 7% of tropical cyclone eyewalls, whereas this dissertation finds that wind intensification occurs about half the time (Table 3.2, p. 169). No statistical study of many tropical cyclones has shown lightning is useful for predicting wind intensification, but a number of case studies are consistent with this idea. *Lyons and Keen* [1994] find ~1 flash/minute in the eyewall of intensifying tropical cyclones. *Black and Hallett* [1999] find ≥ 1 flash/minute in the eyewalls of intensifying tropical cyclones and 0.17 flashes per minutes in the eyewalls of

non-intensifying tropical cyclones. Section 4.4 finds ~1 flash/minute in the eyewall of Hurricane Georges (1998) during a period of intensification (Figure 4.3, p. 211). *Cecil et al.* [2002, Part 2, Figure 1] report 1 flash/minute in 50% of eyewalls that also have a minimum 85 GHZ Polarization Corrected Brightness Temperature (PCT) of less than 150 K (which is loosely associated with intensification). In contrast, *Cecil et al.* find almost no chance of lightning in eyewalls with a minimum 85 GHZ PCT of over 200 K.

2.1.2. Tall eyewall cells as a mixture of air and water

A tall cell is a moving mixture of air and water that extends to near or beyond tropopause (~14–18 km in the Tropics). For every kilogram of dry air near the top of the cell, there is approximately 0.6 grams of precipitating ice falling at about 2 m/s, 1 gram of cloud ice too small to fall, and no more than 0.1 grams of water vapor. The precipitating ice was not formed at the 15 km altitude where it is observed because upper tropospheric air is so dry. Based on the vertical variation of the saturation water vapor mixing ratio (Figure 2.12, p. 121), the observed precipitating ice must have formed below 13 km and have been lifted by updrafts by at least 2 km to have reached the observed 15 km altitude. The precipitating ice is observed by radar, the cloud ice makes the cloud opaque to visible and infrared radiation, and water vapor can be detected at certain microwave frequencies.

The presence of 0.6 grams of precipitating ice for each kilogram of air can be estimated in the following way. At the top of the cloud, the radar reflectivity is approximately 20 dBZ (Figure 3.5, p. 155), which corresponds to approximately a

precipitation rate R of 1 mm/h of ice hydrometeors (Table 2.2, p. 56). The 2 m/s fall speed for small ice hydrometeors in the upper troposphere (Figure 2.13, p. 122) causes a 1 mm/h precipitation rate to imply approximately a 0.6 grams of precipitating ice water per kilogram of air. This result can be derived starting with equation 2.1, which leads to equation 2.2.

$$R = M \frac{\rho_{air}}{\rho_{water}} v \frac{1 \text{ m}^2}{1 \text{e4 cm}^2} \frac{10 \text{ mm}}{1 \text{ cm}} \frac{3600 \text{ s}}{1 \text{ h}} \quad (2.1)$$

$$\text{unit analysis : } \frac{\text{mm}}{\text{h}} = \frac{\text{g}}{\text{kg}} \frac{\frac{\text{kg}}{\text{m}^3}}{\frac{\text{g}}{\text{cm}^3}} \frac{\text{m}}{\text{s}} \frac{\text{m}^2}{\text{cm}^2} \frac{\text{mm}}{\text{cm}} \frac{\text{s}}{\text{h}}$$

Equation 2.1 can be derived in the following way. Multiply the precipitation water mixing ratio M (g/kg) by the fall speed v of 2 m/s for small ice in the upper troposphere and then divide by the density of water ρ_{water} of 1 g/cm³. This calculation produces the cubic centimeters of water falling each second per kilogram of air. Next, multiply by the density of air ρ_{air} at 15 km, which is 0.22 kg/m³ (Table 2.3, p. 58), to come up with the cubic centimeters of water falling through each square meter of horizontal area each second. Then, multiply by 1 m² / 1e4 cm² and by 10 mm / 1 cm to calculate the millimeter thickness of water falling through each square meter per second. Last, multiply by 3600 s / 1 h to convert to a precipitation rate with units of mm/h. For a 2 m/s fall speed and the density of air at 15 km, equation 2.1 simplifies to the following:

$$R = 1.6 \frac{\text{mm kg}}{\text{h g}} M \quad (2.2)$$

$$\text{unit analysis : } \frac{\text{mm}}{\text{h}} = \frac{\text{mm kg}}{\text{h g}} \frac{\text{g}}{\text{kg}}$$

Typical values for the cloud ice and water vapor at the top of a cell are easier to find in the literature, so no equation needs to be derived here to calculate them. *Black and Hallett* [1999] give 1 g/kg as a typical concentration of cloud ice. The upper tropospheric saturation water vapor concentration places a 0.1 g/kg upper bound on water vapor in upper tropospheric clouds (Figure 2.12, p. 121).

2.1.3. Discussion of CAPE in tall eyewall cells

Convective Available Potential Energy (CAPE) is both difficult to measure and rarely measured inside of the eyewall. *Holland* [1997, p. 2527] states that "there is significant difference of current opinion on the direct role of CAPE in [tropical] cyclone development, but there is no doubt that substantial vertical motion, and hence CAPE, exists in the eyewall of some tropical cyclones."

Outside of tropical cyclones, the energy available to drive a convective cell is often quantified using CAPE. CAPE is the energy per kilogram (J/kg) of boundary layer air that could be converted, in ideal cases, into the kinetic energy of updrafts. A qualitative treatment of this subject is presented in the following paragraphs, while numerical definitions are presented in section 2.7.

The first question is how much available energy exists in the boundary layer air under the eyewall. *Emanuel* [1986; 1988; 2003, Figure 4b] and *Smith* [2000] claim that CAPE in the eyewall is near zero along the slanted ascent path that air parcels travel in the eyewall. In other words, they claim that there is just enough CAPE to produce a low steady eyewall updraft despite the slight turbulent friction in the rising column. In

contrast, *Eastin et al.* [2005, part 1, section 4b] claim that the consensus is only that the eyewall CAPE is ≤ 1200 J/kg.

The second question is how to calculate the available energy in a tropical cyclone eyewall. CAPE is an line integral. Researchers generally use one of two sets of terms in the integral and they integrate along one of two different paths. The most widely cited formula for CAPE is the vertical integral of thermal buoyancy, i.e., the acceleration due to gravity scaled by the parcel's fractional temperature deviation from the background temperature. A few researchers use additional terms for the water loading and the deviation of the parcel's pressure from the background pressure [*Houze*, 1993, p. 36; *Braun*, 2002]. Aircraft observations through tropical cyclone eyewalls suggest that these additional terms modify the thermal buoyancy (and therefore CAPE) by less than 10% [*Eastin et al.*, 2005, part 1].

A more significant issue for calculating available energy in a tropical cyclone is the integration path. In meteorology, CAPE values are generally stated for a vertical path. However, in a tropical cyclone eyewall, the parcels' path slant outward away from the eye as the parcels ascend. The result is a slant CAPE (called "SCAPE") that is greater than vertically-integrated CAPE (referred to as just "CAPE") [*Bogner et al.*, 2000, section 2g]. One way to remember that the eyewall's SCAPE is greater than its CAPE is to remember that the eye's warm anomaly extends to a larger radius from the storm center at high altitudes than it does at low altitudes (Figures 1.2a, 2.4, and 5.2; pp. 3, 35, and 232). If an eyewall parcel travels straight up (i.e., for CAPE), then the parcel would enter the eye at high altitudes which would inhibit convection because the eye is so warm. If

an eyewall parcel were to move away from the eye's center as it rose (i.e., for SCAPE), then the parcel would remain outside of the eye, have a cooler background profile, and therefore be able to experience faster updrafts.

The third question is how much the "background" CAPE can influence the intensity of a tropical cyclone. Total CAPE can be divided up into the background CAPE and the local enhancement to CAPE due to fast surface winds increasing the air-sea flux of heat and moisture. The simulation of *Persing and Montgomery* [2005, Table 2 and Figure 3] found that the background CAPE did not alter the intensity of a tropical cyclone whether the background CAPE was 1100 J/kg or 2600 J/kg. Similarly, the observations reported in *Bogner et al.* [2000, Figure 3b] show that CAPE several hundred km away from the eye can have a wide range of values from 500 to 3000 J/kg, but regardless of what the CAPE is far from the eye, CAPE stays under 300 J/kg within 70 km of the eye's center. In contrast, *Persing and Montgomery* [2003] find that entraining low-level eye air into the eyewall can locally increase CAPE sufficiently to increase the tropical cyclone's wind intensity by 63%.

2.1.4. Updraft speed in tall eyewall cells

Updraft speed is another property of tall eyewall cells that is difficult to quantify. Some studies report >20 m/s updrafts in eyewall cells (Table 2.12, p. 129), but the consensus view is that eyewall updrafts are generally only 5 m/s in the most vigorous few percent of the eyewall (Table 2.11, p. 128). The updraft speed determines how far the tall cells can overshoot the local tropopause. Observations presented in this dissertation show eyewall

cells reaching 16 or 17 km (Figure 3.3a, p. 149), which is much higher than the ~15 km high climatological tropopause in the tropical cyclone formation region [*Hoinka*, 1999].

2.1.5. Surface rain rate of tall eyewall cells

In 10% of tropical cyclone overflights, the TRMM Precipitation Radar observes an average surface rain rate of ≥ 180 mm/h in a 200 km² area of a tropical cyclone's eyewall (Figure 5.6, p. 271). It is reasonable to ask if such heavy rain can be sustained for 6 to 18 hours, the duration of a burst of tall eyewall cells. If a 180 mm/h rate fell in one location for 12 hours, it would result in 2160 mm (7 feet) of rain accumulation, which far exceeds the largest 12 hour rain accumulation ever recorded at a single location on Earth (~800 mm in 12 hours [*Lamb*, 2001]). A rainfall of 2160 mm represents about twice the annual 1 meter of rainfall at many non-desert locations [*McGregor and Nieuwolt*, 1998, p. 192]. However, if rainfall fell at 180 mm/h for 30 minutes at a time in different locations in the eyewall, that rain rate would stay within the range of 30 minute rain rates observed by other instruments (Table 2.13, p. 130).

2.1.6. Other properties of tall eyewall cells

Two other properties of tall eyewall cells are the duration of convective bursts that they are part of and the precipitation efficiency of individual cells. The observed duration of bursts appears to be 3 to 48 hours, with most bursts lasting approximately 6 to 12 hours (Table 2.14, p. 131).

Precipitation efficiency is the fraction of the water vapor entering the bottom of the cell that falls out of the bottom of the cell as precipitation. Precipitation efficiency can range from 0% to 100% [*Lamb*, 2001, section 8.5]. For this reason, the calculations in chapter 5 avoid precipitation efficiency. *Lamb* [2001] reports that the precipitation efficiency of a convective cell is very sensitive to the vertical wind shear. Increase the shear from 2 to 8 m/s, and the average precipitation efficiency drops from 50% to 15%. The precipitation efficiency determines how much latent heat a convective cell releases into the atmosphere. When less latent heat is released, the convective cell reaches less high, all other factors being equal. This suggests that vertical shear, which is known to reduce tropical cyclone wind intensity, may also prevent eyewall cells from growing tall.

2.1.7. Tropical climatological freezing height

Freezing height divides a convective cell into regions of liquid precipitation below and ice precipitation above. Based on 4 years of TRMM observations, *Thurai et al.* [2003] find that the freezing height for all seasons and years within 20 degrees of the equator is relatively constant at about $4.8 \text{ km} \pm 0.3 \text{ km}$. Rounding of the nearest kilometer, is it an acceptable to say that the climatological freezing height in the Tropics is approximately 5 km. Approximately the same climatological freezing height can be estimated by taking the mean surface temperature of the tropical ocean ($\sim 27^\circ\text{C}$) and applying the mean saturated lapse rate ($\sim 6^\circ\text{C/km}$) for the lower troposphere: $4.5 \text{ km} = 27^\circ\text{C} / 6^\circ\text{C/km}$ [*Wallace and Hobbs*, 2006, pp. 31, 85, 422f; *TRMM Precipitation Radar Team*, 2005, p. 85].

2.1.8. Tropical cyclone wind intensity

Because the dissertation relates tall cells to wind intensity change, this section discusses how wind intensity is measured. In theory, a tropical cyclone's intensity is the maximum wind speed that exists anywhere at a height of 10 meters above the Earth's surface under the tropical cyclone and that is sustained for a one-minute period [*Franklin et al.*, 2000; *NOAA*, 2007, p. 1–31]. In practice, surface wind speed cannot be measured at all locations in a tropical cyclone, and when a tropical cyclone is over ocean, there are generally no wind measurements taken at a 10 meter height. Generally once per day, at best, wind intensity is measured 3 km above the surface in a few aircraft fly-throughs during which a few dropsondes may be released in the eyewall. The 10 meter surface wind is estimated as ~90% of the 3 km observed wind [*Franklin et al.*, 2003]. When 3 km winds are unavailable, then the best estimate of 10 meter surface winds comes from pooling many observations indirectly related to wind speed.

Wind intensity is often stated in units of knots ($1 \text{ m/s} = 1.94 \text{ knots} = 2.24 \text{ mph}$) or in tropical cyclone "categories". Each of the five categories on the Saffir-Simpson scale covers about a 20 knot interval of wind speed [*Simpson*, 1974; *Simpson*, 2003, chapter 7], as can be seen from Table 2.1. Based on 20 knot intervals, several tropical cyclones have had brief periods when they could have been called "category 6" tropical cyclones. More specifically, the author has found, in the world-wide best track estimates of tropical cyclone wind intensity, that a tropical cyclone was more than 20 knots above the 135 knot minimum for category 5 in 44 of the six hourly reporting periods during 1995 to

2006. The 44 reporting periods are approximately 0.5% of the total number of reporting periods with tropical cyclone strength winds.

Table 2.1. The Saffir-Simpson tropical cyclone disaster potential scale

Designation ¹	Minimum intensity in category, i.e. minimum wind speed ²			Minimum strength, i.e. maximum surface pressure (mbar)
	knots	m/s	mph	
Tropical wave ³	N/A	N/A	N/A	Δ 3 mbar
Tropical depression ³	N/A	N/A	N/A	N/A
Tropical storm ³	34	18	40	N/A
TC Category 1	64	33	74	N/A
TC Category 2	83	43	96	980
TC Category 3	96	50	111	965
TC Category 4	114	59	131	945
TC Category 5	135	67	155	920

¹ "TC" = tropical cyclone

² 1 m/s = 3.600 km/h = 1.944 knots = 2.237 mph. 1.852 knots = 1 km/h [AMS, 2000, p. 433]. 1.6093 km = 1 mile [CRC, 2004, p. 1–41].

³ Tropical waves, depressions, and storms were not part of the original scale, but have been added in recent decades [Elsner and Kara, 1999, p. 16].

2.2 The thermodynamic importance of water in the atmosphere

A convective cell is just a moving mass of air and water. The water is important because it can absorb and release a large amount of energy when it changes phase between solid, liquid, and gas. Water is arguably the most important constituent of the atmosphere in

terms of thermodynamics. In addition, atmospheric water influences atmospheric dynamics, which is the circulation of air described in sections 2.7 and 2.8.

It is widely known in scientific circles that water vapor has a larger direct impact on the Earth's energy balance than does carbon dioxide (CO₂) at either the pre-industrial concentration or at double that concentration. Pre-industrial CO₂ at 300 parts per million directly accounts for a radiative flux of approximately 25 watts/m² [Houghton, 2004, p. 25]. If the carbon dioxide concentration were to double from the pre-industrial concentration, only an additional 4 watts/m² of forcing would occur because the portion of the radiation spectrum affected by carbon dioxide is already near saturation at the pre-industrial concentration [Houghton, 2004, p. 24]. In contrast, condensing water vapor warms the atmosphere by adding 80 watts/m² of latent heat while clouds cool the Earth by reflecting an approximately equal amount of solar energy [Thomas and Stamnes, 1999, p. 439]. Water's contribution to the Earth's radiation budget is considerable since 235 watt/m² of solar energy are absorbed by the Earth and atmosphere [Thomas and Stamnes, 1999, p. 439]. In addition, the mid-troposphere's humidity has a large influence on the rate of radiative cooling to space. Mapes [2001] states that "water vapor is the dominant radiatively active gas even in dry regions of the atmosphere" [See also Harries, 1997].

Another way to emphasize the thermodynamic importance of water vapor is to consider the heat that a gram of water vapor transports when it moves through the troposphere compared with a gram of carbon dioxide. Carbon dioxide has approximately a 20% lower specific heat than does the troposphere's main constituent, diatomic nitrogen.

In contrast, water vapor's specific heat is almost twice that of diatomic nitrogen ($c_p \text{ carbon dioxide} = 843 \text{ J / K kg}$, $c_p \text{ water vapor} = 1867 \text{ J / K kg}$, $c_p \text{ N}_2 = 1039 \text{ J / K kg}$)¹. Furthermore, water is the only major constituent of the troposphere that exists in all three phases: gas, liquid, and solid. In air parcels that reach the upper troposphere, most of the water vapor has condensed, possibly frozen, and then fallen out of the atmosphere. The water vapor's latent heats of vaporization and fusion are huge. For comparison, water's latent heat of vaporization is approximately two thousand times greater than the specific heat of diatomic nitrogen ($L_v \text{ water} = 2.5\text{e}6 \text{ J/kg}$, $c_p \text{ N}_2 = 1039 \text{ J / K kg}$ [*Wallace and Hobbs*, 2006, p. 468; *CRC*, 2004]).

Climate change authorities omit or at least de-emphasize water in their list of greenhouse gasses. According to *Houghton* [2004], climate scientists decided to restrict the term "greenhouse gas" to refer only to radiatively important gasses whose atmospheric concentration is being significantly altered by direct emission from human activity (See also *Harries*, 1997, p. 2173). A typical statement is found on the first page of the introduction of the *Global Warming Desk Reference*: "Carbon dioxide and the other 'greenhouse gasses', such as methane, nitrous oxide, and chlorofluorocarbons (CFCs), retain heat in the atmosphere" [*Johansen*, 2002, p. xiii]. The introduction makes no mention of water vapor.

¹ *CRC* [2004, pp. 5-22, 5-18, and 5-28] gives the molar heat capacity of N_2 gas as 29.1 J/mole K, of H_2O gas as 33.6 J/mole K, and CO_2 gas as 37.1 J/mole K. To convert to the meteorological units for heat capacity of (J/kg K), one must use the atomic weight of these substances (28, 18, and 44 g/mole, respectively). More specifically, first multiply by 1000 g/kg and then divide by the atomic weight. The result is the following values for the heat capacity: 1039 J/kg K for N_2 , 1867 J/kg K for H_2O , and 843 J/kg K for CO_2 . For the heat capacity of water vapor and dry air, see also *Wallace and Hobbs* [2006, p. 467].

The statements in *Houghton* [2004] are somewhat more complete. In Houghton's chapter on "greenhouse gasses" the only sentence that mentions water vapor is the following: "The most important of the greenhouse gases is water vapor, but its amount in the atmosphere is not changing directly because of human activities [p. 28]." In actual fact, the amount of water vapor in the atmosphere is changing slightly due to direct emission from human activities in the form of contrail clouds formed from airplane exhaust [*Wallace and Hobbs*, 2006, p. 455]. However, the fractional change in atmospheric water vapor concentration due directly to human activities is much smaller than the fractional change in atmospheric carbon dioxide concentration due directly to human activities. The "major" greenhouse gas discussed in Houghton's chapter are carbon dioxide, methane, and nitrous oxide—all of which are less important radiatively than water vapor.

A search for the phrase "most important greenhouse gas" in the journal abstracts in the Web of Science database reveals a systematic difference between scientific papers and policy papers. Scientific papers mention in passing that water vapor is the most important greenhouse gas [e.g., *Markson*, 2007; *Quante and Mattias*, 2006; *Ruckstuhl et al.*, 2007; and *Dong et al.*, 2006]. Policy papers claim that carbon dioxide is the most important greenhouse gas [e.g., *Tunc et al.*, 2007; *Spokas et al.*, 2006; *Backeus et al.*, 2005; and *Monni et al.*, 2004].

2.3. Satellite observations

2.3.1. Techniques for observing precipitation

This section describe how various kinds of radar can observe the different forms that water takes in the atmosphere and then describes the three kinds of precipitation measuring instruments on the Tropical Rainfall Measuring Mission (TRMM) satellite. In addition, section 2.5 provides details about the radar reflectivity observed by the TRMM Precipitation Radar.

It is difficult to remotely sense precipitation for several reasons. For one thing, satellites fly hundreds of kilometers above Earth, while precipitation only occurs in the bottom ~15 km of the atmosphere. Second, even in the lower troposphere, water vapor accounts for rarely more than 2% of the atmospheric density over the ocean (20 grams of water vapor per kilogram of air)². Liquid and solid water is even more rare in the atmosphere, rarely above 0.2% of the atmospheric density (2 g/kg) even in the lower troposphere [*Wallace and Hobbs*, 2006, p. 219]. According to *Black and Hallett* [1999], the vigorous part of the tropical cyclone's eyewall (with updrafts of 5 to 10 m/s) have a liquid water content of 1–2 g/kg. The rarity of liquid water and ice in the atmosphere make them difficult to observe because the much more plentiful constituents of the atmosphere can mask water's radiative signal.

Another reason why satellite remote sensing is difficult is that satellites are

² *Wallace and Hobbs* [2006, p. 80] give the 20 g/kg value for the Tropics. *Emanuel* [2003b] uses an 80% relative humidity over the Tropical ocean. A surface temperature of 30C is a typical for the Tropics, and thermodynamic charts and the formula $w_s = 0.622 e_s / (p - e_s)$ give $w_s = 25$ g/kg for a saturation vapor pressure e_s of 40 mbar at 30 C and standard atmospheric pressure [*Wallace and Hobbs*, 2006, pp. 81-82].

moving at about 8 km/s, giving the satellite very little time to observe the atmosphere at any one location.³ Another reason why precipitation, in particular, is difficult to remotely sense is that precipitation varies on many space and time scales. In comparison, surface air temperature is more uniform spatially and varies more slowly with time.

Water can take many forms in the atmosphere, but an individual remote sensing technique can generally observe only one of these forms: vapor, cloud droplets, and hydrometeors that are large enough to fall out of the atmosphere such as rain or snow. The radar onboard the TRMM satellite (13.8 GHz, 2.17 cm, K band) operates in the frequency range that allows it to detect rain drops and ice hydrometeors, as do most weather radars [Kozu *et al.*, 2001; Kummerow *et al.*, 1998; Okamoto, 2003]. Radars working at higher frequencies (94 GHz, 4 mm, W band) can observe clouds [Kollias *et al.*, 2007; Im *et al.*, 2005]. Measuring water vapor by radar is still in the early stages of development [Meneghini *et al.*, 2005a and 2005b].

In orbit since November of 1997, the TRMM satellites carries the first and only radar in space that can observe the detailed three dimensional structure of rainfall. The TRMM Precipitation Radar was built by the Japanese Communications Research

³ The orbital speed of the TRMM satellite can be estimated using its orbital period of 91.3 minutes at a 350 ± 1.25 km altitude before August of 2001 and 92.4 minutes at a 402.5 ± 1 km altitude after August of 2001 [Bilanow and Słojkowski, 2006, Table 1]. $\text{speed} = \text{distance} / \text{time} = \text{orbital distance} / \text{orbital period} = 2 \pi (402.5 + 6371) / (60 * 92.4) = 7.7 \text{ km/s}$.

Laboratory (CRL⁴). In April of 2006, the first cloud radar in Earth orbit was launched, NASA's CloudSAT [Haynes and Stephens, 2007].⁵

Radar is the most recently developed satellite technique for measuring rainfall among the three most important satellite techniques. In chronological order of their development, the three techniques are infrared observation, passive microwave observation, and radar (active microwave observation). In addition, an instrument that can determine the location of lightning flashes can be used to identify which storms contain strong updrafts [Rakov and Uman, 2003; Christian, 2000]. The TRMM satellite carries one of each of these four kinds of instruments [Kummerow *et al.*, 1998], and the TRMM satellite has for this reason been nicknamed "the flying rain gauge." [NASA, 2000; Greenstone, 1996]. The TRMM instruments are summarized in Tables 2.7 and 2.8 (pp. 124, 125). Some of the standard algorithms that process the data from these instruments are listed in Table 2.9 (p. 126).

The atmosphere's 11 micron emission has been observed from space since the 1960s. The first weather satellite with an infrared instrument was TIROS-II, launched in November of 1960, and it carried an 11 micron sensor [Bandeem *et al.*, 1961; Astheimer *et al.*, 1961]. The early TIROS satellites were built at the Naval Research Laboratory in Washington DC. The recently formed NASA launched the satellites, operated them, and processed their data for use by scientists and weather forecasting agencies [Jakes, 1966; WMO, 1963; NASA, 1962; NASA, 1964; NASA Goddard, 1970; Chapman, 1969]. This

⁴ Since 2004, CRL is now referred to as NICT, the Japanese National Institute of Information and Communications Technology [NICT, 2004].

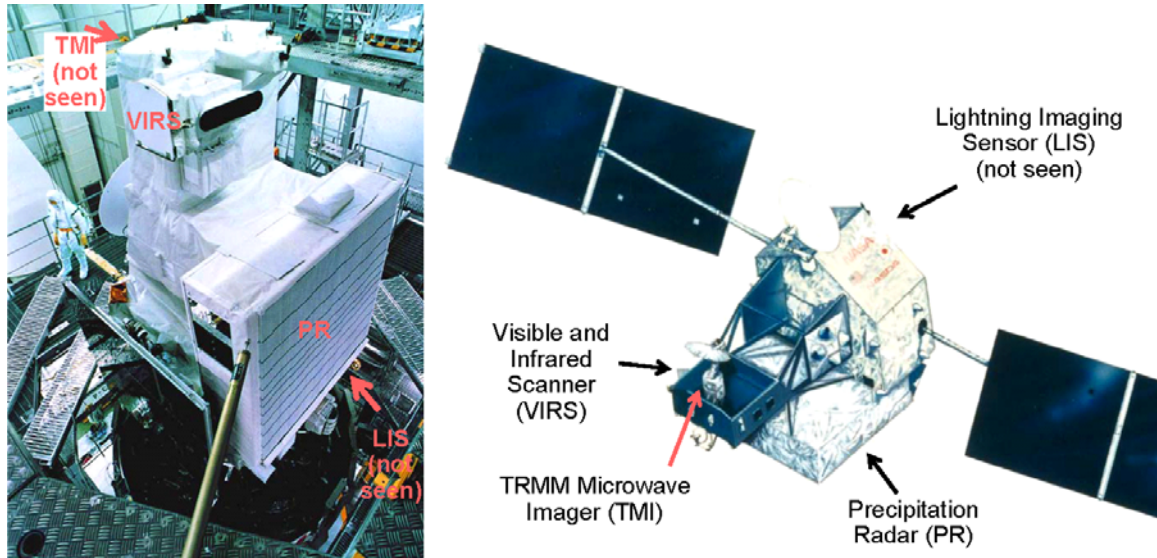


Figure 2.2. The TRMM satellite. (left) A photo of the TRMM satellite mounted to the H2 launch vehicle in Japan. (right) An artist's rendering of the TRMM satellite in Earth orbit. These two images are from the JAXA photo archive [http://jda.jaxa.jp/jda/p1_e.php] and are listed as #P-019-03543 and #P-019-03502.

dissertation uses the 11 micron infrared channel from the TRMM Visible and Infrared Scanner (VIRS). The 11 micron channel measures cloud-top temperature, which can be used to estimate cloud-top height [*Chiu et al.*, 1993; *Sherwood et al.*, 2004].

Since the 1970s, the primary way to track a tropical cyclone is using visible and infrared observations from geosynchronous weather satellites. The first geosynchronous satellites with an infrared sensor was the Geostationary Operation Environmental Satellites – 1 (GOES 1), launched in 1975 [*Pryor*, 1978, p. 1]. Generally, an image of the whole North Atlantic is collected every 30 minutes, but the GOES satellites can scan a limited portion of the Earth more frequently (such as every 15 minutes) when a tropical

⁵ At the 2005 AMS hurricane conference, David Atlas asserted that 94 GHz cloud radars should really be called "small raindrop radars" because they are most sensitive to spheres 0.4 to 0.5 mm in diameter whereas

cyclone or other event of interest is occurring

(<http://www.met.fsu.edu/explores/satellites/Sms/goes1/goes1.html>). In 1975, Dvorak published a method for forecasting tropical cyclone intensity and track using just visible geosynchronous observations, and in 1984, he published a more accurate version of the technique that uses infrared observations as well [Zehr, 2004; Velden *et al.*, 2006].

Some scientists assert that tropical cyclone wind intensity estimates had a low bias until the Dvorak infrared technique achieved wide-spread use [Landsea *et al.*, 2006].

Passive microwave estimates of precipitation rate use channels that observe a combination of emission from and scattering by water vapor, clouds droplets, rain drops, and ice particles. Since the late 1980s, passive microwave sensors have provided operational estimates of precipitation rate from space [Kummerow *et al.*, 2001; Janssen, 1993; Hawkins *et al.*, 2001]. The disadvantage of passive microwave sensors is that they do not measure the precise vertical profile of precipitation rate.

cloud droplets are generally 0.05 to 0.2 mm in diameter and raindrops are generally 0.3 to 2.0 mm.

The radar technique was first used in space in 1997, and radar is the only space-based technique that gives vertical profiles of rainfall rate with a 250 meter vertical resolution. Various texts describe radar detection of hydrometeors [*Iguchi et al.*, 2000, *JAM*; *Rinehart*, 1997; *Doviak and Zrnice*, 1993; *Meneghini and Kozu*, 1990; *Battan*, 1973; *Marshall et al.*, 1947]. Radar observation of hydrometers is described in more detail in section 2.5. The TRMM Precipitation Radar is the 2 by 2 meter box bolted onto the bottom of the TRMM satellite (Figure 2.2).

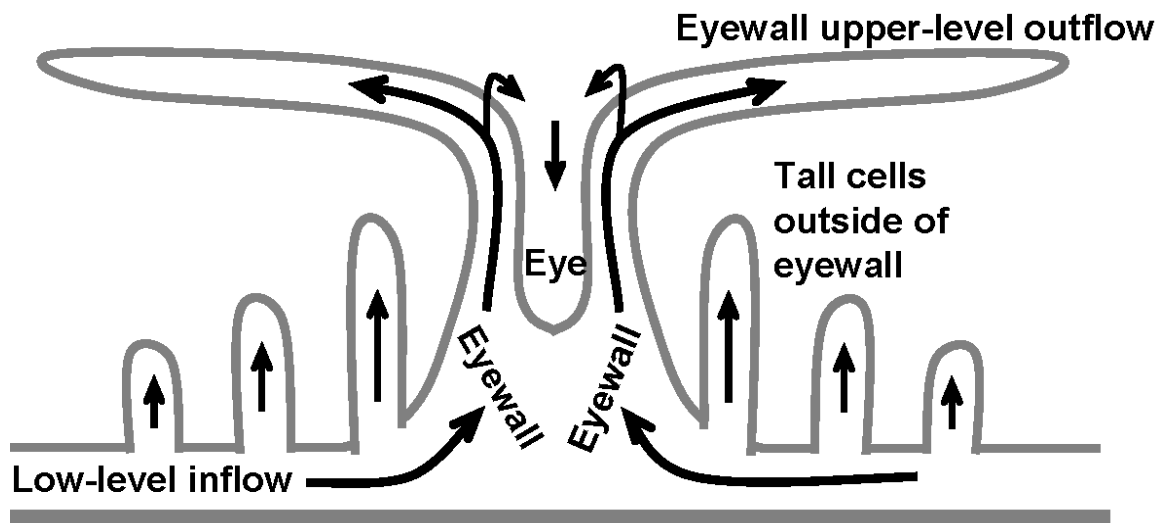


Figure 2.3. A vertical cross section of an idealized hurricane showing the eyewall cloud and the clouds of convective cells outside of the eyewall. This schematic shows how upper level clouds can obscure convective cells when viewed from above. This figure is a simplified version of *Palmen and Newton* [1969, Figure 15.12] and *Anthes* [1982, Figure 2.2].

Radar is the best technique for observing rainfall because it observes the three dimensional structure of rainfall. Figure 2.4 shows the structure of four tropical cyclone eyewalls using radar reflectivity. The point of view has been rotated so that the tall eyewall cells, if any, are located on the left half of the image. Precipitation radars can also estimate the liquid water concentration and the latent heating rate due to condensing water vapor [Tao *et al.*, 2006].

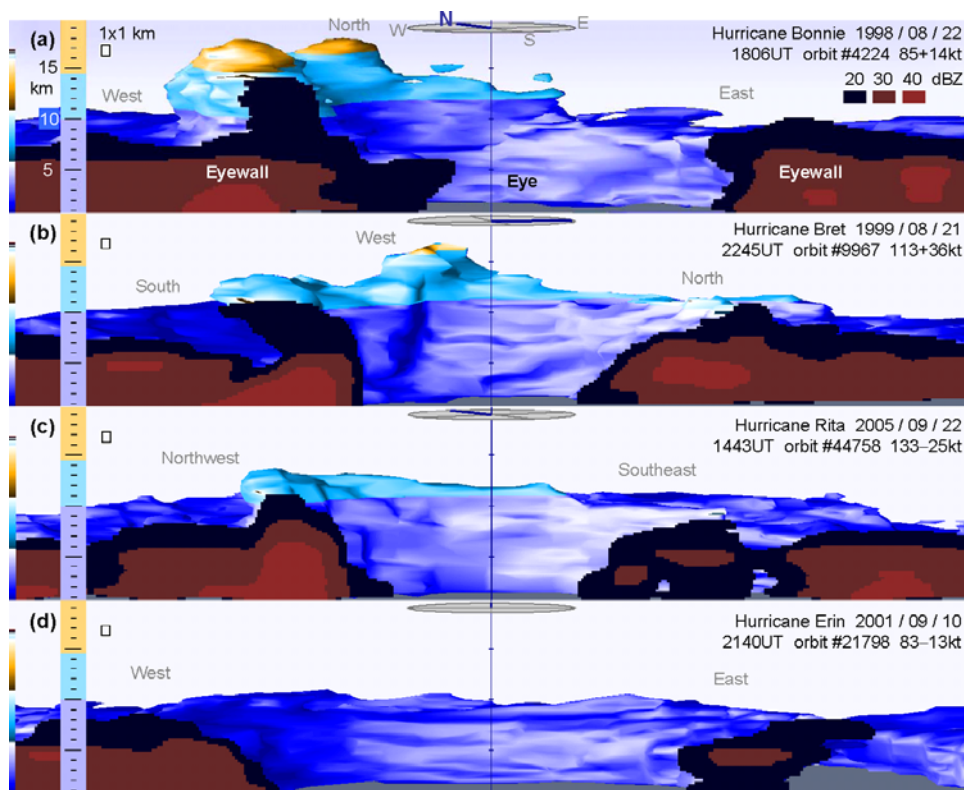


Figure 2.4. 3D observations of tropical cyclone eyewalls by the TRMM Precipitation Radar. The shaded volume contains the points where the radar reflectivity is at least 20 dBZ, corresponding to regions of light rain. Blue indicates regions below a 10 km altitude, cyan indicates a 10 to 14.5 km altitude, and orange indicates regions above 14.5 km. The 3D reflectivity has been cut in half through the center of the eye and only half of the eyewall is shown. Along the vertical cut, radar reflectivity is contoured in black and deep red. The left-right and up-down dimensions have an aspect ratio of 1, as indicated by the 1x1 km box on the left side of the image. A 10 km radius circle is plotted at a 17 km altitude above the eye.

While visual images of the cloud tops are dramatic, they do not reveal what goes on inside of the storm. Figure 2.3 gives a schematic representation of the cloud structure in a tropical cyclone. The upper-level outflow of the eyewall obscures from view the cells forming below it. See also the photos in Figure 1.2c, 1.2d, and 1.2e (p. 3).

Although it does not affect this study, it may be useful to keep in mind that the TRMM satellite underwent an orbit change 3.5 years after launch. During the first 3.5 years of the mission, the satellite's altitude was 350 km. Then, in August of 2001, the satellite was boosted to a 402.5 km altitude in order to conserve fuel and extend the mission [Takahashi and Iguchi, 2004]. The boost increased the swath width and pixel footprint of TRMM instruments by 15%, i.e., by the fractional increase in orbital altitude, $(402.5-350)/350$. The TRMM Precipitation Radar footprint size stated in this dissertation (5 km) is within round off error of the nadir footprint size before the boost (4.3 km) and after the boost (5.0 km) [Kummerow *et al.*, 1998].

2.3.2. Revisit time

One aspect of the TRMM Precipitation Radar that is of interest in this dissertation is how often it observes rainfall above a given point on the Earth's surface. This information is useful in section 3.3 when estimating if all TRMM tropical cyclone overflights have been located in certain years of the TRMM mission.

An upper bound for the revisit time occurs at the Equator. The lower bound for the revisit time is twice per day, which occurs when the tropical cyclone happens to be at a location where an ascending and descending node cross that day. At the northern edge

of the 35°S to 35°N coverage of the orbit, the revisit time reaches the same lower limit when two subsequent orbits each day observe the same point approximately 92 minutes apart. The latitudinal variation of the revisit time is shown in Figure 2.5.

Using a simple geometric argument, equation 2.4 for the revisit time can be derived. The number of days $t_{revisit}$ between visits can be calculating by dividing the circumference of the Equator $d_{Equator}$ by the number of kilometers of the Equator $d_{each\ day}$ that are observed each day by the Precipitation Radar's swath. Following the orbit boost, the swath width d_{swath} is 248 km. At a 402.5 km orbital altitude, the TRMM orbit lasts 92.4 minutes [Bilanow and Słojkowski, 2006, Table 1], which means $n_{per\ day} = 31.2$ Equator crossings each day. Equation 2.3 takes into account that the satellite crosses the Equator at a $\theta = 35^\circ$ angle, since its orbit is a 35° inclination orbit. The Earth's mean radius r_{Earth} is 6371 km. The expression for the revisit time can be derived in equation 2.3:

$$\begin{aligned}
 n_{per\ day} &= \left(2 \frac{\text{crossings}}{\text{orbit}}\right) \frac{60 \cdot 24 \frac{\text{minutes}}{\text{day}}}{92.4 \frac{\text{minutes}}{\text{orbit}}} \approx 31.2 \frac{\text{crossings}}{\text{day}} \\
 d_{Equator\ crossing} &= \frac{d_{swath}}{\sin \theta} \\
 d_{Equator} &= 2 \pi r_{Earth} \\
 d_{each\ day} &= n_{per\ day} d_{Equator\ crossing} \\
 t_{revisit} &= \frac{d_{Equator}}{d_{each\ day}}
 \end{aligned} \tag{2.3}$$

Expressing the revisit time solely as a function of the swath width results in the following equation.

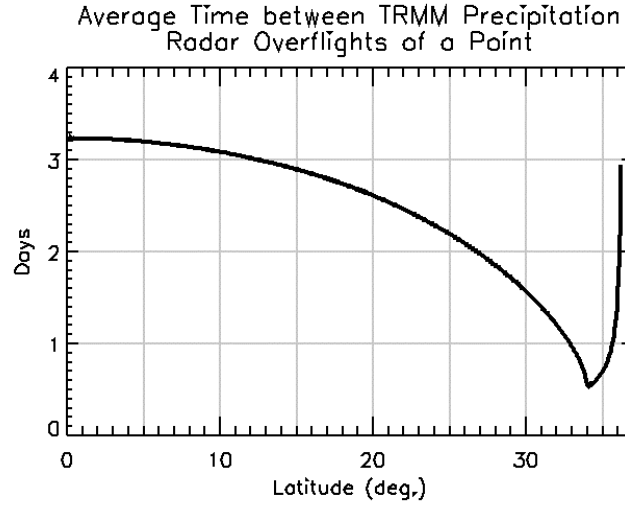


Figure 2.5. The average number of days between times that the TRMM Precipitation Radar observes a particular point on the Earth's surface as a function of degrees of latitude from the Equator. This calculation is based on one month of TRMM Precipitation Radar orbits.

$$t_{\text{revisit}} = \frac{2 \pi r_{\text{Earth}} \sin \theta}{n_{\text{per day}} d_{\text{swath}}} = \frac{736}{d_{\text{swath}}} \quad (2.4)$$

For the post-boost swath width d_{swath} of 248 km, equation 2.4 estimates that the TRMM Precipitation Radar revisits a point on the Equator every 3.0 days. Consistent with this result, *Schumacher and Houze* [2000, p. 2154] found a 3 to 4 day TRMM revisit time at Kwajalein Atoll (9°N, 168°E).

The revisit time for observing the entire eyewall of a tropical cyclone is considerably longer than the 0.5 to 3.0 days shown in Figure 2.5. The inner edge of the eyewall is approximately 20 to 40 km from the center of the eye, and the outer edge of the eyewall is generally about 50 km from the center of the eye. Equation 2.4 provides an easy method to estimate the average revisit time for the Precipitation Radar if one requires that the point be 50 km away from the edge of the swath each time it is observed. The method is to reduce the swath width d_{swath} by 100 km, which allows a 50 km buffer

on each edge of the swath. The Equatorial revisit time for observing the entire eyewall is 5.0 days ($d_{swath} = 248 \text{ km} - 100 \text{ km}$).

2.4. Ground-based observations

The weather radars prior to the WSR-88Ds commissioned in the mid-1990s had defects that could make observations of tall cells suspect. For example, the large sidelobes of older WSR-57 radar had this problem [Atlas, 1963]. The WSR-88D acronym stands for Weather Surveillance Radar - 1988 Doppler [Heiss and McGrew, 1990]. The WSR-88D are the operational weather radars used by U.S. National Weather Service (NWS). A common nickname for the WSR-88Ds is "Nexrad" because in the 1980s, they were the "next generation" of weather radar. Figure 2.6 shows a photo of a WSR-88D radar.

WSR-88D radars are fairly accurate, but it can still be challenging to determine cloud-top height using them [Howard *et al.*, 1997; Brown *et al.*, 2000]. The NWS WSR-88D handbook includes the following three cautions about the operationally created convective height product:

- There is no correction for data contaminated from side lobes; this factor could cause overestimation of echo tops heights in areas of very strong reflectivity such as that due to the presence of hail. There is also no correction for the effects of beam broadening with range; this can lead to a "stair-step" product appearance as an area of uniformly high storms are estimated to be higher and higher with range.
- An echo top height will be incorrectly estimated if the volume coverage pattern is such that the true echo top lies in the vertical gap between successive elevation scans or if it is above the highest elevation scan. The latter condition will frequently be true for storms that are close to the radar.

- Echo top height can differ significantly from visual cloud top heights. Additional operational experience is required to determine the most useful Minimum Significant Reflectivity threshold for estimating cloud tops. [*Fed. Coord.*, 1991, Part C, p. 2–28]

There is nothing obvious to be done to avoid the first bullet. The second bullet is not a concern in this study because the tropical cyclones are far from the radar. A major thrust of the TRMM satellite radar analysis is to determine the best reflectivity threshold for determining the height of a convective cell, which is an effort encouraged by the third bullet. The National Weather Service echo-top product uses 18.5 dBZ as the default reflectivity threshold but the threshold can be changed by the radar operator [*Fed. Coord.*, 1991, part C, p. 2–27].

Figure 2.7 shows a vertical cross section of a typical scanning pattern employed by a WSR-88D radar when monitoring convective precipitation. Altitude is calculated

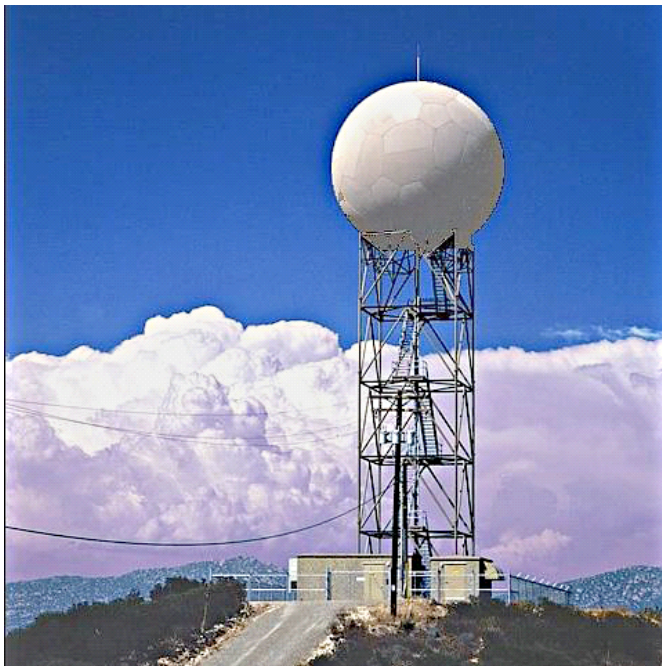


Figure 2.6. A WSR-88D ground radar. The dome is made of fiberglass and foam and is 13 meters in diameter (39 feet). The antenna inside of the dome is 9 meters (28 feet) in diameter and parabolic in shape [*Heiss and McGrew*, 1990]. Photo from [<http://www.spc.noaa.gov/faq/tornado/doppler.htm>].

using the standard propagation formula [Rinehart, 1997, p. 62]. The parameters for this calculation come from Table 2.10 (p. 127), such as the beam width of ~ 1 degree (i.e., a half beam width of 0.475°). The 14 elevation angles shown here are used in the WSR-88D Volume Coverage Pattern (VCP) 11 [Brown *et al.*, 2000, Figure 1]. The observations analyzed in this chapter are in this VCP or a similar VCP. A data volume occurs every 1 km along a line of sight, and all of the data volume centers are shown using black dots. Every tenth data volume has its approximate boundary shaded with a gray line. The 14.5 km height threshold developed in chapter 3 is shown here with a horizontal gray line. The vertical line at 230 km indicates how far from the radar doppler velocity and echo tops are calculated in the standard level 3 National Weather Service product. When interpreting Figure 2.7, keep in mind that the vertical scale has been exaggerated by about a factor of 10, as is commonly done in meteorology. Because of the curvature of the Earth, an increasing fraction of the troposphere falls below the horizon as the beam moves away from the radar. On the right side of the figure is labeled the names of various parts of the atmosphere at their approximate altitude in the Tropics.

The NWS chooses the elevation angles of each line of sight so that the gaps between elevation angles are small, especially at the elevation angles below 8° that fill most of the observed volume 100 to 460 km away from the radar. Even though there are minimal gaps, the vertical resolution is coarse because vertical distance between the center of the lines of sight can be several kilometers in the outer portion of the ground radar's 460 km range. Several kilometers is much coarser vertical resolution than the TRMM satellite radar's 250 meters.

This dissertation suggests that some information in this routinely collected ground radar data is not being used by forecasters when a tropical cyclone approaches land. In particular, the operationally collected ground radar data contains information about the height of convective cells in the tropical cyclone's eyewall and this height information is not currently being used by the NWS to predict tropical cyclone wind intensification. The WSR-88D handbook makes no mention of echo tops in its discussion of tropical cyclones:

The WSR-88D provides Mean Radial Velocity and Reflectivity products that will allow the tracking and prediction of wind and precipitation patterns associated with tropical cyclones as they make landfall. As these destructive phenomena come within range of coastal areas, information on system center, spiral rainbands, and wind distribution will increase. [*Fed. Coord.*, 1991, Part D, p. 4–31]

Based on the NWS approach stated above, it is not surprising that there are organizational impediments to using the data collected in the outer portion of the ground radar's range.

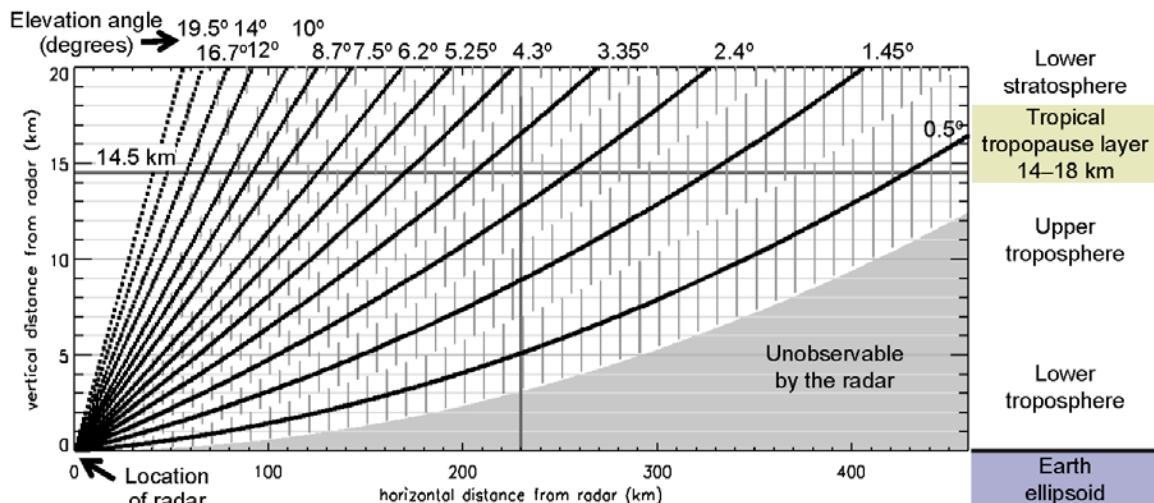


Figure 2.7. Vertical cross section of a typical ground radar volume scan. The figure is explained in section 2.4

More specifically, the NWS does not even calculate echo tops beyond 230 km from the radar for their most widely used standard product, the level 3 color-coded image product [*Fed. Coord.*, 1991, part C, p. 2–27 and A–3; and more recently at <http://www.ncdc.noaa.gov/oa/radar/productsdetail.html>]. The vertical resolution of that level 3 product is only 5,000 feet, so where the echo-top measurements are more accurate than 1.5 km, the extra accuracy is lost.

In order to have several hours of ground radar data prior to landfall, this dissertation must use some data from the outer portion of the ground radar's range. In 80% of the volume scans that the dissertation examines, the vertical distance between radar sweeps is 2.2 to 4.3 km at a 15 km altitude in the tropical cyclone's eye. In these volume scans, the eye is 100 to 290 km away from the radar. Since the eyewall's radius can be 50 km, a portion of the eyewall can be further than 290 km from the radar.

This dissertation is able to use data from the outer portion of the ground radar's range because this dissertation is only interested if the rain region inside the cell reaches a 14.5 km altitude. In the outer portion of the radar range, the lowest elevation sweep (0.5 degrees of elevation above the horizon) rises to near a 14.5 km altitude (Figure 2.7). Normally, forecasters are interested in estimating surface rain, so when the bottom sweep rises above the bulk of the precipitation volume, i.e., ~8 km, forecasters become less interested in the radar data. The exception is that forecasters do examine echo tops when intense mid-latitude thunderstorms are expected over land. The WSR-88D handbook encourages forecasters to consider echo tops useful for the following purposes:

- Echo Tops heights are primarily useful as part of briefings prepared for aviation interest and the general public.

- They can be useful to the user in defining strong updraft regions or the presence of vertical tilt within a storm.
- Observation of collapsing echo tops can aid in timing the onset of a severe weather event.
- The beginning of convective development can sometimes be seen as midlevel echo tops before appearing as low-level reflectivity. [*Fed. Coord.*, 1991, part C, pp. 2–27 and 2–28]

This dissertation does something unconventional and looks at radar-observed echo tops over ocean in tropical cyclone. It is somewhat puzzling that no one has done this before with ground radar data because infrared satellite observations of cloud-top height have been routinely used to estimate tropical cyclone wind intensity for the past three decades.

2.5. Radar reflectivity

Radar reflectivity is the most important observation in this text, so it is important to understand it. For decades, radar reflectivity has been the most common measure of the energy scattered by hydrometeors (rain drops and ice particles) [*Rinehart*, 1997, p. 91]. Reflectivity can be calculated from observed quantities because it is proportional to the scattering cross section [*Rinehart*, 1997, equation 5.7]. While reflectivity is linearly related to scattering cross section, the precipitation rate is not linearly related to the scattering cross section [*Rinehart*, 1997, p. 142]. Worse yet, the functional relationship between scattering cross section and precipitation rate depends on a unobserved property of precipitation, namely the distribution of the sizes of the precipitating hydrometeors

[Doviak and Zrnic, 1993, p. 224]. For this reason, many studies, including this dissertation, use radar reflectivity whenever possible [e.g., Zipser *et al.*, 2006].

Radar reflectivity is a quantity that lies midway between the instrument units of returned power (watts) and the geophysical units of precipitation rate (the depth of liquid water that would accumulate in one hour, i.e., mm/h, if this rate persisted). In this way, radar reflectivity is analogous to the brightness temperature of a passive microwave sensor such as the TRMM Microwave Imager (TMI). Reflectivity is based on the assumption that hydrometeors are spheres of liquid water even in situations when one knows that the hydrometeors are ice or are not spherical [Rinehart, 1997, p. 89]. It is convenient to think of raindrops as spheres because then the Rayleigh scattering approximation can be used [Rinehart, 1997, p. 72].

In Rayleigh scattering, the power scattered is proportional to the sum of the sixth power of each sphere's diameter and inversely proportional to the fourth power of the radiation's wavelength [Rinehart, 1997, p. 70]. Due to the sixth power dependence on drop diameter, the scattering increases rapidly with drop diameter until the Mie scattering regime begins when the drop diameter equals $\sim 1/3$ of the wavelength of the radiation. Deviation from strict Rayleigh scattering begins with smaller drops, whose diameters are $\sim 6\%$ of the radiation's wavelength. These boundary values are usually stated in terms of $\alpha \equiv \pi d / \lambda$ where d is the drop diameter and λ is the radiation wavelength. In other words, radiation begins to deviate from Rayleigh scattering at $\alpha = 0.2$ and starts to oscillate around its asymptotic value around $\alpha = 1$ [Battan, 1973, p. 41, Figure 4.3; Doviak and Zrnic, 1993, p. 41, Figure 3.4; Rinehart, 1997, p. 72, Figure 4.2; See also

Janssen, 1993, p. 302, Figure 6.29]. For the 2.17 cm wavelength of the TRMM Precipitation Radar, drops with 0.14 to 0.69 mm diameters are in the region where the Rayleigh approximation can still be used but is not perfectly accurate, i.e., they are smaller than 6% of the radar's wavelength. In light rain, only a small portion of the rain drops are larger than 0.69 mm in diameter (equation 2.19), but larger raindrops become more common in heavy rain, making the Rayleigh scattering approximation less accurate.

The most commonly published unit for radar reflectivity is the logarithmic unit of “dBZ”, which can be calculated by dividing the linear unit by $1 \text{ mm}^6/\text{m}^3$, taking the log base 10, and then multiplying by 10 [*Rinehart*, 1997, p. 93]. Even for the obviously frozen upper troposphere, radar reflectivity is by convention always stated in units based on the liquid water assumption [*Doviak and Zrnica*, 1993, p. 228]. This convention is followed in the standard data products in the TRMM satellite data archive. When one wants to make it perfectly clear that this convention is being followed, one says that one is using “liquid-water-mass-equivalent radar reflectivity” (See also *Doviak and Zrnica*, 1993, p. 82).

The assumption of liquid spherical scatters causes no trouble in interpreting dBZ values as long as one knows, from other sources, the phase of the precipitation and to what extent the hydrometeors deviate from spherical. Around the tropical freezing level of 5 km (section 2.1), there are both liquid, solid, and liquid-coated solid hydrometeors, which makes interpreting radar reflectivity difficult. However, in the upper troposphere, one knows that the hydrometeors are ice.

To a certain degree, radar reflectivity is instrument independent.⁶ When the scattering is Rayleigh scattering, then to a first approximation, radars of different wavelengths will report the same reflectivity for a given storm. When the hydrometeors are too big to be governed exactly by Rayleigh scattering, then radars operating at different wavelengths (say 10 cm ground radars vs. the 2.17 cm TRMM radar) will report different reflectivity for the same storm. In an extreme case, *Black* [1990] shows an order of magnitude (10 dB) difference in radar reflectivity based on the size distribution of ice particles for a given water mass.

A description of how the TRMM Precipitation Radar works will aid in understanding what radar reflectivity represents. In this description, keep in mind that the radar is orbiting the Earth at a 403 km altitude. For each line of sight, the radar sends out approximately 64 pulses of energy with 616 watts of power and a 1.67e-6 second pulse duration at a rate of 2800 pulses per second (i.e., a 2.8 KHz pulse repetition frequency) [*Kozu et al.*, 2001]. As each pulse travels towards the Earth at the speed of light, it expands, constantly filling a 0.71 x 0.71 degree solid angle and filling a 125 meter range along the line of sight [*Kozu et al.*, 2001]. After a pulse travels for almost 1/1000th of a second and as it nears the end of its 400 km long journey downward, the pulse encounters oxygen, water vapor, and cloud droplets which absorb some of the pulse's power [*TRMM Precipitation Radar Team*, 2005, p. 91]. By the time that a pulse encounters rainfall, it has expanded to approximately a 5 x 5 km horizontal area and

⁶ Passive microwave brightness temperature is also only partially instrument independent. The footprint of the instrument can have a big effect on the observed brightness temperature when there is large variations in precipitation at scales smaller than the footprint. *Wimmers and Velden* [2007, Appendix] find that they need to apply up to a 30K adjustment to cold 85 to 92 GHz passive microwave brightness temperatures to

remains 125 meters thick. Since raindrops (0.03 to 0.3 cm across) are much smaller than the wavelength of the radiation (2.17 cm), a fraction of the radiation scatters directly back toward the radar by means of Rayleigh scattering [*Doviak and Zrnic*, 1993, section 3.2]. Out of the 616 watts emitted by the radar, a 250 meter thick slab of rain cloud will scatter back toward the radar about 0.6 watts. On the 400 km journey back up to the radar, the pulse loses a little more power due to absorption by oxygen, water vapor, and cloud droplets. The pulse also expands perpendicular to its direction of motion as if it were on the surface of an expanding sphere centered on the storm cloud that scattered the pulse toward the radar. The 2 by 2 square meter antenna of the TRMM Precipitation Radar (Figure 2.2, p. 32) intercepts a tiny portion of the expanding pulse. Approximately $1\text{e-}12$ watts of power out of the original 616 watts is actually intercepted by the radar. The radar accurately measures that power and the time that it took to travel at the speed of light to the rain cloud and back. These two pieces of information are used to calculate the radar reflectivity of the storm cloud and the storm cloud's location along the radar's line of sight.

2.5.1. Mathematical derivation of radar reflectivity

This section calculates radar reflectivity from received power. Reflectivity is the starting point for calculating precipitation rate in section 2.5.2. The reflectivity equation can be stated in linear or logarithmic units, which are respectively equations 2.5 and 2.6:

compensate for the footprint size and calibration of various satellite instruments.

$$Z_{linear} = \frac{P_{received} r^2}{C} \quad [Rinehart, 1997, p. 92] \quad (2.5)$$

$$\text{unit analysis : } \frac{\text{mm}^6}{\text{m}^3} = \text{watts m}^2 \div \left(\text{watt } \frac{\text{m}^5}{\text{mm}^6} \right)$$

$$Z \equiv 10 \log_{10} \frac{Z_{linear}}{1 \frac{\text{mm}^6}{\text{m}^3}} \quad [Rinehart, 1997, p. 93] \quad (2.6)$$

In the above two equations, Z is the radar reflectivity, $P_{received}$ is the power received from the hydrometeors, r is the distance between the radar and storm, and C is the radar constant that is calculated from instrument specific quantities such as the radar's wavelength and the antenna's gain.

In a TRMM 1B21 file, the total power received from somewhere within a storm cell is typically -100 to -90 dBm. The units of dBm stand for “dB” of milliwatts ($1\text{e-}3$ watts), so -90 dBm equals $1\text{e-}12$ watts. From that power, the system noise of around -110 dBm must be subtracted to obtain the power received from the scattering hydrometeors. Heavy precipitation (with approximately a -90 dBm received power) has a signal to noise ratio of ~ 100 , so the signal strength is almost as great as received power. The distance between the radar and scatterer is approximately 400 km, so the r^2 term in the above equations introduces a factor of $\sim 1.6\text{e}11 \text{ m}^2$. The radar constant is -20 dBm for the TRMM precipitation, which can be converted into linear units of $1\text{e-}2$ (milliwatts m^5 / mm^6) or $1\text{e-}5$ (watts m^5 / mm^6). For example, substituting a signal strength of $1\text{e-}12$ watts into equation 2.6 gives a radar reflectivity of 42 dBZ:

$$42 \text{ dBZ} = 10 \log_{10} \frac{1\text{e} - 12 \text{ watt } 1.6\text{e}11 \text{ m}^2}{1\text{e} - 5 \text{ watt } \frac{\text{m}^5}{\text{mm}^6}} \frac{1}{\frac{\text{mm}^6}{\text{m}^3}} \quad (2.7)$$

$$42 \text{ dBZ} = 10 \log_{10} 1.6\text{e}4$$

Scientists do not need to calculate radar reflectivity from returned power because the TRMM 1C21 algorithm performs this calculation for them. The 1C21 algorithm calculates the radar constant in logarithmic units in the following way [*TRMM Precipitation Radar Team*, 2005, pp. 14, 16, 21, and 28]:

$$\begin{aligned}
 C = & P_{transmitted} + G_{transmit} + G_{receive} + 10 \log_{10}(\Delta\theta \Delta\phi) + 10 \log_{10}(c \Delta t) \\
 & - 20 \log_{10}(\lambda) + 10 \log_{10}\left(\pi^3 \frac{|K|^2}{2^{10} \ln 2} 10^{-18}\right) \\
 & (2.8) \\
 C = & -20 \text{ dB} = 57 \text{ dB} + 47 \text{ dB} + 47 \text{ dB} + (-38 \text{ dB}) + 27 \text{ dB} \\
 & - (-33 \text{ dB}) + (-194 \text{ dB})
 \end{aligned}$$

The constants used in this equation can be read from the "ray header" and "power" objects in TRMM 1B21 and 1C21 HDF files in the TRMM archive. In the above equation, the transmitted power $P_{transmitted}$ is expressed as 57.75 dBm, which is equivalent to 595e3 milliwatts or 595 watts. The gain $G_{transmit}$ and $G_{receive}$ of the TRMM Precipitation Radar's antenna is 47.1 dB and 46.8 dB when the radar is transmitting or receiving, respectively. The along track and across track beam width are $\Delta\theta = 0.0122$ radians and $\Delta\phi = 0.0126$ radians. The pulse length in meters is the speed of light c (3e8 m/s) times the duration of the transmitted pulse Δt (1.53e-6 seconds). The wavelength λ of the TRMM radar is 0.0217 meters. The scattering coefficient $|K|^2$ at 13.86 GHz and at 0°C for liquid water is 0.9255 (unitless) [*TRMM Precipitation Radar Team*, 2005, p. 16; *Rinehart*, 1997, p. 146].

Equations 2.6 and 2.8 look rather complicated, so to understand them, it can help to start with a simpler form. In equation 2.9, the power received by the radar $P_{received}$ is express as the product of four quantities. The received power is proportional to transmitted power $P_{transmitted}$, to the ratio that expresses the reduction in power density as the beam travels away from the radar, to the reduction in power density as the beam returns to the radar, and to the attenuation as the beam travels through clear area ($e^{-2\tau}$):

$$P_{received} = P_{transmitted} \frac{A_{precip}}{A_{sphere}} \frac{A_{antenna}}{A_{sphere}} e^{-2\tau} \quad (2.9)$$

$$\text{unit analysis : watt} = \text{watt} \frac{\text{m}^2}{\text{m}^2} \frac{\text{m}^2}{\text{m}^2} 1$$

In the above equation, A_{precip} is the horizontal area of precipitation illuminated by the radar beam ($\sim 20 \text{ km}^2$ for a 5 km diameter pixel), $A_{antenna}$ is the effective area of the antenna, and A_{sphere} is the surface area of a sphere with a radius equal to the distance between the radar and the precipitation. These areas can be defined in the following way [Rinehart, 1997, pp. 68, 85]:

$$\begin{aligned} A_{precip} &= G V \sigma & \text{units : } \text{m}^2 &= 1 \cdot \text{m}^3 \cdot \frac{\text{m}^2}{\text{m}^3} \\ A_{antenna} &= \frac{G \lambda^2}{4\pi} = \frac{5e4 \cdot 0.0217^2}{4\pi} \approx 1.9 \text{ m}^2 & \text{units : } \text{m}^2 &= 1 \cdot \text{m}^2 \\ & & \text{Rinehart, 1997, p. 68} & \\ A_{sphere} &= 4\pi r^2 & \text{units : } \text{m}^2 &= 1 \cdot \text{m}^2 \end{aligned} \quad (2.10)$$

In equation 2.10, G is the gain of the antenna, V is the volume illuminated by the radar beam, σ is the scattering area per unit volume illuminated by the beam, λ is the wavelength of the radar, and r is the distance between the radar and the precipitation.

Scattering area per unit volume can be calculated with the Rayleigh scattering formula. Scattering can be expressed in terms of radar reflectivity Z [Rinehart, 1997, p. 88]. Radar reflectivity is written using millimeters instead of meters for the hydrometeor's diameter, which introduces a $1\text{e-}18$ unit conversion factor into equation 2.11: $(1\text{e-}3 \text{ m/mm})^6 = 1\text{e-}18 \text{ m}^6/\text{mm}^6$.

$$\sigma \equiv \frac{\pi^5 |K|^2}{\lambda^4} \sum_{\text{unit volume}} d^6$$

$$\text{unit analysis : } \frac{\text{m}^2}{\text{m}^3} = \frac{1}{\text{m}^4} \frac{\text{m}^6}{\text{m}^3}$$

$$Z_{\text{linear}} \equiv \sum_{\text{unit volume}} d^6$$

$$\text{unit analysis : } \frac{\text{mm}^6}{\text{m}^3}$$

$$\sigma \equiv 1\text{e} - 18 \frac{\pi^5 |K|^2}{\lambda^4} Z_{\text{linear}}$$

$$\text{unit analysis : } \frac{\text{m}^2}{\text{m}^3} = \left(1\text{e} - 18 \frac{\text{m}^6}{\text{mm}^6} \right) \frac{1}{\text{m}^4} \frac{\text{mm}^6}{\text{m}^3} \quad (2.11)$$

Before the horizontal area of the precipitation A_{precip} (equation 2.10) is fully defined, an expression must be found for volume V illuminated by the radar's beam. Volume V is generally expressed as a modified form of the equation for the area of a cylinder V_{cylinder} [Rinehart, 1997, p. 86]:

$$\begin{aligned}
V_{cylinder} &= \pi \text{ radius}^2 \text{ height} \\
V_{cylinder} &= \pi r^2 \left(\frac{\Delta\theta}{2} \right)^2 \left(\frac{\Delta h}{2} \right) = \frac{\pi r^2 \Delta\theta^2 \Delta h}{8} \\
V &= \frac{\pi r^2 \Delta\theta^2 \Delta h}{16 \ln 2}
\end{aligned} \tag{2.12}$$

Substituting equations 2.10 to 2.12 into equation 2.9 results in the following equation for received power:

$$\begin{aligned}
P_{\text{received}} &= P_{\text{transmitted}} \left(\frac{G \frac{\pi r^2 \Delta\theta^2 \Delta h}{16 \ln 2} \sigma}{4\pi r^2} \right) \left(\frac{A_{\text{antenna}}}{4\pi r^2} \right) e^{-2\tau} \\
P_{\text{received}} &= P_{\text{transmitted}} \left(\frac{G \Delta\theta^2 \Delta h}{64 \ln 2} \right) \left(\frac{A_{\text{antenna}}}{4\pi r^2} \right) \left(1e - 18 \frac{\pi^5 |K|^2}{\lambda^4} Z_{\text{linear}} \right) e^{-2\tau} \\
P_{\text{received}} &= P_{\text{transmitted}} \left(\frac{1e - 18 \pi^4 |K|^2 G \Delta\theta^2 \Delta h A_{\text{antenna}}}{256 \lambda^4} \right) \frac{Z_{\text{linear}}}{r^2} e^{-2\tau}
\end{aligned} \tag{2.13}$$

A radar constant C can be extracted from the above equation for received power:

$$\begin{aligned}
P_{\text{received}} &= C \frac{Z_{\text{linear}}}{r^2} e^{-2\tau} \\
\text{unit analysis : watt} &= \left(\text{watt} \frac{\text{m}^5}{\text{mm}^6} \right) \frac{\frac{\text{mm}^6}{\text{m}^3}}{\text{m}^2} 1 \\
& \tag{2.14}
\end{aligned}$$

$$\begin{aligned}
C &= P_{\text{transmitted}} \left(\frac{1e - 18 \pi^4 |K|^2 G \Delta\theta^2 \Delta h A_{\text{antenna}}}{256 \lambda^4} \right) \\
\text{unit analysis : watt} &= \text{watt} \left(\frac{\text{m}^6}{\text{mm}^6} \text{ m m}^2 \div \text{m}^4 \right)
\end{aligned}$$

The value of the radar constant can be evaluated using parameters stated in the preceding paragraphs:

$$C = 595 \text{ watt} \left(\frac{1e - 18 \frac{\text{m}^6}{\text{mm}^6} \pi^4 0.9255 5.0e4 0.0122^2 500 \text{ m } 1.9 \text{ m}^2}{256 0.0217^4 \text{ m}^4} \right) \quad (2.15)$$

$$C \approx 1e - 5 \text{ watt} \frac{\text{m}^5}{\text{mm}^6} = 1e - 2 \text{ milliwatt} \frac{\text{m}^5}{\text{mm}^6} = -20 \text{ dBm}$$

In equation 2.14 for radar reflectivity Z , the only quantity that has yet to be defined is optical depth τ :

$$\tau = \int_{\text{transmitter}}^{\text{reciever}} \left(k_{\text{O}_2} \rho_{\text{O}_2} + k_{\text{water vapor}} \rho_v + k_{\text{cloud droplets \& cloud ice}} \rho_c + k_{\text{rain \& precipitation ice}} \rho_r \right) dx \quad (2.16)$$

The two-way attenuation factor $e^{-2\tau}$ is quantified using the one-way optical depth τ .

Optical depth is the sum of absorption by atmospheric oxygen ρ_{O_2} , water vapor ρ_v , cloud droplets ρ_c , and hydrometers ρ_r between the scattering volume and the antenna [TRMM Precipitation Radar Team, 2005, p. 91; Doviak and Zrnic, 1993, section 3.3; Rinehart, 1997, pp. 154–165]. Iguchi *et al.* [2000, JAM] describe the computational implementation of the attenuation calculation in the TRMM 2A25 algorithm, whose attenuation-corrected reflectivity is used in this dissertation.

2.5.2. Calculating the precipitation rate from radar reflectivity

Having calculated radar reflectivity in the previous section, this section calculates the precipitation rate R from radar reflectivity Z . The Z-R relationship can be empirically defined using radar-observed reflectivity and rainfall rates observed by another instrument. Alternatively, a disdrometer can be used to observe the drops size distribution, and both the rain rate and radar reflectivity can be estimated from the observed drops size distribution [Rinehart, 1997, p. 141]. The Z-R relationship has the following form with two coefficients a and b :

$$Z = a R^b \quad (2.17)$$

In this equation, reflectivity Z is stated in linear units of mm^6/m^3 , not in logarithmic units of dBZ.

The a and b coefficients in the rain-reflectivity relationship vary with the drops size distribution [Doviak and Zrnic, 1993, Figure 8.6; Battan, 1973, Table 7.1]. Doviak and Zrnic [1993, p. 214] state that "actual drop-size spectra differ greatly depending on geographical location, type of rainstorm, season, and region within the storm" (See also Kozu [1991, p. 24]). To partially address these issues, the TRMM 2A25 algorithm uses a different drops size distribution for stratiform vs. convection rainfall regions [Iguchi *et al.*, 2000, JAM].

To calculate the precipitation rate, different coefficients must be used in the Z-R relationship above and below the freezing level (Table 2.2). The coefficients for ice take into account several issues. For one thing, the dielectric constant for ice is less than for liquid water which weakens the observed reflectivity for a given water mass. Second, ice

hydrometeors tend to be larger than raindrops which would increase the observed reflectivity for a given water mass. Third, small precipitating ice particles (0.1 to 1.0 mm in diameter) have a slower falls speed (~ 2 m/s) than liquid hydrometeors (~ 7 m/s) (Figure 2.13, p. 122) which would increase the observed reflectivity for a given rain rate. Fourth, the liquid water density of ice hydrometeors varies from compact hail to low density flakes and composites that contain air pockets. The variable density can have large effects on the precipitation rate and the fall speed.

Table 2.2. Reflectivity (dBZ) to precipitation (mm/h) relationship for convective precipitation observed by the TRMM Precipitation Radar. The "initial" row gives Z-R relationship coefficients assumed initially in the TRMM 2A25 algorithm [Iguchi *et al.*, 2000, *JAMS*, Table 1]. The "final" row gives the outputted 2A25 precipitation rate during the overflight of Hurricane Bonnie (1998) during TRMM orbit #4224. The range of precipitation rates in column 4 are the middle 50% of the distribution of precipitation rates for ± 2 dB of the stated reflectivity values. The number of observations within ± 2 dB of stated reflectivities for the Hurricane Bonnie overflight are stated in the "obs. count" row.

1. Above freezing height?	2. Value	3. Z-R coeff.		4. Radar reflectivity			
		<i>a</i>	<i>b</i>	20 dBZ	30 dBZ	40 dBZ	50 dBZ
yes	initial mm/h	174	1.32	0.7	4	22	123
	final mm/h			0.6–0.9	4–6	13–20	–
	<i>obs. count</i>			11943	803	21	–
no	initial mm/h	148	1.55	0.7	4	15	67
	final mm/h			0.5–0.7	2–3	12–18	63–98
	<i>obs. count</i>			6883	10749	4444	180

2.5.3. Hydrometeor fall speed

When calculating the precipitation rate from radar reflectivity, as done in the previous section, a fall speed for the hydrometeors must be assumed. This section provides more information about fall speed.

For a summary of the dependence of fall speed on hydrometeor size, altitude, and water phase, see Figure 2.13 (p. 122), which is described in the following paragraphs. A hydrometeor is simply a liquid or solid particle of water that is large enough to fall through the air. A radar detects the square of the volume (the sixth power of the diameter) of a hydrometeor, and a radar does not detect the fall speed of the hydrometeor. For this reason, the precipitation rate cannot be estimated from observed radar reflectivity without assuming a fall speed. The TRMM 2A25 algorithm assumes a reasonable fall speed for ice above the freezing level and for rain drops below the freezing level and adjusts the fall speed for the climatological variation of density with altitude [Iguchi, 2000, JAM; *TRMM Precipitation Radar Team*, 2005, p. 94].

The fall speeds assigned by the TRMM 2A25 algorithm are averages over the entire dropsize distribution. The fall speed of an individual hydrometeor depends on the diameter d (mm) of the hydrometer. Above the freezing level, *Doviak and Zrnica* [1993, p. 218] state that the fall speed v (m/s) of low-density ice (such as snow flakes) is $0.98 d^{0.31}$. For high-density ice (ice pellets and hail), the fall speed is $3.62 d^{0.5}$.

To a first approximation, a solid or liquid hydrometeor's fall speed also varies with altitude according to the square root of the air density [*Doviak and Zrnica*, 1993, p. 217; *TRMM Precipitation Radar Team*, 2005, p. 94]. As shown in equation 2.18, air

density ρ (kg/m³) at any altitude can be calculated from the pressure p (mbar) and temperature T (K) using the ideal gas law.

$$\rho = \frac{1}{R} \frac{p}{T} \quad \text{Wallace and Hobbs [2006, p. 63]}$$

$$\text{unit analysis : } \frac{\text{kg}}{\text{m}^3} = \frac{1}{\frac{\text{J}}{\text{K kg}}} \frac{\text{Pa}}{\text{K}} = \frac{\text{kg}}{\text{J}} \frac{\text{N}}{\text{m}^2} = \frac{\text{kg}}{\text{Nm}} \frac{\text{N}}{\text{m}^2} \quad (2.18)$$

$$\rho = 3.48 \times 10^{-3} \frac{p}{T} \quad \text{with } p \text{ in Pa and } T \text{ in K}$$

$$\rho = 0.348 \frac{p}{T + 273.16} \quad \text{with } p \text{ in mbar and } T \text{ in C}$$

In the above equation, the gas constant for dry air R_d (287 J / K kg) is used in place of the almost equal gas constant for moist air R . In Table 2.3, density is approximated along a typical temperature-pressure profile inside a tropical cyclone eyewall. A typical profile is the 28C saturated adiabat up to 15 km (See the thick green line in Figure 2.12, p. 121), with a 20 km value supplied by the NCEP climatological background profile for the North Atlantic tropical cyclone formation region from July through October.

Table 2.3. The 28 C saturated adiabat at specified altitudes, plus the climatological profile at 20 km

Variable	Surface	5 km	10 km	15 km	20 km
Pressure (mbar)	1013	550	280	130	80
Temperature (C)	28	7	-21	-68	-67
Temperature (K)	301	280	252	205	206
Density (kg/m ³)	1.17	0.68	0.39	0.22	0.14
Relative fall speed (unitless) ¹	1	1.3	1.7	2.3	2.9

¹ The relative fall speed can be thought of as the increase in fall speed relative to the fall speed at the surface.

Based on the bottom row of Table 2.3, the variation in fall speed with altitude is shown in Figure 2.13 (p. 122).

Next, the dissertation relates radar reflectivity to drop size, as summarized at the bottom of Figure 2.13. Two radar reflectivities (~ 20 dBZ and ~ 40 dBZ) come up in this dissertation, and they roughly correspond to light and heavy precipitation rates (~ 1 mm/h vs. 20–100 mm/h) (Table 2.2, p. 56). To interpret the meaning of these two reflectivities, it would be helpful to know the fall speeds of the hydrometeors that contribute the most to these two reflectivities. Most hydrometeors in tropical cyclone eyewalls are between 0.5 and 5 mm in diameter. Because radar reflectivity varies with the sixth power of diameter, if the number of small drops (0.5 mm diameter) is less than a million times greater (10^6) than the number of large drops (5 mm diameter) then the large drops will be the primary scatterers. The slope of the dropsize distribution varies with the rain rate and is often expressed using a natural exponent [*Doviak and Zrnic*, 1993, p. 213]. However, the dropsize distribution is easier to use in order-of-magnitude estimates if it is rewritten in terms of powers of 10. As shown in equation 2.19, the rewriting can be done using the fact that $\ln x = \frac{1}{\log e} \log x$ [*CRC*, 1991, p. 140].

$$\begin{aligned}
\frac{N}{N_0} &= e^{-4.1 R^{-0.21} d} && \text{Doviak and Zrnic, 1993, p. 213} \\
\ln \frac{N}{N_0} &= -4.1 R^{-0.21} d && \text{Take the natural log of both sides} \\
\log \frac{N}{N_0} &= -4.1 (\log e) R^{-0.21} d && \text{Convert to log base 10} \\
\frac{N}{N_0} &= 10^{-1.78 R^{-0.21} d} && (2.19) \\
\frac{N}{N_0} &= 10^{-1.78 d} && \text{for } R = 1 \text{ mm/h} \\
\frac{N}{N_0} &= 10^{-0.67 d} && \text{for } R = 100 \text{ mm/h}
\end{aligned}$$

In the above equations, the number N ($1/\text{m}^3 \text{ mm}$) is the number of drops per cubic meter in a 1 mm diameter range of drop diameters. The range of drop diameters is centered on drop diameter d (mm). The rain rate is R (mm/h), and the constant N_0 is $8\text{e}3 \text{ } 1/\text{m}^3 \text{ mm}$ [Doviak and Zrnic, 1993, p. 213]. Next, the dissertation substitutes into the above equations to determine that large drops ($d = 5 \text{ mm}$) have the following relative frequency compared with small drops ($d = 0.5 \text{ mm}$) when the rain rate is light or heavy ($R = 1 \text{ mm/h}$ vs. 100 mm/h):

$$\begin{aligned}
\frac{N_{d=5 \text{ mm}}}{N_{d=0.5 \text{ mm}}} &= 10^{-8.01} && \text{for } R = 1 \text{ mm/h} \\
\frac{N_{d=5 \text{ mm}}}{N_{d=0.5 \text{ mm}}} &= 10^{-3.02} && \text{for } R = 100 \text{ mm/h}
\end{aligned} \tag{2.20}$$

Equation 2.20 shows that, since the dropsize distribution of light rain (corresponding to $\sim 20 \text{ dBZ}$) falls by more than six orders of magnitude for each order of

magnitude increase in drop diameter, the 20 dBZ signal is most sensitive to the concentration of the smallest hydrometeors. Equation 2.20 also shows that the dropsize distribution of heavy rain (corresponding to ~ 40 dBZ) drops off less than six orders of magnitude for each order of magnitude increase in dropsize, so the 40 dBZ signal is most sensitive to the concentration of the largest hydrometeors. Equation 2.20 is consistent with *Doviak and Zrnic* [1993, p. 214, Figures 8.3b and 8.5a].

Next, the dissertation relates the drop sizes to passive microwave observations, which is summarized along the bottom of Figure 2.13 (p. 122). Radiation with 85 GHz, 37 GHz, and 19 GHz frequencies have wavelengths of 3.5 mm, 8 mm, and 16 mm, respectively. Ice particles scatter upwelling radiation out of the line of sight of the TMI instrument. The larger the ice particle, the lower the frequency at which it can scatter out radiation. As discussed on page 45, the scattering is Rayleigh scattering when the hydrometeors are smaller and Mie scattering when the hydrometeors are larger [*Janssen*, 1993, p. 302].

As mentioned earlier in section 2.5, Rayleigh scattering increases rapidly with drop diameter until Mie scattering regime begins when the drop diameter equals $\sim 1/3 \approx 1/\pi$ of the wavelength of the radiation. Based on the $1/\pi$ factor, the 85 GHz signal is most sensitive to scattering by 1.1 mm diameter hydrometeors (ice pellets smaller than hail), the 37 GHz signal is most sensitive to scattering by 2.5 mm diameter hydrometeors (small hail), and the 19 GHz signal is most sensitive to scattering by 5.1 mm diameter hydrometers (pea to grape sized hail). *Cecil et al.* [2002, part 1, p. 774] gives a somewhat smaller size: several tenths of a mm for 85 GHz and ~ 1 mm for 37 GHz.

2.6. Future instrumentation

For studying tropical cyclones, only one satellite currently being planned could improve on the TRMM satellite. This satellite is the core satellite of the Global Precipitation Measuring (GPM) Mission that is currently scheduled for launch in 2013.

The GPM Mission will include a core satellite with a precipitation radar and a constellation of smaller satellites each carrying just a passive microwave instrument [Hou, 2006; NOAA, 2007, p. 4-7]. The constellation satellites will be in polar orbit and the core satellite in a 65 degree inclination orbit so that it intersects the paths of the constellation satellites [Hou, 2006]. At these intersection points, the precipitation radar on the core satellite will be used to calibrate the passive microwave instruments on each constellation satellite. On the core satellite, the GPM radar will have the advantage of being dual frequency, allowing for estimation of the drop size distribution. On some of the constellation satellites, a GPM Microwave Imager (GMI) will have the advantage of carrying several high frequency channels for detecting cloud ice and precipitating ice [Jackson, 2005].

In some respects, the GPM core satellite will be less useful for observing tropical cyclones than the TRMM satellite currently is. The GPM core satellite will orbit at a higher inclination of 65 degrees compared with TRMM's 35 degrees. This means that, for most of its orbit, the GPM radar will be outside of the tropical cyclone formation

region. On the other hand, the GPM radar will reach far enough north to observe a tropical cyclone-like phenomenon called "polar lows" that threaten life and property in northern Europe [Rasmussen, 2003]. A second disadvantage of GPM will be that it is not expected to carry an infrared instrument or lightning instrument. Infrared and lightning observations will have to come from other satellites or from instruments on the ground. There can be practical difficulties and costs associated with obtaining data from other projects. Furthermore, when instruments are on different satellites, the times of observation can differ by an hour or more. A convective cell only lasts about an hour, so a time mismatch is not helpful [Doswell, 2001; Cotton and Anthes, 1989, p. 462; Houze, 1993, p. 270]. Last, the GPM core satellite is being designed for a three year mission with fuel for 5 years. TRMM was also only designed for a three year mission, but TRMM appears to have been launched with sufficient fuel for 14 years in space [NRC, 2004, p. 18].

2.7. Dynamics of tall convection

2.7.1. Parcel theory of convective updrafts

Some of the dynamics of a tall convective cell can be explained by "parcel theory" [Wallace and Hobbs, 2006, chapter 3; Djuric, 1994, chapter 5; Bohren and Albrecht, 1998, chapter 6; Houze, 1993, chapter 7; Emanuel, 1994, chapter 2]. In particular, parcel

theory provides a simple way to estimate the maximum possible height of a convective cell for a given background atmosphere.

A parcel of air is an imaginary volume of air that is small enough to rise and fall as a unit relative to the rest of the atmosphere. An important simplification in parcel theory is that the atmosphere is considered to be a motionless "background" in which the air parcel moves. At times, it can be convenient to imagine a parcel of air as a kilogram of air ($\sim 1 \text{ m}^3$ at the surface) that expands as it rises in altitude. At other times, it can be convenient to think of a parcel as a much larger volume of air, perhaps a cubic kilometer of air. For an example, the rising top of the cells shown in Figures 1.1a and 1.1b (p. 3) can be thought of as a rising bubble of air that is governed by parcel theory to a rough approximation [Doswell, 2001, p. 6].

If an air parcel becomes supersaturated with water vapor, then condensing water vapor can make the parcel warmer than the parcel's surroundings, which causes the parcel to rise, which causes additional water vapor to condense. At its new altitude, the pressure of a small parcel ($\sim 1 \text{ m}^3$) adjusts almost immediately (on order 1 second) to the pressure of its new surrounding. Air is a good insulator, so depending on how large the parcel is, it could take several minutes to 30 minutes or longer for a parcel's temperature to equalize with the background temperature of its new surroundings [Ray, 1986, p. 276].

By the ideal gas law, the parcel expands and cools as it rises to a lower pressure area. This cooling is called "adiabatic cooling" because it occurs without any heat being added or removed from the parcel. The word "adiabatic" comes from the Greek prefix *a-* meaning "not" and the root *diabatos* for "passable." Literally, "adiabatic" means a

process in which heat does not pass through the outer boundary of the parcel. However, because latent heat is being released as water vapor condenses in the parcel, the parcel is warmer than it would have been otherwise and also warmer than the background air at that pressure. If the parcel rises above about 5 km in the Tropics, then the condensing water vapor can freeze, which releases about an additional 13% of latent heat ($L_f / L_v = 13\%$). If rain or ice hydrometeors fall through an unsaturated parcel, then the parcel can be cooled by melting or evaporation, and the parcel will become heavier than its surroundings and move downward.

The vertical acceleration of a parcel is determined by its buoyancy. The buoyancy force per unit mass of air is the fractional difference in density between the parcel and its surroundings multiplied by the acceleration due to gravity ($g = +9.8\text{m/s}^2$). In the notation below, a positive force indicates an upward acceleration. The expression can be written in terms of density or in terms of temperature due to the ideal gas law [Emanuel, 2004, p. 4]. The ideal gas law states that pressure p in Pascals (mbar times 100) equals the product of air density ρ in kg/m^3 , the ideal gas constant R ($\sim 287 \text{ J/K kg}$), and absolute temperature T in degrees Kelvin ($p = \rho R T$). When pressure is constant, density must increase by the same percentage that temperature decreases to satisfy the ideal gas law. Putting this information together, the buoyancy force F per unit mass of air can be written in the following way:

$$F_{\text{buoyancy per unit mass}} = g \frac{\rho_{\text{background}} - \rho_{\text{parcel}}}{\rho_{\text{background}}} = -g \frac{T_{\text{background}} - T_{\text{parcel}}}{T_{\text{background}}} \quad (2.21)$$

$$\text{unit analysis } \frac{\text{N}}{\text{kg}} = \frac{m}{s^2} = \frac{m}{s^2} 1$$

Force per unit mass (equation 2.21) has units of acceleration (m/s^2), as used in equation 2.28. When the buoyancy force is zero, the parcel is said to be at its level of neutral buoyancy.

Parcel theory estimates the maximum height that a convective cell can reach as the level of neutral buoyancy plus the overshooting distance. The overshooting distance is limited by the parcel's updraft speed when it passes through its level of neutral buoyancy (section 2.7.3).

2.7.2. Vertical distribution of temperature and pressure

Figure 2.12 (p. 121) shows the variation of temperature with height in the tropical troposphere. This section explains how the figure is generated. In the figure, the conversion from pressure to altitude is performed using the 10°N climatological temperature profile for September found in *Houghton* [1986, p. 234].

In Figure 2.12, the diagonal straight blue lines show the saturation water vapor mixing ratio w (g water vapor per kg air) for the given temperature T (K) and air pressure p (mbar). The mixing ratio is only weakly a function of air pressure, so to a first approximation, the mixing ratio increases from 0.01 g/kg at the coldest part of the troposphere to as high as approximately 30 g/kg in warm moist surface air. The

saturation mixing ratio w can be calculated from temperature and air pressure using equation 2.22 [Emanuel, 1994, p. 116]. The derivation of this formula for w uses the saturation water vapor pressure p_{water} , which is solely a function of air temperature. To generate a vector of pressure \vec{p} and temperature \vec{T} coordinates for a particular mixing ratio w , use the following equations:

$$p_{water}[\vec{T}] = e^{53.68 - 6744.0 \vec{T} - 4.845 \ln \vec{T}} \quad \text{Emanuel [1994, p. 116]}$$

$$w = 0.622 \frac{p_{water}[\vec{T}]}{p - p_{water}[\vec{T}]} \quad \text{Djuric [1994, p. 71]} \quad (2.22)$$

Solve the w equation for p :

$$\vec{p} = p[w, \vec{T}] = \frac{0.622 + p_{water}[\vec{T}]}{w} + p_{water}[\vec{T}]$$

In Figure 2.12, the diagonal straight yellow lines show the temperature and pressure of a dry parcel of air as it moves up and down adiabatically following the ideal gas law. These lines are known as dry adiabats and are lines of constant potential temperature θ (K) [Djuric, 1994, p. 73]. To generate the vector of pressure \vec{p} and temperature \vec{T} coordinates for a particular potential temperature θ , the bottom formula is used. In equation 2.23, potential temperature θ is by definition the same as the reference temperature T_0 .

$$\frac{T}{T_0} = \left(\frac{p}{p_0} \right)^{\frac{R}{c_p}} \quad \text{Emanuel [1994, p. 111]} \quad (2.23)$$

$$\vec{T} = T[\theta, \vec{p}] = \theta \left(\frac{\vec{p}}{p_0} \right)^{\frac{R}{c_p}}$$

In the above equation, R / c_p is $278/1004 = 0.285$, i.e., the ratio of the gas constant R for dry air (J / K kg) to the heat capacity of dry air c_p (J / K kg). The observed and reference pressures, p and p_0 , are in mbar. The observed and reference temperatures, T and T_0 , are in degrees Kelvin. The dry adiabats are labeled in units of degrees Kelvin in the upper left corner of Figure 2.12.

In Figure 2.12, the green curved lines show the temperature of a parcel of air that is saturated with water vapor as it rises. These lines are known as saturated adiabats and are lines of constant equivalent potential temperature θ_e (K).

The saturated adiabats calculated in this section are approximations because they make the assumption that the water stays in the parcel after it condenses, whereas in reality, most if not all of the water falls out of the parcel after condensing. *Bohren and Albrecht* [1998, p. 295] show a saturated adiabat (condensed water stays in the parcel) becomes 3 K warmer than a pseudo-adiabat (condensed water is immediately removed from the parcel) when they are both traced from the surface up to 200 mbar. *Bohren and Albrecht* [1998, p. 295] also assert that saturated ascent in the troposphere lie somewhere in between saturated adiabats and pseudoadiabats.

It simplifies the computation to assume that water stays in the parcel after it condenses. The calculation starts at the top of the troposphere, where there is almost no water vapor and then moves down the moist adiabat in small temperature steps of dT_{step} , incorporating the effect of the condensing water vapor as one goes. It makes sense to start on a dry adiabat by specifying a starting point of $[p, \theta]$ so that the figure can show

the gradual departure of a saturated adiabat from the associated dry adiabat as one descends to the Earth's surface.

The details of tracing out a saturated adiabat follow. Start with a θ_e to follow and an initial temperature T at the top of the troposphere where lines of constant θ are identical to the lines of constant θ_e . Set the starting potential temperature θ equal to the given θ_e . In each of the following steps, the potential temperature θ will be increased to account for the amount of heat released by water vapor condensing, were the parcel to be rising. The first step is to calculate the starting pressure p using the current potential temperature θ and the reference pressure p_0 of 1000 mbar:

$$p = p[\theta, T] = p_0 \left(\frac{T}{\theta} \right)^{\frac{c_p}{R}} = p_0 \left(\frac{T}{\theta} \right)^{3.5} \quad (2.24)$$

Calculate the starting saturation water vapor mixing ratio w_{sat} from temperature T and pressure p :

$$p_{water} = e^{53.68 - 6744.0/T - 4.845 \ln T} \quad \text{Emanuel [1994, p. 116]}$$

$$w_{sat} = 0.622 \frac{p_{water}}{p - p_{water}} \quad \text{Djuric [1994, p. 71]} \quad (2.25)$$

Now for each step, increase the observed temperature T by a temperature step dT_{step} which is equivalent to moving the parcel down to a slightly lower altitude. Then, calculate the pressure at the new temperature, then the saturation water vapor mixing ratio at the new temperature and pressure. The difference in the mixing ratio Δw_{sat} from the initial value to the current value is the amount of water vapor that would have condensed if the parcel were rising through this altitude change. The amount of water

vapor condensing is proportional to the amount of latent heat released and the resulting temperature change. Equation 2.26 calculates the temperature change ΔT due to the change in the saturation water vapor mixing ratio Δw_{sat} :

$$\begin{aligned}\Delta T &= \frac{H}{c_p} & H &= L_v \Delta w_{sat} \\ \Delta T &= \frac{L_v}{c_p} \Delta w_{sat}\end{aligned}\tag{2.26}$$

Next, convert from a change in temperature to a change in potential temperature θ by multiplying by the familiar term for converting from temperature to potential temperature:

$$\Delta \theta = \Delta T \left(\frac{p}{p_0} \right)^{\frac{R}{c_p}} = \Delta T \frac{T}{T_0}\tag{2.27}$$

Last, add the potential temperature increment $\Delta \theta$ to the current potential temperature θ to arrive at the new potential temperature. This new potential temperature has the desired property that it is still on the given equivalent potential temperature θ_e line that defines the saturated adiabat that these calculations are tracing out.

In Figure 2.12, gray dots indicate the mean climatological temperature profile in the region and season that most North Atlantic tropical cyclones form. More specifically, the gray dots identify the NCEP reanalysis mean temperature profile for 15°N to 30°N, 60°W to 20°W, and the months of July through October. The long-term mean air.mon.longTermMean.nc NetCDF file that contains these data was downloaded from <http://www.cdc.noaa.gov/cdc/data.ncep.reanalysis.derived.pressure.html> [Kalnay *et al.*,

1996]. The NCEP temperature is only available at the pressures marked with gray points in Figure 2.12. Connecting these points with a straight line could be misleading because the dataset does not provide information about how the temperature profile varies between the reported pressures.

Rain drops and cloud droplets begin to freeze at 0 C (the thick gray vertical line in Figure 2.12). In the gentle updrafts of tropical cyclones, almost all of the liquid water has frozen by the time the parcel reaches -5C [*Black and Hallett*, 1986], but supercooled water drops were once observed at in a tall eyewall cell at -35 to -42 C (a 12 km altitude), which implies a strong updraft [*Black et al.*, 2003].

2.7.3. Mathematical derivation of vertical CAPE

This section goes beyond the discussion in section 2.1.3 (p. 19) by presenting the mathematics behind the most commonly published kind of CAPE, i.e., vertical CAPE due to thermal buoyancy. As previously mentioned, CAPE stands for Convective Available Potential Energy. Some texts define CAPE as an integral with respect to pressure [e.g., *AMS*, 2001], but the author finds CAPE is easier to visualize as a integral with respect to distance [*Doswell*, 2001, p. 1; *Wallace and Hobbs*, 2006, p. 345; *Vasquez*, 2003, p. 148; *Emanuel*, 1994, p. 169]. In the following equation, CAPE is the integral from the level of free convection z_0 to the level of neutral buoyancy z_1 . A schematic representation of CAPE appears in Figure 3.5 (p. 155), and CAPE can be estimated by comparing a background profile with a saturated adiabat in Figure 2.12 (p. 121).

In equation 2.28, T_{envir} is the background temperature (K), ΔT is the difference between the parcel's temperature and the background temperature (K), g is the acceleration due to gravity (9.8 m/s^2), dz is the altitude increment (m), Δz_{ascent} is the distance (m) between the level of free convection z_0 and the level of neutral buoyancy z_l , and $a_{buoyancy}$ is the parcel's upward acceleration (m/s^2). Acceleration $a_{buoyancy}$ can be called the thermal buoyancy, i.e., the buoyant force per unit mass of air in the parcel.

$$a_{buoyancy} = g \frac{\Delta T}{T_{envir}}$$

$$CAPE = \int_{z_0}^{z_l} a_{buoyancy} dz \quad (2.28)$$

$$CAPE_{\text{fixed } \Delta T} = a_{buoyancy} \Delta z_{ascent}$$

$$\text{unit analysis : } \frac{\text{J}}{\text{kg}} = \frac{\text{Nm}}{\text{kg}} = \frac{\text{m}}{\text{s}^2} \text{ m}$$

Thermal buoyancy is the simplest and the most commonly stated form of buoyancy. *Houze* [1993, p. 36] states a more complicated form for buoyancy that includes three additional terms. These terms are related to (1) the pressure of the parcel being different than the background pressure, (2) the water vapor in the air altering the parcel's heat capacity away from the heat capacity of dry air, and (3) the downward drag on the air parcel due to precipitation falling through it. *Braun* [2002] uses this full expression for buoyancy. *Eastin et al.* [2005, part 1] finds in aircraft in-situ observations that the additional terms only alter the total buoyancy by approximately $\pm 10\%$ from the thermal buoyancy. The thermal buoyancy (equation 2.28) alone is sufficiently accurate for the discussion in this section.

Under the assumptions of no drag and no entrainment of background air, a parcel of air can convert all CAPE into kinetic energy, reaching an easily calculated maximum velocity. Equation 2.29 defines the time of ascent t_{ascent} from altitude z_0 to z_l and the final velocity v_{max} for constant acceleration $a_{buoyancy}$:

$$\begin{aligned}
 t_{ascent} &= \sqrt{\frac{2 \Delta z_{ascent}}{a_{buoyancy}}} && \text{based on } d = \frac{1}{2} a t^2 \\
 v_{max} &= a_{buoyancy} t_{ascent} && \text{based on kinematics, } v = a t \\
 v_{max} &= \sqrt{2 CAPE} && \text{from [Djuric, 1994, p. 87]}
 \end{aligned} \tag{2.29}$$

Assuming a constant temperature above the level of neutral buoyancy, the CAPE also determines the overshooting distance $\Delta z_{overshoot}$ using equation 2.30 [Djuric, 1994, Appendix L]. This dissertation uses a background temperature $T_{background}$ of 205 K at the level of neutral buoyancy. Djuric [1994] uses a 250 K temperature at the level of neutral buoyancy because he is concerned with the mid-latitudes.

$$\begin{aligned}
 \Delta z_{overshoot} &= v_{max} \sqrt{\frac{T_{background} c_p}{g^2}} = v_{max} \sqrt{\frac{205 \cdot 1005}{9.8^2}} \\
 \Delta z_{overshoot} &= v_{max} \cdot 46 && v_{max} \text{ in m/s, } \Delta z_{overshoot} \text{ in m} \\
 \Delta z_{overshoot} &= 0.046 v_{max} && v_{max} \text{ in m/s, } \Delta z_{overshoot} \text{ in km}
 \end{aligned} \tag{2.30}$$

Assuming no entrainment or drag, Table 2.4 calculates CAPE for several temperature differences ΔT . In Table 2.4, the buoyant acceleration is $a_{buoyancy}$, the time of ascent is t_{ascent} , the updraft velocity at the top of the ascent is v_{max} , and the distance of overshooting is $\Delta z_{overshoot}$.

Table 2.4. Maximum updraft speed and minimum ascent time for a given value of CAPE under the assumption of no entrainment, constant buoyancy, and an isothermal 205 K tropopause. The values in this table are rounded off although the calculations are done with more accuracy.

ΔT (K)	a_{buoyancy}^1 (m/s ²)	Δz_{ascent} (km)	$CAPE^1$ (J/kg)	t_{ascent}^2 (minutes)	v_{max}^2 (m/s)	$\Delta z_{\text{overshoot}}^3$ (km)
0.5 K	0.02	10	200	17	20	1
2.5 K	0.1	10	1000	7.5	44	2
5 K	0.2	10	2000	5.3	62	3
10 K	0.4	10	4000	3.8	88	4

¹ See equation 2.28. ² See equation 2.29. ³ See equation 2.30.

The theoretical updraft velocity v_{max} stated in Table 2.4 is unlikely to occur in reality because parcels interact with their environment. The exact extent of the interaction varies with each convective cell and is difficult to quantify based on observed variables. Table 2.5 gives a rough estimate of how entrainment or drag can reduce the updraft speed to less than half of the theoretical maximum updraft speed.

For Table 2.5, entrainment is calculated by increasing the volume V of the parcel at the rate of 20% for each kilometer z of rise (equation 2.31). Prior to beginning the ascent, the parcel's volume is V_0 . The entrained air is background air so it reduces the temperature excess of the parcel and therefore the parcel's acceleration a . The 20% entrainment rate is slightly higher than the 2% to 15% rate used by *Jensen and Del Genio* [2006, Figure 1]. The 20% entrainment rate results in a factor of 6 increase in the volume of the parcel during the 10 km ascent (equation 2.31), which is somewhat larger than the factor of 3 dilution used by *Zipser* [2003, section 4].

$$V = V_0 (1 + 0.2)^{z / 1 \text{ km}}$$

$$a = \frac{a_0}{\frac{V}{V_0}} = \frac{a_0}{(1 + 0.2)^{z / 1 \text{ km}}} \quad (2.31)$$

The acceleration a in equation 2.31 can be numerical integrated to calculate the maximum updraft velocity shown in column 5 of Table 2.5.

The drag experienced by a parcel is due to air resistance against the environmental air and due to drag from precipitation falling through the parcel. A simple method to parameterize the sum of the two drag terms is presented by *Scorer and Ludlam* [1953, p. 99]. Applying *Scorer and Ludlam's* method results in column 6 of Table 2.5. Drag reduces acceleration a by a constant fraction K of the current updraft speed v , which results in a terminal updraft velocity v_{max} after a few minutes of ascent (equation 2.32; see also *CRC* [1991, p. 284] and *Serway and Jewett* [2004, p. 163]). The reduction in updraft velocity due to drag is sensitive to *Scorer and Ludlam's* choice of constant $K = 1/50$ second⁻¹. *Scorer and Ludlam* chose this constant K to fit observations of isolated cells only ~5 km tall, so this value for K is not necessary appropriate for cells in tropical cyclone eyewalls that reach the upper troposphere.

$$a = a_{buoyancy} - K v \quad \text{the differential equation}$$

$$v[t] = \frac{a_{buoyancy}}{K} (1 - e^{-K t}) \quad \text{the solution to the differential equation} \quad (2.32)$$

$$v_{max} = \frac{a_{buoyancy}}{K} \quad \text{the upper limit of the solution}$$

A much less severe reduction in updraft velocity occurs if one uses an alternative formulation for drag. *Turner* [1962] assumes that drag reduces acceleration by a fixed

fraction of 33%, which reduces the maximum updraft velocity by slightly less than 33% [See also Houze, 1994, p. 235].

Table 2.5. Maximum updraft speed as affected by a simple estimate of drag or entrainment

1. ΔT (K)	2. Δz_{ascent} (km)	3. CAPE (J/kg)	Maximum updraft velocity v_{max} ² (m/s)		
			4. No interaction ¹	5. With entrainment ²	6. With drag ³
0.5 K	10	200	20	13	1
2.5 K	10	1000	44	29	5
5 K	10	2000	62	41	10
10 K	10	4000	88	58	20

¹ From Table 2.4. ² Using equation 2.31. ³ Using equation 2.32.

Tables 2.4 and 2.5 can help interpret statements about CAPE and updraft velocity found in several papers relevant to this dissertation. *Eastin et al.* [2005, part 1] assert that a CAPE of just 200 J/kg is sufficient to generate 20 m/s updrafts. Table 2.4 shows that 20 m/s updrafts are possible from 200 J/kg of CAPE only if all of the CAPE is converted into updraft kinetic energy. A 100% conversion of CAPE to updraft kinetic energy is somewhat unlikely. In mid-latitude weather forecasting, a CAPE of under 300 J/kg is considered insufficient to generate any convective cells, let alone vigorous convective cells [Vasquez, 2003, p. 148]. The most vigorous 5% of updrafts in eyewalls were found by *Black et al.* [1996] to have only 5 m/s speeds in the upper troposphere. If *Jorgensen* [1985] is correct that there is typically a CAPE of 800 J/kg in eyewalls and *Black et al.* [1996] are correct that the maximum updraft speed is ~5 m/s, then equation 2.29 suggest that 13% of CAPE is converted into updraft kinetic energy. This 13% is lower than the

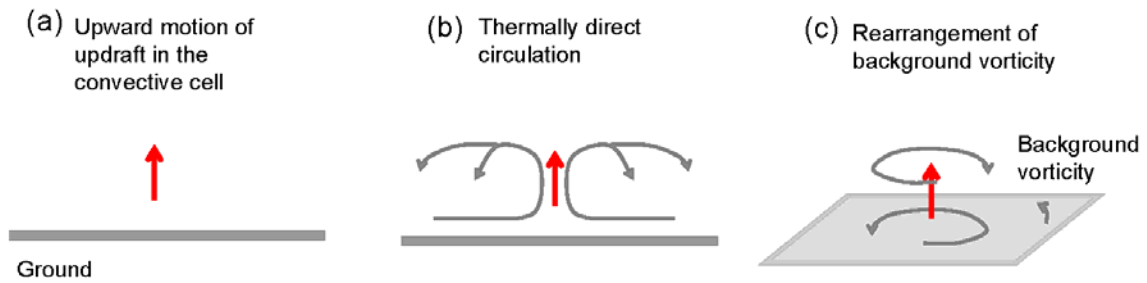


Figure 2.8. Schematic diagrams of convective cell dynamics. (a) The upward motion of air parcels. (b) The thermally direct circulation set up by an updraft. (c) The low-level cyclonic vorticity and upper-level anti-cyclonic vorticity that is collected by the convective cell's updraft.

50% used by *Zipser* [2003, section 4]. As discussed in Table 2.12 (p. 129), there are some reports of 40 m/s updrafts in tropical cyclones eyewalls, which are theoretically possible according to Table 2.4 if almost all CAPE is converted into kinetic energy and the temperature excess ΔT of the parcel over the background temperature profile averages 3 K or more in the troposphere. Aircraft in-situ observations reported in *Eastin et al.* [2005, part 1] find buoyancies in the eyewall from 1.5 km to 5.5 km altitude that can reach 1 to 2 K. The same paper cites no occurrences of eyewall buoyancies of ≥ 3 K in hundreds of observations. *Zipser* [2003] suggests that the temperature excess is typically 1 to 2 K in oceanic convective cells but can be 5 to 7 K in mid-latitude continental convective cells.

2.7.4. Circulation set up by a tall convective cell

Parcel theory is an incomplete description of the dynamics of a convective cell because it ignores the horizontal and vertical circulation outside of the cell that is set up by the

upward motion of parcels inside of the cell. Such circulations are unavoidable because a parcel cannot rise unless the air above it moves out of the way.

The circulation set up in the vertical plane is called a thermally direct circulation because it is driven by the latent heat released by water vapor condensing inside of the cell (Figure 2.8b) [*Wallace and Hobbs*, 2006, p. 299]. In the 30 minutes or so of vigorous updraft, a vertical circulation exists where the low-level air flows into the bottom of the cell, flows up inside of the cell, and flows outward at the top of the cell. Some of the outflow forms downdrafts while the rest of the outflow spreads far from the cell to eventually cool radiative and fall in a matter of days.

The updraft of a convective cell also sets up a circulation in the horizontal plane because it rearranges the background vorticity [*Hendricks et al.*, 2004]. This aspect of a convective cell has been studied when a cell forms in a rain band of a tropical cyclone [*Hendricks et al.*, 2004; *Nunez*, 1981, Ph.D.; *May and Holland*, 1999; *Franklin et al.*, 2006]. In the vicinity of the cell, there is generally at least a little cyclonic vorticity because mesoscale cyclonic vorticity contributes to convective cell initiation. The air approaching the cell can be thought of as being composed of rotating cylinders 2 km tall and 100 meters in diameter. As the air rises in the convective cell, the cylinders are stretched vertically, which causes their angular velocity to increase in order to conserve angular momentum.

One can think of the updraft as wringing out the vorticity from the air that passes through it. This concentrates the low-level vorticity as shown in Figure 2.8c (p. 77). The air reaching the top of the updraft is compressed vertically, which results in anti-cyclonic vorticity gathering around the top of the cell. These concentrations of vorticity can outlast the convective cell and survive to influence future convective cells [Reason *et al.*, 2000, section 5c1].

Another way for vorticity to appear in the horizontal plane is for there to be vertical wind shear, which is vorticity with a horizontal axis. When low-level horizontal flow changes direction and turns upward into an updraft, the horizontal axis of the

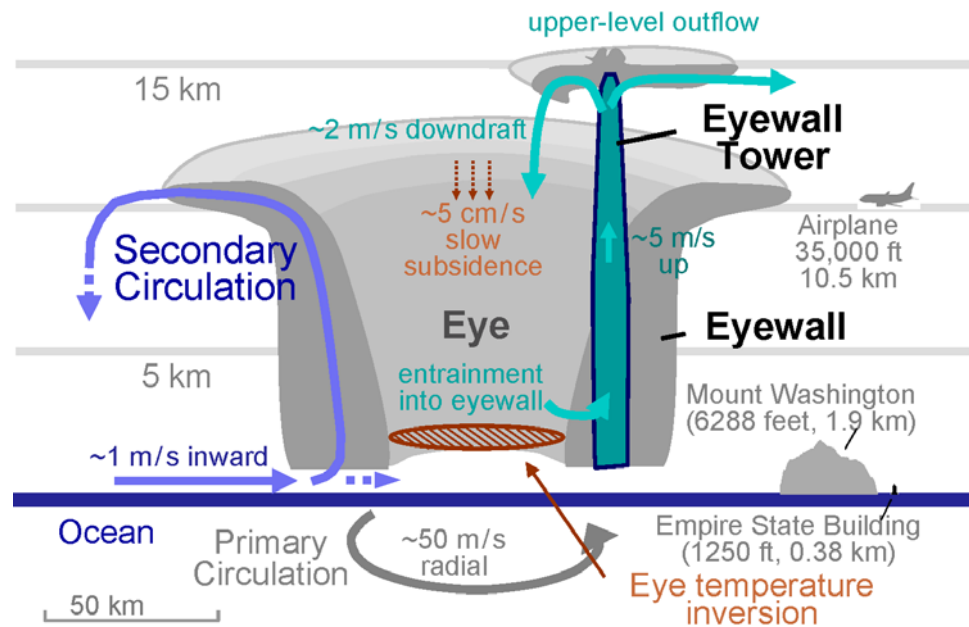


Figure 2.9. Schematic diagram showing a cross section through the center of a tropical cyclone. For related schematic diagrams, see Halverson *et al.* [2006, Figure 12], Heymsfield *et al.* [2001, Figure 12], Braun *et al.* [2006, Figure 18], or Hennon [2006, Ph.D., Figures 2 and 8].

vorticity can tilt toward the vertical direction [*Franklin et al.*, 2006]. *Holton* [1992, p. 304] states that a tropical cyclone's wind intensity is primarily due to the first process (vortex stretching) rather than the alternative (vorticity tilting): "The rapid rotation observed in hurricanes is produced by the concentration of the vertical component of absolute vorticity by vortex stretching, not by tilting horizontal vorticity into the vertical." In mesoscale convective systems, *Chen and Frank* [1993, p. 2417] finds that 60% of vorticity comes from vortex stretching and 30% from tilting of vertical plane vorticity into the horizontal plane.

2.8. Dynamics of tropical cyclones

A cyclone is an atmospheric phenomenon involving a large air mass circling a low pressure center. As stated by *Djuric* [1994, p. 167], mid-latitude synoptic cyclones (~1000 km across) "govern" the weather in many mid-latitude locations, such as the much of the continental United States. What distinguishes a tropical cyclone from a mid-latitude synoptic cyclone is that a tropical cyclone has a "warm core", i.e., the air at its center is significantly warmer than the background air at the same altitude. This temperature difference can be 10 to 15 C in the mid- and upper troposphere [*Anthes*, 1982, p. 28]. Around the often cloud-free warm-core eye of a tropical cyclone, there is often an arc of tall vigorous storm clouds that is called the eyewall. A schematic diagram of the eyewall is shown in Figure 2.9.

Because the essential characteristic of a tropical cyclone is its warm core, there is no requirement that a tropical cyclone remain in the Tropics or even that it form in the Tropics. Based on the seasonal motion of the sun, the astronomical boundary of the Tropics is 23.5 degrees of latitude from Earth's equator. This distance is the furthest north and south that a directly overhead sun occurs at some day of the year. Atmospheric scientists sometimes use ± 30 degrees as the boundary of the Tropics. Climatologists prefer to define the Tropics as locations with tropical climate, i.e., a climate without a cold season [McGregor and Nieuwolt, 1998, pp. 1–2]. Based on Elsner and Kara [1999, Figure 4.10], only half of North Atlantic tropical cyclones form north of 23.5°N and approximately 10% form north of 30°N.

2.8.1. Gradient wind balance

To a first approximation, the dynamics of a tropical cyclone can be explained by the gradient wind balance [Emanuel, 1986].

The only forces at work in gradient wind balance are the radially inward force due to the central low pressure balanced by two radially outward forces: the coriolis force and the centrifugal force [Holton, 1992, section 3.2]. If a "pure" gradient wind balance could exist, the wind would continue circling indefinitely due to conservation of vorticity until the vortex exchanged angular momentum with another vortex or broke up into smaller vortices due to the inherent instability of vortices [Schubert *et al.*, 1999; Guinn and Schubert, 1993].

2.8.2. Dissipative forces

Two dissipative forces alter a tropical cyclone, pushing it away from a pure gradient wind balance. These forces would dissipate most of a tropical cyclone's rotational kinetic energy in less than a day if no kinetic energy were added ⁷. The dissipative forces are air turbulence and friction between the atmosphere and ocean surface [*Emanuel, 1995; Bister and Emanuel, 1998*]. Turbulence slows and spreads the winds circling under the eyewall. Surface friction causes the low altitude winds to have a component radially inward toward the low pressure center. Fortunately for the tropical cyclone, this low-level convergence helps to set up an upward leg of convection near the tropical cyclone's eye, which often takes the form of an "eyewall" cloud that partially circles the tropical cyclone's eye. Most of the upper-level outflow from the eyewall convection moves radially outward away from the low pressure center. This in-up-and-out motion is called the secondary circulation. The horizontal circular winds around the low pressure center is called the primary circulation.

Counteracting friction and turbulence, energy is added to the tropical cyclone from various sources. The winds of the tropical cyclone increase the rate of evaporation of ocean water and the rate of extraction of sensible heat from the ocean surface. This added moisture and warmth increases the lower troposphere's equivalent potential

⁷ The rate at which ocean surface friction robs energy from the tropical cyclone is $\sim 3 \times 10^{12}$ J/s [*Emanuel, 1998*]. At that rate, the time to take away half of the kinetic energy would be about 2 hours based on the tropical cyclone's kinetic energy being approximately 4×10^{16} J. The kinetic energy of a typical tropical cyclone can be calculated by the formula $0.5 m v^2$. The mass m is calculated from the column mass of the atmosphere, $\sim 7 \times 10^3$ kg/m², multiplied by the surface area in square meters of the eyewall $\pi (r_1^2 - r_0^2) = \pi (50 \times 10^3)^2 - 30 \times 10^3^2$. A typical velocity in the eyewall is ~ 50 m/s. In this approximation, the kinetic energy outside the eyewall can be ignored because the velocities are lower and kinetic energy varies with the square of velocity.

temperature, making the atmosphere more potentially unstable. Another source of energy is kinetic energy imported from outside the tropical cyclone. This source can take the form of high angular momentum in air entering or leaving the tropical cyclone (in the inflow: *Krishnamurti et al.*, 2005, *Tellus*; in the outflow: *DeMaria*, 1993). A third energy source is that the incoming air could enter with extra moisture that came from far away from the eyewall [*Krishnamurti et al.*, 2005, *MWR*]. A fourth energy source is discussed in section 2.1 and 2.7: there may be some Convectively Available Potential Energy (CAPE) in the background atmosphere that eyewall cells can release.

2.8.3. Eye subsidence

"Subsidence" usually refers to gradual descent of a broad region of air sometimes associated with night-time radiative cooling and sometimes with convective cells [*AMS*, 2000, p. 739]. "Downdraft" usually refers to a narrow column of air that is sinking rapidly [*AMS*, 2000, p. 233]. Downdrafts can be caused by the evaporation of precipitation, which cools the air and lowers its altitude of neutral buoyancy.

A special kind of subsidence can occur even when the level of neutral buoyancy of the air is not being reduced. This kind of subsidence is called "forced subsidence," and it can occur when the upper-level outflow from a vigorous convective cell has a lot of momentum. The outflow momentum can push down on surrounding columns of air, forcing subsidence in that air, pushing that air below its level of neutral buoyancy. If the forcing is short lived, then gravity waves can be set up, as discussed in the next section. If the forcing is constant for a sufficiently long period of time, then the warmed and

subsided air will mix with its new surroundings, reducing the temperature difference to the point that the subsided air has such a small buoyancy that it can no longer rise to its original altitude. When this mixing occurs, a permanent warming of the column has been caused by the forced subsidence. This kind of forced subsidence will be discussed in Chapter 5 in connection with the tropical cyclone's eye, and is also described in the following paragraphs.

Occasionally, scientists seem to deny the possibility of forced subsidence in a tropical cyclone's eye. For example, *Emanuel* [1997] states that "convectively induced secondary circulations cannot by themselves raise the vertically averaged temperature to

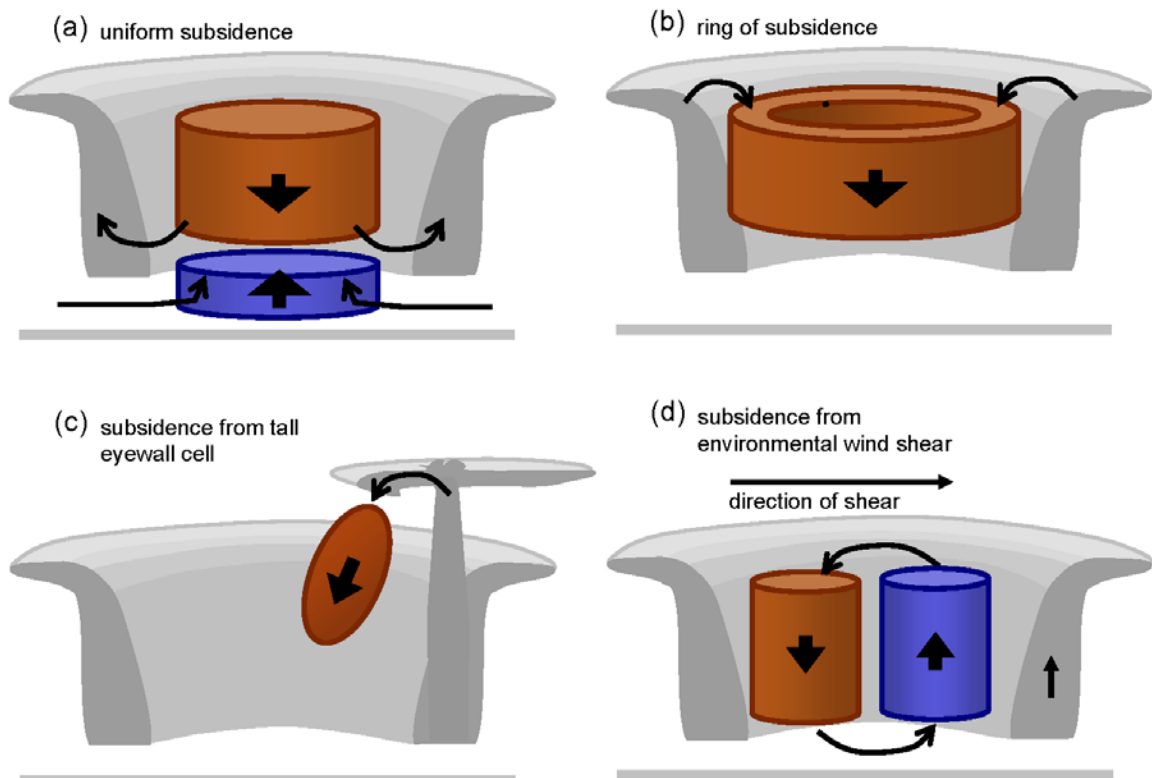


Figure 2.10. A schematic diagram showing various forms of tropical cyclone eye subsidence

a value greater than that inside of convective clouds." However, this statement does not deny the possibility of forced subsidence because it is actually referring to thermally direct circulation. Thermally direct circulation is defined in section 2.7.4 (p. 77).

Several kinds of eye subsidence are shown in Figure 2.10. Figure 2.10a shows uniform eye subsidence during a period of intensification due to mid-level eye air becoming entrained into the eyewall as proposed by *Willoughby* [1998]. The uniform subsidence may be on the order of 1 cm/s [*Willoughby*, 1998]. Also shown is low-level rising air due to eye inflow at the surface as proposed by *Zhang et al.* [2006]. Figure 2.10b shows a ring of subsidence along the outer edge of the eye as a result of an axisymmetric portion of the eyewall upper-level outflow being directing toward the eye as proposed by *Schubert et al.* [2007]. Observational studies suggest that the subsiding ring may be quite thin, perhaps a few 100s of meters thick radially [*Willoughby*, 1998, Figure 6]. Alternatively, the ring may be 5 to 10 km thick radially [*Schubert et al.*, 2007]. A ring of weak subsidence just inside the eye is shown in a simple axisymmetric model between an altitude of 11 km and 15 km [*Emanuel*, 2003, *Ann. Rev.*, Figure 4a and p. 82]. Figure 2.10c shows rapid subsidence in a portion of the eye adjacent to a tall eyewall cell, which has been observed occasionally such as by *Halverson et al.* [2006] and *Heymsfield et al.* [2001]. Figure 2.10d shows a pair of subsiding and rising columns inside the eye as set up by environmental wind shear [*Zhang et al.*, 2006; *Halverson et al.*, 2007].

In most in situ aircraft observations, it is difficult to see what mode of eye subsidence, if any, is occurring. For example, see *Eastin et al.* [2005 part 1], *Black et al.*

[2003, Figure 3] or most figures in *Black et al.* [1999]. Occasionally, flight-level temperature and velocity show a 1 to 4 K of warming in a downdraft just eyeward of the eyewall [*Heymsfield et al.*, 2001, Figure 8; *Black et al.*, 1999, Figures 8 and 14]. However, from these aircraft observations, it is difficult to distinguish between the ring and asymmetric forms of eye subsidence (Figures 2.10b and 2.10c).

A related question is what is the typical magnitude of the temperature anomaly that results from various forms of eye subsidence. Most if not all of the upper tropospheric 10 to 15 K thermal anomaly in a mature tropical cyclone is likely due to some form of eye subsidence over the several day lifetime of a tropical cyclone [*Willoughby*, 1998]. The more difficult question to answer is the scale and distribution of short term eye subsidence associated with a period of tropical cyclone wind intensification. *Holland et al.* [1984] report an extreme case of 18 K of warming in the subsidence region on one side of a tall eyewall cell. *Rogers et al.* [2002] observed 15 K of subsidence warming next to a convective cell involved in the formation of Hurricane Dennis (1999).

2.8.4. The eye's thermal anomaly and wind intensity

In section 2 of chapter 5, it is important to know that a moderate tropical cyclone experiences a wind intensity increase of approximately 7 knots for each 1 K increase in the mean temperature of the tropical cyclone's eye from 120 mbar to the Earth's surface.

A few studies publish wind-to-temperature relations. *Montgomery and Enagonio* [1998, Figure 15] shows a 6 kt/K to 10 kt/K relationship between warming in the central

region of a forming tropical storm and the tangential wind speed of the simulated vortex. *Holton* [1992, p. 305] gives an order of magnitude estimate of 10 kt/K for the wind-temperature relationship. The largest source of error in Holton's estimate is that he uses a fixed radius interval in which the pressure drop occurs.

In this section, the wind-temperature relationship will be split into two parts: a wind-pressure and a pressure-temperature relationship. Both parts are shown in Figure 2.14 (p. 123) and listed in Table 2.15 (p. 132). Figure 2.14 has two horizontal axes. The bottom horizontal axis states the upper tropospheric temperature anomaly in the tropical cyclone's eye. The temperature anomaly is largest between approximately 700 and 200 mbar (approximately 3 to 12 km). The upper horizontal axis states the surface pressure in the eye. The vertical profile of the eye's thermal anomaly is rarely observed through the full depth of the troposphere, although available measurements are plotted in Figure 2.14. Individual tropical cyclones with observed temperature anomalies are plotted against best track wind intensity using green ellipses. These tropical cyclones are listed in Table 2.15 (p. 132). For the same tropical cyclones, their best track pressure and best track wind estimates are plotted with black ellipses.

One way to map wind to surface pressure is with the Saffir-Simpson scale. As listed in Table 2.1 (p. 25), the Saffir-Simpson scale gives a surface pressure drop of 60 mbar and wind speed increase of 52 knots when going from a borderline category 1/2 tropical cyclone to a borderline category 4/5 tropical cyclone. The empirical relationship is close to linear at 0.87 kt/mbar (i.e., 52 kt / 60 mbar). Other ways to map wind to

surface pressure are presented by *Velden et al.* [1998, Table 2] and *Atkinson and Holliday* [1977, equation 7].

One way to map surface pressure to temperature anomaly is with AMSU data. AMSU stands for the Advanced Microwave Sounding Unit. Since 1998, an AMSU instrument has flown on NOAA's polar orbiting satellites. AMSU estimates the troposphere's vertical temperature profile [*Brueske and Velden*, 2003]. *Brueske and Velden* [2003, Figures 5 and 7] examine the AMSU upper tropospheric temperature anomaly in 53 satellite overflights of North Atlantic and East Pacific tropical cyclones. They observe a 6.7 mbar/K ratio (980 mbar – 920 mbar) / (14 K – 5 K). The AMSU relationship should be considered only approximate because the footprint of the AMSU channel used in these estimates is 58 to 100 km across, which is larger than the combined size of the eye and eyewall of most tropical cyclones [*Brueske and Velden*, 2003].

The AMSU 6.7 mbar/K relationship assumes that only the upper troposphere is warmed. A 7.8 mbar/K relationship results if one assumes alternatively that the whole troposphere warms below 120 mbar. To derive the whole-troposphere result, begin with the hydrostatic equation for an isothermal atmosphere [*Wallace and Hobbs*, 2006, pp. 67–69; *Holton*, 1992, p. 21]:

$$p = p_{surface} e^{-\frac{z}{z_0}} \quad \text{hydrostatic equation}$$

$$z_0 = \frac{R T}{g} \quad \text{scale height} \quad (2.33)$$

$$\text{unit analysis : } m = \frac{J}{K \text{ kg}} K \frac{1}{m/s^2} = \frac{m^2}{s^2} \frac{s^2}{m}$$

In the above equation, the gas constant R can be approximated by the gas constant for dry air (287 J/K kg), the acceleration due to gravity g is 9.8 m/s^2 , and the atmospheric scale height z_0 is a function of temperature T (K). The following calculations use the starting pressure p of 120 mbar at an altitude z of 15.5 km (based on Figure 2.12, p. 121). For fair weather conditions (row 1 of Table 2.6), a tropospheric temperature T of 248 K is used in equation 2.34. To simulate a moderate tropical cyclone, a temperature of 248+6 K is used (row 2 of Table 2.6). To simulate the incremental drop in surface pressure for each 1 K further increase in temperature, a temperature of 248+6+1 K is used (row 3). Last, the surface pressure drop is calculated for a moderate tropical cyclone with a 1 K warming that is limited to the 700 to 200 mbar layer (3 to 12 km) (row 4).

As shown in the rightmost column of row 3 of Table 2.6, a 1 K warming to an existing tropical cyclone results a 7.8 mbar/K surface pressure drop if the warming occurs uniformly from 120 mbar to the surface. The pressure drop is only 4.7 mbar/K if the warming is limited to 700 to 200 mbar.

$$p_{surface} = p e^{\frac{z}{z_0}} = p e^{\frac{z g}{R T}} = p e^{\frac{15.5 \cdot 9.8}{287 T}} = p e^{\frac{529.27}{T}} \quad (2.34)$$

$$p_{surface} = 120 \text{ mbar} e^{\frac{529.27}{T}}$$

In a real tropical cyclone, the vertical profile of warming in real tropical cyclones is concentrated in but not limited to the 700 to 200 mbar layer. Qualitatively, the 6.7 mbar/K ratio derived previously from AMSU observations is between the 7.8 mbar/K derived here for uniform warming and 4.7 mbar/K for warming between 700 and 200 mbar (bottom row of Table 2.6). As listed in Table 2.15 (p. 132), the eye's thermal

anomaly is typically observed to be 10 to 15 K in the upper troposphere and around 4 K at the surface.

Malkus [1958, p. 345] reports a 7 mbar/K ratio for uniform heating, which is close to the 7.8 mbar/K ratio reported here for uniform heating. There is a height dependency to these ratios. For example, equation 2.33 shows the ratio goes up to 9.6 mbar/K for uniform heating goes up to 80 mbar instead of the 120 mbar that has been used in this section. This height dependency is an instance of something *Holland* [1997] points out: the maximum altitude of the eye's temperature anomaly sets a limit on how low the eye's surface pressure can fall.

Multiplying the just derived 7.8 mbar/K ratio by the previously derived 0.87 kt/mbar ratio results in a 6.8 kt/K relationship between a uniform warming from 120 mbar to the surface and tropical cyclone wind intensity. This 6.8 kt/K relationship is rounded off to 7 kt/K and will be used in chapter 5.

Table 2.6. The relationship between eye temperature anomaly and surface pressure drop based on the hydrostatic equation. The calculations use equation 2.34 and go from 120 mbar to the surface. The value used in later calculations is the 7.8 mbar/K value in the rightmost column.

State	Surface pressure p (mbar)	$\Delta p / \Delta T$ from state 1 (mbar/K)	$\Delta p / \Delta T$ from state 2 (mbar/K)
1. Fair weather. $T = 248$ K isothermal atmosphere.	1014	NA	NA
2. The center of the eye of a moderate tropical cyclone. A $T = 248+6$ K isothermal atmosphere.	964	8.3	NA
3. 1 K isothermal warming of a moderate tropical cyclone's eye. $T = 248+6+1$ K isothermal atmosphere.	956	8.2	$7.8 = \frac{964 - 956 \text{ mbar}}{1 \text{ K}}$
4. Atmosphere with a $\Delta T = 1$ K warming between 200 and 700 mbar of the moderate tropical cyclone's eye.	959	7.8	$4.7 = \frac{964 - 9559 \text{ mbar}}{1 \text{ K}}$

Having derived the 7 kt/K ratio to be used in chapter 5, the section now goes back to take a closer look at the wind-to-pressure relationship. More specifically, one can approximate the empirical 0.87 kt/mbar ratio built into the Saffir-Simpson scale using the equation for cyclostrophic balance. In cyclostrophic balance, the horizontal surface wind under the eyewall is proportional to the square root of the radial derivative of pressure [Holton, 1992, p. 66], as shown in equation 2.36. If one assumes a reasonable radial variation of pressure [Holland, 1980; Willoughby and Rahn, 2004], then the pressure derivative varies approximately as the square of the pressure drop, which preserves the observed linear relationship between surface pressure and wind intensity in a tropical

cyclone (equation 2.37). According to *Holland* [1980], the gradient of pressure in the eyewall is proportional to the pressure drop Δp times a unitless shape parameter B (equation 2.37). Shape parameter B itself increases almost linearly with pressure drop Δp . For surface winds, one can use $B=1.6$ for a borderline category 1 to 2 tropical cyclone increasing to $B=1.9$ for a borderline category 4 to 5 tropical cyclone. A tropical cyclone eye's surface pressure drop Δp is the following function of the distance r from the center of the eye for an eye of radius r_{eye} [*Holland*, 1980]:

$$\Delta p[r] = \Delta p_{eye} e^{-\frac{r_{eye}^B}{r^B}} \quad (2.35)$$

If you assume that *Holland* [1980]'s pressure function is in cyclostrophic balance, then surface wind intensity v is related to the radial derivative of surface pressure p by the following equation:

$$\begin{aligned} \frac{v^2}{r} &= \frac{1}{\rho} \frac{d}{dr} p \\ v &= \sqrt{\frac{1}{\rho} r \frac{d}{dr} p} \end{aligned} \quad (2.36)$$

Calculating the derivative of the pressure in equation 2.35, and evaluating the derivative at the radius of maximum winds at the inner edge of the eyewall r_{eye} results in the following relation between pressure drop Δp and wind intensity v_{max} :

Evaluate the derivative :

$$\frac{d}{dr} \Delta p = B \frac{r_{eye}^B}{r^{B+1}} \Delta p e^{-\frac{r_{eye}^B}{r^B}}$$

Simplify at radius of maximum winds, $r = r_{eye}$:

$$\frac{d}{dr} \Delta p = \frac{B}{r} \Delta p e^{-1} = \frac{B}{r e} \Delta p$$

Multiply both sides by r :

$$r \frac{d}{dr} \Delta p = \frac{B}{e} \Delta p$$

Substitute into equation 2.36 :

$$v_{max} = \sqrt{\frac{B}{\rho e} \Delta p} \quad p \text{ in Pa and } v \text{ in m/s}$$

Convert units to mbar and knots :

$$v_{max} = 19.4 \sqrt{\frac{B}{\rho e} \Delta p} \quad p \text{ in mbar and } v \text{ in knots} \quad (2.37)$$

$$B = 1.6 + 0.3 \frac{\Delta p}{90 \text{ mbar}} \quad \text{unitless empirical coeff. } B$$

If the pressure drops from the Saffir-Simpson scale are substituted into equation 2.37, then close to the velocity measurements of the Saffir-Simpson scale are calculated. This is possible because the B parameter values used here take into account that the surface winds are approximately 90% of the cyclostrophic winds that occur around 700 mbar [Franklin et al., 2003, section 6]. Given $\rho=1.1 \text{ kg/m}^3$ and $e \approx 2.71828$, and then substituting $\Delta p = 30 \text{ mb}$ and $B = 1.6$ results in $v_{max} = 78 \text{ knots}$. Substituting $\Delta p = 90 \text{ mb}$ and $B = 1.9$ results in $v_{max} = 146 \text{ knots}$. This shows that when the theoretical *Holland*

[1980] pressure distribution is in cyclostrophic balance, one has a similar pressure-wind relationship to the relationship implied by the empirical Saffir-Simpson scale.

2.8.5. Energy conversion ratios

For a parcel rising in a tall eyewall cell, it is reasonable to expect as much as 5% of the latent heat release to end up as some form of kinetic energy. That kinetic energy can be short lived updrafts (~30 minute duration), longer lived rotational motion at the base of the cell, or circulation in a vertical plane triggered by an updraft. *Nolan et al.* [2007] find that as much as 5% of the latent heat released in an eyewall cell becomes kinetic energy of tangential surface winds.

There are a variety of energy conversion ratios that can be calculated for a convective cell, depending on what aspect of the convective cell one wishes to emphasize. "Energy conversion ratio" is a general term applicable to non-cyclic processes. In contrast, "efficiency" is the ratio of mechanical work performed to input energy in a heat engine, i.e., a closed circuit of fluid subjected to repeated cycles of heat addition and work extraction.

Consider a parcel that travels without entrainment from the surface to the tropopause, reaching saturation early in its upward journey. In this section, the unit for energy is J/kg which represents Joules of energy transferred for each kilogram of air in the parcel. During the ascent, temperature drops from 300 K to 200 K and water vapor mixing ratio drops from ~20 g/kg to near zero. During the ascent, a total of approximately 150×10^3 J/kg of energy is converted: 100×10^3 J/kg of sensible heat is lost (ΔE

$= c_p \Delta T = 1004 \text{ J/K/kg} \times 100 \text{ K}$) and $50\text{e}3 \text{ J/kg}$ of latent heat is released ($\Delta E = L \Delta q = 2.5\text{e}3 \text{ J/g} \times 20 \text{ g/kg} = 50\text{e}3 \text{ J/kg}$).

During the parcel's ascent through the troposphere, about 98% of the energy being transformed ends up as either gravitation potential energy or is expended as work to expand the air parcel's volume. Most of the $150\text{e}3 \text{ J/kg}$ of energy being transformed is converted into gravitational potential energy ($\Delta E = g \Delta z = 9.8 \text{ m/s}^2 \times 12\text{e}3 \text{ m} = 118\text{e}3 \text{ J/kg}$). Most of the rest of the energy is expended as work to expand the air parcel against the pressure of the background air ($\Delta E = \Delta(pV) = R \Delta T = 287 \text{ J/K kg} \times 100 \text{ K} = 29\text{e}3 \text{ J/kg}$).

During the ascent, less than 1% of the energy being converted exists temporarily as updraft kinetic energy. If the parcel remains 1.5 K warmer than the background during a 10 km ascent, then $\sim 600 \text{ J/kg}$ of CAPE exist. Under ideal circumstances, all 600 J/kg of CAPE could be converted into updraft kinetic energy (section 2.7.3, p. 71;

$$g \frac{\Delta T}{T} \Delta z = 9.8 \frac{\text{m}}{\text{s}^2} \frac{1.5 \text{ K}}{250 \text{ K}} 10\text{e}3 \text{ m} = 600 \frac{\text{J}}{\text{kg}}).$$

Due to drag and turbulence, only a

fraction of CAPE usually becomes updraft kinetic energy, with the balance of CAPE either remaining as a temperature anomaly or being converted into the disorganized motion of small scale turbulence.

Consistent with the previous paragraph, *Holton* [1992, pp. 246 and 244] points out that only $\sim 0.5\%$ of energy has the possibility of being converted into kinetic energy and only $\sim 0.05\%$ is actually converted into kinetic energy. Similarly, *Wallace and Hobbs* [2006, p. 86, footnote 30] point out that the largest terms in the energy budget of a

convective cell are the latent heat source ($L \Delta q$), thermal energy source ($c_v \Delta T$), the gravitational potential energy increase ($g \Delta z$), and the work done to expand the volume of the parcel ($\Delta(pV) = R \Delta T$). These four terms are the terms listed in the moist static energy, which is commonly said to be a conserved quantity. *Wallace and Hobbs* [2006, p. 86] point out that the reason why moist static energy is called "static" is because kinetic energy terms are excluded. With kinetic energy excluded, moist static energy is only approximately conserved. Typically, expressions for moist static energy include just one term ($c_p \Delta T$) which is the sum of the work of expanding the parcel's volume and the thermal energy source.

When the ascent is finished, the thermal anomaly and vertical displacement oscillate about zero. Virtually all of this oscillatory energy will radiate away from the convective cell as wave motion unless the cell is imbedded in a mesovortex. If a mesovortex is present, then a fraction of the oscillatory energy will be trapped near the cell (i.e., within the Rossby radius, section 2.9.3, p. 106) as a gravity wave until the gravity wave dissipates into thermal energy.

Other forms of kinetic energy include cyclonic rotational kinetic energy at the base of the convective cell (Figure 2.8b, p. 77), anti-cyclonic rotational kinetic energy at the top of the convective cells, and vertical circulation outside the convective cell known as "thermally direct" circulation (Figure 2.8c).

The rotational and circulation kinetic energy are about two orders of magnitude smaller than typical updraft kinetic energy. Assume that during the lifecycle of an isolated convective cell, the updraft lasts as long as it takes for the 7000 kg/m^2 mass in

the column of air to ascent through the troposphere over a 100 km^2 horizontal area. The rotational velocity increases perhaps $\sim 5 \text{ m/s}$ in the bottom 1000 kg/m^2 of the air column over an equal horizontal area surrounding the cell (Figure 2.8c). That means that the low-level rotational kinetic energy is $\frac{1}{2} m v^2 = (1/2) 1\text{e}3 \text{ kg/m}^2 \times 1\text{e}8 \text{ m}^2 \times (5 \text{ m/s})^2$.

The low-level rotational kinetic energy per unit mass of ascending air is the preceding quantity divided by the $7\text{e}11 \text{ kg}$ of ascending mass, which comes out to within one or two orders of magnitude of 1 J/kg .

The thermally direct circulation in the vertical plane involves a similarly small amount of kinetic energy as the rotational kinetic energy just estimated. If the 8 surrounding $10 \times 10 \text{ km}^2$ square areas to the central $10 \times 10 \text{ km}^2$ square area of the updraft have subsidence of 1 m/s as a result of the 8 m/s updraft in the $10 \times 10 \text{ km}^2$ convective cell, then the kinetic energy of the thermally direct circulation is approximately $\frac{1}{2} m v^2 = (1/2) 7\text{e}3 \text{ kg/m}^2 \times 8\text{e}8 \text{ m}^2 \times (1 \text{ m/s})^2$. Divide that kinetic energy by the mass of the ascending air comes out to within two orders of magnitude of 5 J/kg .

The efficiency with which latent heat is transformed into other forms of energy depends on the time scale one is considering. A fraction of a second after the water vapor condenses, all of the released latent heat is in the form of heat energy. Next, the energy is converted into kinetic energy of an updraft and expansion of the parcel. Within a fraction of a second of becoming updraft kinetic energy, Earth's gravity acts on the updraft, reducing its velocity, and converting the kinetic energy into gravitational potential energy. *Houze* [1993, chapter 7] points out that latent heat released in a convective cell

becomes an updraft before being converted into other forms of kinetic energy such as the cyclonic rotational kinetic energy at the base of the convective cell. On a longer time scale of minutes, some of the gravitational potential energy is released in downdrafts. On a time scale of 10s of minutes to hours, it is difficult to forecast how much of the subsidence warming is permanent and how much is carried away by gravity waves and other wave disturbances and diluted to the point of being unobservable. On time scales of days, basically all wave motion, linear kinetic, and rotational kinetic motion is turned into thermal energy and radiated to space or back to the ground.

2.8.6. Eyewall vorticity stretching

Most energy that ultimately intensifies a tropical cyclone's surface winds is at some point latent heat released in tall eyewall cells by condensing water vapor. There are several paths that might be used for that energy to become wind intensification. Paths discussed in section 5.1 are mixing (when the eyewall cells are warmer than the eye) or forced subsidence (which can work when the eyewall is less warm than the eye). Another path is that the tall cells in the eyewall concentrate the background vorticity due to vortex stretching [*Raymond and Jiang, 1990*].

Some authors find that eyewall mesovortices increase the tropical cyclone's intensity and others find that mesovortices rob vorticity from the eyewall, which reduces the tropical cyclone's intensity. One way to see that either outcome is possible is to consider the source of the inflow air at the bottom of the tall eyewall cell. If most of the inflow air comes from the lower tropospheric eyewall air, then it reduces the average

tangential winds. If most of the inflow air comes from outside the eyewall, then the tall eyewall cells are gathering vorticity from outside the eyewall, which would increase the tangential winds at one spot in the eyewall. With axisymmetric mixing this local increase could spread throughout the eyewall and increase the tropical cyclone's intensity.

May and Holland [1999] find that vortex stretching can contribute significantly to tropical cyclone intensification. *May and Holland* [1999, p. 1227] show during a 10 hour period up to a $1\text{e-}3$ $1/\text{s}$ vorticity increase at a 50 km radius from the center of the eye in the tropical cyclone as a result of latent heat driving vortex stretching in the convective cells in a tropical cyclone's rain bands. By the simple formula $v = r \eta / 2$, this vorticity increase equates to a 25 m/s increase (50 knot) increase which is all of the intensification that is likely to occur over a short period.

2.9. Wave motion

This section introduces two kinds of wave motions that can be set up by convective cells: gravity waves (section 2.9.2) and vortex Rossby waves (section 2.9.4). The reason why gravity waves are of interest is because they can carry far from the eyewall some of the latent heat released in tall eyewall cells. This energy transport is of interest in chapter 5. To estimate how much energy gravity waves carry away, the concepts of inertial stability (section 2.9.1) and the Rossby radius of deformation (section 2.9.3) are discussed. To

understand how gravity waves work, the concept of static stability (section 2.9.1) is discussed.

Chen et al. [1993] discuss gravity and rossby waves in the eyewall. More specifically, *Chen et al.* [1993, section 4a] discuss waves with less than 50 wavelengths fitting around the circumference of a tropical cyclone's eyewall ($\lambda \geq 5$ km). *Chen et al.* [1993] find that 77% of the variance in momentum from the symmetric state occurs on wavelengths > 5 km. On these wavelengths, vortex gravity waves and Rossby waves contribute 10% and 90% of the momentum variation in the eyewall, respectively. *Chen et al.* [1993] do not estimate how quickly these waves carry energy away from the eyewall. *Chen et al.* [1993] find that, in the upper troposphere, Rossby waves generated in the eyewall travel toward the center of the eye, which warms the eye. In particular, *Chen et al.* [1993, p. 1253] find that Rossby waves can warm the eye sufficiently to cause wind intensification at a rate of 14 kt (7.2 m/s) wind intensification during a 9 hour period. *Chen et al.* [1993] do not explore the role that tall eyewall cells may play in generating or amplifying vortex Rossby waves. In a simulation of the formation of a tropical storm, *Montgomery and Enagonio* [1998, p. 3204], find a 15 m/s wind acceleration and 5 K eye warming due to vorticity that convective cells release and Rossby waves mix throughout the eye. *Reasor et al.* [2000, p. 1665] cite *Montgomery and Enagonio* [1998] as evidence that "the interaction of convectively forced vortex Rossby waves with the mean flow will lead to changes in the mean vorticity profile."

2.9.1. Static stability and inertial stability

For vertical displacement in an unsaturated atmosphere, the restorative acceleration is due to buoyancy. The type of wave is called a gravity wave. The angular frequency of the oscillation is the Brunt-Vaisala frequency N . The stability parameter is N^2 [Montgomery and Enagonio, 1998, p. 3177; Gill, 1982, p. 51; Schubert *et al.*, 2007, p. 598]. The sign of N^2 determines if the motion is stable or if there is exponential increase in velocity ($N^2 > 0$ stable atmosphere) [Gill, 1982, p. 51]. The name of the kind of stability is "static stability".

For horizontal displacement on a rotating sphere (i.e., the Earth's surface), the apparent force that "pushes" objects back toward their original location is the coriolis force. The type of wave is called an inertial wave. The angular frequency of the wave is the planetary vorticity f . The kind of stability is called inertial stability.

For horizontal displacement inside a vortex such as a tropical cyclone, the situation is similar to the inertial case just described except that planetary vorticity f is replaced with total vorticity η . Total vorticity η is the sum of the planetary vorticity f and the relative vorticity ζ . The stability parameter is η^2 [Rogers and Fritsch, 2001, p.630]. The kind of stability is called inertial stability.

Some authors use different formulas for static stability and inertial stability. Holton [1992, p. 54] and Pedlosky [1979, p. 330] call the Brunt-Vaisala frequency N a measure of static stability instead of N^2 . Holton [1992, p. 208] calls total vorticity η a measure of inertial stability instead of η^2 (See also Houze, 1993, pp. 55–56). Rogers and Fritsch [2001, p. 630] show that η^2 is close to the more complicated form for inertial

stability used by *Chen and Frank* [1993, p. 2402]: $(f + \zeta) \left(f + \frac{2v}{r} \right)$. *Nolan et al.*

[2007, p. 3402] use $f \eta$ instead of η^2 for inertial stability. (See also equation 7.53 of *Holton*, 1992, p. 207; and *Dutton*, 1986, pp. 298–301). *Schubert et al.* [2007, p. 598] use

the effective coriolis parameter $\left(f + \frac{2v}{r} \right) \left(f + \frac{1}{r} \frac{d}{dr} r v \right)$ as a measure of inertial

stability. Many standard texts fail to name a variable for inertial stability, while they do name a variable for static stability [e.g., *Cotton and Anthes*, 1989; *Gill*, 1982; *Pedlosky*, 1979; *AMS*, 2000].

This discussion of stability and instability is based on linear wave theory. In linear wave theory, when a situation is unstable, an initial displacement grows exponentially. When a situation is stable, an initial displacement sets up an oscillation about the neutral point. In linear wave theory, a displacement h equals $h_{\max} e^{w i t}$ and satisfies the following differential equation: $\frac{d^2}{dt^2} h = -w^2 h$ [*Nappo*, 2002, p. 19, equations 1.39–1.41; *Holton*, 1992, p. 198]. If $w^2 > 0$, then the situation is stable, w is a real number, $h = h_{\max} \cos w t$, and w is the angular frequency (radian/second or 1/s) of the oscillation. If $w^2 < 0$, then the situation is unstable, w is a complex number, and $w i$ is the exponential rate at which the initial displacement increases. In linear wave theory, the magnitude of the initial disturbance h_{\max} does not alter the angular frequency or propagation velocity of the wave. Based on the first time derivative of displacement, the maximum displacement velocity is $v_{\max} = w h_{\max}$.

2.9.2. Gravity waves

If the upper-level outflow of a convective cell had a constant velocity then it would not set up gravity waves. In reality, the updraft moves in fits and starts, and this variability sets up gravity waves that propagate away from the cell, carrying energy with them.

Chapter 5 of this dissertation is concerned with estimating the amount of heat that eyewall convection adds to a tropical cyclone. Gravity waves are known to carry heat away from a cell [*Chen and Frank*, 1993], but there is no simple method in the literature for estimating what fraction of the latent heat a particular convective cell loses to gravity waves. In pure geostrophic flow, *Holton* [1992, pp. 215–216] shows that exactly two thirds of energy released at a point is removed far from the point by gravity waves and only one third of the released energy remains as kinetic energy within the point's Rossby radius of deformation [*Chen and Frank*, 1993]. In more realistic situations, the fraction of energy carried away by gravity waves is more difficult to estimate. In fact, there is not even a consensus as to the mechanism whereby a convective cell sets up gravity waves. *Lane et al.* [2001] review three such mechanisms that were proposed by various authors.

In *Fovell* [1998]'s simulation, most of the latent heat released in an isolated convective cell in a stationary background was carried away by gravity waves in just 6 to 9 minutes. Looking at global averages, *Uno and Iwasaki* [2006] find that only 20% of the latent heat released in convective cells remains as heat energy and 80% of it becomes wave motion of some kind (not necessarily gravity waves) before again becoming heat energy. *Uno and Iwasaki* [2006], however, do not estimate how quickly the waves dissipate or how far they travel from the convective cell before dissipating.

Air mixing and radiative cooling to space transfer energy more slowly than do gravity waves. In 2 hours, a gravity wave with a large vertical wavelength can travel 100 km horizontally away from the cell that formed it, while the mixing of warm air into its surroundings can take several hours to days [Bretherton and Smolarkiewicz, 1989]. Radiative cooling occurs at a rate of only a few degrees per day [Zeng *et al.*, 2005; Zhang *et al.*, 1999; Wallace and Hobbs, 2006, p. 139; Harries, 1997, Figure 1].

The size and velocity of a gravity wave can be observed by aircraft. An aircraft flying through a gravity wave can measure variations in the in-situ updraft velocity and temperature. To calculate the displacement of a non-saturated air parcel, the observed temperature variation can be divided by the difference between the dry adiabatic lapse rate and the environmental lapse rate: $h_{\max} = \Delta T / (\Gamma_{dry} - \Gamma_{envir})$. The dry adiabatic lapse rate is 10 K/km. Near the tropopause, the environmental lapse rate is close to zero, so displacement in km can be calculated as $h_{\max} = \Delta T / 10$. In the mid-troposphere, the environmental lapse rate is 6 to 7 K/km, so displacement in km is between $\Delta T / 4$ and $\Delta T / 3$.

For example, Hauf [1993] observes mid-tropospheric gravity waves triggered by boundary layer convection using aircraft. At a 6.3 km altitude, the maximum displacement and the displacement velocity were 100 meters and 0.5 m/s, respectively. This displacement is calculated from a 0.3 K temperature difference and $h_{\max} = \Delta T / 3$. Similarly, Bohme *et al.* [2004, Figure 4] find mid-tropospheric maximum displacement and displacement velocities of 70 meters and 0.5 m/s. Implied in Bohme *et al.*'s displacement is $h_{\max} = \Delta T / 4.3$ based on the observed 0.3 K temperature change.

These two sets of observations imply an angular frequency of approximately $7\text{e-}3$ radian/second and a period of 15 minutes. If one takes the expected 5 to 30 km horizontal wavelength ($1.3\text{e-}3$ to $0.2\text{e-}3$ radian/meter horizontal wavenumber) and assume the 0.01 radian/second Brunt-Vaisala frequency of *Lane and Reeder* [2001, p. 2427], then the implied vertical wavelength of the observed waves is 3 to 22 km. In the mid-latitude locations of *Bohme et al.* [2004]'s and *Hauf* [1993]'s observations, that implies from three vertical wavelengths to just a half a vertical wavelength can fit in the mid-troposphere's ~ 10 km depth.

Small scale ripples are sometimes seen in tropical cyclone cloud-top infrared satellite imagery. For example in Figure 3.10a (p. 176), the narrow lines may be gravity waves on the north side of the eyewall of Hurricane Carlotta (2000). The ripples are sometimes oriented parallel to lines through the center of the eye. If the ripples are gravity waves, then the wave motion has been deflected until the gravity waves are forced to remain in the vicinity of the eyewall. Gravity waves that circle the eyewall could conceivably contribute to wind intensification by axisymmetrizing latent heat that was released in one part of the eyewall. It is only if the gravity waves travel beyond the eyewall before dissipating that they rob the eyewall of energy that could otherwise be used to intensify surface winds.

The wave-like structures in the northern portion of Hurricane Claudette's eyewall have approximately a 30 K temperature variation (i.e., $\pm 15\text{K}$). If you apply a 10K/km ratio because these waves are near the tropopause, then a $\pm 15\text{K}$ temperature variation implies that the waves experience a ± 1.5 km maximum displacement. Assuming a $3\text{e-}3$

to 6×10^{-3} angular frequency for the waves [Lane and Reeder, 2001] and assuming that a full or half wavelength fits vertically in the troposphere, then the waves' maximum displacement velocity is 4.5 to 9 m/s.

2.9.3. Rossby radius of deformation

This section derives an expression for the Rossby radius that can be applied to the eyewall of a tropical cyclone. It is useful to know the Rossby radius because, to a first approximation, a significant fraction of the energy carried by a gravity wave stays within 1 Rossby radius of the gravity wave source. Holton [1992, pp. 215–216] asserts that, in idealized geostrophic flow, 33% of released energy stays within the Rossby radius and the rest flows indefinitely far away from the wave source. Holton's idealized situation does not permit gravity waves to carry any energy upward out of the troposphere and into the stratosphere. In an actual convective cell, some gravity wave modes do transport energy upward.

For a convective cell in a tropical cyclone eyewall, an appropriate formula for calculating the ~30 km Rossby radius R is the following:

$$R = \frac{v_{gravity}}{\zeta} \quad (2.38)$$

Rogers and Fritsch [2001, p. 632 and Figure 27d] give a 15 to 20 km Rossby radius in a tropical storm eyewall. Other sources quote higher Rossby radius of ~100 to 200 km further from the eye, where the vorticity is smaller. For example, Bister [2001, Table 1]

gives a Rossby radius of 156 km for a point 70 km away from the center of the eye of a tropical storm.

The numerator and denominator of equation 2.38 have the following values. The maximum horizontal group velocity $v_{gravity}$ is near 30 m/s for the gravity waves that are most often excited by convective cells [Bister, 2001; Tulich *et al.*, 2007]. The relative vorticity ζ (zeta) is $\sim 1e-3$ 1/s in the vicinity of the eyewall at the height of the convective cell's upper-level outflow layer [Braun, 2006]. A relative vorticity of $1e-2$ to $1e-3$ 1/s is also a typical value for the vorticity of a mesoscale convective system [Chen and Frank, 1993, p. 2417, Figure 13]. In the bottom 1 km of a tropical cyclone's eyewall, the vorticity can be two to four times greater (i.e., $2e-3$ 1/s to $4e-3$ 1/s).

Based on equation 2.38, the Rossby radius increases by a factor of two with altitude due to vorticity decreasing by a factor of two (15 km to 30 km) between the surface and 12 km in a tropical cyclone's eyewall. This altitude variation in the Rossby radius makes sense based on the typical horizontal dimension of tall eyewall cells. Tall eyewall cells and eye mesovortices have approximately a 15 km radius in the mid-troposphere, while the upper-level outflow of a tall eyewall cell can spread out to form a "convective dense overcast" (CDO) that is sometimes large enough to obscure the entire eye and eyewall region below it.

People give different maximum group horizontal propagation speeds for gravity waves, which effects the Rossby radius calculated with equation 2.38. Bister [2001] and Rogers and Fritsch [2001, p. 630] use 30 m/s for the maximum speed in a tropical cyclone inner core. Chen and Frank [1993, p. 2422] find a 28 m/s propagation speed in

their model of a developing mesoscale convective system. *Tulich et al.* [2007] state that gravity waves have a slow and fast mode. The slow mode has a full vertical wavelength in the troposphere and propagates at 16 to 18 m/s horizontally. The fast mode has half a vertical wavelength fitting into the troposphere and propagates at 35–45 m/s horizontally. *Mapes* [2001] also describes a slow and fast mode with the same two vertical wavelengths, but *Mapes* [2001] gives a slightly different value for the average vertical group velocities: 15 m/s and 50 m/s.

Horizontal group velocities can be calculated in the following way. The horizontal phase velocity of any wave is the angular frequency divided by the horizontal wavenumber ($v_{horiz}=w/k$, *Nappo*, 2002, p. 13; *Lane and Reeder*, 2001, p. 2427; *Holton*, 1992, p. 202]. The horizontal and vertical group velocities of any wave are the partial derivatives of angular frequency with respect to the horizontal and vertical wave numbers, $v_{horiz}^{group} = \frac{\partial}{\partial k} w$ and $v_{vert}^{group} = \frac{\partial}{\partial m} w$ [*Nappo*, 2002, pp. 16–17]. Taking these derivatives of the dispersion relation for this kind of gravity wave results in the following group velocities: $v_{horiz}^{group} = v_{horiz} \approx 20 \text{ m/s}$ and $v_{vert}^{group} = v_{horiz} \frac{k}{m} \approx 6 \text{ m/s}$. The 20 m/s horizontal group velocity calculated in this paragraph is somewhat smaller than the 30 m/s cited by other researchers.

As shown in the preceding paragraph, the horizontal group speeds for gravity waves depend on the dispersion relationship for gravity waves in a non-rotating background at rest: $w = \frac{Nk}{m}$ [*Lane and Reeder*, 2001, JAS]. Angular frequency w

typically has values of 3e-3 to 6e-3 radian/second [*Lane and Reeder, 2001*, p. 2435, Figure 7]. This corresponds to periods T of 18 to 35 minutes ($T = 2\pi/\omega$, *Nappo, 2002*, p. 10), the approximate duration of a active phase of a convective cell.

The quantities in the dispersion relation are the Brunt-Vaisala frequency N , horizontal wavenumber k , and vertical wave number m . Numerical values for these variables are given in the following paragraphs. The Brunt-Vaisala frequency averages 11.5e-3 radian/second in the troposphere according to *Lane and Reeder* [2001, p. 2427]. This value corresponds to buoyant oscillations with vertical displacement and horizontal phase and group speeds [*Nappo, 2002*, pp. 20–22]. Such oscillations have periods of approximate 9 minutes. The period for displacements at an angle $\beta \neq 90^\circ$ is $N \sin \beta$ where $\beta \equiv \sin^{-1} \frac{m}{k}$ [*Nappo, 2002*, pp. 20–22; *Holton, 1992*, p. 203]. This section only considers horizontally propagating gravity waves ($\beta = 90^\circ$) because they have the fastest horizontal velocity. The Rossby radius of deformation is defined by the gravity waves with the fastest horizontal velocity. The Brunt-Vaisala frequency varies with altitude, being approximately 12e-3 1/s over most of the lower and mid troposphere. It dips to 5e-3 1/s in the boundary layer it dips to 7e-3 1/s around 200 mbar (12 km), and it rises above 12e-3 1/s above a 14 km altitude [*Mapes, 2001*, Figure 7]. The Brunt-Vaisala frequency N can be calculated using the following formula [*Mapes, 2001*, p. 2362]:

$$N = \sqrt{\frac{g}{\theta} \frac{\partial \theta}{\partial z}} \quad (2.39)$$

In this formula, g (m/s^2) is the acceleration due to gravity, θ (K) is the potential temperature at the given altitude, and $\frac{\partial}{\partial z}$ is the derivative with respect to altitude z (m).

The horizontal wave number k has typical values of $1\text{e-}4$ to $2\text{e-}4$ (radian/meter) [Lane and Reeder, 2001, p. 2435]. This corresponds to horizontal wavelengths of 32 to 63 km ($\lambda=2\pi/k$, Nappo, 2002, p. 9), which is about two to four times larger than the horizontal scale of a convective cell. The vertical wave number m has typical values of $2\text{e-}4$ to $5\text{e-}4$ radian/meter, which corresponds to a 12 to 30 km vertical wavelength [Lane and Reeder, 2001, Figure 7].

In contrast to equation 2.38, the Rossby radius of deformation R is often stated using an equation that is inappropriate for tropical cyclones [Houze, 1993, p. 51, equation 2.137]:

$$R = \frac{\sqrt{gH}}{f} \quad (2.40)$$

In this equation, g is the acceleration due to gravity (9.8 m/s^2), H is the height of the tropopause (m), and f is the coriolis parameter at the given latitude ($1/\text{s}$). Both the numerator and denominator of this expression are inappropriate for tropical cyclones. The numerator of equation 2.40 is 300 m/s [Gill, 1982, p. 207, 196] for mid-latitude shallow water gravity waves [Houze, 1993, p. 51]. A 300 m/s phase speed is very fast since gravity waves must travel slower than the speed of sound and the speed of sound is 295 to 340 m/s in the troposphere (See the definition of v_{sound} on page xviii; CRC, 2004, p. 14-20 to 14-21). The denominator of equation 2.40 is $8\text{e-}5 \text{ 1/s}$ in the Tropics and slightly higher in mid-latitudes.

2.9.4. Rossby waves

When a convective cell forms in the eyewall of a tropical cyclone, it is sometimes associated with a Rossby wave in the eyewall that has properties similar to planetary-scale Rossby waves that are familiar to mid-latitude meteorologists. There is nothing odd about Rossby waves forming due a tropical cyclone's rotation rather than the Earth's rotation. All that is needed to set up a Rossby wave is a two dimensional field with the background vorticity varying in one dimension. In the case of the Earth, vorticity increases with latitude. In the case of the tropical cyclone, vorticity is a function of distance from the eye's center.

To create a Rossby wave, there is no actual restorative force, instead there is just the principle of conservation of absolute momentum. One way to think about conservation of absolute momentum is to consider it a special case of Newton's law of motion that can be stated in the following way: a body maintains it velocity except to the extent that it is acted upon by forces [*Serway and Jewett*, 2004, p. 114]. This concept can be expanded in the following way: a body that is rotating about its center of gravity will maintain a constant angular velocity except to the extend that it is acted upon by forces. This extension can be understood by thinking of the particles at the edge of the disk trying (and succeeding) to move in a straight line at constant speed except to the extend that they are constrained to stay the same distance away from the center of the rotating disk because they are mechanically attached to the rest of the disk. Imagine that a solid disk were embedded in a large vortex. The disk would rotate once every time that the

vortex did. If the disk were slightly perturbed, then it would begin rotating at a slightly different angular velocity. A point on the edge of this disk would be seen to oscillate in and out of the vortex.

A tropical cyclone's eyewall is an inherently unstable vortex because it does not rotate as a solid body. The instability is due to maximum angular velocity under the eyewall being much greater than the angular velocity further away or close to the center of rotation [Guinn and Schubert, 1993]. Rossby waves on the inside edge of the eyewall may contribute to the formation of mesovortices [Schubert *et al.*, 1999]. These mesovortices have a wavelength of approximately 1/8 the circumference of the eyewall, and they can persist for a day or longer [Braun 2002; Braun, 2006; Braun *et al.*, 2006]. These mesovortices provide favorable locations for tall eyewall cells to form.

2.10. Maximum potential intensity of a tropical cyclone

To a first approximation, the latent heat added to the tropical cyclone through evaporation increases linearly with the wind speed. Meanwhile, it is commonly assumed that the frictional energy dissipation at the ocean's surface increases as the cube of the wind speed. From these two relationships, it is clear that some maximum wind speed exists at which friction removes energy from the atmosphere as quickly as the ocean adds energy to the atmosphere (Figure 2.11).

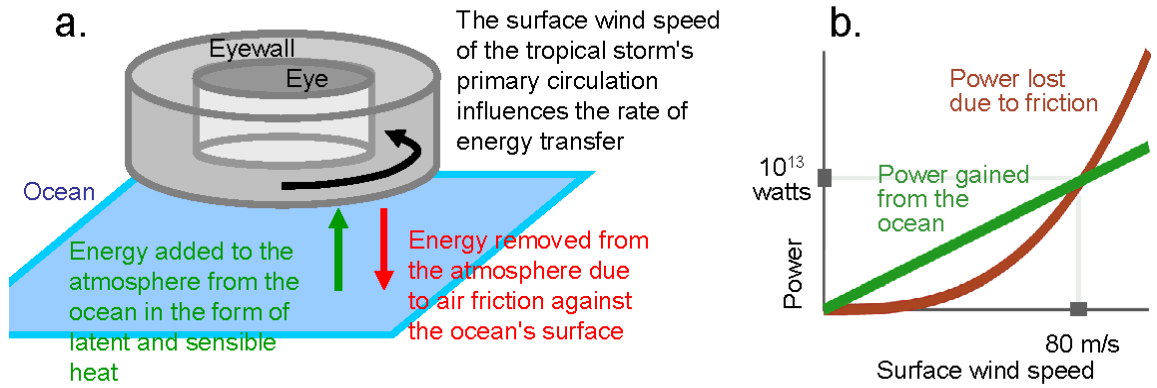


Figure 2.11. Emanuel's Maximum Potential Intensity (MPI) theory. The energy added to a tropical cyclone is linearly proportional to the surface wind speed (green line), while the energy removed due to friction is proportional to the cube of wind speed (red line). There is a maximum wind speed at which all the energy added must be used to counteract frictional loss.

To calculate the maximum possible wind speed, one begins with the equation for flux F_{input} (J/s m² or watts/m²), i.e., energy transferred into the atmosphere each second per unit surface area of ocean [Emanuel, 1995].

$$F_{input} = C_{enthalpy} \rho_{air} v_{surface} (k_{saturation} - k_{air})$$

$$\text{unit analysis... } \frac{\text{watt}}{\text{m}^2} = \frac{\text{J}}{\text{s m}^2} = 1 \frac{\text{kg}}{\text{m}^3} \frac{\text{m}}{\text{s}} \frac{\text{J}}{\text{kg}} \quad (2.41)$$

Equation 2.41 states that the input flux is equal to the product of the coefficient of enthalpy transfer ($C_{enthalpy} \approx 1.1 \times 10^{-3}$), the density of the air at the surface ($\rho_{air} \approx 1 \text{ kg/m}^3$), the surface wind speed ($v_{surface}$ in m/s), and the difference between the saturation enthalpy ($k_{saturation}$ in J/kg) and observed enthalpy (k_{air}) of surface air. In the past decade, enthalpy has become a more popular name for the quantity formerly known as moist static energy. The enthalpy of the air is the sum of the latent and sensible heat of the air. Simplifying

the expression of *Emanuel* [1995, JAS] specific enthalpy (J/kg) can be defined as the following:

$$k = c_p T + L_v q$$

$$\text{unit analysis... } \frac{J}{kg} = \frac{J}{K \text{ kg}} K + \frac{J}{g} \frac{g}{kg} \quad (2.42)$$

In this equation, c_p is the heat capacity of dry air (J/K kg), T is the surface air temperature (K), L_v is heat of vaporization of water (J/g), and q is the specific humidity (g water per kg total weight of moist air). The latent heat of fusion is left out of the equation for specific enthalpy because while some precipitation forms above the freezing level (releasing heat of fusion), the precipitation melts before leaving the atmosphere (reabsorbing an equal amount of heat of fusion). Because water vapor rarely gets above 2% of the mass of the parcel, specific humidity q (g water per kg water+air) is similar to the more commonly reported value of the water vapor mixing ratio w (g water per kg dry air). At a typical tropical cyclone wind speed $v_{surface}$ of 50 m/s, the energy flux into the atmosphere F_{input} is 550 watt/m². For comparison, this is double the 235 watts/m² of solar energy that the Earth and atmosphere absorb [*Thomas and Stamnes*, 1999, p. 439].

Next, a thermodynamic efficiency must be calculated that is the fraction of the input energy that is transformed into the work of accelerating the surface winds. In an early work, *Emanuel* [1986, equations 17 and 38] derived equation 2.43 as the thermodynamic efficiency of a tropical cyclone. Equation 2.43 works out to a maximum efficiency of ~0.33. Emanuel's sole assumption was that the tropical cyclone was in gradient wind balance. In the next few years, *Emanuel* [1987, 1988] provided an alternative derivation of the same equation 2.43, this time using the pedagogical tool of

calling a tropical cyclone a Carnot heat engine. Ten years later, *Bister and Emanuel* [1998] increased the efficiency above Carnot efficiency, which suggests that it was merely a coincidence that the original expression for a tropical cyclone's efficiency was the same as the expression for the efficiency of a Carnot heat engine. The new expression is $(T_{inflow} - T_{outflow})/ T_{outflow}$, which gives a maximum efficiency of ~ 0.5 . The trouble with considering a tropical cyclone to be a Carnot engine is that it implies that the same air molecules pass through the eyewall multiple times. In contrast, a tropical cyclone is not a closed circulation, and so the thermodynamic limits of a heat engine do not constrain a tropical cyclone. Nonetheless, an empirical study shows that the observed maximum efficiency of a tropical cyclone is somewhat similar to the numerical value of Carnot efficiency [*Emanuel*, 2000].

Wallace and Hobbs [2006], *Rolle* [2005], and *Serway and Jewett* [2004] discuss the principles behind heat engines. A heat engine converts a fraction of the input heat (microscopic kinetic energy) into work (macroscopic kinetic energy). A heat engine has the following theoretical maximum efficiency ε [*Wallace and Hobbs*, 2006, p. 93; *Emanuel*, 1997]:

$$\varepsilon = \frac{T_{inflow} - T_{outflow}}{T_{inflow}} \quad (2.43)$$

In the above equation, the efficiency ε is unitless. In tropical cyclones, the surface inflow and upper-level outflow temperatures are approximately 300 K and 200 K, respectively.

Equations 2.41 and 2.43 for flux and efficiency can be combined to estimate the rate at which usable energy $F_{usable\ input}$ is added to the tropical cyclone:

$$F_{usable\ input} = \varepsilon F_{input} = \varepsilon C_{enthalpy} \rho_{air} v_{surface} (k_{saturation} - k_{air}) \quad (2.44)$$

The last step is to calculate the rate at which energy is lost. Energy is lost from the air due to friction between the air and the ocean surface because the ocean surface is almost at rest in comparison with the air that moves rapidly over it. The faster the wind, the rougher one expects the sea to be. For this reason, the frictional energy loss is expected to increase with increasing wind speed. One starts with the equation for flux F_{loss} , i.e., energy transferred out of the atmosphere each second per unit surface area of ocean [Emanuel, 1995].

$$F_{loss} = C_{friction} \rho_{air} v_{surface}^3$$

$$\text{unit analysis... } \frac{\text{watt}}{\text{m}^2} = \frac{\text{J}}{\text{s m}^2} = \frac{\text{kg}}{\text{s}^3} = 1 \frac{\text{kg}}{\text{m}^3} \left(\frac{\text{m}}{\text{s}} \right)^3 \quad (2.45)$$

Equation 2.45 states that the flux of energy loss is equal to the product of the coefficient of friction ($C_{friction} \approx 1.5\text{e-}3$), the density of the air at the surface ($\rho_{air} \approx 1 \text{ kg/m}^3$), and the cube of the surface wind speed ($v_{surface}$ in m/s). At a typical tropical cyclone wind speed $v_{surface}$ of 50 m/s, the frictional flux of energy out of the atmosphere F_{loss} is 190 watts/m².

At low wind speeds, energy input is greater than energy loss (Figure 2.11b, p. 113). As wind speed increases, frictional losses increase faster than do the energy gains (cubic loss vs. linear gain). The maximum sustainable wind speed occurs when frictional losses catches up with the energy input. For this reason, one can find the maximum possible wind speed by setting equal the input energy flux (equation 2.44) and the frictional loss (equation 2.45) [Emanuel, 1995]:

$$F_{input}(v) = F_{friction}(v) \text{ at } v = v_{max}$$

$$v_{max} = \sqrt{\frac{C_{enthalpy}}{C_{friction}} \mathcal{E} (k_{saturation} - k_{air})} \quad (2.46)$$

Over the past 20 years, a number of refinements have been made to the original formulation of Emanuel's maximum potential intensity theory. For example, the empirical coefficients of enthalpy transfer and friction had, until recently, only been measured in winds much slower than tropical cyclone intensity. Although it is difficult to measure these coefficients in the hazardous environment of a tropical cyclone, field campaigns during the past four years suggest that the coefficients change at tropical cyclone wind speeds [*Black et al.*, 2007, p. 357]. Initial results from these field campaigns suggest that, at high wind speeds, the ocean's surface becomes covered with foam and spray that are whipped up by the choppy sea. Foam reduces the coefficient of friction [*Powell et al.*, 2003], which allows a tropical cyclone to grow more intense for a given amount of energy input. Spray either increases or decreases energy transfer from sea to air depending on how long the spray is airborne before falling back into the ocean [*Emanuel*, 2003, *Ann. Rev.*, p. 89; *Andreas and Emanuel*, 2001].

A second modification to Emanuel's theory is that sometimes the details of eyewall convection do have an influence on the tropical cyclone's maximum possible intensity. In particular, eyewall cells can sometimes pull in low-level air from the eye that has an even higher equivalent potential temperature θ_e than the rest of the low-level inflow. The high θ_e of the inflow air invigorates eyewall convection and ultimately causes intensification of surface winds [*Montgomery et al.*, 2006; *Persing and*

Montgomery, 2003; Braun, 2002; Cram et al., 2007]. As stated by Montgomery et al. [2006]:

The combined mean and asymmetric eddy flux of high- θ_e air from the low-level eye into the eyewall represents an additional power source to the hurricane heat engine. This "turbo boost" of the engine invokes significant surface enthalpy fluxes well inside the radius at which the [Emanuel Maximum Potential Intensity] E-MPI theory assumes they operate.

Emanuel himself made a third modification to his theory. A statistical study of tropical cyclone intensity found that sometimes tropical cyclones exceeded their maximum possible potential [*Emanuel, 2000*]. Emanuel opined that some of the heat lost to friction reentered the system because the frictional heating occurs at the input (warm) side of the heat engine [*Bister and Emanuel, 1998*]. This is an odd situation. It is analogous to an engine in which all of the friction between parts occurs in the combustion chamber, which warms the combustion chamber and increases the efficiency of the engine.

Holland [1997] proposes a different method for calculating the maximum potential wind intensity of a tropical cyclone. One of the variables in Holland's method is the height of the eyewall convection, which is assumed to be uniform everywhere around the eyewall. Figure 9 of *Holland [1997]* shows approximately a 9 kt variation in maximum potential wind intensity for each 1 km rise in the average height of the eyewall convection. Eyewall height matters in Holland's method because height affects the eyewall's ability to increase the eye's thermal anomaly.

2.11. Factors affecting the actual intensity of a tropical cyclone

During the past 20 years, there has developed a school of thought that intensity forecasting can be broken into two parts [*Wang and Wu, 2004*]. First, one estimates the maximum possible intensity a tropical cyclone could achieve. Second, one estimates the fraction of that potential that the tropical cyclone will realize. The first step was described in the previous section and the second step is described in this section.

At any given time, a tropical cyclone's wind speed is influenced by many factors not yet discussed. Some of these factors are easily measured and are included in operational estimates of future intensity [*DeMaria and Kaplan, 1999; DeMaria et al., 2005*]. Other factors are more difficult to measure or are poorly understood. These factors include tilt in the tropical cyclone vortex [*Braun et al., 2006; Braun, 2002*], synoptic scale temperature and pressure [*Kaplan and DeMaria, 2003*], and wind shear [*DeMaria et al., 2005*].

DeMaria et al. [2005] mention three intensity forecasting methods used at the National Hurricane Center. The simplest and least accurate method is to use persistence and climatology. Two other methods vie for most accurate method: a statistical algorithm and a tropical cyclone mesoscale model. The statistical algorithm takes a numerical model forecast of the thermodynamic and dynamic situation up to 5 days in the future and generates a forecast using statistical regression on decades of previous tropical cyclones [*DeMaria et al., 2005; DeMaria et al., 1999*]. This statistical algorithm is called the Statistical Hurricane Intensity Prediction Scheme (SHIPS), and it will be

discussed in section 5.6. The other operational method is to run a mesoscale model. The mesoscale model used operationally at the National Hurricane Center is called the Geophysical Fluid Dynamics Laboratory (GFDL) tropical cyclone model. The GFDL model is initialized with the National Center for Environmental Prediction (NCEP) global analysis of the atmosphere and ocean surface [*Kurihara et al.*, 1998].

Because latent heat is the primary energy source for increasing winds, one might make the mistake of thinking that one could measure the rain falling out of the bottom of a tropical cyclone and then easily predict the future wind intensity. There is a Ph.D. dissertation that attempted to do just this. *West* [1998, Ph.D.] found that the surface precipitation observed by the satellite microwave instruments could explain 16% of the variance in the +12 hour to +5 day change in wind speed [Tables 8 and 19]. No other study has confirmed this result, although *Lonfat et al.* [2004] do show that the surface rain rate is roughly proportional to the current wind intensity. *Lonfat et al.* [2004] show that the radial distribution of rain rate peaks at 7 mm/h for a category 1 or 2 tropical cyclone and at 12 mm/h for a category 3 or 4 tropical cyclone.

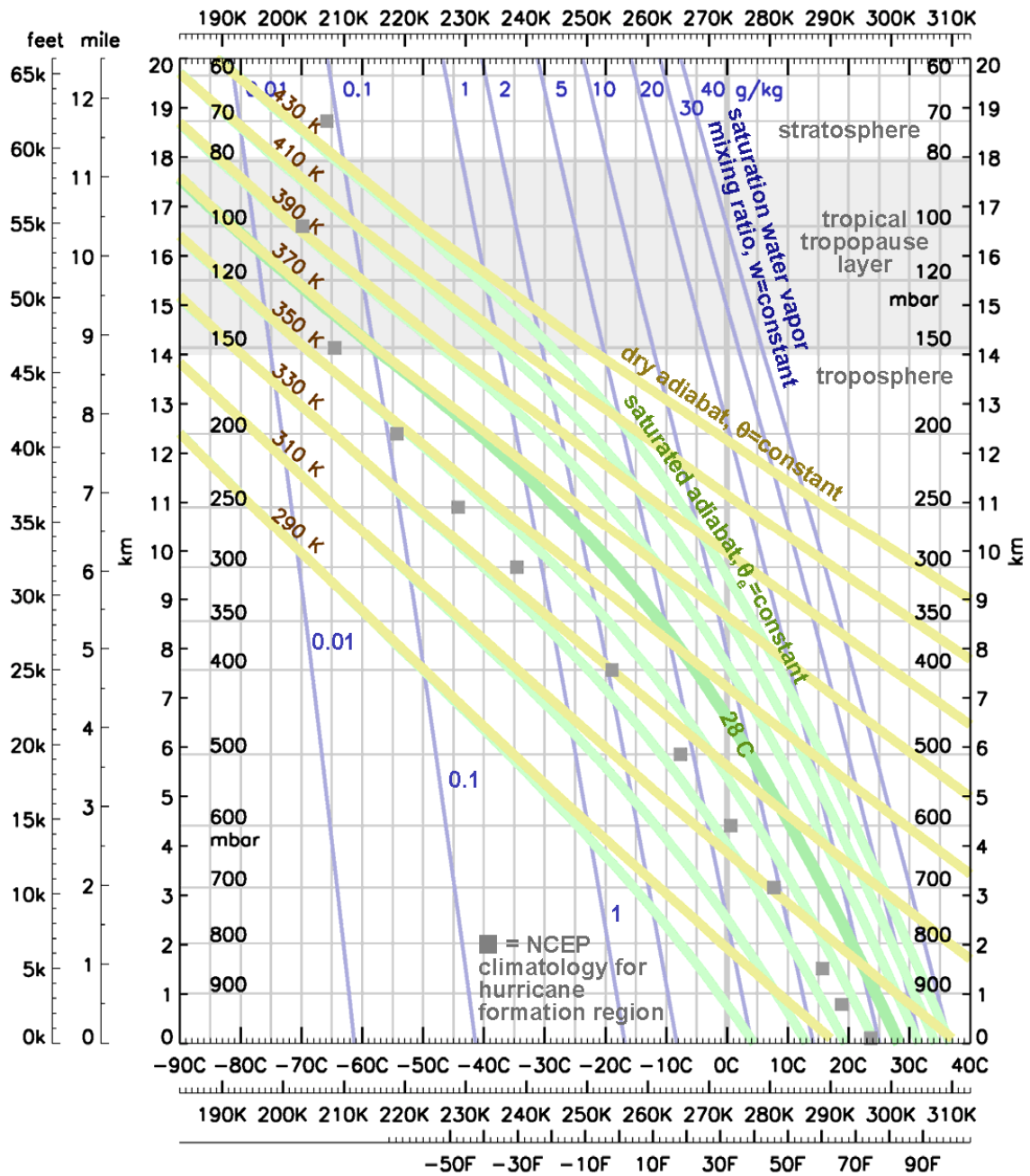


Figure 2.12. Variation of temperature with height in the tropical troposphere. The figure is described in section 2.7.2 (p. 66). The horizontal axis is temperature and the vertical axis is height.

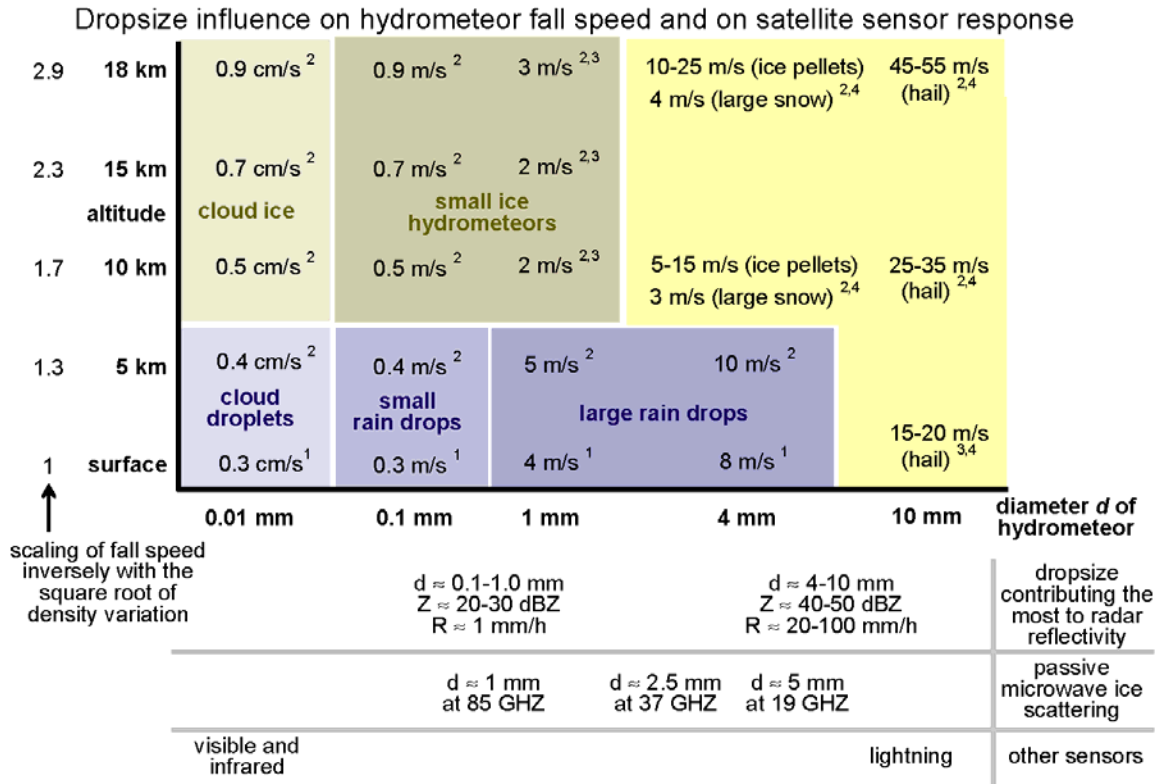


Figure 2.13. Hydrometeor size and its effect on fall speed. The figure is described in section 2.5.3 (p. 57). Notes in the figure correspond to the data source: ¹ *Wallace and Hobbs* [2006, p. 225]. ² Extrapolated from surface using square root of density. ³ *Bohm*, 1989, Figure 3. ⁴ *Doviak and Zrnic* [1993, p. 218] state for low-density ice (such as snow flakes) the fall speed is approximately $v(\text{m/s}) = 9.8 d(\text{mm})^{0.31}$ and the fall speed for high-density ice (ice pellets and hail) is $v(\text{m/s}) = 3.62 d(\text{mm})^{0.5}$. *AMS* [2001] states that high-density ice at least 5 mm in diameter is considered hail. In the Tropics, hydrometeors above about 5 km are generally frozen. Rain drops over 8 mm in diameter are unstable, break up quickly, and therefore are rare [*Doviak and Zrnic*, 1993, p. 212].

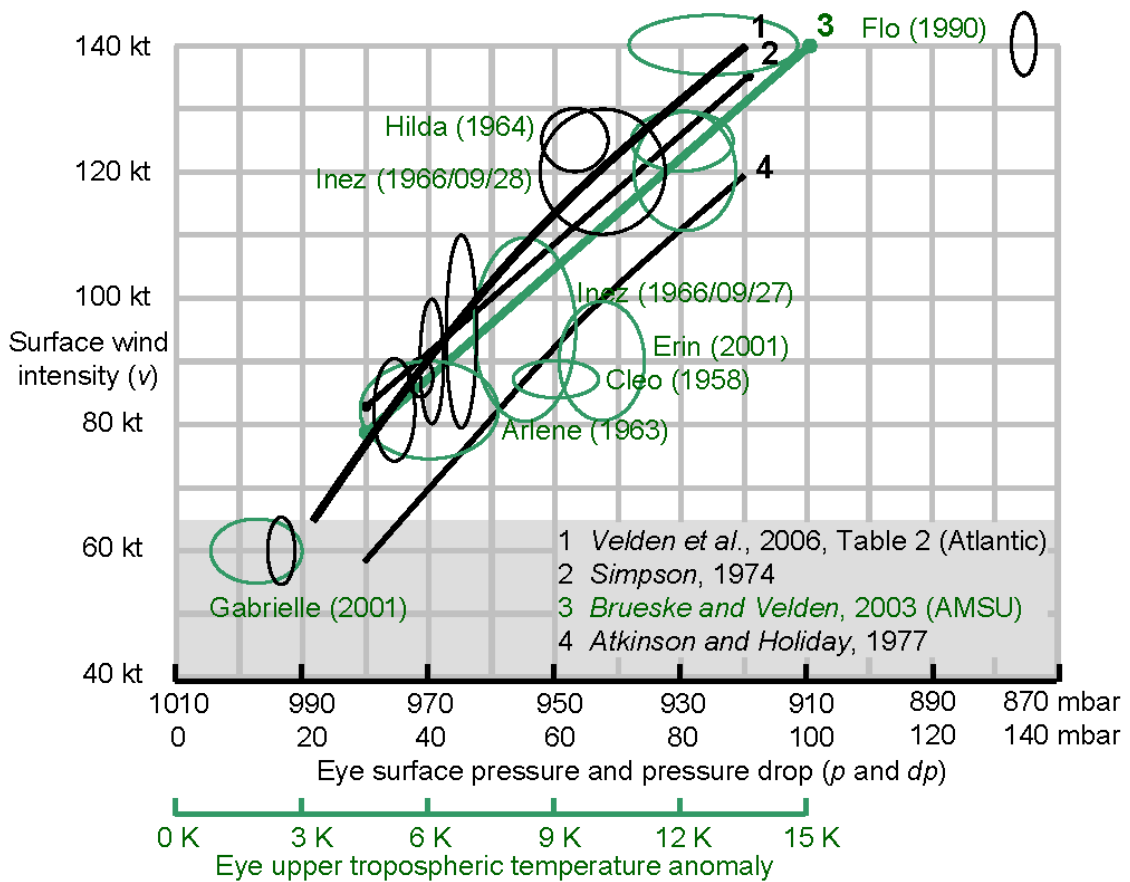


Figure 2.14. Tropical cyclone wind intensity and the eye's upper tropospheric thermal anomaly. This figure is explained in section 2.8.4 (p. 86). Upper tropospheric eye temperature anomaly vs. wind intensity is plotted in green and uses the bottom scale on the x axis. Eye surface pressure vs. wind intensity is plotted in black and uses the top scale on the x axis.

Table 2.7. TRMM precipitation-related instrument properties

Instrument property	TRMM Precipitation Radar ^{1,3}	TRMM Microwave Imager (TMI) ¹	TRMM Visible and Infrared Scanner (VIRS) ¹	TRMM Lightning Imaging Sensor (LIS) ²
Frequency or wavelength	13.8 GHz, $\lambda=2.17$ cm wavelength, Ku band ⁴	10.7 GHz (2.8 cm) 19.4 GHz (1.5 cm) 21.3 GHz (1.6 cm) 37.0 GHz (8.1 mm) 85.5 GHz (3.5 mm) ⁴	$\lambda=0.62$ μ (visible), 1.6 μ (near IR), 3.8 μ 10.8 μ , and 12.0 μ (thermal IR)	$\lambda=0.78$ μ (visible)
Scan geometry	Cross track	Conical	Cross track	2D imager
Horizontal resolution	5 km	9.1 x 63 km for low frequency, 4.6 x 7.2 km for high frequency	2.1 km at nadir, 3 km at swath edge	10 km
Vertical resolution	250 meters	Coarse: an altitude weighting function for each channel	None	None
Integration time per field of view	64 one microsecond pulses per field of view	3.3e-3 or 6.6e-3 s for low / high frequency channels	0.29 millisecond	80 seconds
Physical units	Radar reflectivity, Z (dBZ)	Brightness temperature, Tb (K)	Brightness temperature	Flash count and radiance

¹ Kummerow *et al.*, 1998

² Christian, 2000

³ Kozu *et al.*, 2001

⁴ TRMM documentation states the frequency, not the wavelength, of the Precipitation Radar and TMI. Wavelength λ in cm can be calculated from frequency f in GHz (1e6 cycles per second) using the speed of light c (3.00e8 m/s) in the following formula:

$$\lambda_{\text{meters per cycle}} f_{\text{cycles per second}} = c_{\text{m/s}} \quad \text{or} \quad \lambda_{\text{cm per cycle}} = \frac{30.0}{f_{\text{GHz}}}$$

Table 2.8. TRMM precipitation-related instrument properties (continued)

Property	Precipitation Radar	TMI	VIRS	LIS
Accuracy / sensitivity	Minimum detectable signal of 17 dBZ ¹ with 0.8 dBZ calibration accuracy ²	1 K	1 K ⁴	~75–90% detection efficiency for cloud-to-cloud lightning, minimum detectable flash rate ~1–2 flash/minute ³
Swath width	215 km at 350 km altitude	759 km at 350 km altitude	720 km at 350 km altitude	580 x 580 km continuous observation field
Manufacturer	Japan's Communication Research Laboratory (CRL) now called NICT ⁵	NASA	NASA	NASA
Heritage instrument in Earth orbit	None	Special Sensor Microwave Imager (SSM/I)	Advanced Very High Resolution Radiometer (AVHRR)	Optical Transient Detector (OTD)
Other satellites with similar instruments	Global Precipitation Measuring (GPM) Mission with launch scheduled in 2013	NOAA polar orbiters since 1987	NOAA polar orbiters since 1978	OTD launched in 1994

¹ *Anagnostou et al.* [2001] give the 17 dBZ sensitivity value.

² *Kozu et al.* [2001] state that the Precipitation Radar's accuracy is 0.8 dBZ. See also *Takahashi et al.* [2003].

³ *Christian* [2000] states a 90% efficiency and a 10% false detection rate. In contrast, analyzing TRMM LIS data leads *Boccippio et al.* [2000] to estimate that LIS only has as a 75% detection efficiency. *Ushio et al.* [2001] use 2 flashes per minute as the minimum flash rate for LIS.

⁴ *Lyu and Barnes*, 2003

⁵ *NICT*, 2004

Table 2.9. Algorithms that generate TRMM standard products for various TRMM satellite instruments. Some of the more popular variables in each algorithm are listed. See *TSDIS* [2005], *TSDIS* [2006], and *TRMM Precipitation Radar Team* [2005].

Instrument name	TRMM Precipitation Radar	TMI	TRMM VIRS	TRMM LIS
Level 1 algorithm	1C21, uncorrected radar reflectivity	1B11, microwave brightness temperature	1B01, infrared radiance	TRMM_LIS_SC, lightning flash location
Level 2 algorithm	2A25, attenuation corrected radar reflectivity, precipitation rate, and precipitation mass	2A12 precipitation rate, precipitation mass, and latent heating rate	none	none

Table 2.10. WSR-88D instrument properties

Property	WSR-88D value
Frequency and wavelength	2.8–3.0 GHz, 10.7 cm wavelength, S band [<i>Rinehart</i> , 1997, p. 350].
Scan geometry	Volume scans composed of ~14 elevation angles. At each elevation angle, the radar makes a complete azimuth circle. The array of elevation angles are defined in the Volume Coverage Pattern (VCP) [<i>NOAA</i> , 2006, part a, Table 4-1]
Accuracy / sensitivity	Minimum detectable signal of -20 dBZ at 50 km [<i>Rinehart</i> , 1997, p. 350] dropping to approximately +10 dBZ at 400 km [<i>Fed. Coord.</i> , part b, p. 2–5]. ± 2 dBZ calibration bias [<i>Anagnostou et al.</i> , 2001] although the specification was for 1 dBZ calibration bias [<i>Heiss and McGrew</i> , 1990] and 0.5 dBZ precision [<i>Fulton et al.</i> , 1998].
Resolution	1 km along line of sight for radar reflectivity, 0.95 degree beam width [<i>Heiss and McGrew</i> , 1990]
Integration time per field of view	Integration time is 0.13 milliseconds per field of view with 460 range bins, 360 azimuth angle bins, and 14 elevation angles in 5 minutes
Units	Radar reflectivity (dBZ) and doppler velocity (m/s)
Max range	460 km along line of sight for radar reflectivity at 1 km increments [<i>NOAA</i> , 2006, part c, p. 2-128]. 230 km along the line of sight at 1 km increments for line of sight doppler wind velocity [<i>NOAA</i> , 2006, part c, p. 2-62].
Vertical resolution	Varies with elevation angle and distance from radar
Power	0.75 megawatt peak transmitted power with 0.0021 max duty cycle [<i>Heiss and McGrew</i> , 1990; <i>NOAA</i> , 2006, part c, p. 2-3]. 0.3 to 1.3 megawatts of electrical power is used to generate this signal (http://roc.noaa.gov/eng/nexradtech.asp).

Table 2.11. Estimates of eyewall updrafts in the vicinity of 4 m/s

Data source	Area of eyewall	Updraft speed	% of eyewall mass transport	Reference
175 aircraft passes through 14 intense tropical cyclones at altitudes of 1.5 to 5.5 km	6% 1% 0.1%	≥ 2 m/s ≥ 4 m/s ≥ 6 m/s	50% 15% 3%	<i>Eastin et al.</i> , 2005, part 1, Figure 10
Hurricane Bob (1991) high resolution simulation. The storm was slowly intensifying.	30% 16% 7%	≥ 1 m/s ≥ 2 m/s ≥ 4 m/s	— 64% 37%	<i>Braun</i> , 2002
185 aircrafts passes through 7 tropical cyclones	5%	≥ 5 m/s		<i>Black et al.</i> , 1996

Table 2.12. Estimates of eyewall updrafts of 10 to 40 m/s

Data source	Updraft speed	Reference
Observed in hectors, which are systems that are hybrids between tropical cyclones and continental storms	40 m/s	<i>Kennan, 1994</i>
Inferred from observations of Hurricane Daisy (1958)	40 m/s	<i>Malkus, 1960, 1st conference</i>
Observed from a dropsonde in the eyewall of Hurricane Isabel (2003) on September 13	25 m/s	<i>Abersson et al., 2004</i>
They must model cells with 20–25 m/s updrafts in order to simulate their observations of Hurricane Oliver (1993)	20–25 m/s	<i>Simpson et al., 1998</i>
Possible based on the amount of CAPE observed in tropical cyclone eyewalls.	20 m/s	<i>Eastin et al., 2005, part 1, section 4b</i>
Observed in Hurricane Emily (1987)	19–24 m/s	<i>Black et al., 1994</i>
Tropical Cyclone Hilda (1990) following a 2 day period of wind intensification	10–20 m/s	<i>Ebert and Holland, 1990</i>
33 dropsondes released in 10 North Atlantic tropical cyclone eyewalls in 1998 to 2005 that experience such strong updrafts at 1 to 2 km above the ocean that the dropsondes' altitude increases temporarily	≥ 12 m/s	<i>Stern and Abersson, 2006</i>
When lightning occurs in the eyewall such as in Typhoon Paka (1998), the updraft is at least ~ 10 m/s	≥ 10 m/s	<i>Rodgers et al., 2000</i>

Table 2.13. Heavy convective rain rates

Area	Duration	Rain rate	Reference
Point	18 hours	91 mm/h	Reunion Islands off the coast of Madagascar on 12–13 September 1963, with the passage of Typhoon Gloria [<i>Paulhus</i> , 1965; cited in <i>Lamb</i> , 2001]
Point	12 hours	66 mm/h	800 mm (31.5 inches) in 12 hours [<i>Lamb</i> , 2001]
20 km ²	1 hour	170 mm/h	A supercell over Dallas, Texas, on 5 May 1995 [<i>Smith et al.</i> , 2001]
200 km ²	Satellite overflight	180 mm/h	90th percentile of rain rate averaged over a 200 km ² area inside of 166 tropical cyclone eyewalls observed by the TRMM Precipitation Radar (Figure 5.6, p. 271)
Point	1 hour	254 mm/h (10" in one hour!)	A chart of world-record point measurements of rainfall, sorted by duration and rainfall accumulation [<i>Jennings</i> , 1950]
16 km ²	1 hour	130 mm/h	Maximum rain rate from GATE storm observations [<i>Hudlow and Patterson</i> , 1979]
Point	1 hour	114 mm/h	The estimate of the 100 year flood rainfall rate for Miami, Florida [<i>Chow</i> , 1964]
Point Point	1 hour 15 minutes	102 mm/h (4") 204 mm/h (8")	Precipitation rate within 200 km of U.S. gulf coast and southeast coast with 100 year return period [<i>NOAA</i> , 1977, pp. 17 and 25]

Table 2.14. Duration of bursts of tall eyewall cells and concurrent change in wind intensity

Data source	Duration (ΔT), intensity change (ΔI)	Reference
344 bursts world-wide 1999–2001. Six criteria for manual identification include (1) a ≥ 3 hour long cloud cover area of larger than 2 by 2 degrees containing a minimum 11μ Tb ≤ 200 K and (2) a minimum 85 GHz Tb ≤ 190 K occurring within 100 km of the center of the IR cloud cover.	$\Delta T = 10\text{--}30$ hrs (25 th to 75 th percentile) $\Delta I = 5\text{--}15$ kt	<i>Hennon</i> , 2006, Ph.D.
3 bursts in Typhoon Paka (1997). Identified subjectively using IR and microwave observations.	$\Delta T = \sim 24\text{--}48$ hrs $\Delta I = 10\text{--}20$ kt	<i>Rodgers et al.</i> , 2000
21 bursts in 12 Atlantic tropical cyclones 1974–1979. Identified with a 6 hour running mean of GOES 11μ Tb observed within 2° of the cyclone center. During the first 9 hours, there is a ≥ 5 K drop in Tb to below 250 K with Tb not increasing more than 1 K at any time during that period. After the cooling trend is established in this way, keep only the briefer period when Tb < 238 K.	$\Delta T = 9\text{--}24$ hrs $\Delta I = 0$ to 40 kt	<i>Steranka et al.</i> , 1986
2 bursts in Hurricane Bonnie (1998) subjectively identified using IR observations	$\Delta T = 24$ or 10 hrs $\Delta I = +40$ kt or +0kt	<i>Heymsfield et al.</i> , 2001
2 bursts in Hurricane Floyd (1999)	$\Delta T = 24$ hours?	<i>Richie et al.</i> , 2003, p. 270
Several bursts formed one after another during the genesis of Tropical Cyclone Chris (2002)	$\Delta T = 6\text{--}12$ hours?	<i>Tory et al.</i> , 2006

Table 2.15. Observations of the vertical profile of the eye's thermal anomaly

Tropical cyclone	Properties ¹	Reference
Hurricane Cleo, 18 August 1958, 1700–2200 UT	$\Delta T_{200-700\text{mbar}} = 9 \text{ K} \pm 1 \text{ K}$ $v_{\text{surf}} = 90\text{--}85 \text{ kt}$ $p_{\text{surf}} = 973\text{--}971 \text{ mbar}$	Aircraft observations at 800, 560, and 240 mbar [<i>La Seur and Hawkins</i> , 1963, Figure 8; <i>Schubert et al.</i> , 2007] ³
Hurricane Arlene, 9 August 1963, 1313 UT	$\Delta T_{200-700\text{mbar}} = 6 \text{ K} \pm 2 \text{ K}$ $v_{\text{surf}} = 75\text{--}90 \text{ kt}$ $p_{\text{surf}} = 979\text{--}974 \text{ mbar}$	One radiosonde released from the ground [<i>Stear</i> , 1965, Figure 5]
Hurricane Hilda, 1 Oct. 1964, 1300–1800 UT	$\Delta T_{200-700\text{mbar}} = 12 \text{ K} \pm 1 \text{ K}$ $v_{\text{surf}} = 120\text{--}130 \text{ kt}$ $p_{\text{surf}} = 951\text{--}941 \text{ mbar}$	Aircraft observations at 900, 750, 650, 500, and 180 mbar [<i>Hawkins and Rubsam</i> , 1968, Figure 9] ³
Hurricane Inez, 27 Sept. 1966	$\Delta T_{200-700\text{mbar}} = 8 \text{ K} \pm 1 \text{ K}$ $v_{\text{surf}} = 80\text{--}110 \text{ kt}$ $p_{\text{surf}} = 965\text{--}962 \text{ mbar}$	Aircraft observations at 750, 650, 500, and 180 mbars [<i>Hawkins and Imbembo</i> , 1976, Figure 6]
Hurricane Inez, 28 Sept. 1966	$\Delta T_{200-700\text{mbar}} = 12 \text{ K} \pm 1 \text{ K}$ $v_{\text{surf}} = 110\text{--}130 \text{ kt}$ $p_{\text{surf}} = 955\text{--}932 \text{ mbar}$	Aircraft observations at 750, 650, 500, and 180 mbars [<i>Hawkins and Imbembo</i> , 1976, Figure 14]
Typhoon Flo, 17 Sept. 1990, 0600 UT ²	$\Delta T_{200} = 12 \text{ K} \pm 1 \text{ K}$ $v_{\text{surf}} = 135\text{--}145 \text{ kt}$ $p_{\text{surf}} = 881 \text{ mbar}$	Aircraft observations at 190–200 mbar [<i>Holland</i> , 1997, Figure 10a]
Hurricane Erin, 10 Sept. 2001, 1700 UT	$\Delta T_{200-700\text{mbar}} = 10 \text{ K} \pm 1 \text{ K}$ $v_{\text{surf}} = 90 \text{ kt} \pm 10 \text{ kt}$ $p_{\text{surf}} = 970 \pm 2 \text{ mbar}$	Several GPS dropsondes released by NASA's ER-2 [<i>Halverson et al.</i> , 2006, Figure 6]
Tropical Storm Gabrielle, 16 Sept. 2001, 2139 UT	$\Delta T_{200-700\text{mbar}} = 2 \text{ K} \pm 1 \text{ K}$ $v_{\text{surf}} = 55\text{--}65 \text{ kt}$ $p_{\text{surf}} = 995\text{--}991 \text{ mbar}$	ER-2 dropsonde in eye compared with DC-8 dropsondes of environment ⁴

¹ Eye thermal anomaly $\Delta T_{200-700\text{mbar}}$, the range of best track surface wind intensity v_{surf} , and the range of best track surface pressure in the eye's center p_{surf} .

² There is an obvious chronological gap in this table between the observations in 1950 – 1965 and the more recent observations. *Holland* [1970] called the Typhoon Flo DC-8 aircraft observations "the first direct upper-tropospheric observations of a severe cyclone in 30 years, together with a dropsonde of the inner eyewall and eye region. [p. 2532]"

³ Also cited in *Holland* [1997].

⁴ This profile has not been previously published. It was downloaded from the CAMEX-4 web site [http://camex.msfc.nasa.gov/camex4/data_search.jsp]. In the search, specify 16 Sept. 2001 and "Dropsonde ER2" or 15 Sept. 2001 and "Dropsonde DC-8". See also the field report for 16 Sept. 2001.

3.

Correlation examined with satellite observations

The goal of this chapter is to use satellite data to establish that the maximum height of convective cells in a tropical cyclone's eyewall is statistically linked to tropical cyclone wind intensification. To do so precisely, this chapter derives an accurate method for calculating the height of a satellite radar observation. Next, the chapter chooses a radar reflectivity threshold (20 dBZ) and a height threshold (a 14.5 km height) that are useful for establishing the correlation between tall cells and wind intensification. Last, the chapter uses a similar approach to define "high" clouds using infrared data and "significant" ice scattering using passive microwave data. All of the satellite data in this chapter comes from the Tropical Rainfall Measuring Mission (TRMM) satellite.

Because the TRMM Precipitation Radar flies over a given tropical cyclone's eyewall only once in approximately five days, just the existence or absence of a tall eyewall cell can be determined at the moment of the overflight. In contrast, chapter 4 discusses continuous observations of tropical cyclones using ground radars.

3.1 Preparatory calculations

Different preparatory steps are required before analyzing the observations made by the various instruments on the TRMM satellite. The instrument observation geometry is shown in Figure 3.1, and the instrument characteristics are summarized in Tables 2.7 and 2.8 (pp. 124, 125).

First, the preparatory calculations for the passive infrared instrument are described. The dissertation converts 11 micron infrared observations from units of radiance to brightness temperature. Scientific literature almost exclusively uses units of brightness temperature, but in the TRMM satellite data archive, the Visible and Infrared Scanner (VIRS) 1B01 data files use units of spectral radiance ($\text{mW cm}^{-2} \text{ micron}^{-1} \text{ sr}^{-1}$). Brightness temperature at 11 microns tends to be about 280 to 320 K over land and ocean and as low as 180 to 200 K for tall dense clouds [Barnes, *et al.*, 2000]. The dissertation performs the unit conversion using linear interpolation on the two closest radiance values in a look-up table of radiance and brightness temperature. In January of 1998, the author obtained this look-up table from Cheng-Hsuan Lyu, a TRMM science team member and VIRS researcher. In April of 2007, the author verified with Dr. Lyu and with VIRS specialist Yimin Ji that the look-up table has not changed since 1998. Because radiance and brightness temperature are both instrument independent units, the look-up table would remain constant even if the VIRS instrument calibration changed (Y. Ji, private communication, 2007).

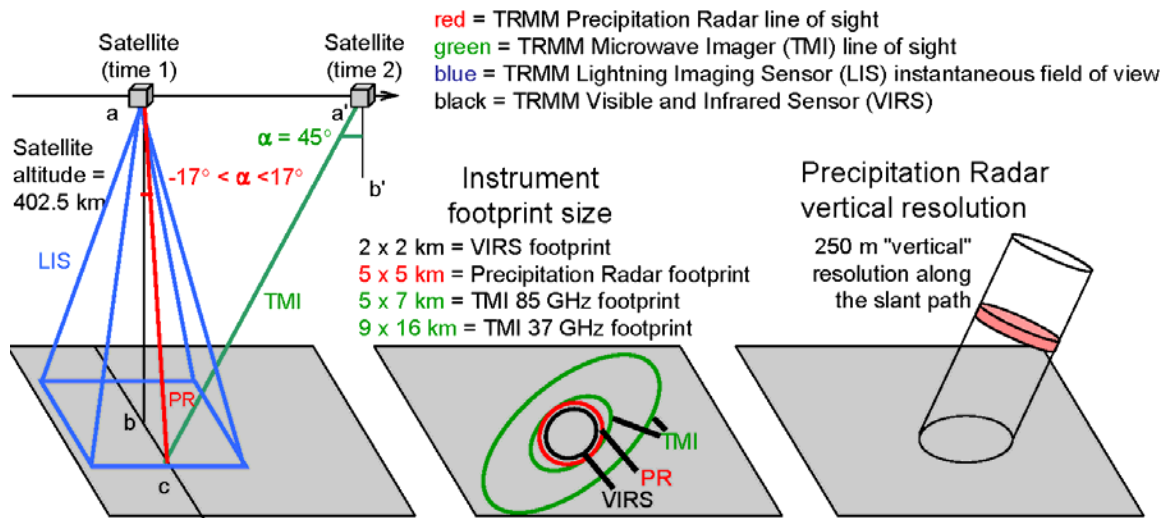


Figure 3.1. Schematic diagram of the observation geometry of instruments on the Tropical Rainfall Measuring Mission (TRMM) satellite

Next, the preparatory calculations for the passive microwave instrument are described. The dissertation converts microwave brightness temperature (T_b) into polarization corrected brightness temperature (PCT). In the TRMM satellite data archive, the TRMM Microwave Imager (TMI) 1B11 files store observations in units of brightness temperature. For the past 15 years, it has been common for atmospheric scientists to publish PCT values instead of ordinary brightness temperature because the PCT of convective cells is not altered whether the cells occurs over land or ocean [Spencer *et al.*, 1989]. In contrast, ordinary brightness temperatures can be very different for identical precipitation cells if they happen to occur over land instead of over ocean. This difference is caused by the ocean's emissivity being much lower than land's emissivity in the frequency range of the TMI instrument. For frequencies from 10 to 100 GHz, dry land's emissivity is approximately 0.95, a body of water's emissivity is 0.4 and 0.6, and moist soil's emissivity is somewhere in between dry land and water [Janssen, 1993, p.

318, Figure 6A.1]. Because this study examines storms over ocean, it is not strictly necessary to use PCT instead of observed brightness temperature. Nonetheless, it is convenient to use PCT in this study so that comparisons can be made to PCT values published elsewhere [Zipser *et al.*, 2006; Liu and Zipser, 2005; Cecil *et al.*, 2002]. TMI's 85 GHz channel has 5 km x 7 km horizontal pixels with a 5 km x 14 km distance between pixel centers [Kummerow *et al.*, 1998]. Spencer *et al.* [1989] were the first to define the 85 GHz PCT as $1.818 \text{ Tb(V)} - 0.818 \text{ Tb(H)}$. The 37 GHz PCT is defined by Cecil *et al.* [2002, part I, p. 774] as $2.20 \text{ Tb(37V)} - 1.20 \text{ Tb(37H)}$.

No preparatory calculations are needed for TRMM lightning data because merely the flash locations are used in this study. The latitude and longitude of each observed flash are provided in the files of the TRMM Lightning Imaging Sensor (LIS) archive.

Preparatory calculations are needed to put ground-truth tropical cyclone wind intensity estimates into a form that can be used by the calculations in the dissertation. The official intensity estimates were established without reference to TRMM Precipitation Radar observations, allowing the dissertation to test if the radar provides new information about intensity change. For most of the chapter, "intensification" will refer to an increase in wind intensity from 6 hours before the TRMM overflight to 6 hours after the overflight. The only exception is section 3.8, when future intensity change will be discussed, i.e., intensity change between the time of observation and 24 hours in the future.

The official intensity estimates are available for each day at 0000, 0600, 1200, and 1800 UT. These estimates are commonly referred to as "best track" estimates and are

generated from post-season analysis by two organizations. For tropical cyclones in the North Atlantic and East Pacific, the best track estimates come from the U.S. National Hurricane Center (NHC) at NOAA, and the best track estimates for all other ocean basins come from the Joint Typhoon Warning Center (JTWC) at the U.S. Department of Defense. The best track data can be downloaded from the "Archive of Hurricane Seasons" in the NHC web site (<http://www.nhc.noaa.gov/pastall.shtml>) and the "Best Track Data Site" in the JTWC web site (https://metocph.nmci.navy.mil/jtwc/best_tracks).

There is no world-wide accepted format for storing best track data, so this dissertation's software reads in two common formats and outputs one easy-to-use format for later analysis in the dissertation. An example of the NHC format [*Jarvinen et al.*, 1984] is shown below for the first North Atlantic tropical cyclone of 2006:

```
65695 08/24/2006 M=12 6 SNBR=1359 ERNESTO XING=1
65700 08/24*0000000 0 0*0000000 0 0*0000000 0 0*1270616 30 1008*
65705 08/25*1300630 30 1007*1330644 30 1005*1370658 35 1005*1400671 35 1004*
```

An example of the JTWC format [*Chu et al.*, 2002] is shown below for the first day of tropical cyclone strength winds in the northwest Pacific in 2006:

```
WP, 02, 2006051000, , BEST, 0, 93N, 1304E, 55, 984, TS, 34, NEQ, 65, 65,
65, 65, 1005, 180, 15, 0, 0, W, 0, , 0, 0, CHANCHU, D,
WP, 02, 2006051000, , BEST, 0, 93N, 1304E, 55, 984, TS, 50, NEQ, 15, 15,
15, 15, 1005, 180, 15, 0, 0, W, 0, , 0, 0, CHANCHU, D,
WP, 02, 2006051006, , BEST, 0, 97N, 1297E, 55, 984, TS, 34, NEQ, 65, 65,
65, 65, 1004, 190, 10, 0, 0, W, 0, , 0, 0, CHANCHU, M,
```

The dissertation reformats these two best track formats to a single format that simply lists one of the 6 hour reporting periods on each row. Each row contains the following information: storm name, date, time, latitude, longitude, wind speed in knots, the Julian day, and the name of the ocean basin.

There are several facts that make this reformatting somewhat tricky. For one thing, one occasionally needs to remove double or triple entries for a single 6-hour reporting period in the JTWC files. Generally, for a given year, a storm name is only used for one storm, but a manual inspection of the world-wide best tracks found one case during the TRMM mission when the same name was used twice during the same year (two separate storms named "Frank" occurred in 2004, one in the East Pacific and one in the South Pacific). Sometimes the same storm will move from one basin into another (such as from East Pacific to West Pacific) but that does not cause difficulty with knowing which best track estimate goes with a particular overflight.

Another tricky thing is that many JTWC files do not mention the commonly used name of the tropical cyclone (such as Chanchu), and instead list only the JTWC storm number for that year (such as 02). In contrast, the TRMM overflight subset files that the author downloaded from JAXA do use the storm name. For this reason, the author created a database that maps JTWC storm number to storm name. A caution in doing this is that different organizations, such as JTWC and the Japanese Meteorological Agency (JMA), give the same storm different storm numbers.

Another thing that makes the reformatting difficult is that there are different ways to categorize the ocean basin in which a tropical cyclone forms [*Chu et al.*, 2002, Appendix 2b]. For example, the JTWC currently uses the following ocean basins: North West Pacific (NP), Southern Hemisphere (SH), and Indian Ocean (IO). In contrast, the JAXA tropical cyclone database divide world's oceans into the following categories that overlap or are subsets of the JTWC categories: North West Pacific (W), North Central

Pacific (C), South Indian Ocean (S), South Pacific Ocean (P), Bay of Bengal (B), and Arabian Sea (A).

3.2. Height calculation

To make the height calculation technique easier to apply to ground radars, this chapter calculates storm height instead of using the storm height values in TRMM 1B21 and 2A23 algorithms. These TRMM algorithms examine the instrument noise and returned power in 250 m range gates above the storm, whereas a ground radar is looking at a storm from the side and lacks 250 meter vertical resolution.

The first step to having an accurate determination of height is to keep in mind that the TRMM 2A25 files contain slant path s (line df in Figure 3.2c) not the height h_{obs} of the precipitation. If the TRMM radar always looked straight down, then this slant path along the line of sight would equal the height h_{obs} , i.e., the perpendicular distance above the ellipsoid. However, the TRMM radar scans up to $\theta = 17^\circ$ from nadir.

Some published studies ignore the difference between slant path along the radar's line of sight and height (e.g., *Zipser et al.* [2006] and *Liu and Zipser* [2005]). Confusing slant path s with height h_{obs} can lead to significant overestimates of height of convective cells that reach the upper troposphere, as described below. Consider Figure 1 of *Liu and Zipser* [2005], which is based on slant path, not height. Some of the 17 km slant-path signals (red) over the oceans in that figure fall short of a 17 km height by as much as 830

meters if they occur at the edge of the TRMM Precipitation Radar swath. Using the equation 3.4 (p. 144) this 830 meter error can be calculated ($s - h_{obs} = 830$ m when $s = 17$ km, $h_{sat} = 405$ km, $r_{Earth} = 6371$ km, and $\theta = \pm 17^\circ$).

The 2A25 algorithm reports the slant path because slant path is easier than height to calculate from radar observations. The 2A25 slant path calculation method is described in this paragraph. The radar precisely measures the time it takes a pulse of radiation to travel from the satellite to the precipitation and back. Based on the travel time, it is easy to calculate the distance between the satellite and the precipitation (line fa in Figure 3.2b). The NASA Flight Dynamics Facility determines the spacecraft's altitude above the Earth's ellipsoid to within 100 meters [*TRMM Project Office*, 1996], and with that information, the TRMM 2A25 algorithm determines which 250 meter radar range gate contains the Earth ellipsoid. The 2A25 algorithm can then report the slant distance s (line df). The remainder of this section explains the calculation of height from slant path.

In all of the TRMM radar calculations used in the dissertation, the top of each bin is assumed to be a multiple of 250 meters away from the ellipsoid starting with bin 79 covering from 0 to 250 meters away from the ellipsoid along the slant path. At the top of the grid, bin 0 is assumed to go from 19.75 to 20.00 km away from the ellipsoid. This assumption is actually an approximation of the true definition of the TRMM 2A25 height grid. The true definition is that the Earth's ellipsoid occurs somewhere within the 250 meter slant path of bin 79, not exactly at the bottom edge of bin 79. This approximation introduces an average bias of 125 meters ($250 \text{ m} \div 2$) in the height values stated in this dissertation. There are other sources of height error, such as the fact that the radar has a

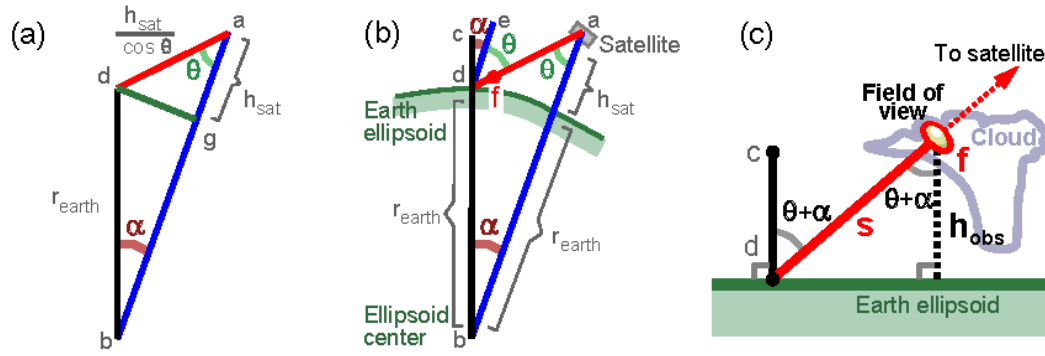


Figure 3.2. Diagrams for calculating the height of a Precipitation Radar observation. (a) The diagram used to calculate angle α . (b) A diagram that shows how the Earth's curvature causes the zenith angle $\theta + \alpha$ at point d on the Earth's surface to be greater than the nadir angle θ at the satellite. Line ab is parallel to line ed . Line cd is perpendicular to the Earth ellipsoid. The TRMM satellite's height is h_{sat} and the Earth's radius is r_{earth} . (c) A close up that shows the height of the observation h_{obs} .

Gaussian response function within the 250 meter range gate, i.e., precipitation near the middle of the bin will contribute most of the signal. In addition, some of the signal comes from outside the boundary of the 250 meter bin. Considering the variation of the instrument response function only along the line of sight, approximately 68% of the signal comes from within the bin because the 250 meter vertical by 5 km diameter horizontal resolution is set by the half power limit of the signal [Kozu *et al.*, 2001, Table 1, equation 3]. Approximately 68% of a one-dimensional Gaussian distribution occurs within 1 standard deviation of the mean value, and the Gaussian probability distribution function drops to half of the central value around 1 standard deviation from the mean value [Bevington and Robinson, 1992, p. 30]. Separate from the instrument considerations, the top of a convective storm itself is "fuzzy", i.e., there is small scale horizontal variation (~ 1 km across) in the upper bound of the 5 km across data volume.

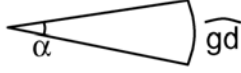
Visual inspection of high resolution data in *Heymsfield et al.* [2001, Figure 7a] suggests that there is a ~100 meter ambiguity in the altitude of the top of the cell.

The second step to accurately determining height is to note that the zenith angle of the line of sight at the Earth ellipsoid (angle cda in Figure 3.2b) is larger than the zenith angle θ of the line of sight at the satellite. Ignoring Earth's curvature, as the TRMM 3A25 algorithm does, would result in an 80 meter overestimate of the height of a 17 km tall signal at the edge of the Precipitation Radar swath (equation 3.4).

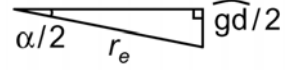
Equation 3.4 for calculating height includes both the slant path effect and the Earth curvature effect that have just been described. The equation is derived geometrically by the author using the Law of Sines and the assumption that the Earth's ellipsoid can be approximated by a sphere in the neighborhood of the radar observation. Height h_{obs} is the height of a Precipitation Radar field of view above the Earth ellipsoid (Figure 3.2c). Ellipsoidal height can be informally thought of as height above the surface of the tropical North Atlantic because satellite altimetry shows that these quantities differ by generally less than 50 meters [Seeber, 1993, p. 454].

It is necessary to make one approximation in order to derive an expression for angle α , which is shown in Figure 3.2a and 3.2b. The approximation is that the arc of the Earth ellipsoid between the sub-satellite point g and the intersection of the line of sight with the Earth ellipsoid point d is so small that arc gd can be approximated by a straight line gd and that the angle dga can be approximated as a right angle. The straight-line approximation is accurate to 1 part in 10^5 , as described below, because arc gd is quite small ($\sim 1^\circ$). Arc gd is largest at the edge of the Precipitation Radar swath. At that point,

arc gd is half of the swath width of 215 km at the TRMM satellite's original 350 km altitude orbit [Kummerow *et al.*, 1998]. Without making the straight-line approximation, angle α can be calculated using the fraction of the Earth's circumference covered by arc

gd: $\frac{\alpha}{360^\circ} = \frac{\text{arc } gd}{2\pi r_e}$  . Angle α is 0.8993308 using this formula

without the straight-line approximation, arc gd is 107.5 km (215 km \div 2), and the Earth mean radius r_e is 6371 km. When the straight-line approximation is made, angle α can be

calculated using a right angle triangle: $\alpha = 2 \sin^{-1}\left(\frac{\text{arc } gd/2}{r_e}\right)$ 

. Angle α is 0.8993216 using this formula with the straight-line approximation. As mentioned above, the two values for angle α differ by only 1 part in 10^5 .

Based on the straight-line approximation described above, the definition of cosine gives the following expression for length of side α , i.e., the side of triangle bda that is opposite angle α in Figure 3.2a. The cosine definition is actually applied to angle θ in triangle gda, which shares side α with triangle bda.

$$\cos \theta \equiv \frac{\text{adjacent side } ga}{\text{hypotenuse } da}$$

$$\cos \theta = \frac{h_{sat}}{\text{side } \alpha} \quad (3.1)$$

$$\text{side } \alpha = \frac{h_{sat}}{\cos \theta}$$

In equation 3.1, h_{sat} is the height of the satellite above the Earth ellipsoid. The Law of Sines states the following relationship between angles α and θ and the sides opposite them in triangle bda [CRC, 1991, p. 129]:

$$\frac{\sin \alpha}{\text{side } \alpha} = \frac{\sin \theta}{\text{side } \theta} \quad (3.2)$$

Substituting for the length of the sides of the triangle bda in Figure 3.2a results in the following equation:

$$\frac{\sin \alpha}{\frac{h_{sat}}{\cos \theta}} = \frac{\sin \theta}{r_{earth}} \quad (3.3)$$

In equation 3.3, r_{earth} is the Earth ellipsoid mean radius. Solving this equation for the desired angle α results in equation 3.4. So far, angle α has been considered the angle at the Earth ellipsoid center. Angle α is useful because it equals angle cde at the Earth's surface (Figure 3.2b). Angle cde is the difference between the satellite observation angle θ and the observation angle at the Earth ellipsoid, angle cda in Figure 3.2b. Once angle α is known, the height of the observation h_{obs} can be easily calculated from the slant path s and from the definition of cosine as shown in Figure 3.2c and equation 3.4.

$$\alpha = \sin^{-1} \left(\frac{h_{sat} \tan \theta}{r_{earth}} \right) \quad (3.4)$$

$$h_{obs} = s \cos (\theta + \alpha)$$

The expression in equation 3.4 for the height of the observation h_{obs} is used in this chapter.

In calculating the maximum height of the 20 dBZ radar reflectivity signal in the eyewall, only lines of sight are used that are labeled by the TRMM 2A25 algorithm as both "convective rain" and "rain certain."

3.3 Case selection

The first step in data analysis is to examine individual TRMM satellite overflights of tropical cyclones to determine which overflights are of sufficient quality to use in the later analysis steps.

Case selection is important because a factor limiting the usefulness of the Precipitation Radar is the small number of times that it observes a tropical cyclone's eyewall (section 2.3.2, p. 36). Most times that the Precipitation Radar flies over a tropical cyclone, it sees only an outer rain band and perhaps a small portion of the eyewall. For this study, an overflight is used only if all or almost all of the eyewall is seen by the Precipitation Radar. This way, no important feature of the eyewall is hidden during the author's manual examination of each overflight.

Another selection criteria is that the overflight occur over ocean. More specifically, overflights are excluded if the tropical cyclone's center moves within 100 km of land within 1 day of the TRMM overflight. Intensification is very unlikely after a tropical cyclone's center goes over land, so land-falling tropical cyclones are not useful

for determining if tall eyewall cells are associated with intensification [*Simpson et al.*, 1998].

In addition, an overflight is only selected if there are simultaneous infrared and passive microwave observations from the other instruments on the TRMM satellite. In other words, if an instrument is turned off when an overflight occurs, then that overflight is excluded from this analysis.

An overflight is only selected if the TRMM precipitation radar observed storms at ≥ 60 knots wind intensity, which basically means tropical cyclone intensity (sustained winds ≥ 65 knots or ≥ 33 m/s) as mentioned in Table 2.1 (p. 25). This dissertation excludes weak systems because the dynamic processes involved in tropical cyclone genesis are different than those of tropical cyclone intensification. The role of tall eyewall cells in tropical cyclone formation is described in *Simpson et al.* [1998], *Gray* [1998], *Montgomery et al.* [2006], and *Sippel et al.* [2006].

Once an overflight has been accepted for use in this study, the author uses TRMM radar data to locate the "eyewall area." The eyewall area is defined in this dissertation as a donut-shaped area that contains any 100 mm/h and most of the 10 mm/h surface rain adjacent to the eye. These rain values were chosen informally with the goal that the eyewall area should include the heavy surface rain around the eye. The dissertation restricts the study to the eyewall out of necessity because the 215 to 247 km wide swath of the TRMM Precipitation Radar is too narrow to regularly include all of a tropical cyclone's rain bands.

The dissertation examines the first nine years of TRMM Precipitation Radar overflights of tropical cyclones (1998 to 2006) world-wide. For these nine years, the distribution of the 269 TRMM overflights by ocean basin is shown in Table 3.1. The TRMM observations during each of these overflights are summarized in the appendix at the end of the dissertation (p. 279). The South Pacific category in Table 3.1 includes the southwestern Indian Ocean near Africa all the way east to the south Pacific Ocean that lies east of Australia. Row 1 of Table 3.1 shows the number of tropical cyclones that would be expected in each basin. This expected value is based on the mean annual number of tropical cyclones from 1968 to 1989 [*McGregor and Nieuwolt*, 1998, p. 157].

Table 3.1. Tropical cyclones and TRMM Precipitation Radar overflights of tropical cyclones by ocean basin for 1998 through 2006

	Atlantic Ocean	East Pacific Ocean	North Indian Ocean	South Pacific	West Pacific Ocean	Total world-wide
1. Expected cyclones	49	80	23	109	144	405
2. Actual cyclones	75	67	15	120	141	418
3. Actual cyclone-days	315	208	26	404	603	1559
4. Analyzed TRMM overflights	74	36	3	47	109	269

Row 2 of Table 3.1 includes only those storms that reach tropical cyclone strength during 1998 to 2006. Rows 2 and 3 are calculated by the author from the best track data of the National Hurricane Center and the Joint Typhoon Warning Center. The values in rows 1 and 2 are similar, which shows that 1998 to 2006 has a typical number of tropical

cyclones. The one exception is the North Atlantic, which is well known to be an in active phase during 1998 to 2006 [Klotzbach, 2006; Nyberg *et al.*, 2007]. Row 3 is the sum of the observed duration of all tropical cyclones in units of the 6 hourly reporting periods, divided by 4 to come up with units of cyclone-days. Row 4 lists the number of TRMM satellite overflights of tropical cyclones that satisfy the selection criteria described earlier in this section. The overall number of overflights (right column, row 4) is somewhat less than one fifth of the number of cyclone-days (right column, row 3). This reflects the fact that the revisit time of the TRMM satellite is approximately once every 5 days, as discussed in section 2.3.2 (p. 36).

3.4. Choosing a radar reflectivity threshold

In this section and the next section, the dissertation will define a tall cell by stating that a radar reflectivity signal of a particular strength must reach a particular height. There is no universally accepted or precise definition of tall cell, so there is considerable leeway in how to define tall cells in this dissertation. Within this leeway, the dissertation will look for a definition that identifies cells that occur more often in intensifying tropical cyclones, rather than in non-intensifying tropical cyclones.

First, the dissertation reviews two signal strength thresholds used by other researchers and explains why these previously used thresholds are inappropriate for this study. Some researchers consider the height of a cell to be the top of the cloud [Riehl and

Malkus, 1961; Malkus, 1959]. Cloud tops have a radar reflectivity of -50 to 10 dBZ at frequencies used in standard weather radars [*Doviak and Zrnic, 1993*, pp. 503–5;

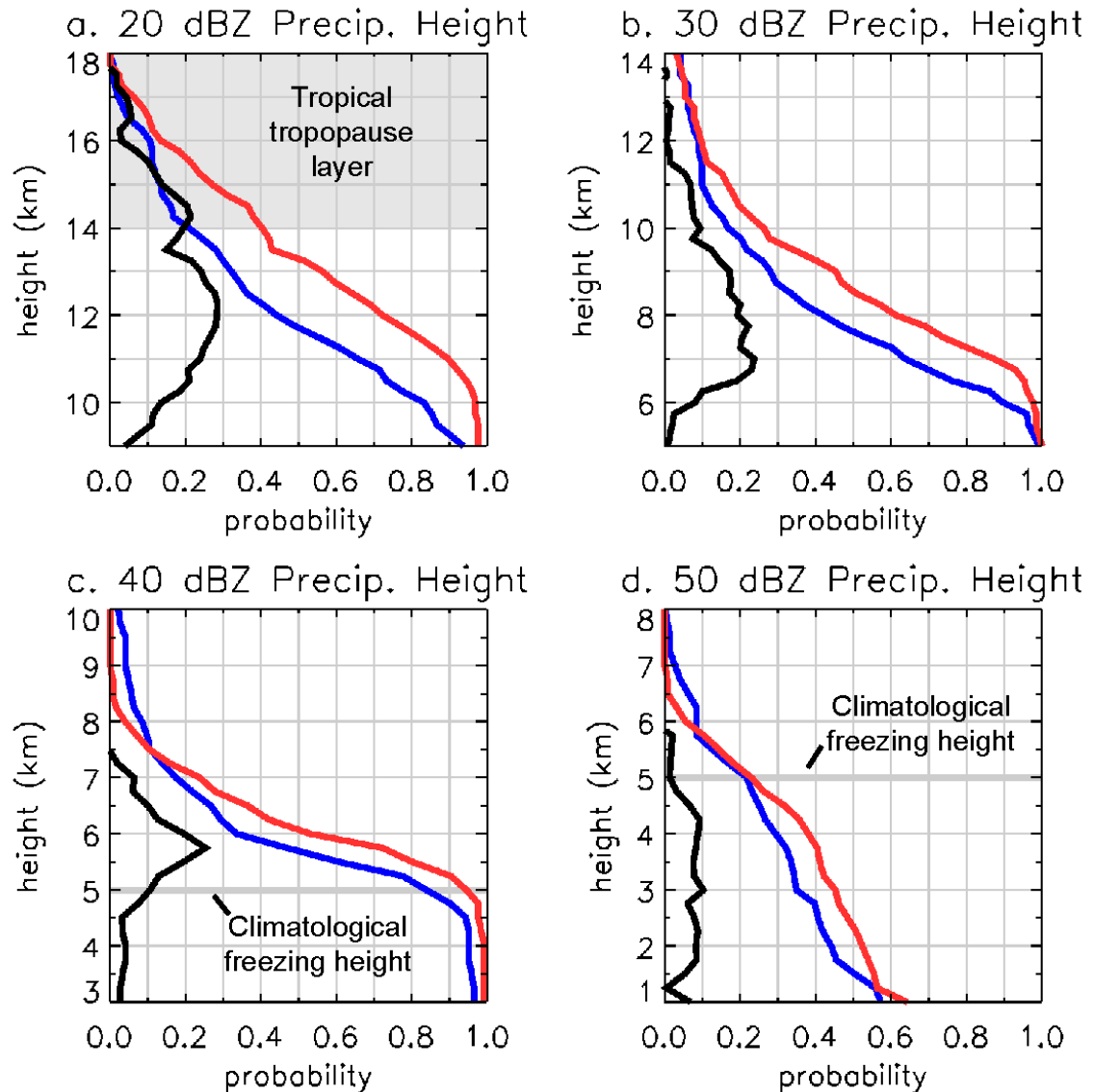


Figure 3.3. The Cumulative Distribution Function (CDF) of radar reflectivity. The data are 269 tropical cyclone overflights observed by the TRMM Precipitation Radar during the first nine years of the mission (1998 to 2006). Red is for intensifying tropical cyclones, blue is for non-intensifying tropical cyclones, and black is the difference between the red and blue lines. The vertical axis is the height of the tallest TRMM Precipitation Radar pixel observed in the eyewall at the radar reflectivity threshold given in the title of each of the four panels. The approximate precipitation rates associated with these reflectivity thresholds are stated in Table 2.2.

Meneghini and Kozu, 1990, p. 146]. Other researchers consider the height of a cell to be the “echo top,” i.e., the height of the lowest detectable radar signal. For some aircraft radars, the echo top can be as low as -10 to 0 dBZ [*Alcala and Dessler*, 2002]. Both of these signal thresholds are too low to be used with TRMM Precipitation Radar data because the Precipitation Radar’s minimum detectable signal is around 16 to 18 dBZ [*Kozu, et al.*, 2001].

Using the TRMM Precipitation Radar, a tall cell could be defined using a 20 , 30 , 40 , or 50 dBZ radar reflectivity threshold. To evaluate these thresholds, a cumulative distribution function (CDF) is calculated for each of them. Starting with the 20 dBZ threshold, the maximum 20 dBZ height in each of 269 eyewalls is calculated. The probability that the 20 dBZ height is above any height from 9 to 18 km is plotted in Figure 3.3a. As discussed in section 2.5.2 (p. 55), a 20 dBZ reflectivity signal at this altitude is associated with light precipitation in the form of ice particles with a precipitation rate of under 1 mm/h. The dissertation uses the attenuation-corrected reflectivity that is found in the output of the TRMM 2A25 algorithm [*Iguchi et al.*, 2000a and 2000b; *Meneghini et al.*, 2000].

Figure 3.3a shows probability $P(h_{20\text{ dBZ}} \geq h_0)$ plotted on the x axis and height h_0 plotted on the y axis. In the figure, the blue line is for non-intensifying cyclones and the red line is for intensifying cyclones. The black line shows the probability difference between the red and blue lines. To interpret Figure 3.3a, find an height where the probability difference is great (the black line is to the right) and the probability of a false alarm is low (the blue line is to the left). One such height is 14.5 km. Only 16% of non-

intensifying cyclones (23 out of 143 overflights) meet that criterion, while a full 37% of intensifying cyclones meet the criterion (46 out of 126 overflights).

Having found one definition of tall eyewall cells based on a 20 dBZ radar reflectivity threshold (20 dBZ at ≥ 14.5 km), the dissertation now considers if there might be any better radar reflectivity thresholds. Figures 3.3b, c, and d show CDFs that use a radar reflectivity threshold of 30, 40, or 50 dBZ for the tallest pixel in each tropical cyclone's eyewall. As discussed in section 2.5.2 (p. 55), these reflectivities corresponds to precipitation rates of roughly 4 to 100 mm/h. As before, the black line shows the difference in the CDFs of the intensifying and non-intensifying populations.

Generally, intensifying and non-intensifying populations are more similar at 30 to 50 dBZ than they are at 20 dBZ. The one exception is a spike in the 40 dBZ probability difference at 5.5 km, which is roughly 0.5 km above the climatological freezing height in the Tropics. The ~ 5 km freezing height of the tropical atmosphere was discussed in section 2.1.7 (p. 23). The 40 dBZ spike at 5.5 km is not useful for predicting tropical cyclone intensification because it has a huge false positive rate, i.e., a 60% chance of occurring in non-intensifying tropical cyclones (the blue line in Figure 3.3c).

Nonetheless, the 40 dBZ ≥ 5.5 km combination is interesting because *Doviak and Zrnic* [1993, p. 229] report that a similar threshold (45 dBZ at 1.5 km above the freezing level) can be used to detect hail, i.e., large ice particles associated with storms with strong updrafts. *Gilmore and Wicker* [2002] associate a strong 40 dBZ signal above the freezing height with lightning production. This suggests that intensifying tropical cyclones are more likely than non-intensifying tropical cyclones to have at least one

eyewall cell vigorous enough to produce large ice hydrometeors and lightning. This possibility is explored in section 3.6 (p. 156) using a passive microwave and lightning sensor.

As discussed above, the 20 dBZ reflectivity threshold is better able to distinguish between intensifying and non-intensifying cyclones than are higher reflectivity thresholds. In other words, no other reflectivity threshold has a higher detection rate without also having a higher rate of false positives. The 30 to 50 dBZ reflectivity thresholds occur at lower heights than the 20 dBZ threshold and are associated with heavy precipitation. This analysis suggests that variation in the height of heavy precipitation (30 to 50 dBZ) in the mid-troposphere is less correlated with tropical cyclone intensification than is variation in the height of light precipitation (20 dBZ) in the upper troposphere.

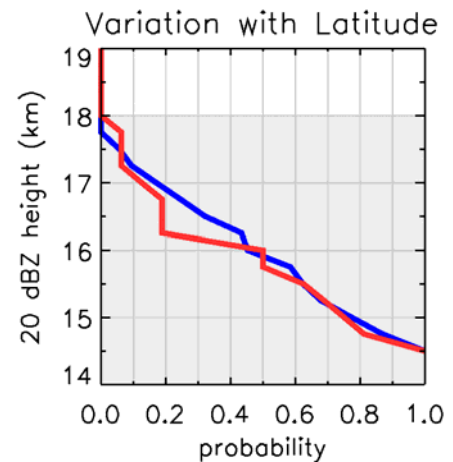
3.5. Choosing a radar height threshold

As mentioned before, there is no universally accepted precise height threshold for identifying which cells are tall. Within the typical range used by other researchers, this dissertation searches for a definition that best distinguishes between the cells that form in intensifying tropical cyclones from those that form in non-intensifying tropical cyclones.

Here is a sample of the height thresholds that other researchers have used. *Alcala and Dessler* [2002] state that 14 km is the average altitude in the Tropics for the lapse rate tropopause, i.e. where the lapse rate of observed temperature approaches zero. Using the *Hoinka* [1999] monthly climatology, the height of the tropopause is 15.0 km with a 0.7 km standard deviation when the tropopause is sampled at the locations of the TRMM tropical cyclone overflights used in this chapter. Other researchers prefer to use a latitudinal variation in the lapse-rate tropopause [*Thuburn and Craig*, 1997]. *Simpson et al.* [1998] use a different tropopause height of 14.3 or 16 km for the North Atlantic and South Pacific, respectively.

The dissertation uses a single height for all oceans and latitudes for several reasons. For one thing, there are barely enough TRMM Precipitation Radar overflights to calculate reliable world-wide statistics using a single height threshold, let alone different height thresholds for groups of overflights. Second, the variation of climatological tropopause height with ocean is less than the day-to-day changes in tropopause height.

Figure 3.4. Latitude dependence of the maximum 20 dBZ height in tropical cyclone eyewalls from 1998 to 2006. Only tropical cyclones with a 20 dBZ height of at least 14.5 km are plotted. The blue line is for tropical cyclones less than 20 degrees latitude from the Equator, and the red line is for tropical cyclones from 20 to 35 degrees latitude from the Equator. The shaded region indicates the 14 to 18 km tropical tropopause layer [*Alcalca and Dessler*, 2002].



Convection can cause the tropopause height to change by ± 1 km over several days at a particular location [Kiladis *et al.*, 2001], whereas the climatological tropopause in the Tropics is generally stays within 14.0 to 15.5 km. It is only after entering mid-latitudes (~ 30 degrees from the Equator) that the climatological tropopause drops rapidly by roughly 1 km for every 10 degrees latitude [Hoinka, 1999, Figure 1].

Figure 3.4 uses TRMM overflights of tropical cyclones to support the dissertation's decision to include no latitude variation in the definition of tall cell. The figure shows that, inside tropical cyclone eyewalls, tall cells reach approximately the same height regardless of the latitude. To generate the figure, only tropical cyclone overflights with a 20 dBZ height of at least 14.5 km were included. Based on this method of calculation, the 1.0 value of the CDF must be at 14.5 km. The 0.0 value of the CDF happens to be near the top of the tropopause layer, but that is determined by the radar data, not the method of calculation. The blue line is for tropical cyclones within 20 degrees of latitude of the Equator, and the red line is for tropical cyclones 20 to 35 degrees from the Equator.

Until the past few years, the tropopause was defined as the single altitude where the observed temperature stops decreasing with increasing altitude (i.e., the lapse-rate tropopause) [Haltiner and Martin, 1957, p. 302; Hess, 1959, pp. 234–235; Djuric, 1994, p. 8; AMS, 2000, p. 793]. In recent years, the tropopause has been described as a “layer” [Highwood and Hoskins, 1998; Dessler *et al.*, 2006]. For example, Alcala and Dessler [2002] state:

Sherwood and Dessler [2000, 2001] have called this region the tropical tropopause layer and define it to extend from the level of zero net radiative heating (~14 km, 150 hPa) to the highest level of overshooting convection (~18 km, 70 hPa). . . . The maximum level of neutral buoyancy of tropical deep convection is around 14 km, coincident with the base of the tropical tropopause layer.

Using nine years of TRMM observations, Figure 3.3a suggests that 14.5 km is the best height threshold. Based on nine years of world-wide TRMM tropical cyclone observations (1998–2006), intensifying cyclones are twice as likely as non-intensifying cyclones to have at least one 5 km wide Precipitation Radar pixel in their eyewall with a 20 dBZ reflectivity signal that reaches 14.5 km. The 14.5 km height threshold will be

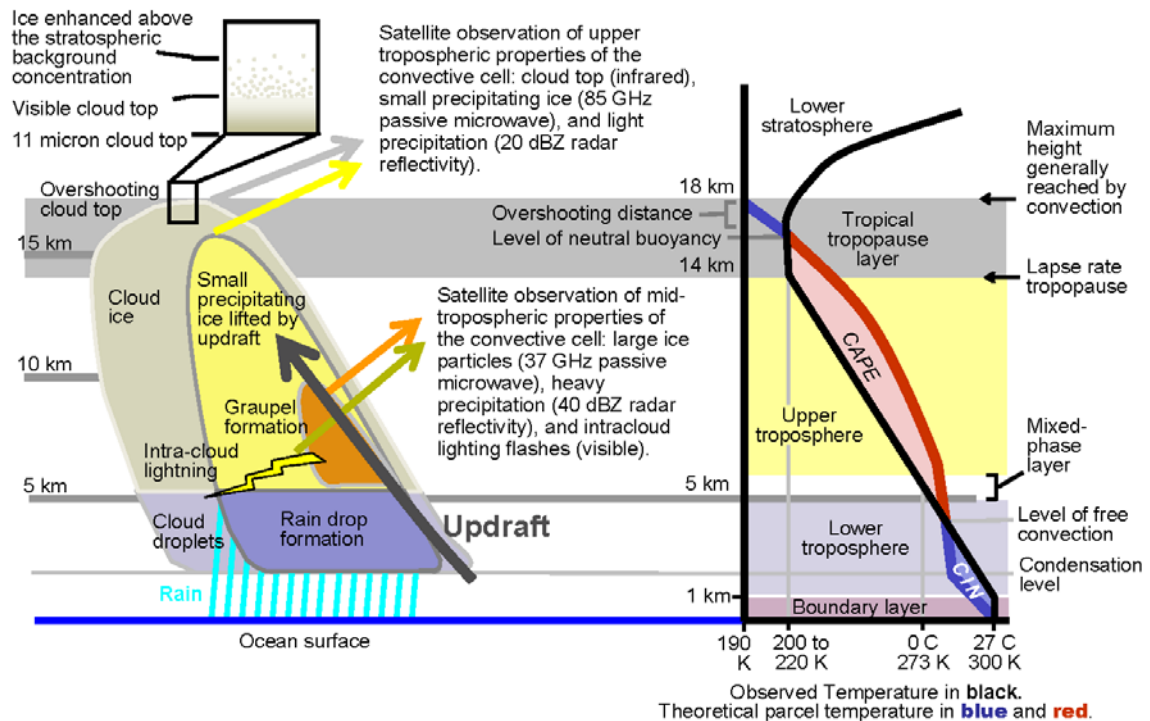


Figure 3.5 Schematic diagram of a tall convective cell. The figure is loosely based on Figure 16.5 of *Ray* [1986, p. 370], Figure 8.49 of *Wallace and Hobbs* [2006, p. 352], and *Houze* [1993, pp. 270–281].

used in the rest of the dissertation when analyzing TRMM Precipitation Radar data. This same 14.5 km threshold was chosen in *Kelley et al.* [2004, *GRL*] using only six years of TRMM observations.

3.6. Choosing thresholds for other instruments

The primary way that the dissertation identifies "tall" eyewall cells is the height of the radar signal. To confirm that the radar signal is reliable, this section develops a definition of high clouds and significant ice scattering using measurements independent of the TRMM radar.

The dissertation defines "high" clouds using the 11 micron infrared brightness temperature (T_b) of the TRMM Visible and Infrared Scanner (VIRS). Because temperature decreases with altitude in the troposphere, the dissertation looks for very cold temperatures (Figures 3.5 and 2.12, pp. 155, 121). The VIRS field of view is only 2 to 3 km across compared with the TRMM Precipitation Radar's 5 km across field of view [*Kummerow et al.*, 1998], which means that it requires three VIRS pixels to cover the same area as a single Precipitation Radar pixel ($3 \times 7 \text{ km}^2 \approx 20 \text{ km}^2$). To keep the area of observation similar, the dissertation locates the third lowest VIRS temperature. The black line in Figure 3.6a shows that intensifying eyewalls (red) have at least twice the chance of non-intensifying eyewalls (blue) of having an 11 micron $T_b \leq 192 \text{ K}$ in a 20 km^2 area. The difference between intensifying and non-intensifying tropical cyclones is

slightly less clear if one uses the minimum 11 micron Tb (not shown) instead of the third lowest value.

A threshold of 192 K is colder than the coldest point in the climatological

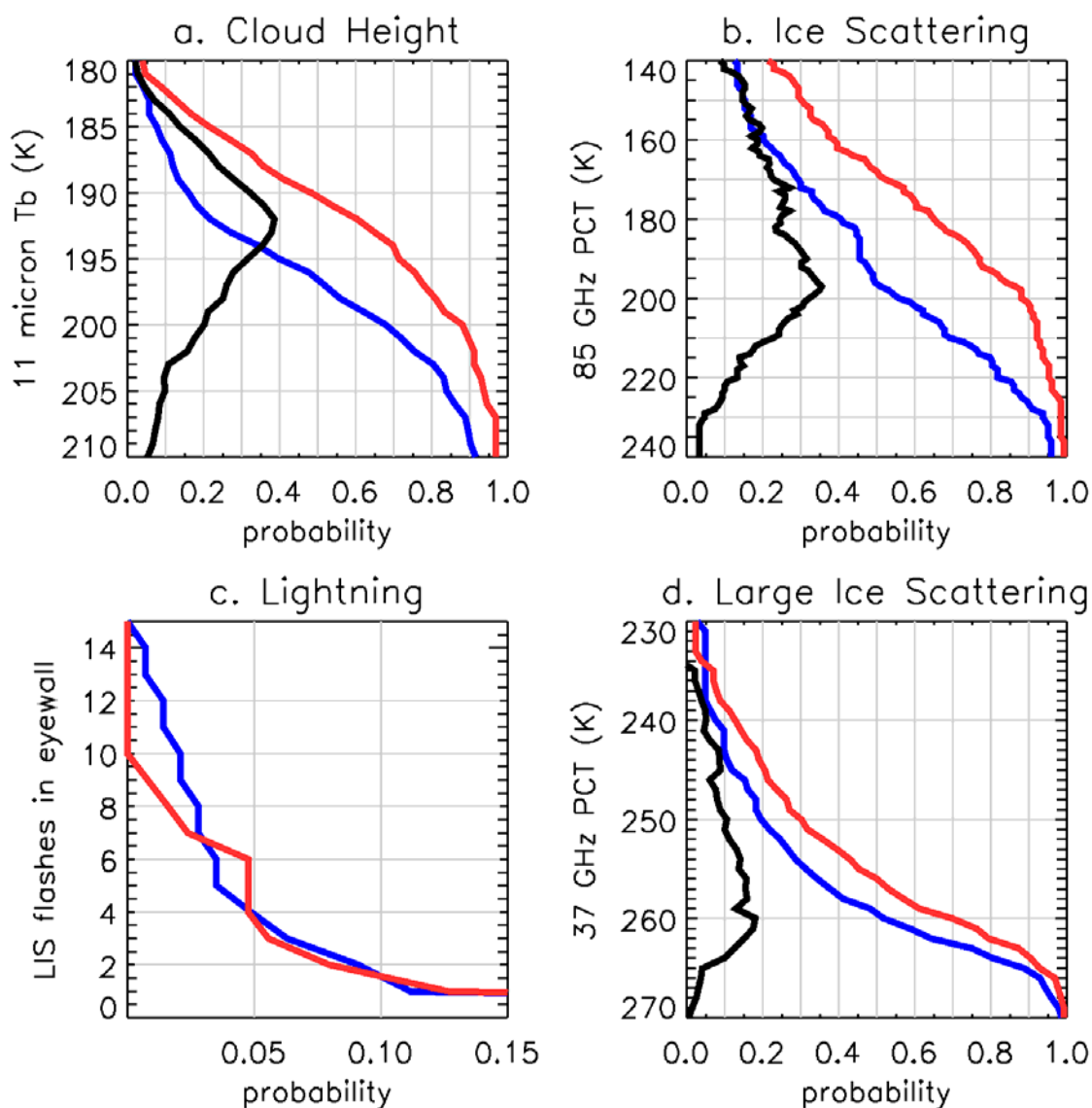


Figure 3.6. Cumulative Distribution Functions (CDFs) for non-radar observations of 126 overflights of intensifying tropical cyclones (red) and 143 overflights of non-intensifying tropical cyclones (blue). This data comes from nine years of TRMM observations (1998 to 2006). Intensification is defined as an increase in intensity between six hours before and after the overflight. The black line shows the difference between the intensifying and non-intensifying CDFs.

temperature profile of the bottom 40 km of the atmosphere, which requires an explanation. The climatological temperature profile for the months and location of most North Atlantic tropical cyclones has its minimum of ~203 K at ~16.5 km according to the NCEP reanalysis (See Figure 2.12, p. 121). Similarly, according to the climatology of *Hoinka* [1999], the climatological lapse rate tropopause has a temperature of 202 K to 212 K in the region and season where North Atlantic tropical cyclones form. A simple explanation for 11 micron infrared brightness temperatures in the 180s and 190s K is that they represent overshooting of the entire 20 km² horizontal area observed by the 3 VIRS pixels. The dry adiabatic lapse rate is 10 K/km for the entire depth of the troposphere [*Bohren and Albrecht*, 1998, p. 109]. Assuming that the height of the tropical cyclone's tropopause is equal to the climatological tropopause, a 192 K infrared cloud-top temperature would indicate approximately a 1 km overshooting of the tropopause.

To look for a significant concentration of small ice hydrometeors, the dissertation examines the 85 GHz polarization-corrected brightness temperature (PCT) of the TRMM Microwave Imager (TMI) (section 3.1, p. 134). Cloud ice interacts very little with 85 GHz radiation in comparison with small precipitating ice (0.2 to 1.0 mm in diameter). Scattering by small precipitating ice causes the satellite to observe a lower 85 GHz brightness temperature (section 2.5.3, p. 57). Because the TMI field of view is larger than the TRMM Precipitation Radar field of view, the dissertation looks for the minimum TMI brightness temperature in the eyewall. The black line in Figure 3.6b shows that there is a large difference in the frequency with which intensifying vs. non-intensifying

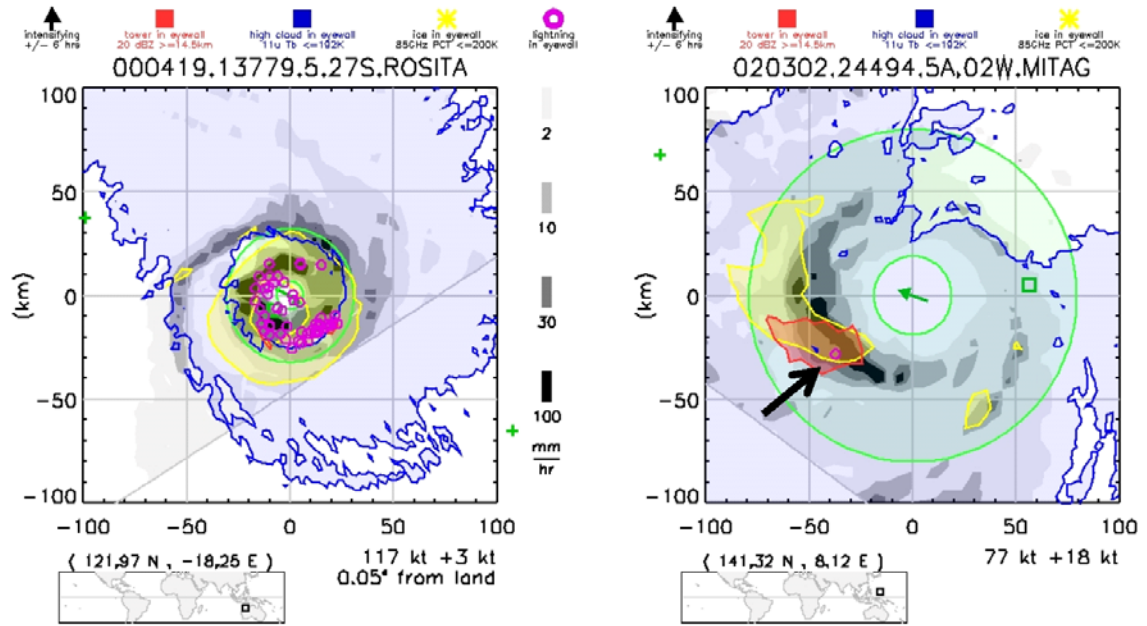


Figure 3.7. Multi-instrument TRMM overflights of tropical cyclone eyewalls. The figure is described in section 3.6

tropical cyclones have a 85 GHz PCT ≤ 200 K. The 200 K threshold is also used by Cecil *et al.* [2002a].

The dissertation also examined lightning and low frequency microwave scattering of large ice particles, but these two variables do not provide useful checks on the radar observations of tall eyewall cells. These two variables are associated with the cells properties in the mid-troposphere (Figure 3.5), unlike the upper tropospheric properties of the cells that have been described so far in this section (i.e., high clouds and ice scattering).

Figure 3.5 shows schematically both the upper tropospheric and mid-tropospheric properties of tall cells observed by the various instruments of the TRMM satellite. The following information is useful for interpreting Figure 3.5. The lapse rate tropopause temperature is 202–212 K in tropical cyclone formation region [Hoinka, 1999]. GOES

11 micron observations typically record the temperature occur ~1 km below the "visible" cloud-top height (visible lidar optical depth of 1). Approximately 1 km above the visible cloud-top height, there is an enhancement in the concentration of non-precipitating ice particles above the stratospheric background concentration [*Sherwood et al.*, 2004].

When the parcel's temperature exceeds the temperature of the background (red in the figure), Convectively Available Potential Energy (CAPE) exists (See section 2.7, p. 63).

When the parcels temperature is below the background temperature (blue in the figure) in the lower troposphere, Convective Inhibition (CIN) exists. Overshooting occurs when a parcel exceeds its level of neutral buoyancy. The boundary layer is a turbulent layer with strong temperature gradients. The boundary layer is on average 1 km thick and its thickness can vary by a factor of three [*Holton*, 1992, p. 117]. The low-level inflow to a tropical cyclone's eyewall is generally 0.5 to 1.5 km thick (0.5 km [*Black et al.*, 2007, p. 366], 1 km [*Houze*, 1993, p. 410], and 1.5 km [*Cram et al.*, 2007]). Sometimes "boundary layer" and "eyewall inflow layer" are treated as synonyms [e.g., *Cram et al.*, 2007].

The TRMM Lightning Imaging Sensor (LIS) appears not to be useful in this dissertation because it observes a location so briefly. Because of its brief integration time, LIS cannot detect flash rates under about 2 flashes per minute [*Ushio et al.*, 2001], but the entire eyewall generally has less than 1 flash per minute [*Black and Hallett*, 1999]. The lightning flash rate varies with the fifth power of cell height [*Williams*, 2001, p. 532], which motivates the attempt to use lightning data in this dissertation despite the LIS instrument limitations. Figure 3.6c shows that LIS observes any eyewall lightning in

only 12% of TRMM tropical cyclone overflights. The standard explanation for the low or nonexistent flash rate in tropical cyclone eyewalls is that the updraft speeds are too slow to generate considerable lightning [*Cecil et al.*, 2002, part 2].

Two times that LIS did observe lightning in the eyewall are shown in Figure 3.7. The images combine tall convection observed by the TRMM Precipitation Radar (red indicates $20 \text{ dBZ} \geq 14.5 \text{ km}$), high cloud tops observed by the TRMM VIRS (blue indicates $11 \mu \text{ Tb} \leq 192 \text{ K}$), significant ice scattering observed by the 85 GHz TMI PCT (yellow indicates $\text{PCT} \leq 200 \text{ K}$), lightning strikes observed by the TRMM LIS (purple circle), and TRMM Precipitation Radar surface rain (the gray scale). The left side of Figure 3.7 shows Tropical Cyclone Rosita (2000) slowly intensifying, going from 117 to 120 between six hour before and after the TRMM overflight. Rosita is about to make landfall and has dozens of lightning flashes in the eyewall, which is unusual. The right of Figure 3.7 shows Tropical Cyclone Mitag (2002) undergoing rapid intensification far from land. Mitag has only one eyewall lightning flash (indicated by black arrow), which is located inside the tall eyewall cell (red contour). The small green arrow in the middle of the eye indicates the direction of the tropical cyclone's translational motion.

TMI channels lower than the 85 GHz frequency channel appear to be not useful for identifying tall cells in the eyewall because of their large footprint [*Smith et al.*, 1994, p. 863]. Considering only frequency, and not footprint, one might think that TMI's low frequency channels (11, 19, 37 GHz) would be more useful than the 85 GHz channel. The 85 GHz channel is best for detecting small ice particles ($<0.6 \text{ mm}$ diameter) [*Cecil et al.*, 2002, part 1]. Such small particles are created even by low cells, but large particles

can only be created by cells with strong updrafts, which generally means cells that reach high altitudes. Larger ice particles reduce the brightness temperature of TMI's low frequency channels. The larger the particle, the lower the frequency that it can effect. In the most extreme case, grape-sized hail (~1 cm diameter) can scatter out 10 GHz radiation (Figure 2.13, p. 122). To carry 1 cm hail upward requires an updraft in excess of the hail's 30 m/s fall speed [Figure 2.13; *Knight and Knight, 2001*]. While narrow 30 m/s updrafts been reported over ocean (Table 2.12, p. 129), these updrafts are unlikely to be as wide as the TMI 10 GHz pixel size (9 km by 63 km).

In the multi-year survey presented in section 3.9, there were no observations of 10 GHz channel Tb depressions over ocean due to large ice. In the survey, one of the most

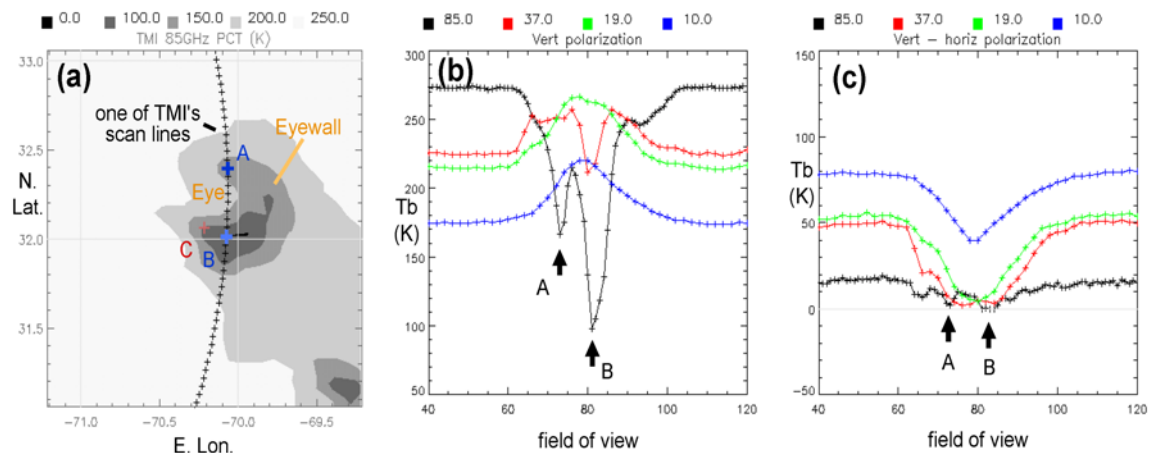


Figure 3.8. Ice scattering by very large ice particles in Hurricane Erin observed by the TRMM Microwave Imager on 07 Oct 2002 (TRMM orbit #27905) off the coast of Georgia. (a) The 85 GHz PCT image showing the eyewall on the southeast side of the storm as cold brightness temperatures as low as 100 K. The blue plus signs indicated by letters A and B are locations of low 85 GHz PCT in the TMI scan line shown in the figure. The red plus sign indicated by the letter C is a location of a 14.5 km tall convective cell observed by the TRMM Precipitation Radar. (b) The vertically polarized brightness temperature for four TMI channels. Points A and B indicate the same fields of view in this panel as they did in panel a. (c) The difference in the vertical and horizontal polarization in the same four TMI channels shown in panel b.

severe examples of ice scattering is shown in Figure 3.8. The figure shows a 170 K Tb depression at 85 GHz, 50 K depression at 37 GHz, a hint of a 2 K depression at 19 GHz, and no depression at 10 GHz. The 19 GHz depression may have occurred only because the long axis of the TMI pixels were oriented east-west, the same orientation as the storm cell's oval shape. The observed proportions between the 85, 37, and 19 GHz depressions are similar to those modeled over ocean for 20 mm/h rain rate in *Spencer et al.* [1989, Figure 3]. The observed proportions is also similar to those modeled at a 90 mm/h rain rate in *Petty* [1994, part 1, Figure 5] if you assume 100% beam filling at 85 and 37 GHz and 66% beam filling at 19 GHz due to the 19 GHz's larger footprint.

Since 37 GHz brightness temperature depressions are observed over ocean, the dissertation calculates a CDF of the minimum TMI 37 GHz PCT in tropical cyclone eyewalls (Figure 3.6d). The CDFs for intensifying and non-intensifying tropical cyclones are similar at 37 GHz, much more similar than the CDFs at 85 GHz (Figure 3.6b). For this reason, 37 GHz is considered less useful for this dissertation than is 85 GHz.

In addition to their large footprint, the lower frequency channels suffer from another a complication. At 37 GHz and lower frequencies, cloud ice emits radiation that can hide the loss of radiation due to ice scattering [Petty, 1994, part 1]. For example, at 37 GHz, this spatially broad emission signal raises the brightness temperature in fields of view 60 to 100 in Figure 3.8b while the narrow scattering signal lowers the brightness temperature in just fields of view 80 to 85 (point B of Figure 3.8b).

3.7. Association with concurrent tropical cyclone intensification

In the previous sections, a definition of tall cell was developed ($20 \text{ dBZ} \geq 14.5 \text{ km}$) to identify a distinguishing feature of tropical cyclones that are undergoing wind intensification. This section evaluates how successful this definition is. Figure 3.9 shows a 67% chance of tropical cyclone intensification if a tall convective cell exists in the eyewall. The chance of wind intensification drops to 44% when the tallest eyewall cell is 10.0 to 14.25 km high and to only 14% when the tallest cell is less than 10.0 km high.

The radar technique presented in this chapter has a similar statistical power as an

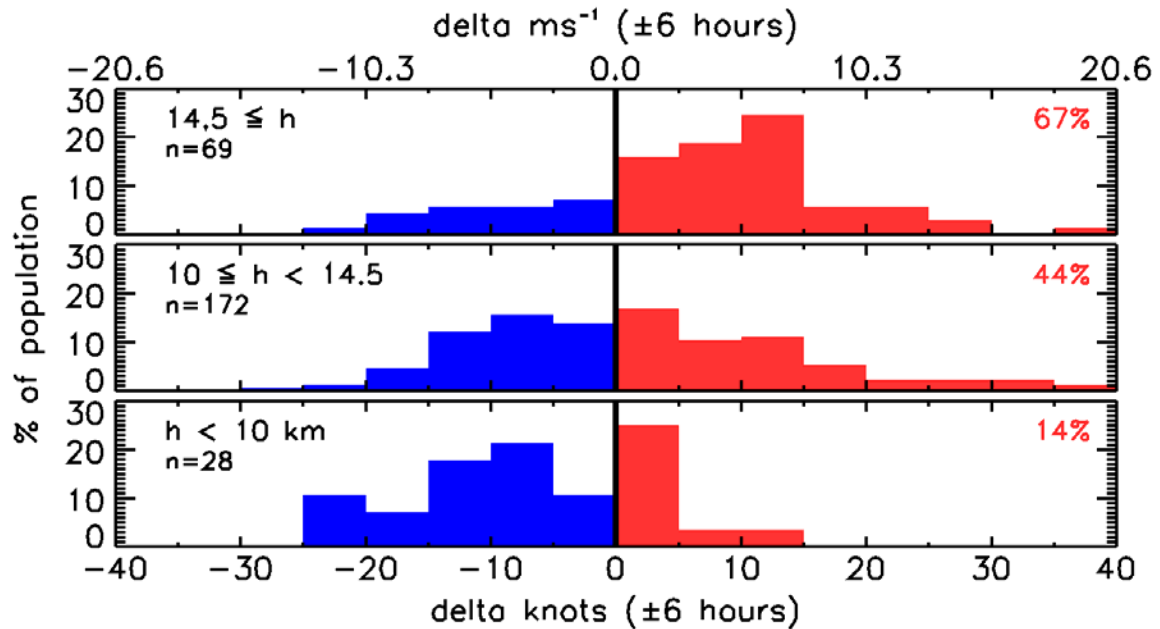


Figure 3.9. Tropical cyclone overflights segregated into three populations of size n based on the maximum height h of their eyewall's 20 dBZ signal. The horizontal axis is the ± 6 hour change in maximum sustained surface winds. The vertical axis is the percent of the population in a 2.6 m/s bin (5 kt bin). The red numbers on the right tell the percent of overflights that were intensifying.

infrared technique developed 20 years earlier [*Steranka et al.*, 1986]. The infrared technique requires a 6 hour average of infrared observations over the entire inner core of the tropical cyclone (i.e., within 222 km of the center of the eye). *Steranka et al.* [1986] found a 71% chance of tropical cyclone wind intensification if the average infrared temperature was below 258 K for at least 9 consecutive hours and a 37% chance of intensification otherwise. The radar technique presented in this chapter achieves the same statistical power with just one overflight, not ≥ 9 hours of observations, and the radar technique only requires that the eyewall be observed not a 222 km radius area around the eye. This comparison of the new radar technique with the earlier infrared technique suggests that the radar observed eyewall cells are a more direct measure of the forces at work in the tropical cyclone than are the cloud-top temperatures observed by an infrared sensor.

The association of tall eyewall cells with tropical cyclone intensification is statistically significant. Based on a one-sided t-test, the mean wind speed change in the eyewalls with a tall eyewall cell ($m_1=5.7$, $s_1=12$, $n_1=69$) is greater than the wind speed change in the eyewalls without a tall eyewall cell ($m_2=-0.2$, $s_2=13$, $n_2=200$). This t-test is significant at the 0.01 level ($\alpha=0.01$). In the formula below, both the sample mean m and sample standard deviation s have units of wind speed change (knots) within ± 6 hours of the TRMM overflight. The formula for calculating the one-sided t-statistic for two samples with unequal variance is the following [*Montgomery and Runger*, 2003, p. 342; *CRC*, 1991, p. 492]:

$$t = \frac{m_1 - m_2 - \Delta\mu}{\sqrt{\frac{s_1^2}{n_1} + \frac{s_2^2}{n_2}}} \quad (3.5)$$

In the above formula, $\Delta\mu$ is the difference in the population means that one is testing against. In the t-test just described, $\Delta\mu$ is set to zero. Because the number of samples is well over 100, the t-statistic is very close to the standard normal curve. Several critical t values for large samples are $t \geq 1.282$ for a significance level α of 0.1, $t \geq 1.645$ for $\alpha = 0.05$, and $t \geq 2.326$ for $\alpha = 0.01$ [Bhattacharyya and Johnson, 1977, pp. 599 and 597]. The t-test remains significant at the 0.01 level when testing to see if the mean intensity change of the intensifying tropical cyclones is at least 2 kt greater than the mean of the non-intensifying tropical cyclones, i.e., with $\Delta\mu = 2$ kt.

A non-parametric test also finds the association of tall eyewall cells with tropical cyclone intensification to be statistically significant. Using the "sign test" at the 0.05 significance level, the median intensity increase in the population of tropical cyclones with a tall eyewall cell is ≥ 4 knots, while the median intensity increase in the population without a tall eyewall cell is ≤ 1 kt. In the case of non-normal and non-symmetric distributions with unequal variance (Figure 3.9), the sign test provides a more reliable evaluation of statistical significance than other tests [Montgomery and Runger, 2003, p. 573; Miller, 1986, pp. 19 and 21; Rumsey, 2007, p. 272]. More specifically, the sign test avoids the t-test's assumption that the two populations are normally distributed, the signed-rank test's assumption that the two populations have a symmetric distribution [Montgomery and Runger, 2003, p. 581; Miller, 1986, p. 22; Walpole and Myers, 1985,

p. 535], and the rank-sum test's assumption that the two populations have equally shaped distributions shifted in their median [*Montgomery and Runger*, 2003, p. 585; *Rumsey*, 2007, p. 286; *Bhattacharyya and Johnson*, 1977; p. 507]. In a journal often cited in this dissertation, the *Monthly Weather Review*, three articles in the past 20 years use the sign test [*Drusch and Viterbo*, 2007; *Leutbecher*, 2005; *McCaul et al.*, 2004] according to the American Meteorological Society's on-line full-text search engine.

The idea behind the sign test is explained in *Montgomery and Runger* [2003, section 15-2] and *Walpole and Myers* [1985, pp. 530–534]. The one property of the sample distribution that the sign test uses is the sample median. The only fact about the underlying population that the sign test uses is that a point taken from the population has an equal chance of being greater than or less than the population's median (i.e., a probability of 0.5 in either case). For a sample of n points, the probability that x of them are greater than the population median is therefore given by the binomial distribution $P_{binomial}$ with a parameter of 0.5. This property of the population median is true for all continuous distributions. To use the sign test to see if a population's median exceeds a given value m_0 (the alternate hypothesis), collect a sample of n points and count the number x of points greater than m_0 . The null hypothesis for this test is that population's median is exactly m_0 . If, under the null hypothesis, the probability P that x or more would occur is less than 0.05, then you can reject the null hypothesis at the 0.05 significance level. This paragraph can be summarized by the following equation:

$$P_{median > m_0} = P_{binomial}(X \geq x ; n , p = 0.5) \quad (3.6)$$

When using the sign test to see if the sample median is less than a given value, follow the same procedure except calculate the lower tail of the binomial distribution:

$$P_{median < m_0} = P_{binomial}(X \leq x; n, p = 0.5) \quad (3.7)$$

For large samples such as the ones in this chapter, $np > 5$ and $n(1-p) > 5$. Under these conditions, the binomial distribution can be closely approximated with the standard normal distribution ($\mu = 0$ and $\sigma = 1$) [Montgomery and Runger, 2003, p. 119]. The large-sample sign test uses the standard normal Z in the following way:

$$P_{median > m_0} = P_{normal}\left(Z \geq \frac{x - 0.5n}{0.5\sqrt{n}}\right) \quad (3.8)$$

As mentioned above, the sign test at the 0.05 significance level states that the median intensity increase m_T in the population of tropical cyclones with a tall eyewall cell is ≥ 4 knots, while the median intensity increase m_{NT} in the population with no tall eyewall cell is ≤ 1 kt. Using the formulation developed in the last few paragraphs, these statements are equivalent to the following equations:

$$\begin{aligned} P_{m_T > 4 \text{ kt}} &= P_{normal}\left(Z \geq \frac{x - 0.5n}{0.5\sqrt{n}}; n = 69, x = 44\right) < 0.05 \\ P_{m_{NT} < 1 \text{ kt}} &= P_{normal}\left(Z \leq \frac{x - 0.5n}{0.5\sqrt{n}}; n = 200, x = 75\right) < 0.01 \end{aligned} \quad (3.9)$$

Another way to evaluate the empirical association of tall eyewall cells with concurrent wind intensification is shown in Table 3.2. This 2 by 2 chart shows that, 62% of the time ($17\% + 45\% = 62\%$), the presence or absence of a tall eyewall cell indicates whether or not wind intensification is occurring. By one measure, this result is only weakly significant. The type I error rate is 9% ($\alpha = 0.09$) as indicated in the lower left

entry of Table 3.2. The type I error rate can be thought of as the rate of "false positives" [Bhattacharyya and Johnson, 1977, p. 170]. This is marginal significance because generally results are only published if they are significant at the $\alpha=0.05$ level, i.e., there is only a 5% chance of a false positive. For this reason, the dissertation examines independent observations that are related both to tall eyewall cells and wind intensification.

Table 3.2. Tall eyewall cells vs. tropical cyclone wind intensification ^a

Wind Intensity Increasing	Tall eyewall cell	No tall eyewall cell	<i>Total</i>
Yes	17.1% (46) ^d	29.7% (80) ^c	46.8% (126)
No	8.6% (23) ^b	44.6% (120) ^d	53.2% (143)
<i>Total</i>	25.7% (69)	74.3% (200)	100% (269)

^a "Tall eyewall cell" refers to tall eyewall cells with a 20 dBZ signal at least 14.5 km tall. Intensification refers to intensity being greater 6 hours after the TRMM overflight compared with 6 hours before the overflight. The number of overflights is stated in parentheses. The number of overflights adds up exactly in each row and column. The percentages do not add up exactly due to rounded to the nearest 1%. ^b Type I error rate or "false positives". ^c Type II error rate or "failure to detect". ^d The total success rate is the sum of the diagonal terms.

Simultaneous observations by two other instruments reinforce these Precipitation Radar results. As discussed in the previous section, the two other observations are high clouds observed with the TRMM VIRS ($11 \mu \text{Tb} \leq 192 \text{ K}$) and ice scattering observed by TMI ($85 \text{ GHz PCT} \leq 200 \text{ K}$). If both tall clouds and ice occur, then the eyewall is likely

to have a tall eyewall cell (row 2 of Table 3.3). When either tall cloud or ice is absent, then the eyewall is unlikely to have a tall eyewall cell. The "high cloud and ice" test identifies the presence or absence of a radar-observed tall eyewall cell 83% of the time. If the "high cloud and ice" test correctly identified all of the radar-observed tall eyewall cells, then radar observations would contain no new information. However, if the "high cloud and ice" test almost never correctly identified the presence of a radar-observed tall cell, then cloud and ice observations could not be used to validate radar observations.

Furthermore, eyewalls that have both high cloud and ice are correlated with increases in a tropical cyclone's wind intensity. The presence or absence of the combined high cloud and ice signature is associated with intensification or the lack of it 68% of the time (row 3 of Table 3.3). Since high clouds and ice are related to the occurrence of tall eyewall cells and to the occurrence of wind intensification, tall cloud and ice provide reassurance that the association of tall eyewall cells and wind intensification is real.

Table 3.3. Independent observations related to tall eyewall cells and tropical cyclone wind intensification

Two predictors	Both occur	Neither occur	Total success rate
1. Tall cell and intensification	17%	45%	62%
2. Tall cell and high cloud + ice	22%	61%	83%
3. High cloud + ice and intensification	25%	43%	68%

"Tall cell" refers to tall eyewall cells with a 20 dBZ signal at least 14.5 km high. "Intensification" refers to intensity being greater 6 hours after the TRMM overflight compared with 6 hours before the overflight. "High cloud" refers to TRMM VIRS 11 micron $T_b \leq 192$ K. "Ice" refers to TMI 85 GHz PCT ≤ 200 K.

3.8. Predicting future tropical cyclone intensification

The preceding results can be thought of as defining a "TRMM hot tower index" for predicting tropical cyclone wind intensification. On other words, when a tall cell occurs with a 20 dBZ radar reflectivity signal at least 14.5 km tall, then the previous sections show that intensification is likely ongoing. This section examines whether the hot tower index would be useful for intensity forecasting in an operational context.

Based on nine year of data (1998 to 2006), the TRMM hot tower index explains 8% of the variance of intensity within ± 6 hours of the radar observation. The fraction of variance explained is the square of the correlation coefficient between the floating point value of the maximum 20 dBZ height (km) and the floating point value of wind intensity change (knots). "Variance explained" is sometimes referred to as "R squared" or the "coefficient of determination" [*Montgomery and Runger*, 2003, pp. 397–398; *Bhattacharyya and Johnson*, 1977, p. 396].

The same technique finds that the hot tower index explains 10% of the intensity change between the wind speed at the time of the TRMM overflight and the wind speed 24 hours in the future. One reason why tall cells may be more strongly associated with intensity change further in the future is that the six hourly intensity values are reported to the nearest 5 knots in the best track data. The intensity change over ± 6 hours is generally smaller in magnitude than the intensity change over 24 hours, so the 5 knot increments

are more of an issue with short term intensity change calculations. This effect has been noted by *DeMaria and Kaplan* [1999].

In some problems, explaining only 10% of the variance with a single predictor would be disappointing. However, it is so difficult to predict tropical cyclone wind intensity that explaining 10% of the variance with a single predictor is potentially useful. As shown in Table 3.4, the operational SHIPS intensity prediction method explains only 37% of the 0 to +12 hour intensity change using eleven predictors.

Furthermore, explaining 10% of the variance with a single parameter in a sample size of 269 is statistically significant at the 0.01 significance level. A test can be performed by calculating the t-statistic with the following formula that uses the variance explained value r^2 of 0.1, which represents 10% of variance explained, and the sample size n of 269 tropical cyclone overflights [*Younger*, 1979, p. 245]:

$$t = r \sqrt{\frac{n - 2}{1 - r^2}} \quad (3.10)$$

The t value can be looked up in a table of t values, and for samples sizes larger than 100, t values larger than 2.326 indicate significance at the $\alpha = 0.01$ level [*Bhattacharyya and Johnson*, 1977, p. 597].

Table 3.4. Association of intensification with various predictors ¹

1. Type of data. Intensification predictor variable.	2. Forecast period	3. % of variance explained	4. Fraction intensifying	4. Reference
Infrared data. Six hour 11 micron running average over the whole tropical cyclone is ≤ 258 K for 9 hours.	+24 hr	37% to 59% ³	0.71 (103 out of 145)	<i>Steranka et al.</i> , 1986
Microwave data. 1 snapshot of surface rainfall rate over whole tropical cyclone.	+24 hr	20%		<i>West</i> , 1998, Ph.D.
Radar data. 1 snapshot of 20 dBZ storm height in the eyewall.	+24 hr	10%	0.62 (43 out of 69 TRMM overflights) ²	This chapter
SHIPS algorithm. 11 statistical predictors from a numerical model forecast and other sources.	+12 hr +5 days	37% 56%		<i>DeMaria and Kaplan</i> , 1999

¹ Column 2 states for how far in the future the intensity forecast is made. Column 3 states the % of variance in the intensity explained by column 1. Column 4 states the fraction of storms that intensify when the intensification predictor variable indicated that intensification was likely.

² The 43 out of 69 cases is different than the 46 out of 69 cases reported in the second column of Table 3.2 because this table is reporting the (0,+24hr) intensity change, rather than the (-6,+6hr) intensity change.

³ The correlation for strong and weak tropical cyclones is 0.771 and 0.610, respectively. Variance explained is the square of correlation.

West [1998, Ph.D.] finds that the surface rainfall rate observed during a passive microwave overflight of a tropical cyclone can explain 20% of the wind intensity change 24-hours later, which is more variance than the TRMM hot tower index can explain. Nonetheless, the TRMM hot tower index is of at least scientific interest because it

explains variance using features that fill up only approximately 5% of the eyewall's horizontal area, whereas the technique of *West* [1998] requires observations of the entire inner core of the tropical cyclone.

For practical reasons, it would be difficult to add the hot tower index to numerical forecast models. In the present form, there is only one phase of the forecast process in which the hot tower index might be relevant. In the United States in recent years, forecasts of ordinary weather are now made by computers with sometimes no modification by human forecasters. However, computer forecasts of severe weather, such as a tropical cyclone landfall, are routinely modified by human forecasters [*Mass*, 2003; *Stuart et al.*, 2006; *NOAA*, 2007, p. 3–39]. As stated in *Roebber and Bosart* [1996]:

The skill advantage of human forecasters over numerical guidance continues to diminish and now largely reflects the human ability to recognize occasional departures from the linear relationship between forecast information and future observations.

The reason for the human intervention is the high financial stakes if a tropical cyclone is mis-forecasted, and because computer forecasts of tropical cyclone intensity are known to be poor. In 2007, human-modified intensity forecasts were more accurate than computer-only forecasts by such a small margin that one needs to average over several seasons to see the improvement [*Franklin*, 2007, Table 5]. In the present form, the TRMM hot tower index could be added to the list of factors considered by the human forecaster. For example, if the SHIPS statistical intensity forecast model were giving a significantly different intensity forecast than the GFDL mesoscale model, the human forecaster would have a few hours at most to decide between them. In such a difficult situation, human

forecasters already do examine satellite imagery to look for features known from past experience to be associated with changes in tropical cyclone wind intensity [*Hawkins et al.*, 2001]. While these same satellite images may be ingested by a computer model, the human eye, experience, and judgment can identify features that computer models fail to fully appreciate [*Roebber and Bosart*, 1996]. TRMM realtime data is available three hours after observation, and a forecaster could quickly determine if a tall eyewall cell were present in TRMM data.

The other limitation of the TRMM hot tower index is that a Precipitation Radar overflight of a particular tropical cyclone's eyewall can only be expected on average once in five days (section 2.3.2, p. 36). When the eyewall falls outside the narrow swath of the TRMM Precipitation Radar, the eyewall is sometimes visible in the wider swath of the TRMM microwave and infrared instruments (759 km and 720 km wide, respectively). Every time that a microwave radiometer with an 85 GHz ice scattering channel flies over a tropical cyclone, a forecaster could create a composite image similar to the right side of Figure 3.10, except without the radar-derived tall eyewall cell location. The image would show the 200 K PCT 85 GHz “ice” contour superimposed on the 192 K “high cloud” contour of the most recent 11 μ geosynchronous infrared image. Whenever both the high cloud and ice signal occur inside of the eyewall region, the dissertation finds a 71% chance that the tropical cyclone is undergoing intensification. When neither signal occurs in the eyewall, the dissertation finds only a 33% chance that intensification is underway. When just one signal occurs, the situation is ambiguous.

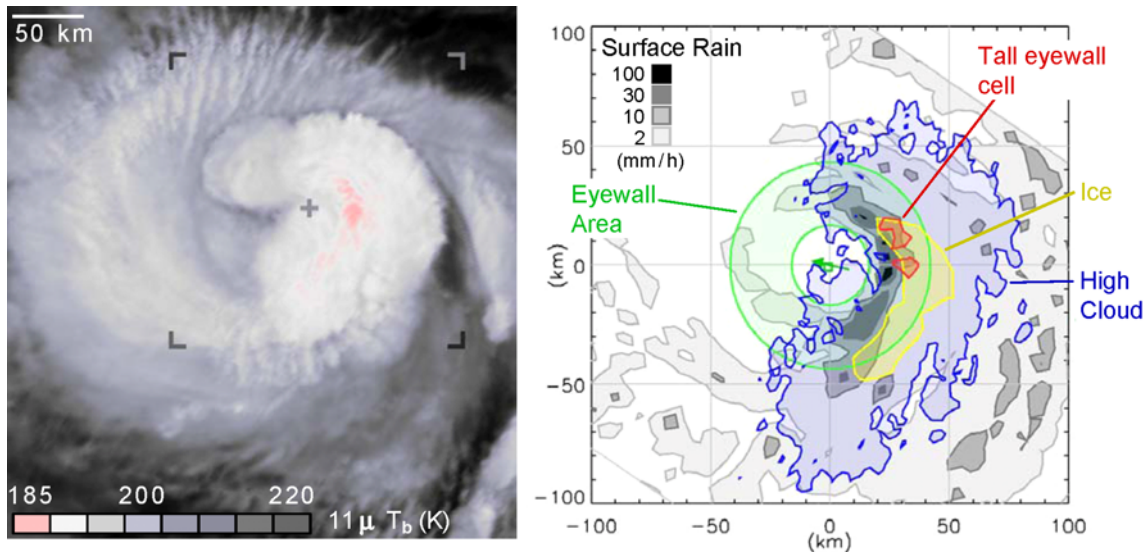


Figure 3.10. Hurricane Carlotta at 1055 UT on 20 June 2000, at 14.66°N, 101.02°W. The left panel shows TRMM VIRS 11 μ infrared brightness temperature (T_b). The image gives a sense of explosive expansion of upper-level outflow from the tall convective cell in the eastern side of the eyewall. The four corner brackets in the left panel locate the boundary of data shown in the right panel. Based on thresholds defined in chapter 3, tall eyewall cells are shown in red, high clouds are shown in blue, and ice scattering is shown in yellow. Interpolating the NHC best track data, the tropical cyclone's intensity was 38 m/s at the time of observation and increased by 10 m/s in ± 6 hours from the time of observation. This figure appeared in Kelley *et al.* [2004, GRL].

Another possible way to overcome the limitation of the TRMM satellite radar is to adapt the hot tower index for use with ground radars. This modification of the technique is the subject of chapter 4.

3.9. Extremely tall cells and tropical cyclones

While examining the TRMM archive to perform the research for this chapter, a number of surprisingly tall convective cells were found in tropical cyclones. While this

dissertation uses all cells with a 20 dBZ signal at 14.5 km, a few cells were observed in eyewalls with a 20 dBZ signal that reached much higher to 17 km.

Other researchers have also occasionally reported ~17 km tall eyewall cells. *Halverson et al.* [2006] report an eyewall cell that is almost 17 km tall in Hurricane Erin (2005). *Liu and Zipser* [2005, Figure 1a, red dots] show a 5 year global plot of cells with a 17 km slant path, but they do not identify which of those cells occurred inside the eyewalls of tropical cyclones. *Heymsfield et al.* [2001] report an 18 km tall cell in the eyewall of Hurricane Bonnie (1998). *Ebert and Holland* [1992] report two eyewall cells that were 19.2 km tall in Tropical Cyclone Hilda (1990). *Malkus* [1960] reports an eyewall cell 18.3 km tall in Hurricane Daisy (1958). By placing the top of the tropical tropopause layer at 18 km, *Alcala and Dessler* [2002] imply that 18 km is the maximum height that convective cells routinely reach in the Tropics.

Because it is difficult to imagine how such extremely tall cells could form over ocean, the dissertation presents a detailed survey of TRMM observations of 17 km tall oceanic cells. The survey establishes what fraction of these 17 km tall cells exist in eyewalls vs. elsewhere over the ocean. The survey is computationally expensive and requires extensive manual examination of intermediate steps in the analysis so the survey was conducted for just the peak of hurricane season (July through October) over the North Atlantic for observations in 1998 to 2005.

It turns out that 17 km tall cells in the North Atlantic generally occur outside of tropical cyclones and are too rare to be of practical use in tropical cyclone intensity forecasts. Nonetheless, the results of the survey are reported here because the ≥ 17 km

tall cells found in this survey are the upper tail of the ≥ 14.5 km tall cells that have been discussed throughout this chapter.

3.9.1. Locating extremely tall cells

When looking for meteorological events that are very rare, it is important to explicitly exclude very rare non-meteorological events that, in other research, are too rare to worry about. For example, this section excludes isolated radar reflectivity signals when they occur far above the continuous or almost continuous region of reflectivity that defines the convective cell. These isolated signals may be instrument noise or small regions of hydrometers. One way to avoid these isolated reflectivity spikes is to ignore stratiform rain, which does not typically reach high altitudes. For this reason, this entire chapter examines only TRMM Precipitation Radar profiles that have been classified as "convective rain certain" by the TRMM 2A23 algorithm. In addition, this section requires that the altitude that defines the top of a convective cell have a 20 dBZ signal in at least six of the ten 250 meter altitude bins below the tallest 20 dBZ signal. This requirement is referred to as the "6 out of 10" rule later in this section.

Next, this section ignores profiles that are contaminated with radar interference, which is a very rare occurrence. The likely cause of the interference is transmitters on the ground or in aircraft. The TRMM file documentation does warn about occasional interference over several cities, but the documentation makes no mention of interference over ocean [*TRMM Precipitation Radar Team*, 2005, p. 21]. In contrast, this survey finds that radar interference is twice as common over the North Atlantic as are 17 km tall cells

over the North Atlantic. Because an interference profile has a near constant reflectivity over the ~20 km vertical range of the radar, an interference profile could be potentially misidentified as a tall convective cell. To avoid interference, one should avoid profiles where the TRMM 1B21 product contains a non-zero value in the System Noise Warning Flag.

Here is how the procedure that has just been presented affects the number of 17 km tall precipitation cells over the North Atlantic during the peak of hurricane season (July to October) during 1998 to 2005. A naive examination of the version 6 TRMM 2A25 product would locate 1323 profiles with a 20 dBZ attenuation-corrected radar reflectivity signal at least 17 km high when one treats slant path as if it were height. The number of profiles is reduced from 1323 to 934 after height is calculated accurately (using equation 3.4, p. 144). The number is reduced from 934 to 325 when only profiles are kept that the TRMM 2A23 algorithm labels as "convective rain certain." The number is further reduced to 320 profiles after this section applies the "6 out of 10" rule, as described above. Only 111 profiles remain after profiles contaminated with radar interference are removed. The rest of this section focuses on the 77 out of 111 North Atlantic profiles that are at least 100 km from shore to avoid ambiguous coastal storms.

In summary, the search for extremely tall convective cells over the North Atlantic during the peak of hurricane season (July through October) found 77 profiles in eight years. These TRMM Precipitation Radar profiles had a 20 dBZ height of at least 17 km. The locations of these tall cells are indicated in Figure 3.11.

3.9.2. External properties of extremely tall cells

Before describing the internal properties of these tall cells, this section describes the cell's external properties, such as where they occur, during what part of the day, and how frequently.

Most of these extremely tall cells occur outside of tropical cyclones. In fact, tropical depressions and tropical storms are more favorable than tropical cyclones for the formation of 17 km tall convective cells. Only 3% of profiles (2 out of 77) are in tropical cyclone rain bands, at a distance of 100 to 500 km from the tropical cyclone's low pressure center. Six percent are in a tropical cyclone's inner core, i.e., within 100 km of the center. In contrast, a full 44% of profiles are within 500 km of the center of a tropical depression or tropical storm. This 44% occurs within 7 named systems. The 44% is approximately equally divided between the inner core and the rain bands. Even after normalizing by their relative frequency, tropical depressions and storms are still a more favorable location for 17 km tall convective cells than are tropical cyclones. In the National Hurricane Center best track data for the years and months of this survey, there are 2.1 times as many days of tropical depressions and tropical storms as there are days of tropical cyclones.

The time of day of the 77 oceanic profiles reinforce the idea that they are truly oceanic convection, not continental convection that has somehow drifted over ocean. *Zipser et al.* [2006] show that intense oceanic convection has a broad peak in the first 12 hours of the day, while intense land convection has a sharp late afternoon peak. The

oceanic 17 km tall convection found in the survey has a broad peak in the first 12 hours of the day.

The actual occurrence of 17 km high convective cells is likely to be more frequent than is observed by the TRMM Precipitation Radar. The reason for the difference is that the Precipitation Radar does not continuously observe the entire Atlantic. Instead, the median revisit time for the Precipitation Radar is 2.5 days for locations between 10° and 30°N latitude (Figure 2.5, p. 38), where most of the 17 km tall cells are located over the North Atlantic. In addition, this section makes the reasonable assumption that tall convective cells have precipitation at their mature height for only 20 to 40 minutes [Kelley *et al.*, 2005]. The dissertation multiplies the observed frequency by 90 to 180 to estimate the true frequency with which 17 km high cells occur. This scaling factor is the

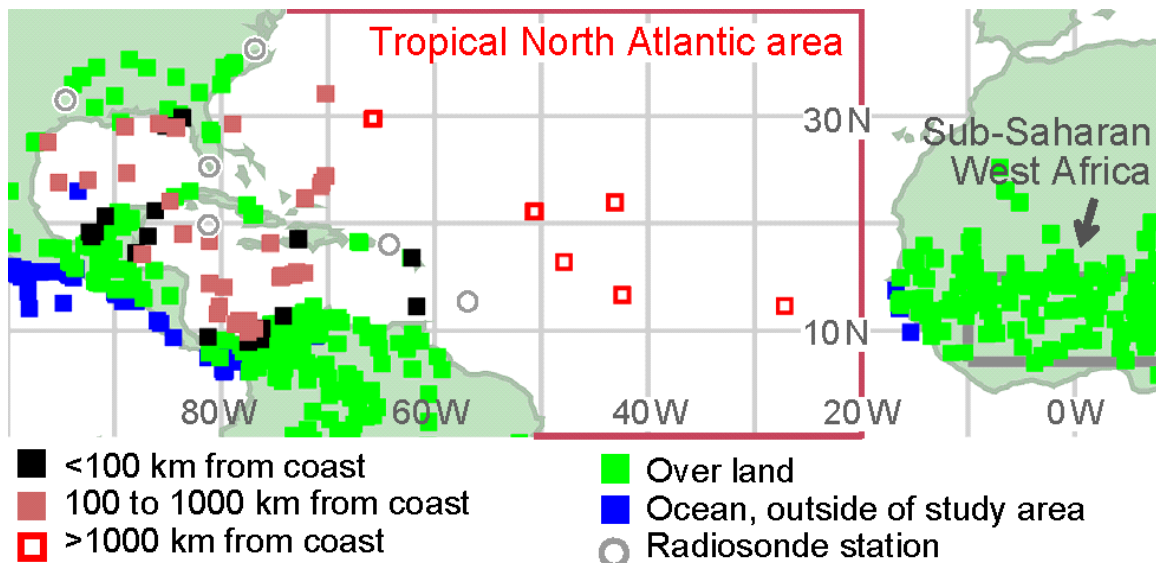


Figure 3.11. The locations of convective cells with a 20 dBZ signal at least 17 km high during July through October of 1998 to 2005

revisit time in days divided by the typical duration of a cell expressed as a fraction of a day. More specifically, the 77 cells observed over the North Atlantic during 8 hurricane seasons scale up to 7 to 14 cells occurring each day. A similar calculation suggests that 30 to 70 convective cells at least 17 km tall occur each day over sub-Saharan West Africa (7°–15°N, 10°W–10°E) using the TRMM Precipitation Radar's 3.0 day median revisit time for this latitude. The West Africa region is smaller than the North Atlantic region, so the difference in relative frequency of tall cells per square kilometer is even greater than the difference between the two stated frequencies.

3.9.3. Internal properties of extremely tall cells

Next, this section describes the internal properties of these extremely tall cells. Table 3.5 (p. 193) lists variables that describe various internal properties that are at least indirectly related to the updraft speed in the cells. Many of these variables were discussed in *Zipser et al.* [2006]. In fact, columns 8 and 9 of Table 3.5 were taken from the database described by *Zipser et al.* [2006] to facilitate comparisons between their work and this dissertation.

Most values in column 2 through 7 of Table 3.5 are based on a 30 km radius around the Precipitation Radar (PR) profile with a 17 km high signal. The 30 km radius is used because the various TRMM instruments examine the storm from different angles and the TRMM Microwave Imager (TMI) has coarse horizontal resolution. The 30 km radius is used for rows b through g, excluding row e, and in columns 2 through 7. When calculating one of these entries for Table 3.5, only the minimum or maximum of the

observations within 30 km of each profile is saved. Table 3.5 reports the 25th and 75th percentile of the distribution of these minimum or maximum values. The 40 dBZ height (row e) is measured along the same line of sight that contains the 17 km high 20 dBZ reflectivity (row a).

The first property to consider is the 20 dBZ height, shown in row a of Table 3.5. An equally high 20 dBZ signal in oceanic cells and African cells requires some explaining. Based on just the climatological tropopause height, one would expect African cells to be taller than oceanic cells. As discussed below, the climatological tropopause is only 13.0 to 14.5 km high over the tropical North Atlantic, while it is 14.5 to 15.0 km high over the sub-Saharan region of West Africa during July to October [Hoinka, 1999].

There are three possible explanations for how oceanic cells can reach the same 17 km height as African cells when the climatological tropopause is 0.5 to 2 km lower over the ocean. The first possible explanation is that the tropopause is elevated above the climatological mean in the neighborhood of these oceanic cells. This is a possibility (1) if most of the oceanic cells occur in mesoscale convective systems that have a chance over hours or days to elevate the tropopause, and (2) if most of the African cells do not occur in mesoscale convective systems.

The second possible explanation is that oceanic cells have more intense updrafts in the upper troposphere. If you take the climatological tropopause height as the level of neutral buoyancy, then North Atlantic convection reaching 17 km generally overshoots its neutral level by ~1 km further than African convection reaching the same 17 km

altitude. For each 1 km of overshooting, approximately 20 m/s of updraft speed is required at the level of neutral buoyancy [section 2.7.3, p. 71; *Djuric*, 1994, Appendix L]. A oceanic 20 dBZ signal at 17 km would then imply a ~2 km overshooting and a ~40 m/s updraft at the tropopause. The possibility of the upper tropospheric updraft speed being ~40 m/s will be mentioned again as other variables in Table 3.5 are examined later in this section.

When interpreting the 20 dBZ height, there is a third possible explanation. The third explanation is that the surface air over ocean could have a much higher equivalent potential temperature θ_e than does the surface air over Africa. Other things being equal, a higher θ_e would raise the level of neutral buoyancy by several kilometers (Figure 2.12, p. 121). Even if the African surface air were 7 K warmer than the ocean surface, the ocean surface air could still have a greater θ_e if the ocean surface air had at least 3 g/kg more moisture. Based on *Djuric* [1994, p. 72, equation 5-22], adding 1 g/kg of water vapor has the same effect on θ_e as a 2.5 K temperature increase (i.e., $2.5 = L_v / c_p = 2.5 \times 10^3 / 1004$). The ocean has fairly constant temperature (<6 C annual variation, *McGregor and Nieuwolt*, 1998, p. 46), but the oceanic boundary layer can be quite humid. For example, several studies use an 80% relative humidity at the ocean surface under a tropical cyclone [*Andreas and Emanuel*, 2001; *Houze*, 1993, p. 423].

In terms of lightning flashes (row d) and scattering by small ice hydrometeors (row b), 17 km tall cells are comparable whether they form over the North Atlantic (columns 2–4) or sub-Saharan West Africa (column 6). This region of Africa is known for frequently having intense convective cells [*Toracinta et al.*, 2002]. In fact, 17 km tall

North Atlantic cells have about the same amount of passive microwave ice scattering and lightning as do the much rarer African cells that are ≥ 18 km tall (column 7 of Table 3.5). Ice scattering is commonly estimated with the TRMM Microwave Imager (TMI) Polarization Corrected Brightness Temperatures (PCT) at 85 and 37 GHz [*Toracinta et al.*, 2002]. As a very rough guide, the colder the 85 GHz PCT relative to 273K [*Petty*, 1994], the more ice scattering is occurring. On the TRMM satellite, lightning is measured by the Lightning Imaging Sensor (LIS) [*Christian*, 2000].

The presence of small ice hydrometeors and lightning does not prove that oceanic 17 km tall cells have equally strong updrafts as do the African 17 km tall cells. Small ice and lightning do set a lower limit to the updraft speed, but that lower limit is a modest one. The updraft speed needs to exceed the hydrometeor fall speed by ~ 5 m/s for the hydrometeors to be carried several kilometers up during a reasonably short period of time. With a 5 m/s exceed updraft speed, the hydrometeor is carried up 1 km every 3 minutes.

For the 85 GHz ice scattering to be significant, there can 0.1 to 1.0 mm diameter ice in the mid and upper troposphere. Such an ice distribution could be accomplished by a ≥ 8 m/s updraft since 0.1 to 1.0 mm diameter ice has only a 2 to 3 m/s fall speed in the upper troposphere (Figure 2.13, p. 122). The 8 m/s updraft speed assumes the 5 m/s offset described in the previous paragraph. Lightning requires the presence of hail at least a kilometer or so above the freezing level, but small hail has a ~ 15 m/s fall speed (Figure 2.13). An updraft of 20 m/s would be sufficient to form hail of this size, and this 20 m/s updraft only needs to extend to the mid-troposphere.

Oceanic and African cells can also be compared using the cloud height and surface rain rate observed by the TRMM satellite (rows f and g of Table 3.5). *Zipser et al.* [2006] have warned about the accuracy issues of surface rain rate observed by the TRMM Precipitation Radar under tall storms and about the very loose connection between cloud height and updraft strength. Nonetheless, the cloud height and surface rain rate provide at least some information about tall cells.

Cloud-top height is here estimated using the 11 micron brightness temperature (T_b) of the TRMM Visible and Infrared Scanner (VIRS). The 180 K to 190 K brightness temperatures reported here are not errors. *Ebert and Holland* [1992] reported an even lower 11 micron T_b of 173 K (i.e., -100 C) in the eyewall of a tropical cyclone a few hours after a two day period of wind intensification. The 11 micron temperature ranges for both oceanic and African 17 km tall cells are an impressive 10 to 20 K colder than the coldest point in the climatological temperature profile. Figure 2.12 (p. 121) shows 203 K as the coldest point in the North Atlantic climatological profile for July through October based on NCEP climatology (section 2.7.2, p. 66). *Hoinka* [1999] reports that the lapse rate tropopause temperature is 202–212 K in the tropical North Atlantic.

The 10 to 20 K cloud-top temperature depression can have two explanations. The first possible explanation is that the tropopause in the neighborhood of the cells could be temporarily elevated by several kilometers and therefore colder than the climatology by 10 to 20 K. As mentioned previously in the interpretation of the 20 dBZ signal, the first explanation is relevant in mesoscale convective systems that have lasted several hours to several days. Based on the single overflight from the TRMM satellite, it is difficult to

evaluate the possibility of an elevated and cooled tropopause in each case of a 17 km tall cell. The second possible explanation is that the tropopause temperature equals the climatological value and the tall cells have very vigorous updrafts causing them to overshoot their level of neutral buoyancy by several kilometers.

With a dry adiabatic lapse rate of 8 K/km in the upper troposphere [*Folkins*, 2002] and a climatological tropopause temperature, it would require approximately 2 km of overshooting to produce the observed 10 to 20 K cloud-top temperature depression. A 2 km overshoot would require approximately a 40 m/s speed updraft at the level of neutral buoyancy [section 2.7.3., p. 71; *Djuric*, 1994, Appendix L]. A 40 m/s updraft was considered in the earlier interpretation of the 17 km tall 20 dBZ signal, while the interpretation of the lightning signal only required a ≥ 20 m/s updraft.

The third possibility mentioned in connection with the 17 km tall 20 dBZ signal cannot be used to explain the 10–20 K cloud-top temperature depression. More specifically, in the absence of overshooting, the observed temperature cannot be colder than the coldest point in the background temperature profile no matter how warm the surface θ_e is.

The surface rain rate can be estimated using the TRMM Precipitation Radar but is subject to large errors due to attenuation inside of tall convective cells. Nonetheless, the surface rain rate for most 17 km tall oceanic cells appears to be almost double the rain rate seen for most 17 km African cells. If the updraft speeds and surface temperatures were comparable, then the higher surface rain rate in oceanic cells would imply at least a somewhat higher water vapor mixing ratio in surface air flowing into the bottom of

oceanic cells. It likely that African cells have higher updraft speeds and surface temperatures (since the diurnal range of temperature is greater over land than over ocean), which would mean that the ocean cells would need to have a much higher water vapor mixing ratio in order to create the high surface rain rates observed.

To ignore the factor of two difference in the surface rain rate of oceanic cells vs. African cells, one could assume that instrument error is the cause, since it is known that surface rain rates are less reliable in tall systems observed by the TRMM Precipitation Radar. However, instrument error is hard to believe in this situation because it would be necessary to explain why there should be a high bias in the attenuation corrected radar reflectivity under tall oceanic cells compared with under tall African cells. A rough estimate suggests that it would be necessary to assume a 4.7 dB high bias in radar reflectivity to get rid of the factor of two difference in the observed surface rain rates R . The author knows of no paper that has asserted such a large bias. This 4.7 dB estimate can be calculated from the TRMM 2A25 algorithm's initial estimate of the Z-R relationship for convective rainfall below the freezing level (Table 2.2, p. 56):

$$4.7 \text{ dB} = 10 \log_{10} \frac{(2R)^{1.55}}{R^{1.55}} = 10 \log_{10} (2^{1.55}) \quad (3.11)$$

Oceanic 17 km tall cells that are more than 1000 km away from shore (column 4 of Table 3.5) generally have less lightning than other oceanic 17 km tall cells. This fact might imply that the cells over 1000 km from shore are less intense, but all of the other variables in Table 3.5 suggest that cells over 1000 km from shore have comparable intensity to the other oceanic cells. The cells over 1000 km from shore might be the only

"pure" oceanic ones because *Petersen and Rutledge* [2001] find that continents can influence the properties of convection within 1000 km of shore. The locations of the "deep ocean" cells are indicated by open red squares in Figure 3.11 (p. 181).

The 40 dBZ echo height is the only variable in Table 3.5 that strongly suggests that 17 km North Atlantic cells have less intense updrafts than 17 km cells over sub-Saharan West Africa. The 40 dBZ echo height is about 3 km lower in oceanic cells. Keep in mind Table 3.5 only gives an estimate of the 25 to 75th percentile range for each variable. It is possible for oceanic cells to occasionally have significantly higher 40 dBZ echo heights than listed in Table 3.5. For example, *Halverson et al.* [2007, p. 875] report a 15 km tall 40 dBZ echo in a tall eyewall cell in Hurricane Emily (2005).

Intense updrafts can increase the distance that the 40 dBZ echo height exceeds the freezing height, which is often near 5 km in the Tropics (See section 2.1.7, p. 23, and *Gilmore and Wicker*, 2002). While the 40 dBZ height suggests that 17 km tall African cells have more intense mid-tropospheric updrafts than do oceanic 17 km tall oceanic cells, these oceanic cells appear to have sufficiently strong mid-tropospheric updrafts to form small hail. The evidence for small hail is that the oceanic cell's 40 dBZ height is 6 to 9 km, which is 1 to 4 km above the climatological freezing height. A common indicator for small hail (~5 mm diameter ice) is that the 40 dBZ height be approximately 1 km above the freezing level [*Doviak and Zrnica*, 1993, p. 229] which requires a ~20 m/s updraft speed (Figure 2.13, p. 122). Similar reasoning was given when interpreting lightning observations earlier in this section.

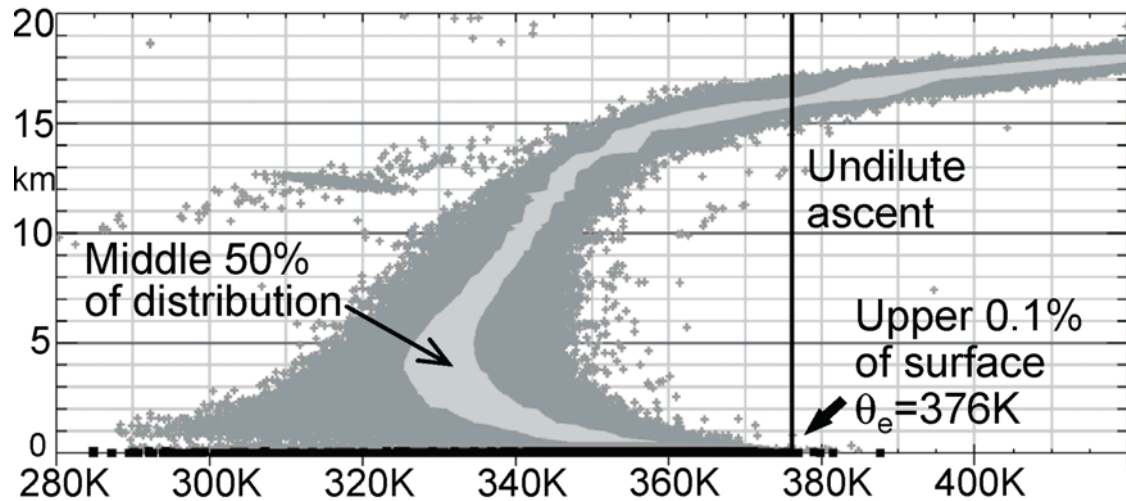


Figure 3.12. The observed distribution of θ_e (K) including heat of fusion. The observations comes from the six coastal radiosonde locations shown in Figure 3.11

3.9.4. Discussion

Having found and described a population of extremely tall convective cells, the last remaining task is to consider how these cells are possible physically. Convective cells that avoid entraining mid-tropospheric air (i.e., "undilute" cells) can have very intense updrafts (Table 2.4, p. 74). Oceanic convection, however, is expected to be dilute and contain weak updrafts [Zipser, 2003; Kuang and Bretherton, 2006]. Hendricks *et al.* [2004, p. 1214] state that some but not all tall cells have a low-level mesovortex associated with them. According to Hendricks *et al.*, the presence of a mesovortex reduces the entrainment of background air in the cell's updraft. A rough way to address the question of entrainment is to look at the climatological range of thermodynamic profiles in the neighborhood of these oceanic cells. This thermodynamic method comes

to the qualitative and very tentative conclusion that 17 km tall convective cells may be close to undilute when they occur over the North Atlantic and outside of tropical cyclones.

The degree of dilution cannot be calculated for the 17 km tall convective cells that TRMM observes over the North Atlantic. The reason why is that the TRMM satellite does not measure the temperature profile. Faced with this obstacle, the dissertation looks at the range of temperatures profiles observed with radiosondes at the six coastal sites indicated in Figure 3.11 (p. 181) during the months of this survey. *Free et al.* [2004] use radiosondes released over oceanic islands in a similar way to estimate the vertical profile of temperature where tropical cyclones exist.

Figure 3.12 is a scatter plot of ~1000 profiles of equivalent potential temperature (θ_e) calculated from operational radiosondes. *Zipser* [2003] shows the importance of heat of fusion, so the dissertation modifies *Bolton's* [1980] formula for θ_e by assuming that all water vapor condensing at or above the 0 C isotherm freezes before falling out of the column. Figure 3.12 is analogous to Figure 3 of *Jensen and Del Genio* [2006].

One way to use Figure 3.12 is to trace a vertical line up from near the "hot" limit of the tropical North Atlantic surface θ_e distribution. This vertical line approximates θ_e of an air parcel undergoing undilute ascent. Most of the time, such undilute ascent would reach its level of neutral buoyancy around 16 km and possibly the air parcel would be moving so fast that it would overshoot to 17 or 18 km. In contrast, if a volume of surface air were significantly diluted with, for example, two volumes of mid-tropospheric air, then the line of ascent would bend to the left in Figure 3.12. An air parcel diluted this

much would have a neutral level below 16 km, a slower updraft speed, and a smaller overshoot distance. Because radiosondes and dropsondes rarely cover a 17 km altitude range inside of tropical cyclones, it would be difficult to compile a plot similar to Figure 3.12 from tropical cyclone observations.

This section has located examples of extremely tall convective cells and presented information that suggests that they are physically possible if convection is near undilute. This examination, however, is merely a survey that leaves to others the careful examination of each of these unusually tall cells.

Zipser [2003] stated that "undilute ascent in equatorial oceanic cumulonimbus is extremely rare, and if found, would constitute a special case requiring some special explanation." The only exception that *Zipser* [2003] gave was near undilute ascent in tropical cyclone eyewalls, which has been observed often enough to require no special explanation. This survey, however, finds that most 17 km tall oceanic cells occur outside of tropical cyclones. To reconcile *Zipser's* comments with this survey, one could speculate that, before the launch of the TRMM satellite, tall oceanic cells outside of tropical cyclones were under sampled. The TRMM satellite collects an unbiased sample of observations of intense convection. In contrast, only North Atlantic tropical cyclones are routinely sampled by aircraft, not random intense convective storms over the North Atlantic.

Table 3.5. Convective cells identified by the maximum height of their 20 dBZ radar reflectivity during July to October in 1998 to 2005 ^a

1. TRMM satellite observations	Convective cells over the tropical North Atlantic, >100 km from shore				Convective cells over sub-Saharan West Africa ^c		Mesoscale precipitation features in the Tropics ^d	
	2. Tall cells in named systems	3. Tall cells outside of named systems	4. Tall cells >1000 km from shore	5. "Short" cells ^b	6. Tall cells	7. Very tall cells	8. 1% most intense	9. 0.1% most intense
a. PR 20 dBZ height (km)	≥17	≥17	≥17	14.5–15.0	≥17	≥18	≥13.75	≥16.5
b. TMI 85 PCT (K) minimum	60–72	60–109	62–72	144–179	69–95	66–94	≤160	≤106
c. TMI 37 PCT (K) minimum	173–208	155–232	175–207	252–267	175–216	145–210	≤255	≤221
d. LIS lightning (flash/minute)	11–66	4–42	11–17	0–2	17–38	15–33	≥3	≥33
e. PR 40 dBZ height (km)	6.3–9.7	5.8–9.4	6.0–9.5	4.5–5.6	8.2–14.2	10.8–16.0	≥6.5	≥10.25
f. VIRS 11μm Tb (K) minimum	182–190	181–187	185–190	193–199	181–184	180–183	≤196	≤185
g. PR surface rain rate (mm h ⁻¹) maximum	41–155	34–80	50–300	21–50	26–51	22–46	—	—
h. PR profiles (count)	41	36	20	59	308	44	—	—
i. Continuous regions (count) ^e	16	24	7	59	114	28	—	—

^a The column names and row names of Table 3.5 are defined in section 3.9. In columns 2 to 7, the ranges state the 25th and 75th percentile by Precipitation Radar profile. ^b Inside 15°N to 30°N and 80°E to 30°E and at least 100 km away from any other ≥14.5 km tall cell. ^c For cells ≥17 km tall, the 7°N to 15°N and 10°W to 10°E region is used, but for the much rarer cells that are ≥18 km tall, a wider longitude range of 20°W to 30°E is used in order to have a larger sample. ^d Columns 8 and 9 come from Figures 2 and 3 of Zipser *et al.* [2006] and related calculations (Daniel Cecil, private communication, 2006). During seven years, the 0.1% or 1% most intense features observed by TRMM anywhere in the Tropics have values in the ranges given by columns 8 and 9. ^e A "continuous" region is either an isolated profile or a group of profiles whose centers are separated by 8.5 km or less.

4.

Correlation examined with ground-based observations

This chapter uses ground radar data to test if frequent occurrence of tall eyewall cells is associated with increases in a tropical cyclone's wind intensity. The test is carried out with the National Weather Service's (NWS) WSR-88D ground radars. WSR-88D stands for Weather Surveillance Radar - 1988 Doppler [*Heiss and McGrew, 1990*]. A ground radar collects a 3D scan approximately every 5 minutes, and the scan is called a "volume scan."

Compared with satellite radar, a ground radar has the advantage of near continuous observation of a tropical cyclone and the disadvantage of coarser vertical resolution. In this chapter, the disadvantage of coarse vertical resolution is overcome using the ground radar's good time resolution and using the height threshold from the previous chapter's analysis of TRMM data. More specifically, the height threshold from the previous chapter defines tall convection as convection with a 20 dBZ signal at least 14.5 km high.

Whereas a satellite radar only requires a height threshold to define "tall" eyewall cells, the ground radar requires both a height and a frequency threshold to define "frequent" tall cells. In this context, the frequency is the fraction of a ground radar's 3D scans that contain tall eyewall cells.

Instead of trying to infer wind intensification from cell height, it is tempting to try to measure the tropical cyclone's wind intensity directly using a ground radar's doppler winds measurements. The direct approach, however, has many pitfalls [*Harasti et al.*, 2004]. One difficulty with the direct approach is that doppler wind measurements have a more limited range than the radar reflectivity measurements that can be used to estimate cell height. Doppler wind measurements are made up to 230 km away from the radar and are best within 150 km of the radar [*Lee et al.*, 1999], while reflectivity measurements can be made up to 400 km away from the radar. Second, doppler radars only measure the component of wind along the line of sight. For this reason, it is computationally difficult to derive the wind speed all of the way around the eye from a single doppler radar without making the gross assumption that the winds are symmetric around the eye [*Reasor et al.*, 2000; *Marks et al.*, 1992]. In the rare situation that two doppler radars are in range, the problem becomes better determined [*Roux and Marks*, 1996]. Third, tropical cyclone wind speeds can easily exceed the maximum measurable doppler wind speed [*Rinehart*, 1997, p. 104]. The WSR-88D handbook states that with the default settings, the fastest observable wind speed is 123 kt, which is a wind speed achieved by category 4 tropical cyclones [Part C, section 5.5.2]. Another limitation of doppler wind measurements is that operational weather radars can only measure the velocity of rain

drops and ice particles in eyewall clouds. The clouds generally start at least 1 km above the ocean surface, whereas wind intensity measurements are supposed to be made at a 10 meter height [*Franklin et al.*, 2000; *NOAA*, 2007, p. 1-31]. Wind speed drops off sharply by a hard-to-define amount in the bottom 1 km of the atmosphere in a tropical cyclone eyewall [*Franklin et al.*, 2003b; *Simpson*, 2003, p. 158].

Ignoring doppler wind measurements, one could still try to directly estimate wind intensification by tracking the radar reflectivity of convective cells as they move around the eyewall. Estimating wind intensity by tracking cell motion also has pitfalls that severely limit its practicality. The big complication is that precipitation cells in the eyewall are often too close together to track individual cells. For example, it would be difficult to come up with an accurate estimate of tropical cyclone intensity by tracking the eyewall cells shown in Figure 4.10 (p. 227).

As has just been discussed, wind intensity cannot be directly measured by ground radars. This fact motivates the research in this chapter, which is an attempt to find an indirect way to identify the periods of wind intensification using ground radar observations. The "ground truth" wind intensity values used in this chapter are the best track estimates that the National Hurricane Center (NHC) generates from a variety of data sources in post-hurricane-season analysis (section 3.1, p. 134). Even the best track wind intensity may have errors of 10 to 15 knots according to *Bankert* [2002] or 6 knots according to *Franklin* [2005, Table 11].

4.1. Calculating height, area, and eyewall location

The first preparatory step is to calculate the height of each data volume. Second, the horizontal area covered by each data volume is calculated. Last, the location of the tropical cyclone eyewall is determined in each 3D volume scan.

Before describing the preparatory steps for analyzing ground radar data, an introduction to radar terminology is useful. A 3D volume scan requires about 5 minutes to collect. During that time, the radar antenna rotates about 12 times around, each time at a different elevation angle. Each rotation at a particular elevation angle is called a sweep. At each point in a sweep, data is collected along a line of sight going away from the radar. Each line of sight is called a ray. A ray is a beam of transmitted energy with a beam width of approximately 1 degree both in the vertical and horizontal direction. Each measurement along a ray is called a data volume. The data volume is a cylinder 1 km thick along the ray and increasing in radius for data volumes further away from the radar. There are approximately 12 sweeps per volume scan, 360 rays per sweep, and 460 data volumes per ray. In total, a 3D volume scan contains approximately two million data volumes.

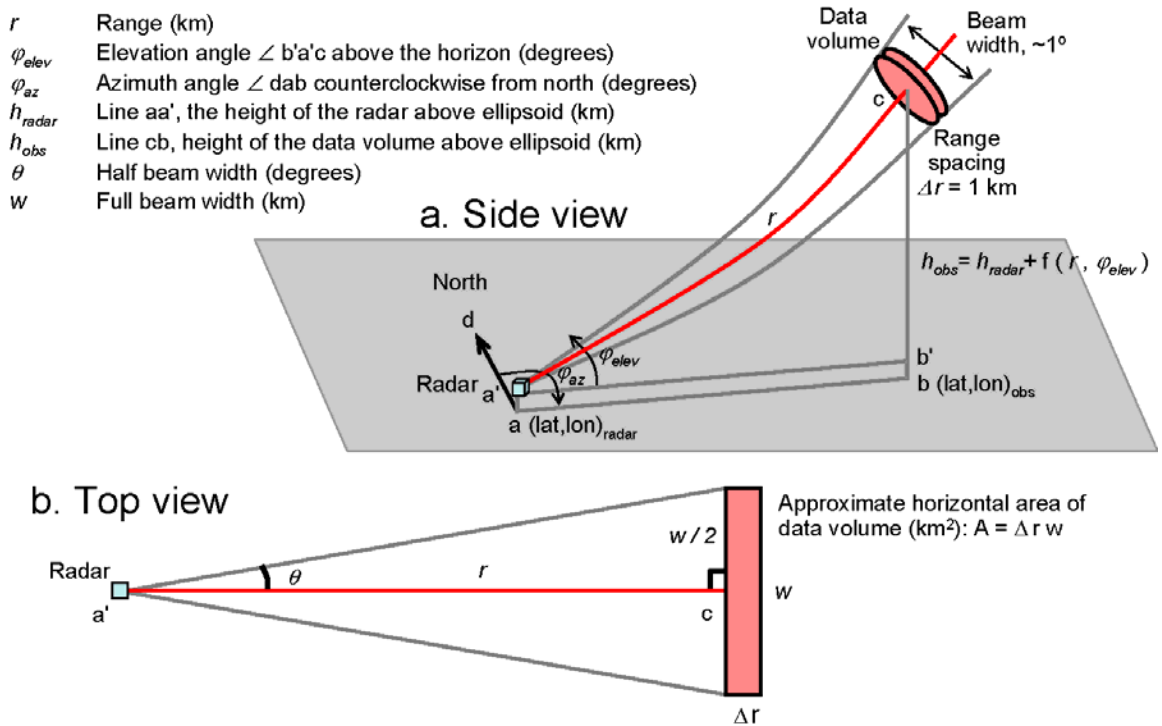


Figure 4.1. Schematic diagram of the observation geometry of a weather radar on the ground. (a) The side view shows the geometry for calculating the height h_{obs} of the data volume. The ground radar data archive contains values of the radar height h_{radar} , radar location $(lat, lon)_{radar}$, data volume distance r along the line of sight, elevation angle φ_{elev} , and azimuth angle φ_{az} . From this information, the dissertation calculates the height h_{obs} and location $(lat, lon)_{obs}$ of each data volume using the formulas given in section 4.1. (b) The top view shows the geometry for estimating the horizontal area A covered by the data volume.

Other terms for "data volume" are "range gate" and "data point." "Range" is a common term for the distance from the radar to the center of a data volume. The radar easily determines range because the time that a signal takes to travel from the radar to the data volume and back is precisely measured and the speed of propagation is close to the speed of light.

The radiation in a ground radar's line of sight travels in a curved line due to the atmosphere's density profile decreasing exponentially with height [Rinehart, 1997, p. 62].

When the height of the beam is plotted against distance along the Earth's surface, an additional amount of upward curvature in the beam is due to the Earth's surface falling away from the beam because the Earth is a sphere.

In the previous chapter, the line of sight of the TRMM satellite radar is assumed to be a straight line. This is a good approximation for a satellite radar because, except for the last 10 km of the distance to the Earth, the atmosphere has negligibly little density. The author knows of no study that quantifies a bend in the TRMM Precipitation Radar's line of sight. In contrast, a ground radar's beam may travel through several hundred kilometers of the dense lower atmosphere before reaching precipitation. Because the ground radar's beam is traveling almost parallel to the ground, the curvature of the path has little effect on the latitude and longitude below the data volume. However, the curvature does have a significant effect on the height of the data volume. The widely used standard for determining the height h_{obs} of a radar beam is called the standard propagation formula (equation 4.1; *Rinehart, 1997, p. 62*).

For ground radars, the height, latitude, and longitude of a data volume have to be calculated from the location of the radar, the orientation of the radar antenna, and the distance along the line of sight between the antenna and the data volume (Figure 4.1).

The quantities necessary for this calculation are the following:

h_{radar}	= Height of the radar above Earth ellipsoid (km)
lat_{radar}	= Latitude of the radar (degrees N)
lon_{radar}	= Longitude of the radar (degrees E)
φ_{az}	= Azimuth angle of the antenna clockwise from north (degree)
φ_{elev}	= Elevation angle of the antenna up from horizontal (degree)
r	= Range, i.e., distance along the line of sight between the antenna and the data volume (km)
r_{earth}	= Earth's radius (km)

The first calculation is the standard propagation formula for the height h_{obs} of the data volume. Next, the Pythagorean Theorem is used to estimate the horizontal distance d_{horiz} along the Earth ellipsoid between the radar antenna and the point directly below the data volume:

$$\begin{aligned} r_0 &= \frac{4}{3} r \\ h_{obs} &= h_{radar} + \sqrt{r^2 + r_0^2 + 2 r r_0 \sin \varphi_{elev}} - r_0 \\ d_{horiz} &= \sqrt{r^2 - h_{obs}^2} \end{aligned} \quad (4.1)$$

In equation 4.2, the distance west-east and south-north in kilometers (Δx , Δy) is calculated between the radar and the point directly below the data volume:

$$\begin{aligned} \Delta x &= d_{horiz} \sin \varphi_{az} \\ \Delta y &= d_{horiz} \cos \varphi_{az} \end{aligned} \quad (4.2)$$

In equation 4.3, the conversion factors k_{lat} and k_{lon} are found for converting kilometers into degrees latitude and longitude. The cosine factor in the calculation of k_{lon} comes from the fact that the Earth is, to a first approximation, a sphere. The latitude and longitude of the data volume (lat_{obs} , lon_{obs}) are calculated using these conversion factors in equation 4.3:

$$\begin{aligned} k_{lat} &= \frac{360^\circ}{2\pi r_{earth}^2} \\ k_{lon} &= k_{lat} \cos lat_{radar} \\ lat_{obs} &= lat_{radar} + \Delta y k_{lat} \\ lon_{obs} &= lon_{radar} + \Delta x k_{lon} \end{aligned} \quad (4.3)$$

The horizontal area A_{horiz} covered by a ground radar data volume increases linearly with distance r from the radar (Figure 4.1b). Equation 4.4 for horizontal area takes advantage of the following two facts. First, the radar beam is very narrow (0.95 degrees), so the data volume can be approximated as a cylinder with its axis pointing toward the radar. Second, the radar beam is close to parallel to the ground, so the horizontal central cross section of the cylinder is approximately a rectangle.

$$\begin{aligned} w &= 2 r \tan \theta \\ A_{horiz} &= \Delta r \cdot w \end{aligned} \tag{4.4}$$

In equation 4.4, the half beam width in degrees is θ and the full beam width in kilometers is w . The horizontal cross section calculated in equation 4.4 should be considered only an approximation because the signal strength of the beam varies with a Gaussian distribution in all three dimensions [Rinehart, 1997, p. 31].

Locating the tropical cyclone's eyewall in ground radar data is a little more complicated than when using the TRMM satellite radar because a ground radar collects dozens of volume scans of a single tropical cyclone, too many volume scans to locate the eyewall manually in each. The National Hurricane Center's best track database reports the center location only once every six hours, so the best track data cannot precisely locate the center of the eye every 5 minutes.

For this reason, the author wrote software to manually locate the eyewall. To start, the software generates an image similar to one panel of Figure 4.10 (p. 227). The author then clicks on the image three times, and the software interprets those clicks as the center of the eye, a point on the inner radius of the eyewall, and a point on the outer

radius of the eyewall. The author manually locates the eyewall for one volume scan in ten, and then, the software replays the sequence of all volume scans. The interpolated location of the eyewall is displayed for each volume scan, allowing the author to verify that the eyewall location is correct.

4.2. The agreement between coincident satellite and ground radar observations

The next step in the analysis is to verify that ground radar observations are similar to the TRMM satellite radar observations when they observe the same tropical cyclone eyewall at close to the same time. No list of these rare events has been published. The author sifted through TRMM eyewall overflights near the U.S. coast to find simultaneous satellite and ground radar observations. The author found four times that an eyewall with a tall eyewall cell was observed simultaneously by TRMM and a ground radar. These events are listed in Table 4.1 (p. 206), and their locations are shown in Figure 4.2.

Figure 4.5a (p. 222) shows a horizontal snapshot of Hurricane Alex (2004) as observed by the TRMM Precipitation Radar and two ground radars. The thin gray and thick black circles indicate locations where the TRMM Precipitation Radar detected a 20 dBZ signal at least 10 km or 14.5 km high, respectively. A 20 dBZ signal 14.5 km tall is the definition of a tall cell that was developed with TRMM satellite data in chapter 3. The blue and red shaded rectangles show observations from the WSR-88D radars located at Wilmington, North Carolina, and Morehead, North Carolina, respectively. As

indicated in the color bar at the bottom of the figure, the very light red and blue rectangles indicate a ground radar observation of 20 dBZ reflectivity at least 2 km tall. Precipitation just 2 km tall exists basically everywhere in the eyewall and rain bands but not in the eye. The medium red and blue rectangles indicate a ground radar observation of 20 dBZ reflectivity at least 10 km tall. The dark red and blue rectangles indicate a tall cell, i.e., a ground radar 20 dBZ height of at least 14.5 km. The TRMM radar and two ground radars are in general agreement that 14.5 km tall convection was occurring in the north side of Hurricane Alex's eyewall. The large black rectangle across the top of Figure 4.5a is the location used to generate the vertical cross section in Figure 4.5b.

Figure 4.5b is a vertical cross section of Hurricane Alex (2004). The data volumes in the large black rectangle in panel a are displayed in panel b as a function of their west-east location and height. Near the bottom of panel b, the thick black contour around a 6 km height is the 40 dBZ echo height observed by the TRMM Precipitation Radar. Near the top of panel b, the thick black contour around a 15 km height is the 20 dBZ echo height observed by the TRMM radar. The blue and red shaded rectangles show observations from the WSR-88D radars located at Wilmington and Morehead, respectively. As indicated by the color bar at the bottom of the figure, the light red and blue rectangles indicate a 20 dBZ reflectivity in the ground radar data. The dark red and blue rectangles indicate a 40 dBZ reflectivity in the ground radar data. The TRMM and ground radars are in general agreement about the location of the 20 dBZ and 40 dBZ signals.

Compared with the TRMM radar, the two ground radars appear to have a +3 km bias in their 40 dBZ height and a +2 km bias in their 20 dBZ height, which can be explained in two ways. Some of the high bias may be explained by the different observation geometries of satellite and ground radars. In connection with this idea, three facts will be discussed in turn: reflectivity has logarithmic units, radar reflectivity generally decreases with increasing height, and the ground and satellite radars have their data volumes oriented differently. A ground radar's ~3 km diameter and 1 km thick

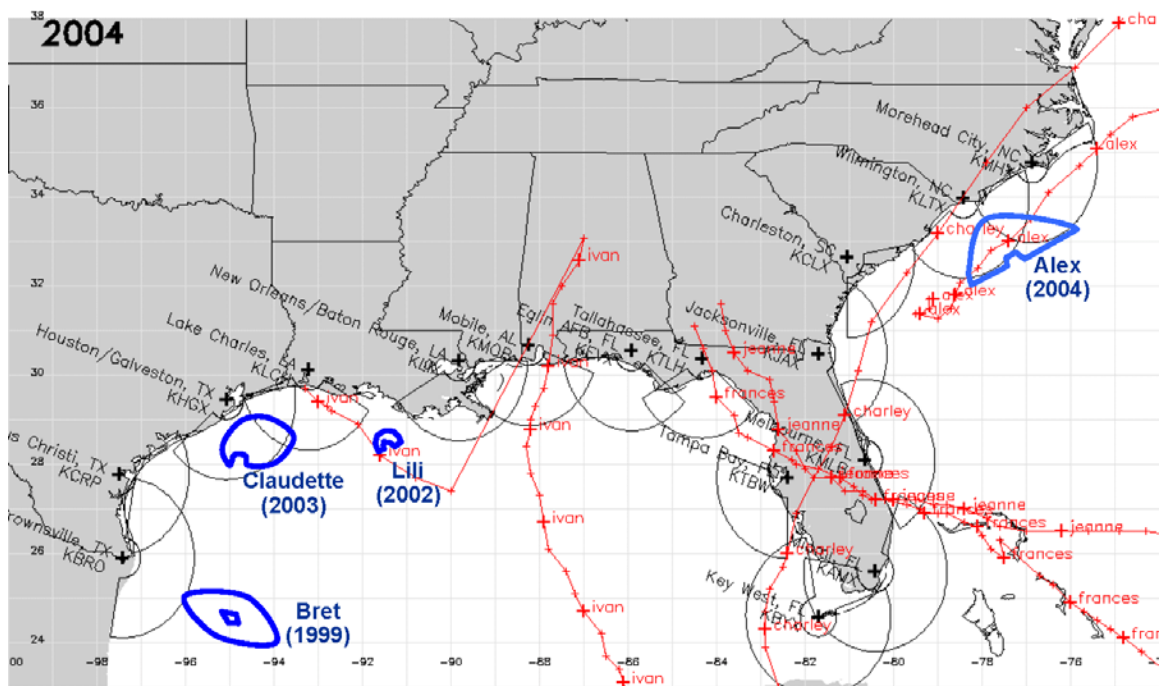


Figure 4.2. Ground radar coverage in the southeast U.S. and 2004 tropical cyclone tracks. The author generated figures such this one for each year from 1998 to 2004. The figures were used in the search for simultaneous TRMM radar and ground radar observations of a hurricane's eyewall. The locations of tracks for the year 2004 are shown in red. Locations of WSR-88D radars are identified by name, 4 letter call sign, and coverage arc. The coverage arcs go from 50 to 200 km from the radar. Reflectivity observations are available further out, to about 460 km away from the radar. A separate sequence of figures were generated for 1998 to 2004 (not shown) in the vicinity of the WSR-88D ground radar in Puerto Rico.

cylindrical data volume is oriented with its axis roughly parallel to the ground so the data volume covers a wide altitude range (~3 km) (Figure 2.7, p. 42). In contrast, the 5 km diameter and 250 meter thick TRMM Precipitation Radar data volume is oriented with its axis nearly vertical (Figure 3.1, p. 135), so the data volume covers a very narrow altitude range (~250 meters). A large dBZ value at the bottom portion of a data volume will basically determine the overall reflectivity of the whole data volume because dBZ values are logarithmic. For example, if you average 43 dBZ at the bottom half of a data volume with 23 dBZ at the top of the data volume, the average reflectivity signal in the data volume would be 40 dBZ:

$$\frac{43 \text{ dBZ} + 23 \text{ dBZ}}{2} \approx \frac{19,950 + 199.5}{2} \approx 10,075 \approx 40 \text{ dBZ} \quad (4.5)$$

The second explanation for the high bias in a ground radar's observed 40 dBZ height is that the actual 40 dBZ height may vary on horizontal scales too small to be fully resolved by either the ground or satellite radars. A ground radar can resolve a little more of the horizontal small-scale 40 dBZ fluctuations so at least some of the ground radar's 40 dBZ data volumes are higher in altitude than the TRMM radar's 40 dBZ data volumes.

Based on the four coincidence events mentioned in Table 4.1, the dissertation finds that the satellite and ground radars are in reasonable agreement with respect to the horizontal location and horizontal area of tall cells in the eyewall. The satellite vs. ground radar comparison discussed above is merely qualitative, but it has the advantage of being a comparison of tropical cyclone eyewalls containing tall cells. For a quantitative comparison of satellite and ground radar observations of rainfall in general, *Anagnostou et al.* [2001] show that various ground radars along the U.S. southeast coast

differ systemically in calibration from the TRMM Precipitation Radar by ± 2 dB. This is a fairly good agreement considering that the TRMM Precipitation Radar's accuracy is 0.8 dB [Kozu *et al.*, 2001; Takahashi, 2003; Heymsfield *et al.*, 2000].

Table 4.1. Tropical cyclone eyewalls with tall eyewall convection ($20 \text{ dBZ} \geq 14.5 \text{ km}$) observed nearly simultaneously by the TRMM Precipitation Radar and one or more WSR-88D ground radars. The intensity and intensity change values come from the National Hurricane Center's (NHC) best track database. The first two events are shown in Figures 4.5 and 4.6 (pp. 222 and 223). The wind intensity change (Δ intensity) is calculated by interpolating the NHC best track intensity to six hours after and before the TRMM overflight. The times of the TRMM overflight and closest WSR-88D volume scan are stated in Universal Time, in the hhmm:ss format.

Tropical cyclone, intensity, Δ intensity	lat, lon, date	TRMM overflight time, hhmm:ss	WSR-88D nearest time, hhmm:ss	WSR-88D name	WSR-88D city and state
Alex 70 +25 kt	33.0°N 77.4°W 03 Aug 2004	0409:46	0411:55 0413:26	KLTX KMHX	Wilmington, NC Moorehead, NC
Claudette 65 +15 kt	27.9°N 94.6°W 15 Jul 2003	0700:15	0657:36 0658:30	KHGX KCRP	Houston, TX Corpus Christi, TX
Lili 105 -45 kt	28.1°N 91.4°W 03 Oct 2002	0705:00	0701:49	KLIX	New Orleans, LA
Bret 100 -40 kt	26.9°N 97.4°W 21 Aug 1999	2245:51	2243:49	KBRO	Brownsville, TX

4.3. Time-azimuth plots

To find cases when a tropical cyclone passed within range of a WSR-88D ground radar along the U.S. coast, the first step is to plot storm tracks (Figure 4.2). For a tropical cyclone that appears within range of a ground radar, the author looks for that case in the NCDC level II archive of WSR-88D radar data. Often the data was not collected for that period because severe weather often disables WSR-88Ds [Gratz, 2005, p. 17; Crum and Smith, 2007]. For the cases that do have data in the archive, the 3D volume scans are downloaded and selected volume scans are examined to verify that the entire eyewall is observed. Then, the eyewall location is determined using the method described in section 4.1.

The next step in the analysis is to use a time-azimuth plot to decide which volume scans in each case should be included in the later analysis steps. To generate a time-azimuth plot, first calculate the 20 dBZ echo height everywhere in the eyewall. Then, divide the eyewall into 100 sectors based on the azimuth angle. Calculate the maximum 20 dBZ height in each sector. The azimuth angle of each sector determines its location on the vertical axis of the time-azimuth plot. The time that the volume scan was observed determines its location on the horizontal axis. A tall eyewall cell circling counter clockwise around the eyewall would appear, in a time-azimuth plot, as a streak of convection moving diagonally upward.

For example, consider the 20 dBZ height of Hurricane George's (1998), as shown in the first panel of Figure 4.7 (p. 224). These WSR-88D observations were collected on

25 September 1998, as indicated in the x axis label of the panel. The horizontal axis shows observations from 5 UT to 23 UT on that day, with the axis labeled with the day of month and hour of day. The vertical axis states the azimuth angle clockwise around the eye with 0° pointing north and 180° pointing south. In the panel, the 20 dBZ height is shaded with light gray indicating a 5 km height, dark gray indicating a 10 km height, and black indicating a 14.5 km height. The panel shows that tall eyewall cells exist on the east side of the eyewall.

To aid in selecting which volume scans to include, several bars appear on the top of the panels in Figures 4.7 through 4.9. When the tropical cyclone eyewall is over land, a green bar is plotted over the panel. When the NHC best track data indicate wind intensification or weakening, a red or blue bar is plotted over the panel. Intensifying and weakening periods are never included in the same event in this chapter. Instead, intensifying and steady periods can be combined to form one "intensifying" period. Weakening and steady periods can be combined to form one "non-intensifying" period. When the ground radar fails to collect any scans, there is a blank region in the plot, such as from 19 UT to 22 UT in the case of Hurricane Georges (1998) in the first panel of Figure 4.7.

Based on the above mentioned considerations, the time period for each event is selected. In the case of Hurricane Georges, the period starts around 7 UT after the eyewall left Cuba (where the green bar ends in Figure 4.7) and extends through the continuous observations prior to the data gap at 19 UT. The chosen period is indicated

with the black bar. The bar is labeled as "inten" to indicate that this period is considered a period of wind intensification in subsequent analysis.

The same procedure is repeated for all of the intensifying cases in Figure 4.7 and all of the non-intensifying cases in Figures 4.8 and 4.9. These plots suggest that tall eyewall cells occur more frequently in intensifying tropical cyclones compared with non-intensifying tropical cyclones. This qualitative observation is made more precise in section 4.5, but first, section 4.4 takes one of the cases and compares the WSR-88D observations with near-continuous observations from other instruments.

4.4. Case study of one tropical cyclone

In this section, a case study is performed on Hurricane Georges (1998), one of the tropical cyclones displayed in the time-azimuth plots discussed in the previous section. In this section, the ground radar data is compared with near continuous observations of the eyewall's infrared brightness temperature (T_b) and eyewall lightning strikes. In addition, the eyewall's strong radar reflectivity (40 dBZ) at low altitudes is compared with its weak radar reflectivity (20 dBZ) at high altitudes.

While infrared observations are usually available only every 30 minutes, the GOES satellites occasionally go into a rapid scan mode in which data is collected every 15 minutes for a severe weather event. Rapid scan infrared observations happened to be collected during a 9 hour period when Hurricane Georges was within range of the WSR-

88D ground radar at Key West, Florida. Continuous lightning observations are made over the continental United States by the network maintained by the Vaisala corporation for the National Weather Service. The network can triangulate lightning off the U.S. coast with reduced spatial accuracy and detection efficiency. This lower quality performance is adequate for this study because the tropical cyclone was only a few hundred kilometers off the coast.

The comparison of the radar, infrared, and lightning observations is shown in Figure 4.3. Everything appears consistent between the radar, infrared, and lightning observations. At the time of observation, the east side of Hurricane George's eyewall experienced a convective burst, i.e., a persistent mesoscale region of convective precipitation [Heymsfield *et al.*, 2001]. This convective burst occurred during a period of wind intensification: from 34 m/s (65 kt) at 6 UTC on September 24 to 46 m/s (90 kt) at 12 UTC on the next day.

In Hurricane Georges, tall eyewall cells with a 20 dBZ WSR-88D signal at least 14.5 km high often have cold infrared cloud tops, lightning strikes, and strong precipitation near the freezing level. Figure 4.3a shows that the infrared cloud-top temperatures are below 193 K for one portion of George's eyewall for a period of several hours, 7 UT to 15 UT. The 193 K threshold was used in the previous chapter for identifying tall convection in the eyewall (See Figure 3.6a, p. 157). Figure 4.3b shows the 20 dBZ height using the same kind of time-azimuth plot just described in the previous section. In Figure 4.3c, the lightning detection efficiency for Hurricane Georges is around 40% because the tropical cyclone was south of the Florida Keys [Cummins *et al.*,

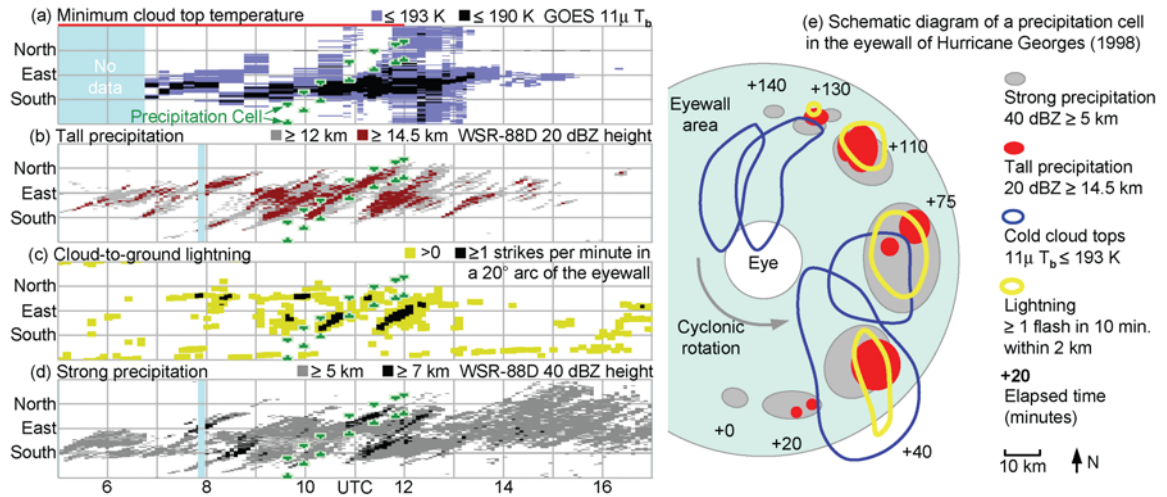


Figure 4.3. Time-azimuth plots of the eyewall of Hurricane Georges on 25 September 1998. This figure appears in *Kelley et al.* [2005]. Observations were made by the GOES satellite (a), the National Lightning Detection Network (NLDN) (c), and the WSR-88D radar at Key West, Florida (b and d). The vertical axis states the azimuth angle clockwise around the center of the hurricane. The time-azimuth plots include data observed 15 to 75 km from the center of the eye. The red bar at the top of panel a indicates when the hurricane's winds were intensifying according to the NHC. The schematic diagram in panel e shows the evolution of a precipitation cell that formed in the eyewall at 0940 UTC. The green brackets in panels a through d correspond to the cell shown schematically in panel e. Panel e can also be thought of as a simplified version of the observations in Figure 4.10.

1998]. In Figure 4.3d, the distinction between 5 km and 7 km altitudes should be considered approximate because the WSR-88D pixels cover a 2.5 to 3.5 km altitude range.

4.5. Selection of cases for further analysis

The next step in the analysis is to select which cases will be used and which volume scans will be analyzed in each case. The cases must see all of the eyewall during at least a three hour period and the eyewall must not make landfall during this period. The

dissertation establishes this requirement because tropical cyclone intensification is rare over land even though vigorous eyewall precipitation can be triggered when the eyewall encounters mountains or land/ocean gradients in surface friction and thermodynamic variables [Geerts *et al.*, 2000]. In each radar volume scan, the dissertation defines "tall" cells as locations with at least a 20 dBZ reflectivity and a pixel center at least 14.5 km high using the same height threshold as chapter 3.

The dissertation linearly interpolates the maximum sustained surface wind intensity from the estimates that the National Hurricane Center (NHC) provides every six hours to estimate the wind intensity at the start and end of each radar observation period. This six hour reporting interval prevents the dissertation from detecting wind fluctuations on shorter than six hour time scales or from determining if the wind increase occurs before, during, or after the tall eyewall cells.

4.6. Statistical summary of cases

The dissertation divides all WSR-88D volume scans into two populations: the 1224 that belong to intensifying tropical cyclones and the 1323 that belong to non-intensifying tropical cyclones. Figure 4.4a shows the Cumulative Distribution Functions (CDFs) for these two populations.

The CDFs of WSR-88D near-land North Atlantic tropical cyclone observations can be compared with CDFs calculated from TRMM Precipitation Radar overflights of

tropical cyclones world-wide. The non-intensifying WSR-88D CDF stays close to the non-intensifying TRMM CDF. However, the intensifying WSR-88D CDF has taller precipitation on average than the corresponding TRMM CDF. This difference might be caused by the tropical cyclones near land having different properties than the world-wide population of tropical cyclones. Alternatively, the difference might be caused by the different observation geometries of the WSR-88D and TRMM Precipitation Radar. Suppose that intensifying tropical cyclones contained narrow cells that had a 20 dBZ signal covering only a 5 km^2 horizontal area at a 14.5 km altitude. In that case, the WSR-88Ds narrow pixels (0.5 km x 2.5 km horizontally) could easily detect those cells while the TRMM Precipitation Radar's wider pixels (20 km^2 horizontally) would fail to detect them.

The dissertation develops a threshold for detecting tropical cyclone wind intensification using ground radar observations of the eyewall. This threshold is based on the frequency of tall eyewall cells. For a radar volume scan to be flagged as having tall precipitation in the eyewall, the eyewall must contain at least a 5 km^2 horizontal area with a 20 dBZ signal at least 14.5 km high. The dissertation does not try to count the number of precipitation cells because it is often difficult to distinguish between several adjacent cells and a single wide cell.

The best frequency appears to be around 33% (1 in 3 volume scans) because many intensifying tropical cyclones have tall eyewall cells that often while few non-intensifying tropical cyclones do. Column 2 of Table 4.5 (p. 221) shows that the height-frequency threshold successfully identifies whether or not intensification is occurring in

83% of the observation periods (25 out of 30). About half of the intensifying periods experience a substantial wind increase of over 5 m/s (10 kt) (Figure 4.4b).

The t-test cannot be used to estimate the statistical significance of the 83% success rate that was just described. The t-test cannot be used because there is such a small number of ground radar observation periods.

The sign test can be used to estimate the statistical significance of small samples. However, there is no way around the fact that small samples often have limited statistical

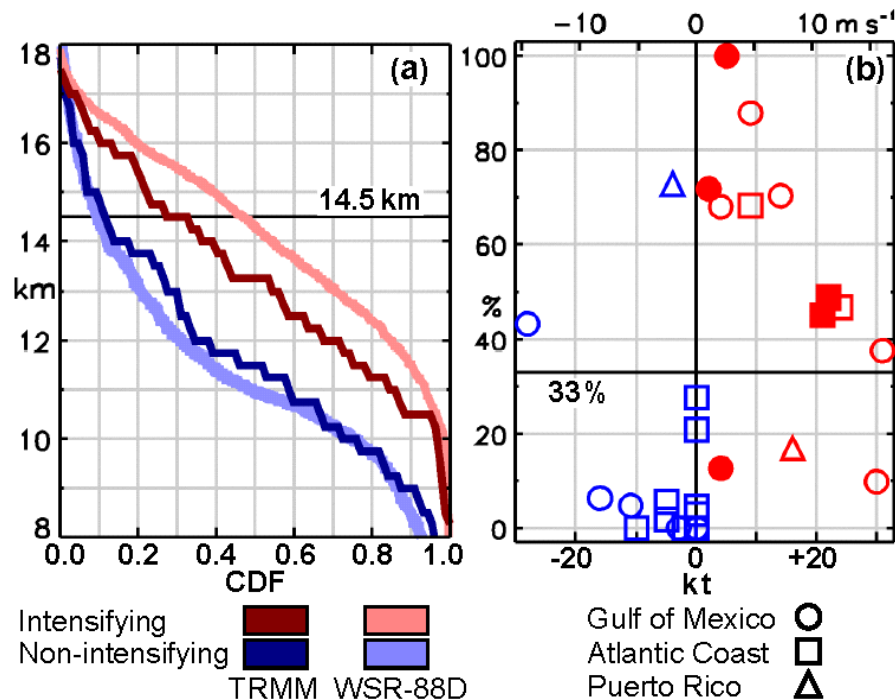


Figure 4.4. Statistical distributions of satellite and ground radar observations of tall eyewall cells. (a) For the WSR-88Ds and the TRMM Precipitation Radar, the CDFs of intensifying and non-intensifying hurricanes. The TRMM CDFs are reproduced from Figure 1a of Kelley *et al.* [2004, *GRL*]. (b) The change in a hurricane's sustained surface wind speed during each WSR-88D observation period. The vertical axis is the percentage of WSR-88D volumes scans that contain extremely tall precipitation in the eyewall. The five filled-in symbols are storms transitioning from tropical storm to hurricane during the WSR-88D observation period. This figure appeared in Kelley *et al.* [2005].

significance. Section 3.7 (p. 164) explains how the sign test works. As described below, the sign test, when applied to the ground radar data, suggests that the 83% success rate is only marginally statistically significant ($\alpha=0.2$). In the next few paragraphs, the sign test is applied to the best track wind intensity change during the ground radar observation periods listed in Table 4.5. These intensity changes are listed in a more convenient form in Table 4.2. When applied to the intensity change, the sign test indicates, at the 0.15 significance level, that the population median m_{FT} of the $n = 11$ observation periods with frequent towers is more than $m_0 = 3$ kt. Eight of the 11 periods have a larger than 3 kt increase ($x = 8$). The probability P of this event occurring at random is expressed in equation 4.6. Similarly, the sign test indicates, at the 0.01 significance level, that the population median m_{IT} of the $n = 18$ observation periods with infrequent towers is less than 1 kt. Three of the 18 periods have a larger than 1 kt increase ($x = 3$).

$$\begin{aligned} P_{m_{FT} > 3 \text{ kt}} &= P_{\text{binomial}}(X \geq 8; n = 11, p = 0.5) = 0.113 < 0.15 \\ P_{m_{IT} < 1 \text{ kt}} &= P_{\text{binomial}}(X \leq 3; n = 18, p = 0.5) = 0.005 < 0.01 \end{aligned} \quad (4.6)$$

The sample median for the observation periods with frequent and infrequent towers is 9 kt and 0 kt, respectively, as indicated with brackets in Table 4.2. However, because of the small sample sizes, all that can be said with some confidence about the population medians is that they are >3 kt and <1 kt, based on the sign test that has just been described.

Table 4.2. Intensity change (knots) in two sets of WSR-88D observation periods, sorted for use with the sign test ¹

Rank	18	17	16	15	14	13	12	11	10	9	8	7	6	5	4	3	2	1
FT								-28	-4	2	4	5	[9]	9	14	24	31	31
IT	-16	-11	-10	-5	-5	-3	-2	0	[0]	[0]	0	0	0	0	0	4	16	30

¹ The rank in row 1 can be interpreted as the number of observation periods with a wind intensity change (rows 2 and 3) that is greater than or equal to the wind intensity change in that column. "FT" identifies the sample of 11 observation periods with frequent tall eyewall cells. "IT" identifies the 18 observation periods with infrequent tall eyewall cells. The units of intensity change are knots. The FT row has bold entries for the 8 observation period whose intensity change is greater than 3 knots. The IT row has bold entries for the 3 observation periods whose intensity change is greater than 1 knot. The sample median of the FT and IT samples is 9 kt and 0 kt, as indicated with brackets in the table.

The success rate of the height-frequency threshold would be slightly lower than 83% if the dissertation assumes that all WSR-88Ds have a ± 2 dBZ calibration error.

Anagnostou et al. [2001] reported that the calibration of WSR-88D radars in the southeastern United States can vary by as much as 2 dBZ relative to the TRMM Precipitation Radar. Whether the dissertation adds or subtracts 2 dBZ from all reflectivity observations, the dissertation finds that the height-frequency threshold correctly identifies the intensity change in 80% of the ground radar observation periods.

Alternatively, the success rate of the height-frequency threshold would be slightly lower than 83% if the dissertation assumes that all estimates of wind speed change are in error by ± 6 kt. Based on *Franklin* [2005, Table 11], errors in NHC wind estimates are likely to be approximately 6 kt. To assess the effect of wind error, the dissertation identifies the 13 observations periods whose intensifying/non-intensifying classification

would not be altered by a 6 kt error in the wind speed change calculated from NHC wind estimates (i.e., periods with $|\Delta v| > 6$ kt). For these 13 observation periods, the height-frequency threshold has a 77% success rate in identifying whether or not intensification is occurring.

The effect of a ± 6 kt best track intensity error can also be evaluated using a sign test. First, consider the 7 observation periods with frequent towers (FT) that also have an intensity change with an absolute value greater than 6 knots. The intensity change during those 7 observation periods is listed in the " $|FT| > 6$ kt" row of Table 4.3. A sign test at the 0.10 significance level finds that the population median of these cases is greater than 8 kt. Using the notation developed in section 3.7 (p. 164), this test can be written in the following way:

$$P_{m_{FT} > 8 \text{ kt}} = P_{binomial}(X \geq 6; n = 7, p = 0.5) = 0.063 < 0.10 \quad (4.7)$$

Because so many of the observation periods with infrequent towers have a near zero intensity change, the dissertation applies a transformation. The benefit of the transformation is that it allows us to keep the many observations with zero intensity change in the population with infrequent tall eyewall cells. The dissertation asks the question: how likely is it that the population median of the infrequent tower periods is 7 kt less than the population median of the frequent tower periods? To answer this question, the intensity change in the infrequent tower (IT) cases is transformed by subtracting 1 kt more than the just established 7 kt cutoff. Next, the transformed intensity changes were removed that had an absolute value smaller than 6 kt. The remaining 17

observation periods are shown in the " $|IT-8| > 6$ kt" column of Table 4.3. Based on this data, a sign test shows at the 0.01 significance level that the population median of the non-intensifying cases is more than 7 kt less than the population median of the intensifying cases:

$$P_{\Delta m_{IT} < -7 \text{ kt}} = P_{\text{binomial}}(X \leq 2; n = 17, p = 0.5) = 0.001 < 0.01 \quad (4.8)$$

Table 4.3. Intensity change (knots) in two sets of WSR-88D observation periods taking into account a possible 6 kt error in the estimation of wind intensity ¹

Rank	17	16	15	14	13	12	11	10	9	8	7	6	5	4	3	2	1
$ FT > 6$ kt											-28	9	9	14	24	31	31
$ IT-8 > 6$ kt	-24	-19	-18	-13	-13	-11	-10	-8	-8	-8	-8	-8	-8	-8	-8	8	22

¹ " $|FT| > 6$ kt" identifies the sample of 7 observation periods with frequent towers and more than a 6 kt absolute intensity change. " $|IT-8| > 6$ kt" identifies the 17 observation periods with infrequent towers used in this sign test. The units of intensity change are knots. The rank states the number of observation periods greater than or equal to a given threshold. For example, the " $|FT| > 6$ kt" row has bold entries for the 6 observation period whose intensity change is greater than 8 knots. The " $|IT-8| > 6$ kt" row has bold entries for the 2 observation periods whose intensity change is more than 7 knot less than the 8 kt cutoff used with the FT population.

4.7. Predicting tropical cyclone intensification

The 14.5km–33% height-frequency threshold developed in this chapter for WSR-88D ground radars is better at predicting tropical cyclone wind intensification than is the 14.5 km height-only threshold developed in the previous chapter for the TRMM satellite radar.

This result is shown in Table 4.4. The table includes only the 29 independent WSR-88D observation periods. In contrast, Table 4.5 includes 30 observation periods, two of which cannot be considered completely independent because two ground radars simultaneously observed Hurricane Alex (2004). Both the WSR-88D height-frequency threshold and the TRMM height-only threshold have similar type I error rates. A type I error is a "false alarm," which occurs when there is a tall eyewall cell but no tropical cyclone intensification.

The WSR-88D height-frequency threshold has a much lower type II error rate than the TRMM height-only threshold. A type II error is "failure to detect." In this situation, failure to detect means the absence of tall precipitation when a tropical cyclone does intensify. There is a simple explanation for why the WSR-88Ds have a lower type II error rate. With a single TRMM observation, it is impossible to know if a tall cell is about to form or if one just disappeared. In contrast, it is hard to miss a tall cell with a WSR-88D volume scan every 4 to 6 minutes.

In summary, Table 4.4 indicates that intensification occurs during 82% of the independent WSR-88D observation periods that exceed the height-frequency threshold (9 out of 11). Intensification occurs during only 17% of the periods that do not exceed this threshold (3 out of 18).

Table 4.4. TRMM vs. WSR-88D ^a

Wind Intensity Increasing	TRMM Overflights			WSR-88D Observation Periods		
	Tower	No Tower	<i>Total</i>	Frequent Towers	Infrequent Towers	<i>Total</i>
Yes	17.1% (46)	29.7% (80) ^c	46.8% (126)	31.0% (9)	10.3% (3) ^c	41.4% (12)
No	8.6% (23) ^b	44.6% (120)	53.2% (143)	6.9% (2) ^b	51.7% (15)	58.6% (17)
<i>Total</i>	25.7% (69)	74.3% (200)	100% (269)	37.9% (11)	62.1% (18)	100% (29)

^a "Tower" refers to tall eyewall cells that achieve the height-only threshold, and "Frequent Towers" refers to the height-frequency threshold. The number of cases is stated in parentheses.

^b Type I error rate. ^c Type II error rate.

Consider the 12 hour tropical cyclone intensity forecast issued by the National Hurricane Center (NHC) during a WSR-88D observation period. For the 24 NHC forecasts that the dissertation examines, the WSR-88D height-frequency threshold would have correctly raised suspicion about six inaccurate NHC forecasts and falsely raised suspicion about only two accurate NHC forecast (See columns 10 and 11 of Table 4.5). This result suggests that the height-frequency threshold could aid forecasters.

In conclusion, the TRMM satellite technique described in the previous chapter is less effective than the ground radar technique developed in this chapter. The limitation of the ground radar technique is that it can only be used when a tropical cyclone is within a few hundred kilometers of a ground radar on the coast. The next chapter will discuss physical mechanisms that can help explain these empirical results.

Table 4.5. WSR-88D observation periods ^a

1. NHC I+	2. Freq.	3. A _{33%}	4. Tropical cyclone Name	5. WSR-88D Location	WSR-88D Volume Scans			9. NHC Start/End Wind (kt)	I+ Predicted	
					6. Start Date yyyymmdd	7. Start Time UTC	8. Duration hh:mm		10. WSR	11. NHC
y	100	629	Erika	Brownsville, TX	2003/08/16	0715	03:45	60→65	y	y
y	87	181	Earl	Eglin, FL	1998/09/02	1428	03:32	76→85	y	y
y	72	33	Irene	Miami, FL	1999/10/15	0400	06:00	63→65	y	y
y	69	18	Erin	Tallahassee, FL	1995/08/03	0100	11:00	66→80	y	-
y	68	92	Georges	Key West, FL	1998/09/25	0717	10:43	86→90	y	y
y	67	187	Bertha	Wilmington, NC	1996/07/12	0851	04:49	77→86	y	-
y	48	20	Alex	Morehead, NC	2004/08/03	0312	09:48	60→82	y	y
y	46	18	Irene	Wilmington, NC	1999/10/17	1231	15:09	65→89	y	n
y	45	17	Alex	Wilmington, NC	2004/08/03	0120	10:11	57→78	y	y
y	37	8	Bret	Brownsville, TX	1999/08/21	1847	11:13	94→125	y	y
y	16	0	Lenny	Puerto Rico	1999/11/17	0418	09:13	104→120	n	n
y	12	0	Claudette	Houston, TX	2003/07/15	0331	07:29	61→65	n	y
y	9	0	Charley	Key West, FL	2004/08/13	0921	08:39	95→125	n	y
n	72	132	Georges	Puerto Rico	1998/09/21	1325	05:35	94→90	y	y
n	43	26	Lili	New Orleans, LA	2002/10/03	0100	07:45	122→94	y	y
n	26	0	Frances	Miami, FL	2004/09/04	1045	03:25	90→90	n	n
n	20	0	Charley	Jacksonville, FL	2004/08/14	0617	04:33	75→75	n	y
n	6	0	Opal	Eglin, FL	1995/10/04	1820	03:14	108→92	n	-
n	5	0	Dennis	Morehead, NC	1999/08/30	0826	11:47	88→83	n	y
n	4	0	Gordon	Tallahassee, FL	2000/09/17	1850	07:10	64→53	n	n
n	2	0	Erin	Melbourne, FL	1995/08/01	2320	03:10	75→75	n	-
n	2	0	Fran	Wilmington, NC	1996/09/05	1543	06:54	100→100	n	-
n	0	0	Bonnie	Wilmington, NC	1998/08/26	0840	07:25	100→100	n	n
n	0	0	Danny	Mobile, AL	1997/07/18	1700	05:00	70→70	n	-
n	0	0	Floyd	Wilmington, NC	1999/09/15	2122	06:40	92→90	n	n
n	0	0	Georges	New Orleans, LA	1998/09/27	1455	12:55	95→92	n	n
n	0	0	Irene	Melbourne, FL	1999/10/16	1616	08:33	65→65	n	y
n	0	0	Isabel	Morehead, NC	2003/09/18	0812	04:48	90→85	n	y
n	0	0	Ivan	Mobile, AL	2004/09/15	1620	11:17	115→115	n	n
n	0	0	Jeanne	Melbourne, FL	2004/09/25	1900	06:09	110→100	n	y

^a Column 1 indicates if the tropical cyclone's winds intensified during the WSR-88D observation period based on the NHC best track wind estimates that were issued every six hours. Column 2 states the frequency of tall precipitation, i.e., the percentage of volume scans with 20 dBZ \geq 14.5 km in the eyewall. Column 3 states the horizontal area (km²) of tall cells that occurs in at least 33% of the volume scans. Column 10 states if the height-frequency threshold is exceeded ($A_{33\%} \geq 5$ km²), which would indicate a likelihood of tropical cyclone intensification. Column 11 shows if the NHC advisory issued at the beginning of the WSR-88D observation period contained a 12 hour forecast

that included tropical cyclone intensification. Lacking NHC advisories, the dissertation leaves column 11 blank for tropical cyclones before 1998.

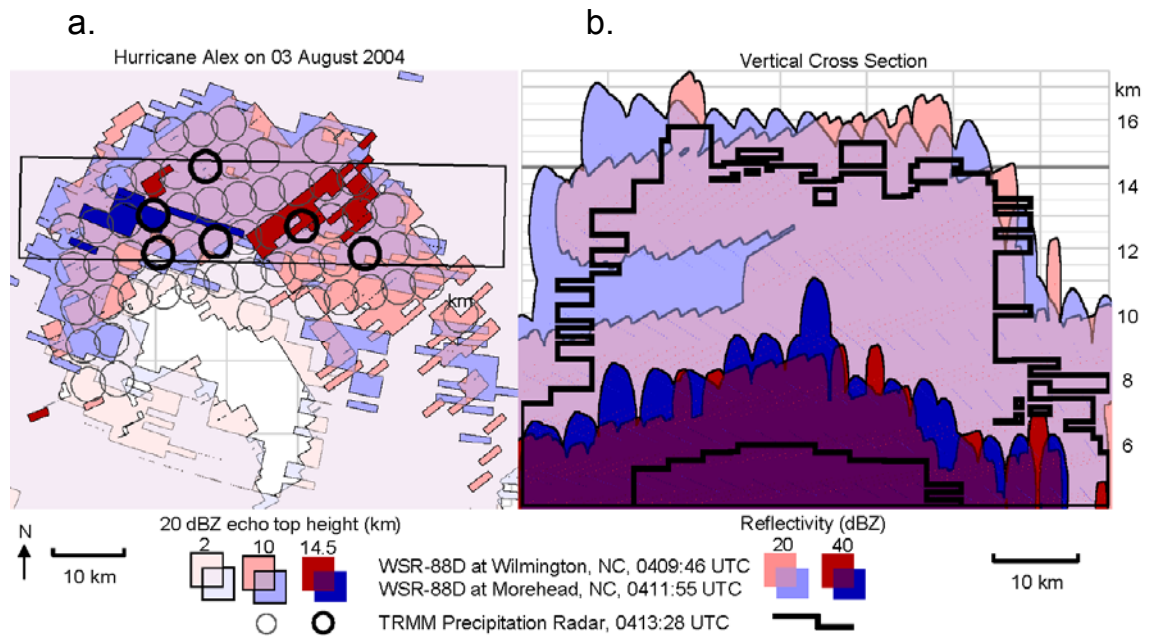


Figure 4.5. Comparison of Hurricane Alex's (2004) eyewall observed nearly simultaneously by the TRMM Precipitation Radar and two WSR-88D ground radars. This figure is explained in section 4.2

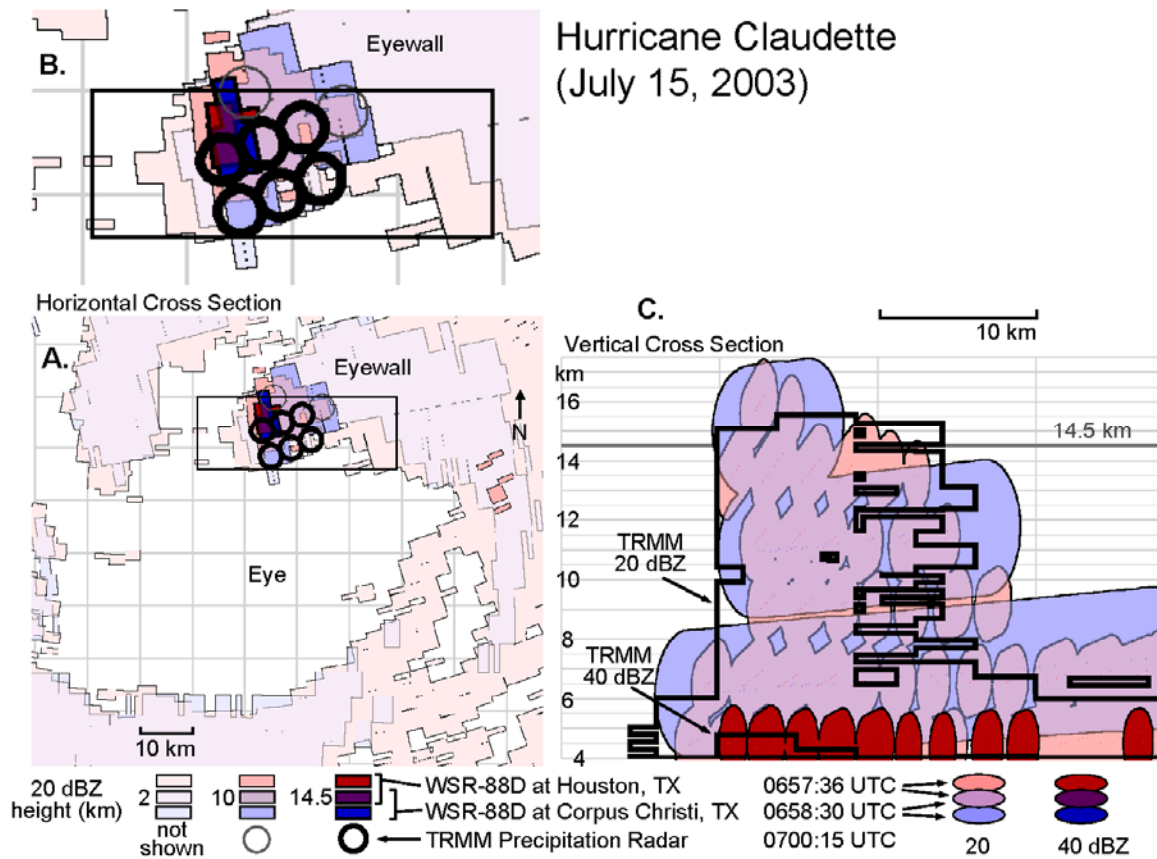


Figure 4.6. Comparison of Hurricane Claudette's (2003) eyewall observed nearly simultaneously by the TRMM Precipitation Radar and two WSR-88D ground radars. The symbols and colors used in this figure are the same as in the previous figure.

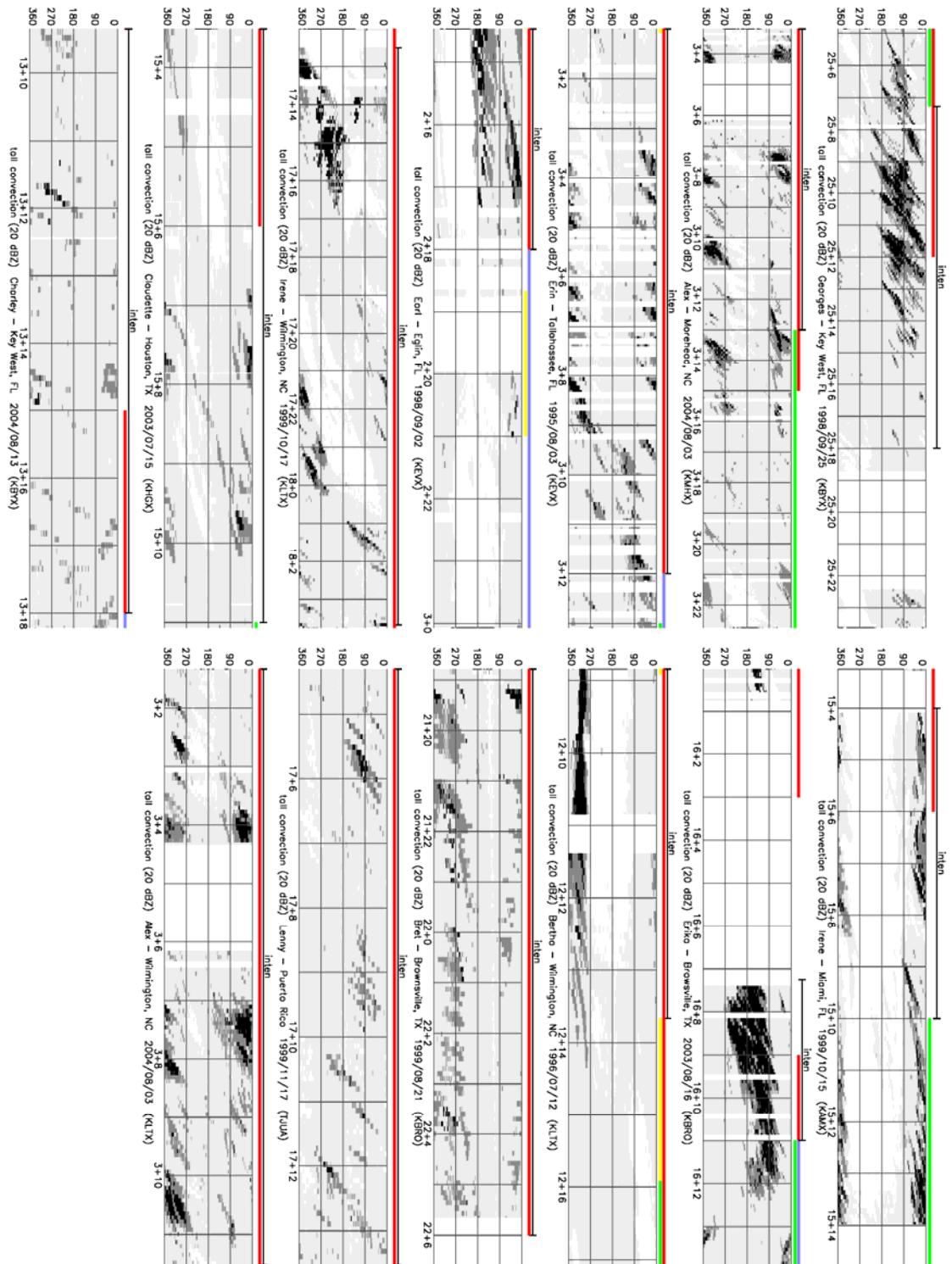


Figure 4.7. Time-azimuth plots for intensifying tropical cyclones

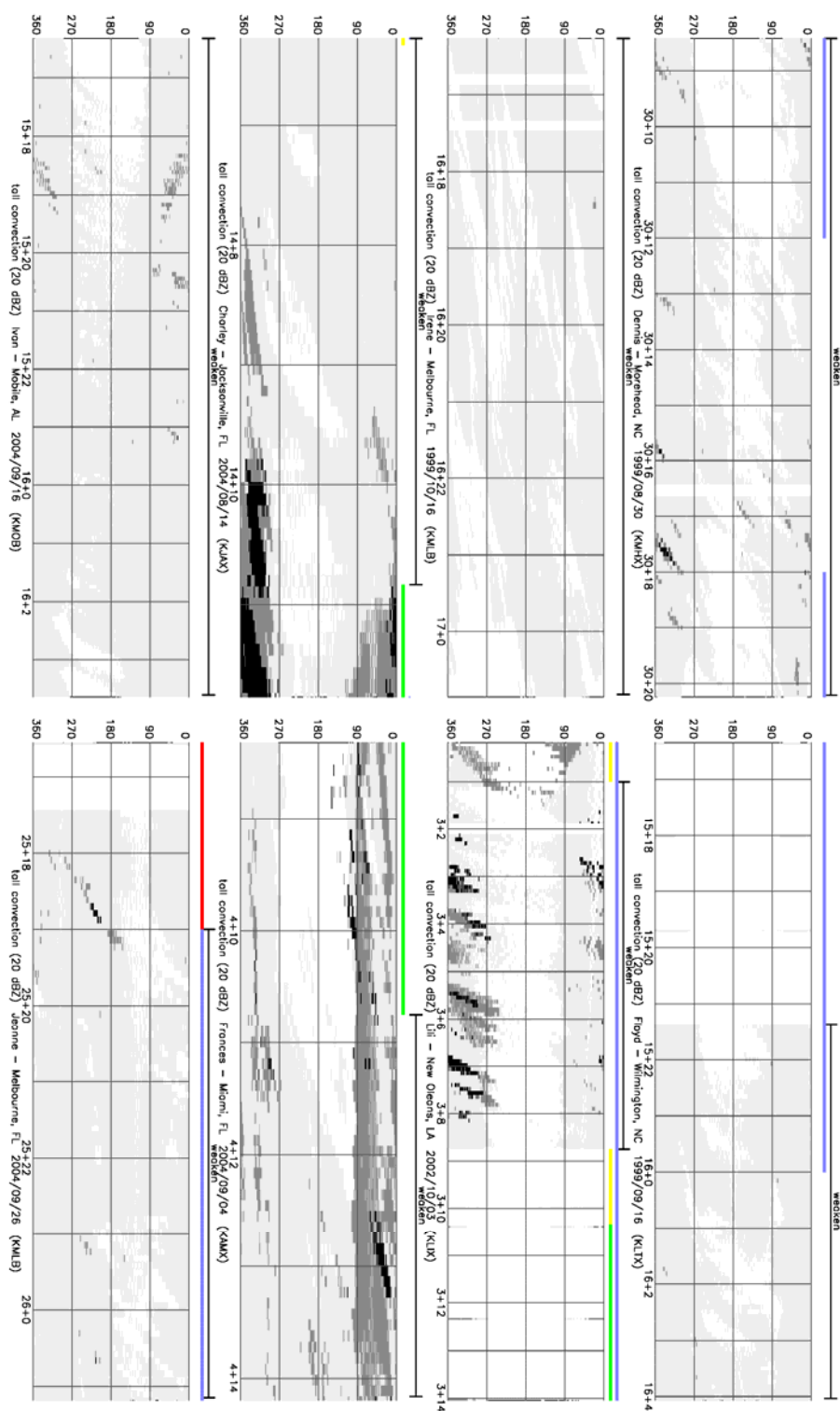


Figure 4.9. Time-azimuth plots for non-intensifying tropical cyclones (continued)

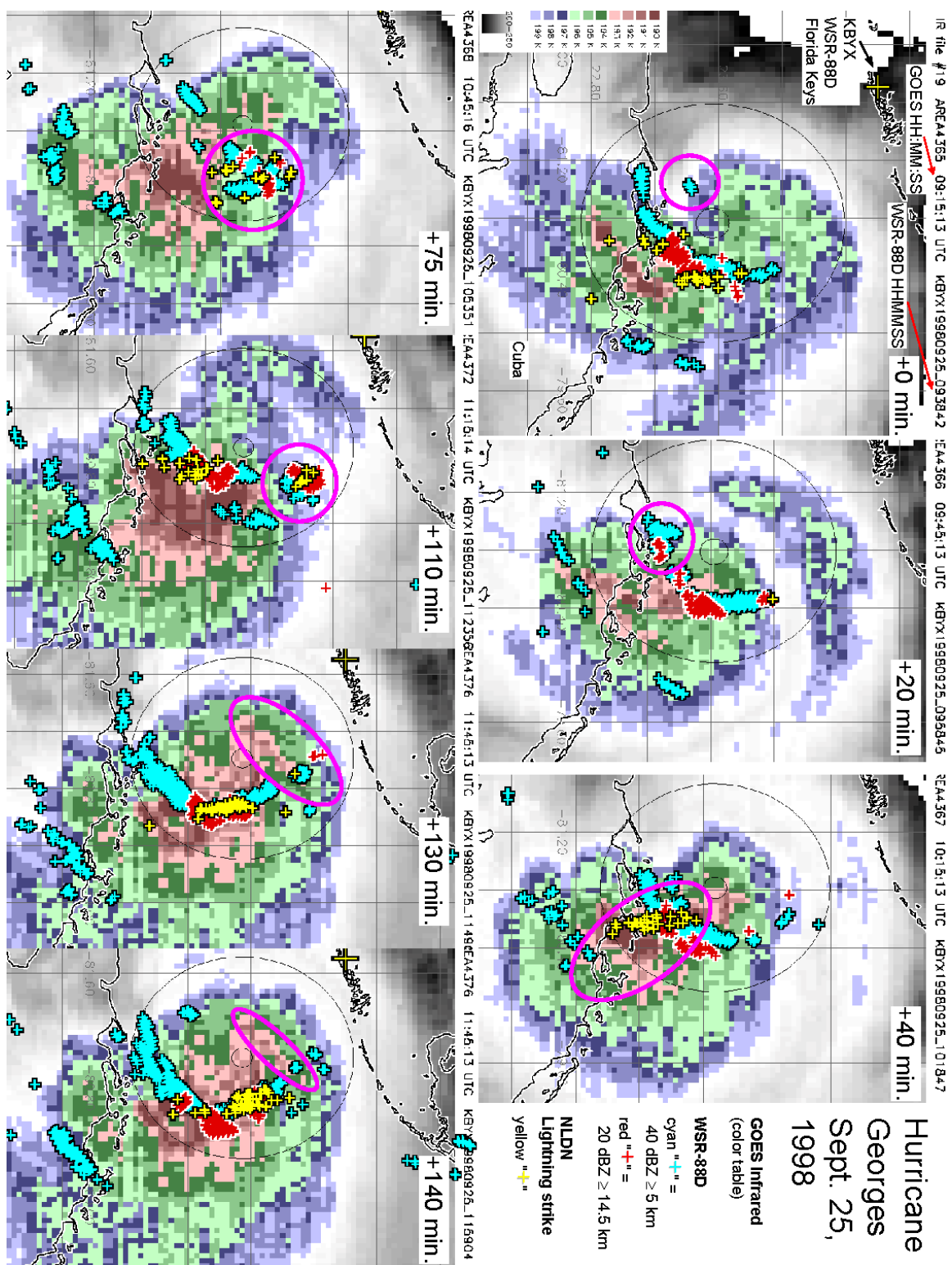


Figure 4.10. Evolution of a convective cell in Hurricane George's (1998) eyewall

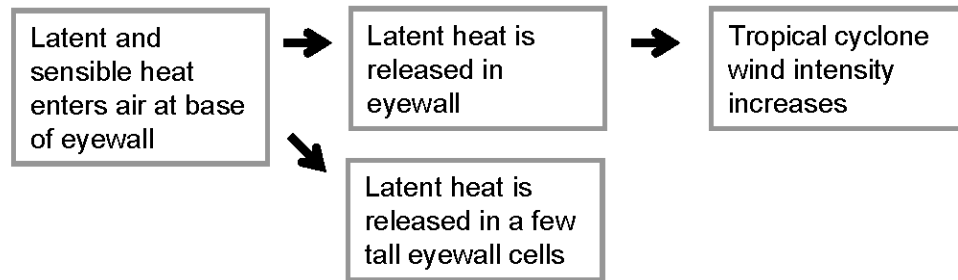
5.

Causation examined with theory and models

5.1. Indicator vs. cause

The goal of this chapter is to show whether a sequence of tall eyewall cells might ever cause wind intensification or if the cells are only an indicator of other causes at work to intensify the winds (Figure 5.1). The question of cause vs. indicator is an open question because previous studies have answered it differently [*Lyons and Reed*, 1994]. Some researchers argue that tall eyewall cells reduce tropical cyclone wind intensity [*Shubert et al.*, 1999; *Yang et al.*, 2007; *Nolan et al.*, 2007]. Other researchers argue that tall eyewall cells have no effect on wind intensity [*Emanuel*, 1997; *Smith*, 2000]. Other researchers argue that tall eyewall cells increase wind intensity [*Rodgers et al.*, 2000; *Rodgers et al.*, 1998; *Steranka et al.*, 1986].

A. Tall cells as indicators



B. Tall cells as causes

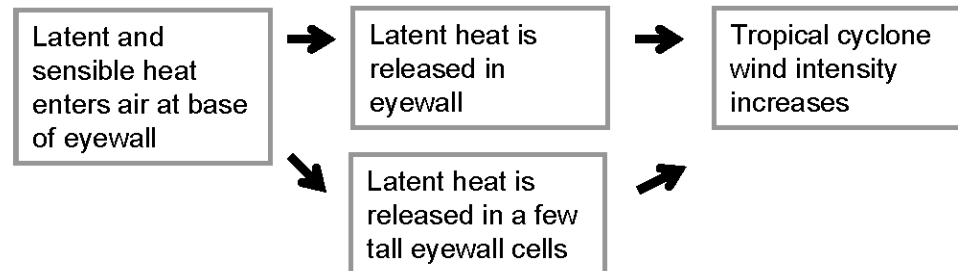


Figure 5.1. Two ways of looking at tall cells

Even if tall eyewall cells were merely indicators, they might still be useful for forecasting wind intensity change. Tall eyewall cells might be an easy-to-observe shortcut to learning the sum of forces that cause tropical cyclone intensification. Direct measurement of any one of these causal forces might be prone to such large errors that one can obtain useful forecasting information by simply looking for tall eyewall cells.

This chapter calculates an upper bound for how much of the released latent heat in a burst of tall eyewall cells will result in warming of the tropical cyclone eye. Once the eye is warmed, the empirical relationship between warm anomaly and wind intensity (section 2.8.4, p. 86) will be applied to estimate wind intensity increase. Processes that can contribute this energy transformation are direct mixing, forced subsidence (section

2.8.3, p. 83), and vortex stretching (section 2.8.6, p. 98). These processes are not described in detail because only an upper bound is estimated in this chapter.

Other studies have used this basic approach of scaling the latent heat release to come up with wind intensification [*Malkus*, 1958; *Emanuel*, 1987]. There is another completely different path to wind intensification: a low-level mass of air with high angular momentum can enter the bottom of the eyewall [*Krishnamurti et al.*, 2005, MWR; *DeMaria et al.*, 1993]. This path is not relevant to this discussion because this discussion is only interested in how much intensification can be called by tall towers, not how the synoptic air masses encountered by the tropical cyclone affect tropical cyclone wind intensity.

5.2. A burst of tall cells as a cause of intensification: thermodynamic upper limit

The pink region in Figures 5.2a indicates the region of the eye's upper tropospheric thermal anomaly that is approximately 10 K and extends approximately from 700 to 200 mbar (3 to 12 km). The much larger region of a >1 K thermal anomaly extends to outside the eyewall at high altitudes (~ 200 mbar). At the center of the eye, the >1 K region extends to the surface where there is typically a thermal anomaly of few degrees K (section 2.8.4, p. 86).

As described in section 2.8, the simplest representation of a tropical cyclone begins with a central eye that contains warm air. The warmth of the eye causes the

surface pressure to be low under it. By the gradient wind balance, the winds that spiral around the eye are proportional to the pressure gradient, which means that they are proportional to the magnitude of the eye's thermal anomaly. Due to this proportionality, surface winds can be increased by warming the eye, which is the path to wind intensification examined in this section. Figure 5.2a is a schematic diagram of a tropical cyclone undergoing intensification due to latent heat released in a burst of tall eyewall cells.

5.2.1. Addition of energy by a burst of tall eyewall cells

This section estimates how much latent heat is released by condensation each second in a

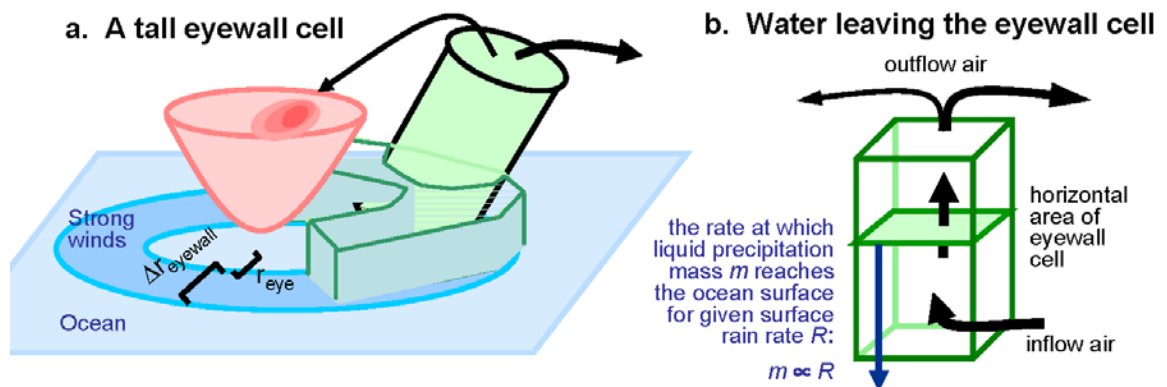


Figure 5.2. A schematic representation of a tropical cyclone whose eye is being warmed by a tall eyewall cell. (a) Some of the outflow from the tall eyewall cell interacts with the eye and warms it. The tall eyewall cell reaches above about a 14.5 km altitude (~ 140 mbar). In the upper troposphere, the eye is ~ 10 K warmer than the background air at the same altitude. The upper tropospheric maximum of the eye's thermal anomaly (shown in pink) occurs at about 700 to 200 mbar, i.e., 3 to 12 km (section 2.8.4). The washer-shaped area of ocean surface with strong winds is shaded in blue. The region of heavy rainfall is represented by the gray 3D box. (b) A method of estimating the mass of water condensing inside of a tall eyewall cell by observing the surface rain rate.

tall eyewall cell. The amount of energy added per second (i.e., power) is proportional to the mass of water vapor condensing each second in the tall eyewall cell minus the amount of precipitation water that evaporates before hitting the ocean surface (Figure 5.2b). The net mass of water condensing is only slightly greater than the mass of precipitation reaching the ocean surface because very little water leaves horizontally as tiny cloud droplets below the freezing height or as tiny ice particles in the upper-level outflow. Compared with other kinds of storms (such as squall lines), cells in tropical cyclones have most of the precipitation fall out their bottom [Braun, 2006, part 2]. The mass of water reaching a square meter of ocean surface is the rain rate in mm/h multiplied by three conversion factors: from hours to seconds, from mm per m² to cm³, and from cm³ to grams of water mass. This idea can be expressed in the following equation for the power $P_{released}$ of a tall eyewall cell:

$$\begin{aligned}
 P_{released} &= \left(\frac{5}{18}\right) L_v R A_{cross\ section} \\
 \text{unit analysis... watt} &= \frac{J}{s} = \left(\frac{1000 \frac{cm^3}{mm \cdot m^2}}{3600 \frac{s}{h}} 1 \frac{g}{cm^3} \right) \frac{J}{g} \frac{mm}{h} m^2 \quad (5.1) \\
 &= \left(\frac{5}{18} \frac{g}{mm \cdot m^2} \frac{h}{s} \right) \frac{J}{g} \frac{mm}{h} m^2
 \end{aligned}$$

In equation 5.1, 5/18 is a unit conversion factor, L_v is the latent heat of vaporization of water (2.5e3 J/g), R is the surface rain rate (mm/h), and $A_{cross\ section}$ is the horizontal area of the tall eyewall cell (m²). Only the latent heat of vaporization is included in this equation, not latent heat of fusion. When ice forms above the freezing height (~5 km altitude in the Tropics), latent heat of fusion is released. However, the latent heat of

fusion is reabsorbed when the ice particles melt before falling into the ocean. The release of latent heat of fusion redistributes heat within the column and helps the cell to become tall [Zipser, 2003], but latent heat of fusion adds no net heat to the air column.

The power calculated with equation 5.1 can be compared to published values. Using reasonable upper bounds for the variables in equation 5.1 as stated in Table 5.1 (p. 237), a tall eyewall cell releases latent heat at a rate of 1.4×10^{13} J/s. If one assumes that tall eyewall cells contribute approximately 37% of the total latent heat released in the eyewall [Braun, 2002], then the eyewall total power is 3.8×10^{13} J/s (i.e., 3.8×10^{13} watts). Rodgers *et al.* [1998] use the SSM/I passive microwave instrument to observe variations over several days of the eyewall total rate of latent heat release in Hurricane Opal (1995). During a 12 hour period of rapid intensification, the observed latent heat release in the eyewall averaged 6×10^{13} J/s, up from the 2×10^{13} J/s during the period of steady intensity. The values reported by Rodgers *et al.* [1998] are consistent with equation 5.1 of this dissertation.

The only difficult part in this derivation is estimating what fraction of the latent heat released in the eyewall is converted into kinetic energy of intensifying tropical cyclone surface winds. This chapter uses a 7% conversion ratio for converting latent heat into eye warming and an empirical relationship between eye warming and surface wind intensification (section 2.8.4, p. 86). This 7% conversion ratio is intended to include all the difficult to quantify processes that are not quantified individually: gravity waves carrying a fraction of the latent heat away, outflow air carrying some of the latent heat away, latent heat being converted into other forms of energy such as gravitational potential energy, energy lost due to the inefficiency of the symmetrization process, etc.

Malkus and Riehl [1960, Table 11] use a 1.4% latent heat to kinetic energy conversion ratio in weak tropical cyclones and a 3.3% ratio in strong tropical cyclones. *Nolan et al.* [2007] estimate a 5% latent heat to kinetic energy conversion ratio in a weak tropical cyclone simulation.

The 7% ratio used here has been justified above using previously published values, but there is an alternate method to derive it. Suppose that $f_{mass} = 20\%$ of the tall eyewall cell's upper-level outflow interacts with the eye and the rest of the outflow traveled away from the eye and has no effect on the eye. Such a mass ratio can be estimated from the high resolution model examined in section 5.5.1 (p. 251). Suppose further that the latent heat previously released in the eye-bound outflow had a $f_{energy} = 33\%$ conversion ratio of latent heat into eye warming. Some studies use 33% as the ratio of conversion of latent heat to work (Table 5.6, p. 269). The net conversion ratio f_{usable} would be 7%, the product of 20% and 33%.

$$\begin{aligned}
 P_{usable} &= f_{energy} f_{mass} P_{released} \\
 P_{usable} &= f_{usable} P_{released} \\
 \text{unit analysis : } \frac{\text{J}}{\text{s}} &= 1 \frac{\text{J}}{\text{s}}
 \end{aligned}
 \tag{5.2}$$

5.2.2. Eye heating rate

Next, the dissertation estimates how quickly the eye would warm if a sequence of tall eyewall cells added energy at the rate calculated in section 5.2.1. The temperature change ΔT_{eye} (K) is the heat H (J) added to the eye divided by the eye's heat capacity c_{eye} (J/K). The eye's heat capacity is the eye's mass m_{eye} (kg) times the heat capacity of dry

air at constant pressure c_p (J/K kg). If one integrates a density profile that decreases exponentially with height, the resulting column mass ρ_{column} (kg/m²) is equal to the surface density ρ_0 (kg/m³) times the scale height z_0 (m). The factor of 0.87 in equation 5.3 for the eye mass m_{eye} comes from the assumption that the eye warming occurs between 120 mbar and the typical surface pressure of a tropical cyclone eye (950 mbar). Based on the hydrostatic equation for an isothermal atmosphere, approximately 87% of the atmospheric column mass ρ_{column} occurs below 120 mbar.

$$\begin{aligned}
 \rho(z) &= \rho_0 e^{-z/z_0} & \text{units : kg/m}^3 & \text{(hydrostatic equation)} \\
 \rho_{column} &= \rho_0 z_0 & \text{units : kg/m}^2 & \text{(column mass)} \\
 A_{eye} &= \pi r^2 & \text{units : m}^2 & \text{(eye area)} \\
 0.87 &= \frac{950 \text{ mbar} - 120 \text{ mbar}}{950 \text{ mbar}} & & (5.3) \\
 m_{eye} &= 0.87 \rho_{column} A_{eye} & \text{units : kg} & \\
 c_{eye} &= c_p m_{eye} & \text{units : } \frac{J}{K} = \frac{J}{K \text{ kg}} \text{ kg} &
 \end{aligned}$$

In equation 5.3, the altitude is z (m), the eye's radius is r (m), and the eye's horizontal area is A_{eye} (m²). Based on the derivation above, the eye's overall heat capacity c_{eye} (J/K) varies with the square of the eye's radius r , as shown in equation 5.4:

$$\begin{aligned}
 c_{eye} &= 0.87 c_p \rho_0 z_0 \pi r^2 \\
 \text{unit analysis : } \frac{J}{K} &= \frac{J}{K \text{ kg}} \frac{\text{kg}}{\text{m}^3} \text{ m}^1 \text{ m}^2 & (5.4)
 \end{aligned}$$

Now, the rate of eye heating H (J/s) can be easily estimated in equation 5.5 as the rate that usable energy is added to the eye divided by the heat capacity of the eye:

$$H = \frac{P_{useable}}{c_{eye}} \quad \text{units} \frac{\text{K}}{\text{s}} = \frac{J}{\text{s}} \div \frac{J}{\text{K}} \quad (5.5)$$

The eye's temperature change ΔT_{eye} (in degrees Kelvin) is equal to the heating rate H multiplied by the duration t_{burst} in seconds of the burst of tall eyewall cells. Substituting into equation 5.5, the temperature change can be expressed as a function of the five free parameters listed at the top of Table 5.1:

$$\begin{aligned} \Delta T_{eye} &= \frac{5}{18} \frac{L_v}{0.87 c_p \rho_0 z_0 \pi} \frac{R A f_{usable} t_{burst}}{r^2} \\ \Delta T_{eye} &= 3.32\text{e} - 5 \frac{R A f_{usable} t_{burst}}{r^2} \\ \text{unit analysis : K} &= \left(\frac{\text{K h}}{\text{mm s}} \right) \frac{\frac{\text{mm}}{\text{h}} \text{m}^2 \text{1 s}}{\text{m}^2} \end{aligned} \quad (5.6)$$

The baseline estimate of the maximum possible eye heating rate in Table 5.2 is based on the preceding equations and Table 5.1.

Table 5.1. Input parameters for estimating eye heating. The value in the table is intended to be the optimal value for maximizing the tropical cyclone intensification.

Quantity	Symbol	Value	Value in computation
Average surface rain rate inside of the tall eyewall cells	R	100 mm/h	same
Horizontal area of the tall eyewall cells	A	200 km ²	200e6 m ²
Fraction of latent heat released in the tall eyewall cells that can warm the eye	f_{usable}	0.07	same
Duration of the burst of tall eyewall cells	t_{burst}	9 hours	3.24e4 s
Radius of the tropical cyclone's eye	r	20 km	20e3 m
Latent heat of vaporization	L_v	2.5e3 J/g	same
Heat capacity of dry air	c_p	1004 J/K g	same
Surface density for a tropical cyclone ($p = 950$ mbar; $q = 20$ g/kg)	ρ_0	1.09 kg/m ³	same
Density scale height	z_0	7 km	7e3 m

Table 5.2. Estimate of eye heating

Quantity	Symbol	Value
The maximum amount of energy available to cause tropical cyclone wind intensification (equations 5.1 and 5.2)	$P_{usable} t_{burst}$	3.15e16 J
Heat capacity of the tropical cyclone eye (equation 5.4)	c_{eye}	8.38e15 J/K
Maximum eye heating from a burst of tall eyewall cells (equations 5.5 and 5.6)	ΔT_{eye}	3.76 K in 9 hours
Baseline estimate of maximum increase in wind intensity for a burst of tall cells using the 7 kt/K empirical ratio (section 2.8.4)	Δv	26 kt in 9 hours

The input parameter values in Table 5.1 are intended to be reasonable upper limits of what can occur in a tropical cyclone experiencing a long burst of tall eyewall cells. A 200 km² horizontal area of tall cells is near the top of the range of values in Table 4.5 (column 3, p. 221). For a 200 km² area of cells, a 100 mm/h rain rate is a reasonable upper bound, based on the review in section 2.1.5 (p. 22). The 9 hour duration of the tall cell burst is a reasonably long period given the observations reviewed in Table 2.14 (p. 131). The 20 km radius is a reasonable lower bound on the eye radius, and the smaller the eye radius, the less eye mass needs to be warmed, and therefore, the greater the eye warming.

The 3.76 K of warming calculated here is only slightly greater than the 3 K of eye warming that *Heymsfield et al.* [2001] suggest a convective burst could cause [*Kakar et al.*, 2006]. *Heymsfield et al.*'s results are based on several fly-throughs of Hurricane Bonnie (1998). *Franklin et al.* [1988, p. 1240] reports a 3 to 10 K warming in 5 hours in the eye of Hurricane Gloria (1985). The warming in Hurricane Gloria, however, was limited to between 775 and 575 mbar in dropsondes that were released at near 500 mbar. *Hack and Schubert* [1986, Figure 7a, 7c, and 7e] show a vertically averaged 13 K/day of eye temperature increase in their tropical cyclone simulation, which would correspond to 5K in 9 hours.

5.2.3. Intensity change

To estimate the wind intensity increase, the dissertation assumes that the wind intensity increase is proportional to the eye warming calculated in section 5.2.2. The

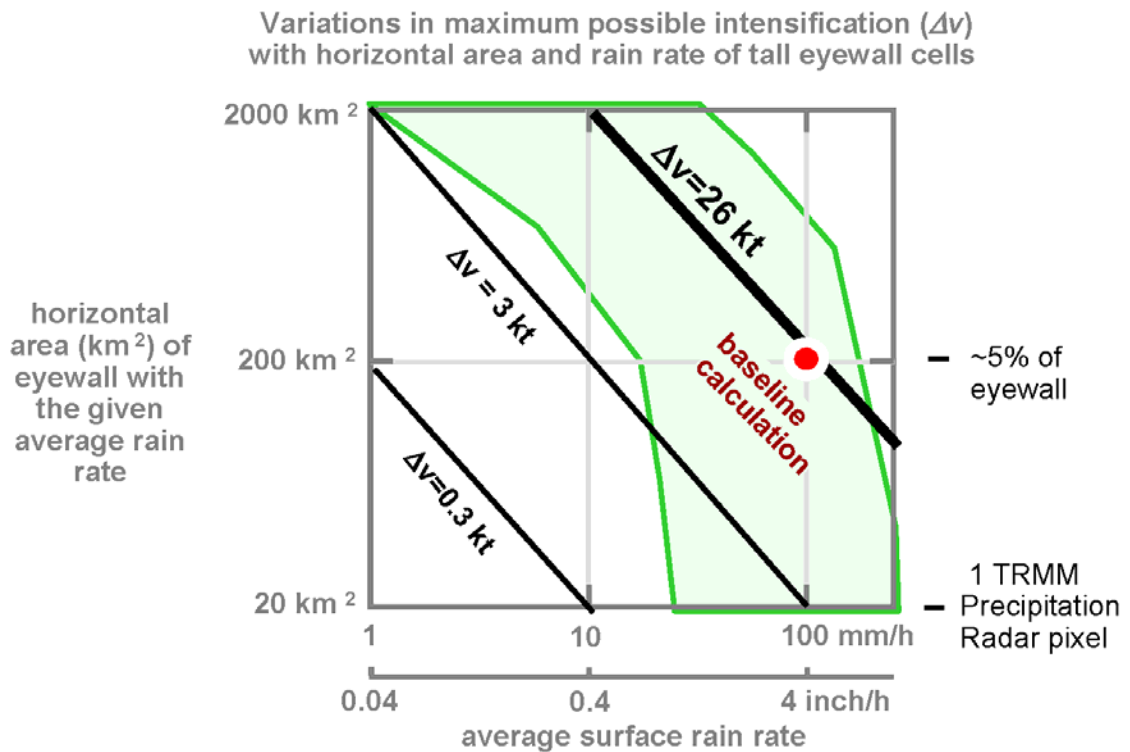


Figure 5.3. Variations in the maximum possible intensification by varying the surface rain rate and the horizontal area of tall eyewall cells. The red dot indicates the baseline estimate of the maximum possible intensity change (Table 5.2). The green region gives, for each horizontal area, the rainfall rates in the middle 80% of tropical cyclones observed by the TRMM Precipitation Radar. See the 10th and 90th percentile lines in panels e and f of Figure 5.6.

wind-temperature relationship was found to be 7 kt/K in section 2.8.4 (p. 86). Based on this relationship, the estimated 3.76 K warming from a 9 hour convective burst would cause a 26 kt wind intensity increase (Table 5.2, p. 237).

At this point in the derivation, it would be incorrect to only include the fraction of energy added that is equivalent to CAPE. CAPE is the relevant measure of available energy only when you are trying to establish a convective updraft. The dissertation is obviously not trying to establish a convective updraft in the eye.

Great care must be taken when considering how close an actual burst of tall eyewall cells could come to causing the maximum possible intensification of 26 kt estimated in this section. For example, if the five input parameters were 20% below the optimal value used in this baseline estimate, then the intensification would be only 9 kt instead of 26 kt, i.e., only 33% of the estimated maximum intensification. The next section conducts a more detailed examination of the sensitivity of the 26 kt baseline estimate to input parameter change.

5.3. Free parameters in the thermodynamic upper limit

The previous section's baseline estimate of wind increase Δv_0 is linearly dependent on four of the free parameters. The fifth free parameter can a different functional form, as represented in the following equation:

$$\Delta v = \Delta v_0 \frac{R}{R_0} \frac{A}{A_0} \frac{f_{usable}}{f_0} \frac{t_{burst}}{t_0} g(r, r_0)$$

$$\Delta v = \Delta v_0 \frac{R}{100 \text{ mm/h}} \frac{A}{200 \text{ km}^2} \frac{f_{usable}}{0.07} \frac{t_{burst}}{9 \text{ h}} g(r, 20 \text{ km}) \quad (5.7)$$

$$\text{unit analysis : } \frac{\text{m}}{\text{s}} = \frac{\text{m}}{\text{s}} \quad 1 \quad 1 \quad 1 \quad 1 \quad 1$$

In the above equation, the wind speed increase Δv (m/s) is equal to the baseline wind speed increase Δv_0 times the fractional change in surface rain rate R (mm/h), horizontal area of tall eyewall cells A (km²), the usable fraction of the energy f_{usable} (unitless), the

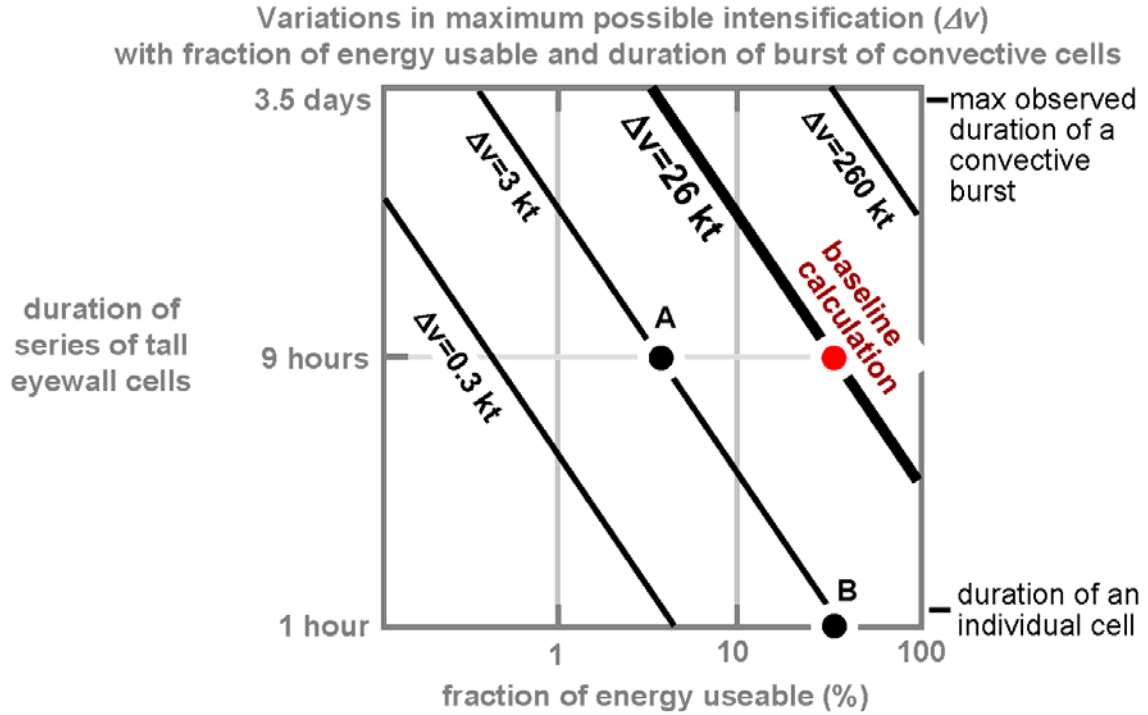


Figure 5.4. Variations in the maximum possible intensity change by altering (1) the efficiency with which the eyewall latent heating is converted into eye warming and (2) the duration of the burst of tall eyewall cells. The red dot indicates the baseline estimate of the maximum possible intensity change (Table 5.2).

duration t_{burst} (hours) of the burst of tall eyewall cells, and the functional dependence $g(r, r_0)$ on the inner radius r of the eyewall. As described below, the first two parameters (rain rate and tall cell area) are varied in Figure 5.3. The next two parameters (fraction of usable energy and burst duration) are varied in Figure 5.4. The variation due to the size of the eye is explored in Figure 5.5.

Figure 5.3 shows the effect of varying the horizontal area of the tall eyewall cells and the average surface rain rate in that horizontal area. The figure assumes that if the storm lacked these tall cells, then this portion of the eyewall's surface rain would not have occurred. In Table 5.1, the initial value for the average rain rate is 100 mm/h and the initial value of the tall eyewall cell area is 200 km². The red dot indicates the baseline

estimate of wind intensification from Table 5.2. The green area outlined in Figure 5.3 represents the average surface rain rates observed in the middle 80% of eyewalls during 166 TRMM overflights (Figure 5.6, p. 271). Based on these TRMM observations, the previously used 100 mm/h rain rate appears to be a reasonable upper bound. There can be errors in the TRMM Precipitation Radar's surface rain rate estimate because of the large attenuation under tall convective cells. Nonetheless, surface rain rates in the vicinity of 100 mm/h with 1 hour duration are also observed on occasion by other instruments (section 2.1.5, p. 22).

Two other parameters that can be varied are the fraction of released latent heat f_{usable} that can be used to warm the eye and the duration t_{burst} of the burst of tall eyewall cells (Figure 5.4). The red dot indicates the baseline estimate from Table 5.2. The intensity change calculated initially may be an overestimate by an order of magnitude if f_{usable} is overestimated by an order of magnitude (point A in Figure 5.4). A wide range of energy conversion ratios are used in the scientific literature (Table 5.6, p. 268). If f_{usable} were an order of magnitude smaller than the value used in the baseline calculation, then the maximum wind speed increase due to the convective burst would be only 2.6 kt instead of 26 kt. Because the best track wind estimates are reported only in 5 kt increments, a 2.6 kt change could go unnoticed.

Point B in Figure 5.4 illustrates how a single tall eyewall cell contributes insufficient energy to cause noticeable wind intensification. The calculation represented by point B has the same parameters as the baseline calculation (red dot) except that the

duration is the duration of a single cell (~30 minutes) rather than that of a burst of cells (~9 hours).

The radius of the tropical cyclone's eye affects the maximum possible intensity increase from a given amount of latent heat (Figure 5.5b). The reason is that the mass of eye air that needs to be heated varies inversely with the square of the radius. The black line of Figure 5.5b shows the inverse square influence on intensity change. Based on Figure 5.5b, a tropical cyclone with a large eye ($r = 40$ km) would have just a 6 kt

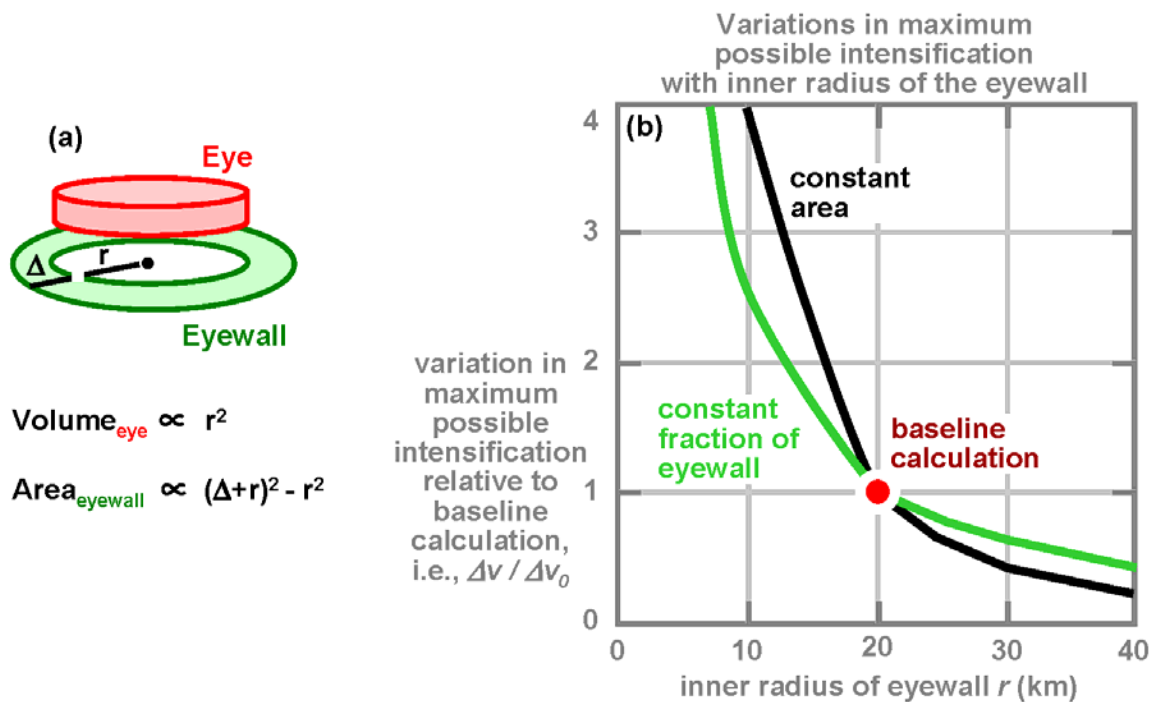


Figure 5.5. Variations in the maximum possible intensity change caused by variation in the size of the inner radius of the eyewall. The inner radius of the eyewall is by definition equal to the radius of the eye. (a) The influence that the eye radius has on the volume of the eye and the area of the eyewall. (b) The black line shows the inverse square relationship when the horizontal area of tall eyewall cells remains a fixed number of square kilometers. The green line is the functional relationship if the horizontal area of tall eyewall cells remains a fixed fraction of the eyewall area.

maximum possible intensification due to tall eyewall cell's energy, rather than the original 26 kt estimate ($6 \approx 26 \div 4$). For example, the high resolution simulation of Hurricane Bonnie (1998) that is examined in section 5.5 has an eyewall radius of 40 km.

An alternate assumption about the burst of tall eyewall cells leads to a slower variation of heating rate for a given change in eye radius. If one assumes that the same fraction of the eye is occupied by tall convective cells, then the intensity change varies proportionally with the area of the eyewall $A_{eyewall}$ and varies inversely with the volume of the eye being heated V_{eye} (Figure 5.5b). Under the constant fraction assumption, the radial dependence is the green line in Figure 5.5b. The two alternatives can be represented in the following equations:

$$\begin{aligned} \frac{\Delta v}{\Delta v_0} &= g_{\text{fixed area}}(r, r_0) = \frac{\text{energy added (unchanged)}}{\text{energy required}} \propto \frac{1}{r^2} \\ \frac{\Delta v}{\Delta v_0} &= g_{\text{fixed eye fraction}}(r, r_0) = \frac{\text{energy added}}{\text{energy required}} \propto \frac{(\Delta + r)^2 - r^2}{r^2} = \frac{\Delta^2 + 2\Delta r}{r^2} \end{aligned} \quad (5.8)$$

5.4. Verifying the thermodynamic upper limit using observations of latent heating

Section 5.2 estimates a thermodynamic upper limit to the amount of wind intensification that could be caused by a burst of tall eyewall cells. To check the physical plausibility of the thermodynamic upper limit, this section calculates the latent heating rate implied by

the upper limit. If the implied latent heating rate is far above observed latent heating rates, then the thermodynamic upper limit must be considered an overestimate.

Measuring the surface rain rate gives a simple way to estimate the net latent heating in a column of air. Water enters the column as vapor (~ 20 g/kg) and most of the water vapor either leaves the column as rain or as water vapor. Only a small fraction of the water vapor condenses and leaves the column suspended in the air as cloud droplets or cloud ice (~ 0.25 to 2 g/kg) [Black and Hallett, 1999]. Up to 2 g/kg of cloud droplets and ice may have condensed hours ago, while the precipitation that is falling on the ocean surface condensed in the past ~ 15 minutes because that is how fast precipitation falls out of the air column. The existence of cloud droplets and cloud ice causes surface rain to slightly underestimate the amount of latent heat released. Another consideration is that rain falls near vertically down [Braun, 2006; Ferrier *et al.*, 1996, Footnote 1; Zipser *et al.*, 1981, Figures 8 and 9], while the TRMM Precipitation Radar line of sight can be up to 17 degrees away from vertical. The slope of the line of sight is only a small source of error in the latent heating estimate because the Precipitation Radar pixel size is wide enough horizontally.

In the equations below, the column total heating rate h_{total} (J/s m^2) is calculated from the mass of liquid water passing through the columns lower boundary, i.e., falling into the ocean. There is a choice between two observed quantities for calculating h_{total} : precipitation water mass Δq near the ocean surface or surface rainfall rate R :

$$\begin{aligned} \text{observing } \Delta q : h_{\text{column total}} &= \Delta q v_{\text{fall}} L_v \rho_0 \\ \text{unit analysis : } \frac{\text{J}}{\text{s m}^2} &= \frac{\text{g}}{\text{kg}} \frac{\text{m}}{\text{s}} \frac{\text{J}}{\text{g}} \frac{\text{kg}}{\text{m}^3} \end{aligned} \quad (5.9)$$

$$\begin{aligned} \text{observing R : } h_{\text{column total}} &= \frac{5}{8} L_v R \\ \text{unit analysis : } \frac{\text{J}}{\text{s m}^2} &= \left(\frac{1000 \frac{\text{cm}^3}{\text{mm} \cdot \text{m}^2}}{3600 \frac{\text{s}}{\text{h}}} 1 \frac{\text{g}}{\text{cm}^3} \right) \frac{\text{J}}{\text{g}} \frac{\text{mm}}{\text{h}} \\ &= \left(\frac{5}{18} \frac{\text{g}}{\text{mm} \cdot \text{m}^2} \frac{\text{h}}{\text{s}} \right) \frac{\text{J}}{\text{g}} \frac{\text{mm}}{\text{h}} \end{aligned} \quad (5.10)$$

In the above equations, L_v (2.5e3 J/g) is the latent heat of vaporization and ρ_0 (1.09 kg/m³) is the surface air density in a moderate tropical cyclone ($p = 950$ mbar). For the sake of consistency, this section uses the same value for the constants as are used in Table 5.1 (p. 237).

With the equations worked out, this section now shows a numerical example. In the most recent reprocessing cycle, the TRMM 2A25 algorithm began producing estimates of precipitation water density from the TRMM Precipitation Radar observations. In the lower troposphere, tall eyewall cells tend to have 1 to 2 g/kg of precipitation water mass. The mass passing through the lower boundary of the atmosphere is the 1–2 g/kg of precipitation water mass multiplied by the typical fall velocity of rain drops near the surface, which is 7 m/s. Using this fall velocity, the net column mass flux of condensed water vapor that leaves the column as rain is 7–14 g/s m². Plugging the value into equation 5.9, the column total latent heating is 1.9e4 to 3.8e4 J/s m². Alternatively, based on a rain rate observation of 100 mm/h, the column total heating rate is 6.9e4 J/s m² (equation 5.10).

Before proceeding with the calculation, the just-calculated column heating rate of $6.9e4 \text{ J/s m}^2$ can be compared with published values. *Rodgers et al.* [2000]'s study of Hurricane Paka (1998) observed by satellite an azimuthally average heating rate of 1 to 3 watts per cubic meter concentrated at an altitude of 1 to 6 km. If one takes the dissertation's $6.9e4 \text{ J/s m}^2$ column heating rate in the tall eyewall cell and assume that the heating occurs in a 5000 meter (5 km) altitude range, then one obtains a 14 watt/m^3 heating rate in the tall eyewall cell. If one assumes that cells this vigorous occupy 10% of the eyewall in the azimuthal average [*Braun*, 2002], then the azimuthal average is 1.4 watt/m^3 , which is in the 1 to 3 watt/m^3 range that *Rodgers et al.* [2000] observe in Hurricane Paka.

Next, the latent heating rate is converted into the more commonly used units of degrees Kelvin per day using equation 5.11. First, it is necessary to calculate the mass m_{column} of the air column being heated below the 120 mbar pressure level. To be consistent with the heating rate calculated in section 5.2 (equation 5.3), the same formula for column mass is used here.

$$\begin{aligned}
 m_{column} &= 0.87 \rho_0 z_0 \quad \text{unit } \frac{\text{kg}}{\text{m}^2} \\
 h_{column} &= 8.64e4 \frac{\text{s}}{\text{day}} h_{column} \div (c_p m_{column}) \\
 \text{unit analysis : } \frac{\text{K}}{\text{day}} &= \frac{\text{s}}{\text{day}} \frac{\text{J}}{\text{s m}^2} \div \left(\frac{\text{J}}{\text{kg K}} \frac{\text{kg}}{\text{m}^2} \right) \\
 h_{column} &= 0.014 h_{column} \\
 \text{unit analysis : } \frac{\text{K}}{\text{day}} &= \left(\frac{\text{day}}{\text{K}} \frac{\text{s}^3}{\text{kg}} \right) \frac{\text{J}}{\text{s m}^2}
 \end{aligned} \tag{5.11}$$

Before the latent heating rate in K/day can be calculate, the column heat capacity ($c_p m_{column}$) must be calculated as the column mass times the heat capacity of one kilogram of air. Based on these considerations, the column heat capacity is $7e6 \text{ J/K} = 1004 \text{ J/kg K} \times 0.87 \times 7e3 \text{ kg} \times 1.09 \text{ kg/m}^3$. For an observation of 2 g/kg of liquid water concentration in the cell, equations 5.9 and 5.11 show that the air column warms by 532 K/day. For an observation of a 100 mm/h surface rain rate under the cell, the air column warms by 966 K/day. The 966 K/day heating rate is the rate implied by the baseline estimate shown in Table 5.2.

At first glance, a 966 K/day heating rate might seem to be two orders of magnitude too great. Convective heating rates are typically reported in the 1 to 5 K/day range. However, those reported values are generally for an average over large areas (1×1 degrees of latitude) and for a period as long as a full day. For such a large area and long period, most of the locations most of the time do not contain a vigorous convective cell.

In contrast, there is evidence for tall cells having heating rates in excess of 100 K/day during the 20 to 40 minutes that they exist with their full vigor. *Montgomery and Enagonio* [1998, p. 3179] report a 360 K/day heating rate in convective cells in mesoscale convective systems. *Hendricks* [2004] presents an even faster heating rate, but his results must first be converted from potential temperature θ to observed temperature T . *Hendricks* [2004, p. 1214] simulates a 960 to 1920 K/day heating rate $\Delta\theta$ for mid-tropospheric potential temperature at the center of a vigorous eyewall cell. The cell had a 7 km diameter. The definition of potential temperature is

$\frac{\theta}{T} = \left(\frac{p_0}{p} \right)^{0.286}$ [Wallace and Hobbs, 2006, p. 78]. Using this definition, the observed temperature change ΔT is 786 to 1574 K/day. *Rodgers et al.* [2000] observe azimuthally averaged latent heating rates of 70 to 210 K/day in the eyewall of Typhoon Paka (1998). The azimuthal average can be converted into a tall cell heating rate using the fact that *Braun* [2002] finds that 37% of the eyewall latent heat is released in the 10% of the eyewall with the most vigorous convection. Multiplying *Rodgers et al.*'s azimuthally averaged heating rate by 37% and dividing by 10% results in a heating rate of 285 to 777 K/day for the vigorous eyewall cells.

In summary, the latent heating rate (K/day) implied by section 5.2's thermodynamic upper limit (Table 5.2) appears high but is just barely within the range of observed and modeled latent heating rates. This result is further evidence that the heating rate and intensification rate estimate in section 5.2 should be considered the maximum possible achievable from a 9 hour long burst of tall eyewall cells.

5.5. Tall eyewall cells as causes of intensification: catching them in the act of warming the eye

This section looks for evidence of eyewall cells heating the eye in a high resolution simulation. This eye heating rate is compared with the maximum possible rate estimated earlier in this chapter.

The 2 km simulation of Hurricane Bonnie from August 22 to 24, 1998, was first described in *Braun et al.* [2006, Part I]. This simulation has a higher resolution than the 4 km simulation of Hurricane Bonnie performed by *Zhu et al.* [2002, 2004, and 2006]. To review, *Braun et al.* [2006, Part I] find that the upward flow of air in the eyewall is concentrated in a few cells that are associated with mesovortices. *Braun* [2006, Part II] discusses the flow of atmospheric water in various forms. *Cram et al.* [2007] find that a significant mass of air flows from outside the eyewall under the eyewall and into the eye.

One reason why August 22 to 24 is chosen for this simulation is that a field campaign collected data during these days [*Heymsfield et al.*, 2001]. The observations of Hurricane Bonnie during the period of simulation show significant subsidence from tall eyewall cells. In particular, *Heymsfield et al.* [2001] observed a subsidence region with downward velocities of several meters per second that extended 25 km into the eye and that had a vertical extent of 9 km.

The simulation discussed in this section is a run of the MM5 mesoscale model run by *Braun et al.* [2006]. The simulation covers 30 hours with 15 minute time steps that are initialized and forced with NCEP reanalysis data. During this period, Hurricane Bonnie intensified from category 2 to category 3, experiencing a 15 kt wind intensification from 85 kt to 100 kt according to the National Hurricane Center (NHC) best track database. The horizontal resolution of the inner grid was 2 x 2 km with 27 vertical levels. The vertical levels are spaced ~100 meter apart in the lower troposphere

and 1 to 2 km apart in the upper troposphere.⁸ *Braun et al.* [2006] concentrate the vertical levels in the bottom 1 km in order to resolve the majority of the low-level eyewall inflow [*Cram et al.*, 2007].

5.5.1. Kinematics and dynamics of a simulated tall eyewall cell

To show the kinematic situation at the top of the tall eyewall cell, Figure 5.7a to 5.7c show simulated radar reflectivity contours (20, 30, and 40 dBZ) with simulated velocity superimposed using arrows for horizontal velocity and symbols for vertical velocity. Velocity is displayed in cylindrical coordinates, scaled differently for each of the three cylindrical components as indicated in the individual legends above panels a to c. Scaling is needed to bring out features of each velocity component. In this tall eyewall cell, at this time step, and at this altitude, the radial transport is predominantly inward toward the eye's center. This eyeward motion is the most important feature of the kinematic situation at the 14.9 km level.

This radially inward mass flux could be circulation forced by the tall eyewall cell. Most cells in the simulation do not have approximately 100% of the outflow going eyeward as this cell does. This cell was chosen because it illustrates how forced subsidence can occur with eyeward outflow. The model results are consistent with the observational results of *Heymsfield et al.* [2001]: the outflow from some of the tall eyewall cells is associated with eye warming through subsidence.

⁸ The vertical levels in Braun's simulation are the following five levels in the bottom 1 km of the atmosphere: 0.040, 0.122, 0.245, 0.453, and 0.753 km. From 1 to 5 km, there are the following ten levels: 1.1, 1.5, 1.9, 2.2, 2.7, 3.1, 3.5, 4.0, 4.5, and 5.0 km. The twelve upper tropospheric levels are 5.5, 6.2, 6.8,

By tracing the evolution of several tall eyewall cells in this MM5 simulation of Hurricane Bonnie, the author estimates that typically 10 to 20% of the mass flux out of the tall eyewall cells flows inward toward the eye's low pressure center. Density is roughly constant at a given altitude, so horizontal velocity is approximately proportional to horizontal mass flux. Similarly, *Schubert et al.* [2007, Table 1] find that 13% to 21% of eyewall outflow tends to subside in the eye. This fact was used in an earlier section of this chapter to select 20% as the upper limit of the fraction of the eyewall outflow that enters the eye. The outflow layer is very close to the top of the simulation's vertical grid, so the simulation is just barely able to estimate outflow velocity.

Having finished with the kinematic situation at 14.9 km, the dynamic situation at the same altitude is now examined. The dynamic situation considers the forcing that causes temperature change. Panels d through g of Figure 5.7 show grayscale images of simulated temperature, water vapor mixing ratio, cloud water mass, and precipitation water mass. Darker shades of gray indicate higher values for each variable. Superimposed on these images is the same vertical velocity shown in panel c. In addition, a green contour line outlines the tall eyewall cell's 20 dBZ radar reflectivity boundary.

The temperature anomaly at 14.9 km altitude (panel d) is interesting for two reasons. First, there is evidence of the cell's updraft overshooting its level of neutral buoyancy because the updraft's temperature is cooler (light gray) than its surroundings (medium gray). It is reassuring to see an "overshooting top" in the model output because

7.5, 8.2, 9.0, 9.9, 10.9, 12.0, 13.3, 14.9, and 17.2 km.

observations (section 3.6) and theory (section 2.7.3) lead us to expect an overshooting top at the top of a vigorous convective cell. Second, the maximum temperature (dark gray) occurs in the downdraft on the eye side of the tall eyewall cell, as indicated by the red circle in panel d. This temperature maximum cannot be due to water vapor condensing because, in a downdraft, one expects precipitation to evaporate, which cools the downdraft air. In fact, panel d shows that the downdraft is warmer (darker gray) than the eye air adjacent to it. The water vapor (panel e) and precipitation (panel g) is consistent with this warm feature. Precipitation mass is in fact low (bright white) in the downdraft, which is consistent with precipitation evaporating in the downdraft, and the water vapor density is higher (dark gray) in the downdraft, which is also consistent with evaporation adding to the water vapor density in the downdraft.

This single snapshot cannot prove that the tall eyewall cell is causing permanent eye warming that mixes throughout the eye. Nonetheless, the just described warm region in the downdraft suggests that the tall cell's outflow is causing at least temporary eye warming in one portion of the eye.

To support the preceding analysis at 14.9 km, it is helpful to interpret the patterns at 10.9 km (Figure 5.8, p. 273). At a 10.9 km altitude, the updraft is much stronger (5 to 10 m/s). The updraft exceeds 6 m/s over a 5 km by 10 km area (panel c), and the horizontal radial motion is much slower at 10.9 km than at the higher altitude previously examined. At the 10.9 km altitude, there is little temperature variation in the eye, but the tall eyewall cell's updraft is significantly warmer and more moist than anything else nearby (the dark gray regions in panels d through g). All of these features are what you

would expect if the motion in the tall eyewall cell were predominantly up at a 10.9 km altitude, with the outflow occurring at a higher altitude. In addition, there is evidence at a 2 km altitude (not shown) of a mesovortex at the base of the tall eyewall cell. The 1 to 4 km altitude range is used by *Braun et al.* [2006, part 1, Figure 16] to track mesovortices associated with tall eyewall cells.

The next step is to examine the vertical structure of the tall eyewall cell and the neighboring region of the eye where subsidence is occurring. Figure 5.9a (p. 274) shows the horizontal location of the tall eyewall cell (black box), the subsidence region (green box), the neighboring region of the eye outside the subsidence region (red box), and the majority of the eye (blue circle) defined as all locations within 40 km of the center of the tropical cyclone. The upper tropospheric profile of updraft velocity for these regions is shown in Figure 5.9b. The tall eyewall cell has the strongest updraft speed and its updraft speed peaks at a 12 km altitude, dropping to near zero at the simulation's top grid box at a 17 km altitude. Figure 5.9b also shows a local maximum downdraft speed of approximately 1 m/s in the subsidence region at 15 km, near the top of the tall eyewall cell.

Figure 5.9c shows the vertical profile of temperature in these regions. To highlight the temperature differences between the regions, the background temperature profile is subtracted from all of the other temperature profiles. The background temperature is the average temperature at a given altitude within 140 km of the center of the tropical cyclone. At 15 km, only the tall eyewall cell is colder than the background profile, which suggests that the strong updraft in the tall eyewall cell may have

overshot its level of neutral buoyancy. A situation mentioned earlier in the chapter is also visible in Figure 5.9c. The eyewall air (black) is cooler than the overall average temperature of the eye (blue) except near 11 km, where there is no outflow from the eyewall.

In this simulation, warming of the eye through mixing with eyewall air is possible because the eyewall air is warmer than the portion of the eye near the eyewall (red) over a broad altitude range (10 to 13.5 km). The subsidence region from the cell outflow (green) is no warmer than the overall temperature of the eye (blue), but the subsidence region is warmer than the nearby portion of the eye (red). This suggests that the forced subsidence could warm the eye. In short, this high-resolution tropical cyclone simulation suggests that the eye could be warmed by both simple mixing and forced subsidence.

There are other possible explanations for the eye warming that have nothing to do with the tall cell, such as gravity waves passing through this region of the eye. Because it is not possible to say with certainty what the cause of the eye warming is, this dissertation supposes for the sake of argument that the eye warming is caused by the tall cell. Having made this assumption, the dissertation can then attempt to quantify how much warming occurred and compare that amount of warming to the theoretical maximum warming rate estimated in section 5.2.

5.5.2. Eye warming and wind intensification

To be more quantitative, several examples of tropical cyclone eye subsidence are evaluated to see what eye heating rate they imply if all of the added heat were to mix

throughout the eye. The examples are the simulated cell discussed above, a cell observed by aircraft in Hurricane Bonnie (1998), and two examples not related to tall eyewall cells.

One of these examples is the subsidence warming displayed in Figure 5.9c. The warming in Figure 5.9c would be sufficient to cause a fraction of the maximum wind intensification estimated in section 5.2 if the tall eyewall cell in Figure 5.9c were part of long-duration convective burst and if the warming shown in Figure 5.9c were permanent. Figure 5.9c shows a 1 K warming due to forced subsidence over approximately a 2 km thick layer at a 15 km altitude over a horizontal area with radius $r_{subsiding}$ of approximately 10 km. It would be reasonable to assume that this mass of air could be warmed by this tall eyewall cell during the cell's ~15 minute long mature phase.

Another example is the tall eyewall cell observed in Hurricane Bonnie (1998) [Heymsfield *et al.*, 2001]. This observed cell could warm the eye at a greater rate than the simulated cell shown in Figure 5.9c. From Figure 10 of Heymsfield *et al.* [2001], it is reasonable to suppose that the eye subsidence warms by 2 K a 5 km radius cylinder of upper and mid-tropospheric eye air over a depth that includes half of troposphere's mass (See also Figure 7 of Heymsfield *et al.*, 2001).

To calculate the eye warming, take the warming rate of the subsidence region and multiply by the duration of the subsidence and by the ratio f of the subsidence mass $m_{subsiding}$ (kg) to the mass of the entire eye below 120 mbar m_{eye} (kg). The mass of the eye below 120 mbars has been previously calculated by equation 5.3 (p. 235).

$$f = \frac{m_{subsiding}}{m_{eye}} = \frac{\pi r_{subsiding}^2 \rho \Delta z}{0.87 \pi r_{eye}^2 \rho_0 z_0} \quad (5.12)$$

In the above equation, Δz is the altitude thickness of the subsidence volume, ρ is the air density at the altitude of the subsidence, $r_{subsiding}$ is the radius of the cylinder of subsiding air, r_{eye} is the radius of the eye (40 km for Hurricane Bonnie (1998) [Braun *et al.*, 2006, Figure 7]), ρ_0 is the surface density, and z_0 is the atmospheric scale height.

Substituting into equation 5.12, the simulated and observed cells just described result in the following fraction of the eye subsiding:

$$f_{simulated} = \frac{(10e3 \text{ m})^2}{0.87 (40e3 \text{ m})^2} \frac{0.15 \frac{\text{kg}}{\text{m}^3}}{1 \frac{\text{kg}}{\text{m}^3}} \frac{2e3 \text{ m}}{7e3 \text{ m}} = 3.1e - 3$$

$$f_{observed} = \frac{(5e3 \text{ m})^2}{0.87 (40e3 \text{ m})^2} \frac{(\frac{1}{2} p_0 z_0)}{p_0 z_0} = \frac{1}{0.87} \frac{1}{2} \left(\frac{5}{40} \right)^2 = 9.0e - 3$$
(5.13)

The results from equation 5.13 appear in row 5 of Table 5.5 (p. 267).

Row 6 of Table 5.5 gives the overall change in eye temperature if the heating rate stated in row 4 occurs for 9 hours in the fraction of the eye stated in row 5. Row 7 of Table 5.5 is the estimate of the increase in wind intensity assuming that a 1 K increase in eye thermal anomaly results in a 7 knot wind intensity increase (section 2.8.4, p. 86).

The entries in Table 5.5 can be compared to the theoretical maximum heating rate calculated earlier in section 5.2. The maximum heating rate in section 5.2 is 26 knots for a small eye ($r_{eye} = 20 \text{ km}$) and 6 kt for a large eye ($r_{eye} = 40 \text{ km}$). Braun *et al.* [2006, Figure 7] found that Hurricane Bonnie's eye in the simulation had a 40 km radius. The wind intensification possible from the Hurricane Bonnie simulation and observed cells in Table 5.5 are 13% and 33% of the theoretical maximum of 6 knots.

Observed values that are just ~10% of the theoretical maximum occur elsewhere in atmospheric physics. For example, section 2.7.3 shows how drag and entrainment can reduce updraft speed to 10% of the theoretical maximum. *Emanuel* [2000] finds that there is an equal probability of a tropical cyclone having any given percent of its maximum possible intensity. In other words, 10% of tropical cyclones achieve no more than 10% of their theoretical maximum intensity.

As points of reference, Table 5.5 also shows two examples of subsidence that are unrelated to tall eyewall cells. First, *Schubert et al.* [2007] model a ring of subsidence along the outer portion of the eye. If the eye radius were 25 km and the ring of eye subsidence were 5 km wide horizontally, then the fraction of the eye mass subsiding in the ring is as follows:

$$f_{ring} = \frac{25^2 - 20^2}{25^2} = 0.36 \quad (5.14)$$

If the heating by the ring of subsidence mixes into the entire eye, then the heating could warm the entire eye by 13 K in 9 hours.

Second, *Willoughby* [1998] states that typical intensifying tropical cyclones have eye subsidence of ~ 1 cm/s between the boundary layer and the top of the tropical cyclone. Suppose a 950 mbar eye surface pressure, a 100 mbar thick boundary layer, and a 120 mbar top of the tropical cyclone eye. Further, suppose an isothermal atmosphere so that pressure change is proportional to the mass inside the layer. Under these assumptions, equation 5.15 states the fraction of the eye mass below 120 mbar that is subsiding:

$$f_{uniform} = \frac{850 - 120}{950 - 120} = 0.88 \quad (5.15)$$

A subsidence at a rate of 1 cm/s would cause, through adiabatic compression, 3 K of warming in 9 hours. This warming is a result of 1 cm/s equaling 0.32 km in 9 hours and the dry adiabatic lapse rate being approximately 10 K/km. This result is shown in row 6 of Table 5.5.

5.6. Tall eyewall cells as indicators of intensification

This section determines that a tall eyewall cell contains statistical information about wind intensification that is not present in other widely used predictors of intensification: recent change in wind intensity, sea surface temperature, and vertical wind shear (section 2.11, p. 119).

The sea surface temperature, wind shear, and other commonly used predictors were obtained by the author from Mark DeMaria, the developer of the Statistical Hurricane Intensity Prediction Scheme (SHIPS). The SHIPS database contains the values of these variables as determined in post-season analysis, which is data of higher quality than the values of these same variables that are available during realtime forecasting. Since 1994, the National Hurricane Center (NHC) uses SHIPS operationally when working on official forecasts of tropical cyclone wind intensity [*DeMaria et al.*, 2005]. Starting before the 1997 launch of the TRMM satellite, the SHIPS predictor variables are available for Atlantic tropical cyclones (i.e., hurricanes) every six hours at the times that

official NHC forecasts are made. Out of 163 TRMM world-wide tropical cyclone overflights in 1998 to 2003 only 43 occur in the Atlantic. Therefore, only these 43 overflights have SHIPS predictor variables available.

The first step in the analysis is to verify that the results of chapter 3 apply to the subset of 43 overflights over the Atlantic. The 43 overflights are segregated into two populations, those with a TRMM-observed tall eyewall cell ($20 \text{ dBZ} \geq 14.5 \text{ km}$) and those without one. The closest NHC reporting time to the TRMM observation is determined and the SHIPS predictors for that time are noted for use later in the analysis. In addition, the change in wind intensity from that reporting time and 12 hours in the future is also noted. This information is tabulated in Table 5.7 (p. 269). A statistical test is applied to determine that the intensity change in these two populations of TRMM overflights are different. More specifically, a one-sided t-test with separate variances shows that the mean intensity change is different in the two populations at the 0.05 significance level. The intensifying population contains 7 tropical cyclone overflights with a mean intensity change of +2.9 kt and a standard deviation of 6.3 kt. The non-intensifying population contains 36 tropical cyclone overflights with a mean intensity change of -2.9 kt and a standard deviation of 10.0 kt. This t-test verifies, on this Atlantic-only overflights, that the results of chapter 3 apply, i.e., the presence of a tall eyewall cell does contain statistical information about wind intensity increase.

The second step in the analysis is to determine if tall eyewall cells contain unique information, information that is not contained in other statistical predictors. A simple way to address this question is to perform multiple linear regression on three predictors

that are known to influence wind intensity plus the eyewall's maximum height of the 20 dBZ signal ($h_{20\text{ dBZ}}$). The three well-established predictors are intensity change during the preceding 12 hours ($\Delta I(0-12)$), sea surface temperature (SST), and wind shear (SHR). Obviously, the statistical power of eyewall cell height will be smaller when other powerful predictors are included in the regression. Using the original floating-point values found in Table 5.7, the statistical significance of the predictors are shown in column 2 of Table 5.3. In this regression, the only predictor that appears significant at the 0.05 level is the previous 12 hour change in intensity. In contrast, the shear parameter was statistically significant in the SHIPS model, but that may be because *DeMaria and Kaplan* [1999] were using a much larger sample of observations than are available in this dissertation. In this dissertation, the SHIPS predictors must have a TRMM Precipitation Radar overflight within 3 hours to be included in the analysis.

Table 5.3. Multiple linear regression to forecast intensity change from the present to 12 hours in the future for TRMM Precipitation Radar overflights of North Atlantic tropical cyclones from 1998 to 2003. Columns 2 and 3 state the statistical significance of the predictors in the regression.

1. Predictor name	2. Floating point predictors of $\Delta I(+12,0)$	3. Binary predictors of $\Delta I(+12,0) > 0$	4. Thresholds for binary predictors
$\Delta I(0,-12)$	0.019	0.066	$\Delta I(0,-12) > 0$ kt
SST	0.182	0.252	$SST > 28$ K
SHR	0.173	0.124	$SHR > 15$ kt
$h_{20\text{ dBZ}}$	0.313	0.114	$h_{20\text{ dBZ}} \geq 14.5$ km

Based on the analysis in chapter 3, it may be more appropriate to perform a multiple linear regression to predict intensification ($\Delta I > 0$ kt) and non-intensification (ΔI

≤ 0 kt), not to predict the floating-point value of intensity change ΔI . Similarly, it may be more appropriate to use binary values for the predictors because the fundamental predictor in chapter 3 was the binary choice of either at least one tall eyewall cell ($20 \text{ dBZ} \geq 14.5 \text{ km}$) or no tall eyewall cells. The binary predictors are defined in column 4 of Table 5.3, and their statistical significance is shown in column 3 of Table 5.3. In the binary regression, the presence of a tall eyewall cell appears similar in statistical power to wind shear and more powerful than sea surface temperature. A possible explanation for this result is that the sea surface temperature used in the SHIPS model is a weekly average, whereas the tall eyewall cell observed by the TRMM satellite occurs within 3 hours of the forecast time. The timeliness of the TRMM overflight may mean that TRMM observations better represent the current state of the tropical cyclone than does the previous week's average sea surface temperature.

The author is not disturbed that the height of eyewall convection appears statistically insignificant (at the 0.05 level) in multiple linear regression. If tall eyewall cells had been statistically significant in multiple linear regression, then tall cells would probably already be in operational use in the SHIPS model and there would be no need to write this dissertation. The height of eyewall convection is a worthy topic for a dissertation precisely because tall eyewall cells are a marginally significant predictor of intensity that has never been fully examined by forecasters. As discussed in this section, tall eyewall cells taken alone are statistically significant predictors of wind intensification and they contain some information that appears to be independent from sea surface temperature and wind shear.

To quantify the amount of information in tall eyewall cells, consider the linear covariance matrix shown in Table 5.4. In the table, the covariance is multiplied by 100 so that it states the percentage of the variance in one variable that is explained by variations in another variable. Variance explained is sometimes referred to as "R squared" or the "coefficient of determination" [Montgomery and Runger, 2003, pp. 397–398; Bhattacharyya and Johnson, 1977, p. 396]. The covariance matrix states that the maximum height of eyewall cells alone explains approximately 7% of the intensity change 12 hours in the future $\Delta I(+12,0)$ and 17% of the intensity change during the 12 hour period centered on the time the tall eyewall cells were observed $\Delta I(+6,-6)$. These two entries are in bold text in Table 5.4. The table shows that wind shear does not completely determine the maximum height of eyewall cells. On the contrary, wind shear explains only 1% of the variance in the maximum height.

Table 5.4. Percent variance explained in TRMM Precipitation Radar overflights of North Atlantic tropical cyclones from 1998 to 2003. Rows 1 through 5 come from the SHIPS predictor database and row 6 comes from TRMM observations.

	$\Delta I(+12, 0)$	$\Delta I(+6, -6)$	$\Delta I(0 -12)$	SST	shear	h_{20dBZ}
1. $\Delta I(+12, 0)$	100	-	-	-	-	-
2. $\Delta I(+6, -6)$	59	100	-	-	-	-
3. $\Delta I(0, -12)$	22	72	100	-	-	-
4. SST	11	16	12	100	-	-
5. shear	9	7	8	14	100	-
6. h_{20dBZ}	7	17	19	4	1	100

Column and row definitions

$\Delta I(+12, 0)$ Future change in intensity (kt) between 12 hours in the future and the present using the NHC best track winds

$\Delta I(+6, -6)$	Current change in intensity (kt) between 6 hours in the future and 6 hours in the past using the NHC best track winds
$\Delta I(0, -12)$	Past change in intensity between the present and 12 hours in the past using the NHC best track winds
SST	Reynolds SST (C) for the previous week
shear	The 850 to 200 mbar wind shear from the NCEP reanalysis (not the realtime estimate of wind shear)
h_{20dBZ}	The maximum height of the 20 dBZ radar reflectivity signal observed by the TRMM Precipitation Radar in the tropical cyclone's eyewall

This section comes to the conclusion that observing the maximum height of tall cells in the eyewall does provide independent information about tropical cyclone intensification that is not present in wind shear estimates. This result holds true even when using the wind shear estimates from the NCEP reanalysis (as is done in this section), which are more accurate than the estimates of wind shear that are available in realtime when operationally forecasting intensity.

It is difficult to choose between two possible interpretation of the results described above. The choice revolves around how much one trusts the sea surface temperature and NCEP estimates of wind shear. The first possibility is that the radar-observed tall cells indicate intensification for reasons independent of the actual shear and sea surface temperature experienced by the tropical cyclone. The second possibility is that radar-observed tall cells provide additional information about shear and temperature that are missing in the limited accuracy of the best available estimates of shear and temperature. *Law [2006, Ph.D.]* discusses the limited accuracy of wind shear estimates.

It is very difficult to measure the sea surface temperature under a tropical cyclone because clouds block most satellite estimates of sea surface temperature and

heavy precipitation blocks all satellite estimates of sea surface temperature [*Chelton et al.*, 2000]. Perhaps for this reason, the SHIPS model uses sea surface temperature estimates averaged over the preceding week. Under mild weather conditions, the ocean's surface temperature does not vary much from the previous week's average temperature [*Chelton et al.*, 2000]. In contrast, a tropical cyclone can lower the sea surface temperature by 5 K in a few hours [*Wentz et al.*, 2000]. During that time, the tropical cyclone's winds are mixing up cool water from below the ocean's surface.

Similarly, it is difficult to come up with a single number to quantify the environmental wind shear that a tropical cyclone experiences. *DeMaria et al.* [2005] experiment with several altitudes and distance thresholds to come up with their preferred estimate of wind shear. This section uses one of their preferred methods: the shear between 850 and 200 mbar calculated between 200 and 800 km away from the tropical storm's center, based on synoptic model output. Even if synoptic scale forecast models were perfectly able to estimate wind shear in normal circumstances, it would still be difficult to separate out the fast winds of the tropical cyclone in order to calculate the background wind shear that is superimposed on the tropical cyclone vortex. In contrast to the difficulty of measuring wind shear or sea surface temperature, the height of convective cells in the eyewall is easy to measure with a radar as precise as the TRMM Precipitation Radar.

5.7. Future work

This chapter has estimated how much of the observed wind intensification could be due to the latent heat released by a burst of tall eyewall cells. This estimate uses coefficients whose values are only approximately known. For example, the ratio of eyewall latent heat release to eye warming is poorly known (section 5.2.2, p. 234). The uncertainty in these coefficients translates into uncertainty in the final estimate of wind intensification. Future work that measures these coefficients could be used to improve the estimates of wind intensification. Because this dissertation primarily focused on data analysis, there is further work that can be done to model tall cells in high-resolution tropical cyclone simulations.

Table 5.5. Examples of eye subsidence warming. The table is described in section 5.5.2 (p. 255).

1. Tropical cyclone	Hurricane Bonnie (1998) simulation	Hurricane Bonnie (1998) observation	Hurricane Guillermo (1997) simulation	An intensifying tropical cyclone
2. Data source	<i>Braun et al.</i> , 2006, part 1	<i>Heymsfield et al.</i> , 2001, Figure 10	<i>Schubert et al.</i> , 2007, Figure 8	<i>Willoughby</i> , 1998
3. Type of eye subsidence, see Figure 2.10 (p. 84)	Subsidence next to tall eyewall cell	Subsidence next to tall eyewall cell	Ring of subsidence	Uniform subsidence above the boundary layer
4. Warming rate H in the subsiding region	4 K/h = 1 K in 15 minutes	4 K/h = 2 K in 30 minutes	4 K/h	0.35 K/h = 8.5 K in 24 hours
5. Fraction f of eye mass subsiding below 120 mbar	$f_{\text{simulated}} = 3.1\text{e-}3$	$f_{\text{observed}} = 9.0\text{e-}3$	$f_{\text{ring}} = 0.36$	$f_{\text{uniform}} = 0.88$
6. Eye temperature change ΔT after 9 hours, $\Delta T = 9 H f$	0.11 K	0.32 K	13 K	3 K
7. Intensification using 7 kt/K relationship (section 2.8.4, p. 86)	0.8 kt	2 kt	91 kt	21 kt

Table 5.6. Energy conversion ratios in atmospheric convection

Data source	Conversion ratio	Carnot efficiency	Reference
The efficiency with which potential energy is converted into kinetic energy that remains within the Rossby radius of deformation in an idealized case of pure geostrophic flow	33%	--	<i>Holton</i> , 1992, pp. 215–216
In tropical cyclones, the fraction of heat transferred from the ocean that ends up as mechanical work of overcoming the friction between ocean and air	0 to 33%	33%	<i>Emanuel</i> , 2000, the statistical study
From solar input to radiation to space ($T_{\text{inflow}} = 295 \text{ K}$; $T_{\text{outflow}} = 255 \text{ K}$)	15%	15%	<i>Michaud</i> , 1995
The efficiency with which latent heat release in the eyewall is converted into convective energy of a tropical cyclone's vortex	5%	--	<i>Nolan et al.</i> , 2007, Figure 21a
The fraction of latent heat released in a hurricane eyewall that is converted into the work of warming the eye	1.4–3.3%	--	<i>Malkus and Riehl</i> , 1960, Table 11
From solar input to radiation to space	0.8%	--	<i>Peixoto and Oort</i> , 1992, cited in <i>Michaud</i> , 1995
From solar input to radiation to space	0.5%	10%	<i>Goody</i> , 2003
Convective precipitation averaged over the whole atmosphere	$0.55 \epsilon_{\text{carnot}}$	--	<i>Pauluis et al.</i> , 2000

Table 5.7. North Atlantic TRMM overflights of tropical cyclones in 1998 to 2003 with SHIPS predictor values available ¹

1. Tropical cyclone, NAME.yymmdd.hh	2. Future intensity change (kt), $\Delta I(+12,0)$	3. Past intensity change (kt), $\Delta I(0,-12)$	4. Weekly sea surface temperature (C), SST	5. Wind shear (kt)	6. 20 dBZ height (km)
BONN.980822.18	10	15	29.6	9.80	17.0
KARL.980925.17	5	15	28.1	9.30	16.0
JEAN.980927.15	0	0	27.8	3.00	16.0
ISID.020921.11	10	25	29.4	13.6	15.5
BRET.990821.22	5	40	29.7	12.8	15.0
KYLE.020927.07	-5	0	28.6	28.9	15.0
FELI.010915.06	-5	0	27.2	13.5	14.5
HUMB.010924.04	-5	-5	25.5	28.1	14.25
DENN.990828.17	0	15	29.4	7.10	13.75
ISAA.000929.21	-10	-20	26.4	21.4	13.5
ISAB.030910.21	10	10	28.4	5.10	13.25
JUAN.030927.17	0	15	27.1	23.2	13.25
GEOR.980927.	0	5	28.5	18.0	13.25
GERT.990916.07	-10	5	28.7	15.8	13.25
CIND.990829.11	-10	-20	27.9	22.9	12.5
JUAN.030926.19	5	10	26.7	14.3	12.25
GEOR.980919.03	30	5	28.9	7.60	12.0
FLOY.990913.09	-20	10	29.4	4.60	12.0
IRIS.000117.03	5	0	29.3	12.6	11.75
ISAB.030912.04	0	-5	28.2	4.10	11.75
BONN.980826.14	-5	0	28.7	2.00	11.75
ISAB.030916.20	0	-5	29.0	23.9	11.5
BONN.980824.10	0	0	29.9	30.7	11.5
KATE.000316.12	-10	-5	25.7	24.2	11.5
JUAN.030926.16	5	10	26.7	14.3	11.0
CIND.990828.11	0	20	28.7	13.8	11.0
ISAB.030914.21	-10	-5	28.8	3.70	11.0
FABI.030906.03	0	-5	27.8	14.0	10.75
FABI.030906.05	0	-5	27.8	14.0	10.75
FELI.010917.06	-10	-5	24.8	22.1	10.75
GERT.990922.09	-10	-5	27.0	27.2	10.75
LENN.991116.16	20	10	28.8	9.90	10.5
KYLE.020926.13	0	10	28.5	11.3	10.5

KATE.000314.15	-15	10	27.3	19.1	10.5
MITC.981029.00	-15	-30	29.0	26.2	10.25
ISAB.030915.03	-10	-15	28.9	5.30	10.0
BONN.980827.12	-10	-20	27.5	6.50	9.75
ERIN.010910.21	0	-20	26.9	16.8	9.50
FELI.010916.08	-10	-5	26.2	20.4	9.25
CIND.990822.10	-15	0	26.6	18.9	8.75
BONN.980826.11	-5	0	28.7	2.00	8.50
CIND.990830.12	-10	-10	27.5	33.4	8.50
ALBE.00810.22	10	5	28.6	10.4	8.25

¹ Column 1 states the first four letters of the name of the tropical cyclone, the date as the two digit year, month, and day of month, and the hour in universal time of the TRMM overflight. Columns 2 to 5 come from the SHIPS database [DeMaria *et al.*, 2005] at the closest reporting time to the TRMM overflight. The database values are available at 0, 6, 12, and 18 UT each day for each North Atlantic tropical cyclone since the mid-1990s. Column 2 is the future intensity change that the multiple linear regression is trying to forecast. Column 2 is the intensity difference between the closest reporting time and 12 hours later. Column 3 is the recent intensity change, i.e., the intensity difference between the closest reporting time and 12 hours prior. Column 4 is Reynolds sea surface temperature for the preceding week, which is designated "RSST" in the SHIPS database. Column 5 is the 850 to 200 mbar wind shear from the NCEP reanalysis, which is designated "SHRD" in the SHIPS database. Column 6 is the maximum height of the 20 dBZ signal in the tropical cyclone's eyewall observed by the TRMM Precipitation Radar. The first seven TRMM overflights (top seven rows) contain an eyewall cell designated as "tall" using the threshold established in chapter 3 ($20 \text{ dBZ} \geq 14.5 \text{ km}$). The remaining rows in the table are for TRMM overflights without any tall eyewall cells. The rows of the table are sorted by decreasing 20 dBZ height. The TRMM overflights in this table are used to calculate the results reported in Tables 5.3 and 5.4.

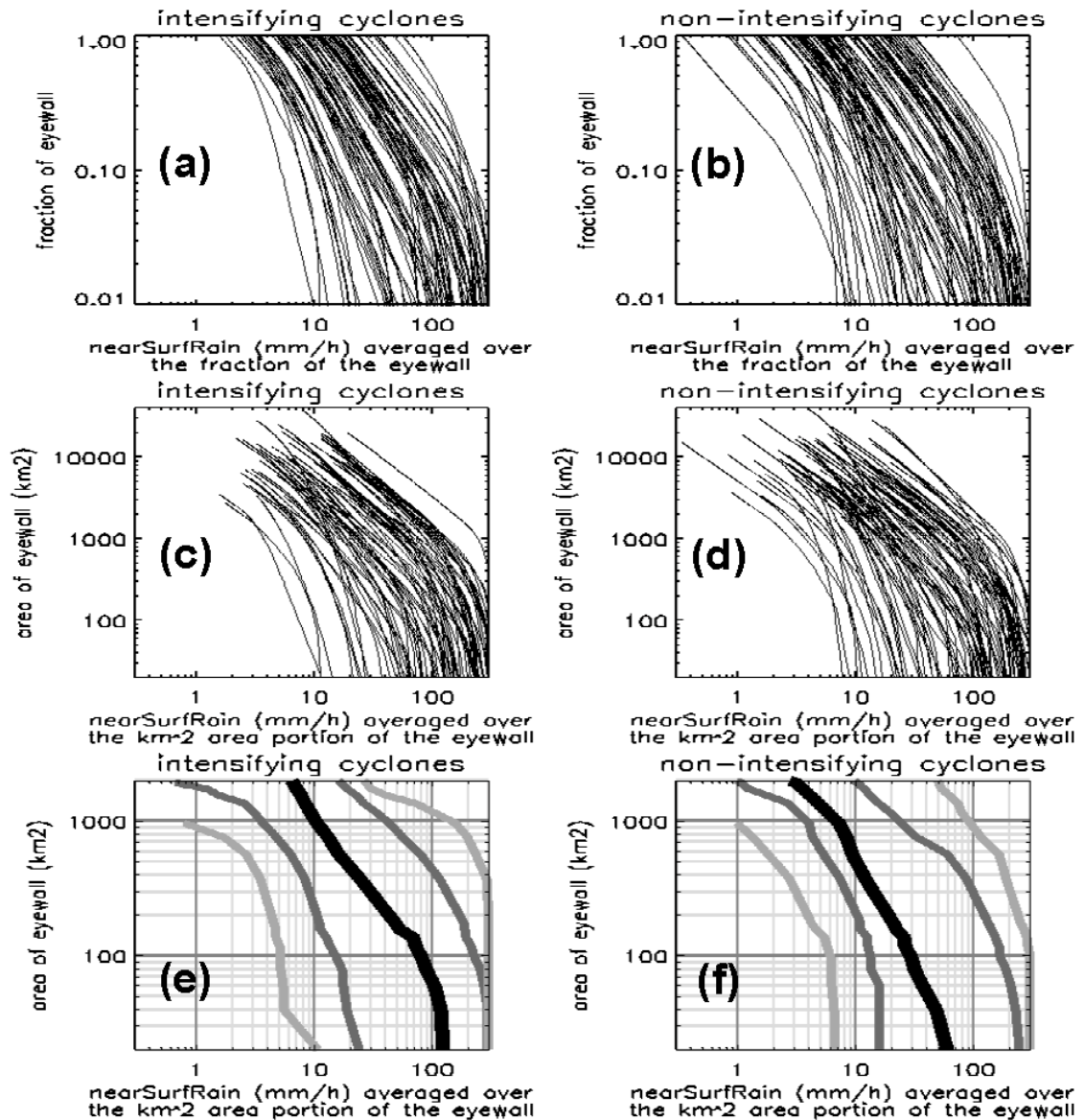


Figure 5.6. The distribution of eyewall average surface rain rates observed by the TRMM Precipitation Radar in 1998 to 2003. (a) For the eyewall of 78 intensifying tropical cyclones, the horizontal axis states the variation in the average surface rain rate as a function of the fraction of the eyewall specified in the vertical axis. (b) The same as panel a, except for 89 non-intensifying tropical cyclones. (c) For intensifying tropical cyclones, the average surface rain rate as a function of the horizontal area specified in the vertical axis. (d) The same as panel c, except for non-intensifying tropical cyclones. (e,f) Panels e and f summarize panels c and d. Panels e and f show the minimum, 10th percentile, 50th percentile, 90th percentile, and maximum of the average surface rain rates shown in panels c and d.

Near the top of a tall eyewall cell: 14.9 km high in a tropical cyclone simulation

Near the top of this cell, the azimuthal outflow superimposed on the counter clockwise (cyclonic) flow results in a net rapid azimuthal flow in front of the cell (to the north) at 30 m/s and a net near zero azimuthal flow behind the cell (to the south).

Schematic diagram

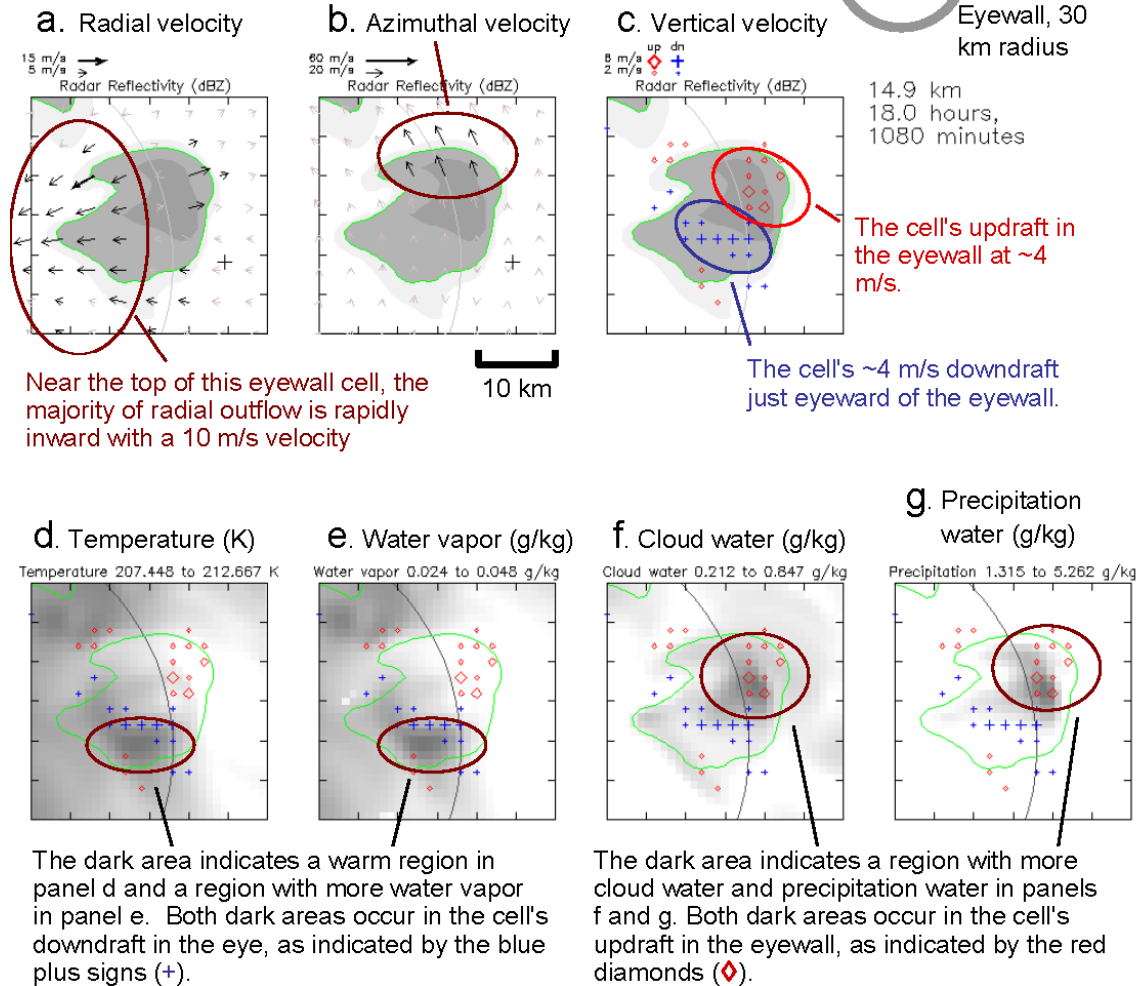
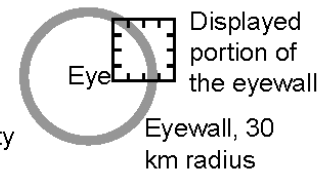


Figure 5.7. Subsidence heating from a tall eyewall cell observed in a simulation of Hurricane Bonnie 1080 minutes (18 hours) after the beginning of the simulation at a height of 14.9 km. The plots show the following simulated quantities: velocity represented by arrows and symbols, radar reflectivity in gray scales, temperature in gray scales, and water density in gray scales. The darker the gray, the higher the value of the variable. The plots show only the northeast portion of the eyewall. The green contour in all panels is the 20 dBZ contour at the 14.9 km altitude. This green contour identifies the tall convective using the definition developed in chapter 3 (20 dBZ \geq 14.5 km).

The vigorous portion of a tall eyewall cell: 10.9 km high in a tropical cyclone simulation

The azimuthal velocity is relatively uniform across the tall cell at this altitude, suggesting that little inflow or outflow is occurring in the azimuthal direction

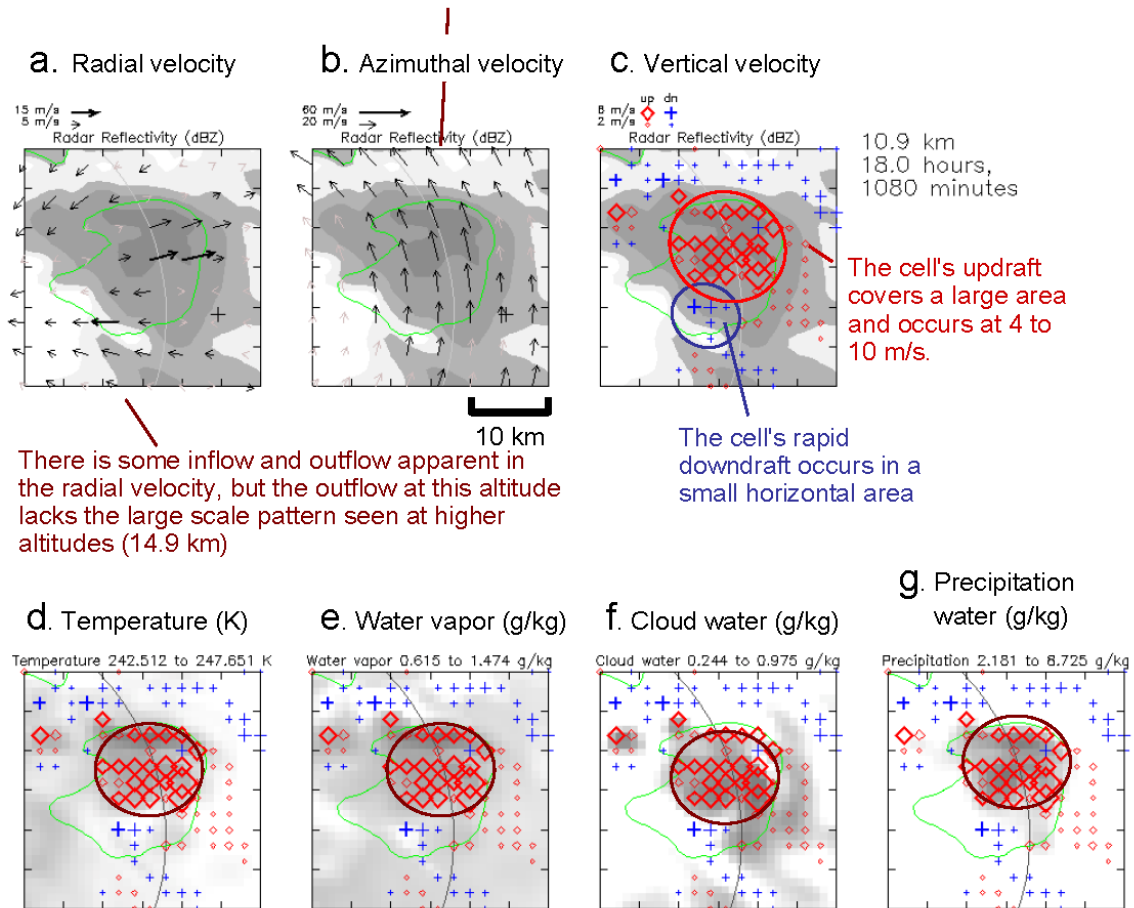


Figure 5.8. Same as Figure 5.7 except at a height of 10.9 km. The green contour in all panels is still the 20 dBZ contour at the 14.9 km altitude to make Figure 5.8 easier to compare with Figure 5.7. The dark areas in panels d through g line up with the strong updraft indicated by red diamonds. This correspondence indicates that the updraft, latent heating, excess water vapor, excess cloud water, and excess precipitation water are all occurring at roughly the same horizontal location at this altitude.

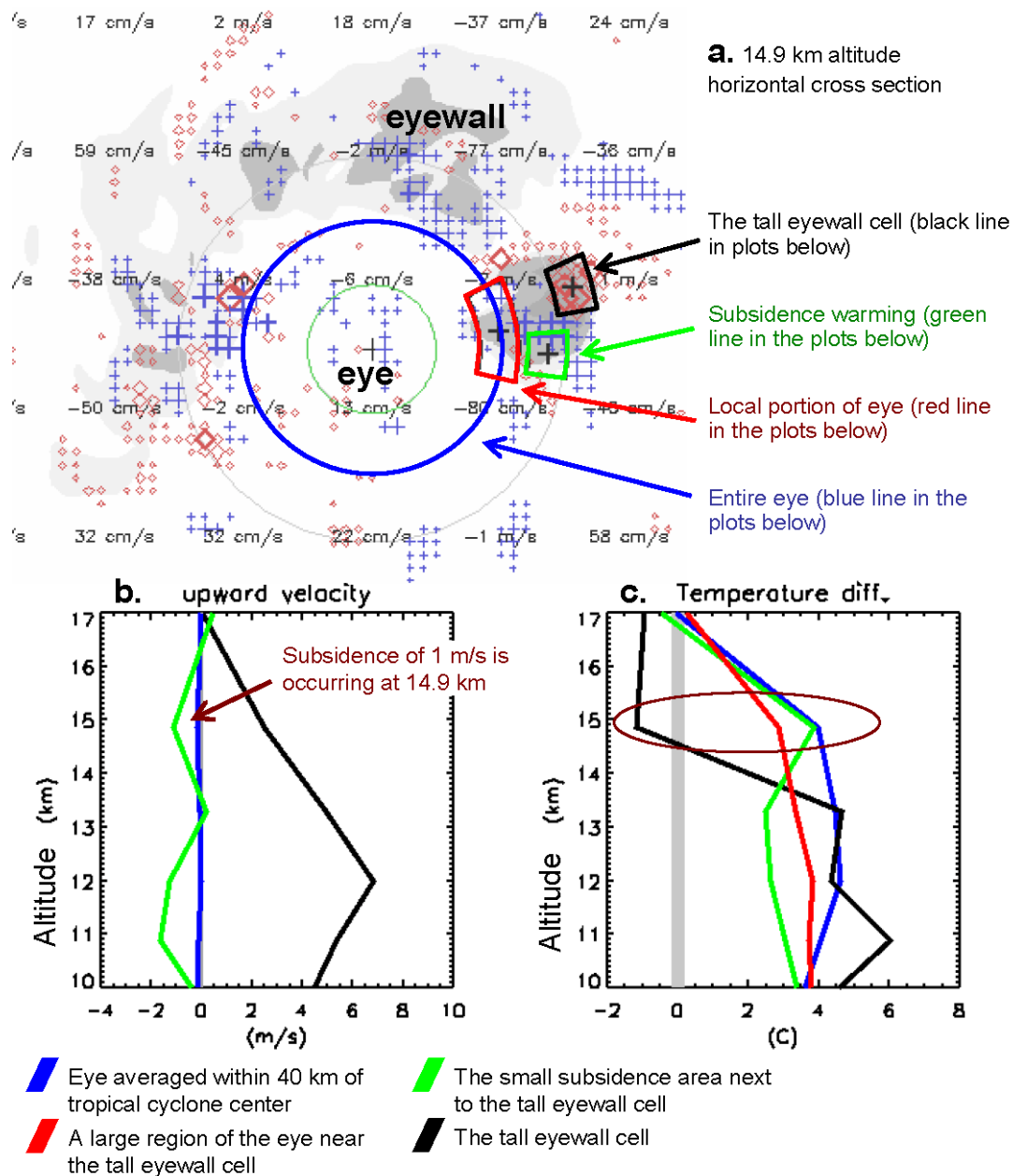


Figure 5.9. Vertical profiles of updraft velocity and temperature for the simulated tall eyewall cell shown in Figures 5.7 and 5.8. Vertical profiles for other regions are also shown to aid in the interpretation of the tall eyewall cell. At 14.9 km, the tall eyewall cell (black) is cold perhaps because it has overshoot its level of neutral buoyancy. The large region of the eye near the tall eyewall cell (red) is colder than the subsidence next to the tall eyewall cell (green) and also colder than the average temperature of the eye (blue) at this altitude. The reference temperature profile in panel c is the temperature profile averaged within 140 km of the tropical cyclone's center.

6.

Conclusions

This dissertation uses radar observations to quantify the empirical relationship between tall eyewall cells and tropical cyclone wind intensification. In addition, physical mechanisms are examined to better understand why this empirical relationship exists.

Both satellite radar and ground radar are used to identify whether or not wind intensification is occurring. One way in which this study differs from previous studies is that it uses a decade of satellite and ground radar observations that had not yet been collected when previous studies were conducted. This study also differs from previous ones by focusing on the precise height of convective cells in the tropical cyclone eyewall.

From a satellite overflight of a tropical cyclone eyewall by the TRMM Precipitation Radar, the maximum height of the 20 dBZ radar reflectivity signal is calculated. Based on whether or not this height is ≥ 14.5 km, one can estimate whether or not the tropical cyclone is undergoing wind intensification at the time of observation. Intensification is defined as an increase in the best track wind intensity six hours after the satellite overflight compared with six hours before the overflight. The dissertation interpolates wind intensity from the best track reports of wind intensity. Sixty-two percent of tropical cyclone overflights can be correctly identified as to whether or not

intensification is occurring using the $20 \text{ dBZ} \geq 14.5 \text{ km}$ height threshold (Table 3.3, p. 170). These results are based on 269 tropical cyclone overflights world-wide during the nine years from 1998 to 2006.

From three or more hours of continuous ground radar observation of a tropical cyclone, the fraction of the time that a tall cell exists in the eyewall can be calculated. Due to the coarseness of ground radar's vertical resolution, the same definition of tall cells is used in the ground radar analysis as was developed using the satellite radar ($20 \text{ dBZ} \geq 14.5 \text{ km}$). When the eyewall contains a tall cell in 33% of ground radar volume scans, then the eyewall is said to have "frequent" tall cells, which is taken as a sign that wind intensification is likely to be occurring during this observation period. Using this height-frequency threshold, 83% of tropical cyclone observation periods can be corrected identified as to whether or not intensification is occurring (Table 4.4, p. 220). These results are based on 29 observation periods of North Atlantic tropical cyclones by the WSR-88D radars along the U.S. coast between 1995 and 2004.

From an operational perspective, predicting future intensity would be more useful than identifying current changes in intensity. The dissertation also presents satellite and ground radar results relevant to this operational concern.

The eyewall's maximum 20 dBZ height calculated from the TRMM satellite radar can be used to estimate the wind intensity change between the time of observation and 24 hours in the future. This predictor explains 10% of the variance in the 24-hour intensity change (section 3.8, p. 171). This may seem like a small amount of variance explained, but it is considerable since the operational SHIPS intensity prediction algorithm in 1999

could only explain 37% of 12-hour intensity change using 11 statistical predictors [DeMaria and Kaplan, 1999].

Using ground radar data, the dissertation does not forecast intensity change after the end of the ≥ 3 hour period of observation because, in most cases, the tropical cyclone makes landfall soon after the observation period. However, there still may be operational implications for the ground radar technique developed in this dissertation. Consider the information available when the observation period ends. Without the technique in this dissertation, one would have only the most recent 12 hour forecast of intensity from the National Hurricane Center (NHC). Sometimes the NHC forecast is correct about whether intensification is occurring and sometimes it is not. The 33% height-frequency rule developed in this dissertation also makes a statement about whether or not wind intensification has occurred during the recent observation period. When both the NHC forecast and the height-frequency rule agree, no new information is added. When they disagree, the height-frequency rule is more accurate than the NHC forecast, using the best-track data from the post-season analysis as the reference point. The height-frequency rule is more accurate 6 times and less accurate 2 times (section 4.7, p. 218).

To provide a physical mechanism for these empirical results, the dissertation considers two possible explanations. One possible explanation is that a burst of tall eyewall cells energizes the tropical cyclone and causes wind intensification. The dissertation finds that a 9 hour burst of tall eyewall cells could add sufficient latent heat to the tropical cyclone's eye to cause a maximum of 26 kt of wind intensification in a tropical cyclone with a small eye ($r_{eye} = 20$ km) (section 5.2, p. 230). In a tropical

cyclone with a large eye ($r_{eye} = 40$ km), only 6 knots of intensification can be caused in this way. This wind intensification is a by-product of a 4 K or 1 K warming of the eye in tropical cyclones with small or large eyes, respectively. Analysis of observations and high resolution model output suggests that most bursts of tall eyewall cells directly cause less than this maximum wind intensification (section 5.5, p. 249). An alternate explanation is that some unobserved process causes both the burst of tall eyewall cells and the tropical cyclone wind intensification. In this explanation, the burst of tall eyewall cells is merely an indicator of wind intensification rather than its cause (section 5.1, p. 228).

In summary, it is energetically possible for a portion of the wind intensification to be caused by latent heat released by a burst of tall eyewall cells. The rest of the energy for wind intensification may come from an overall acceleration of the convection in the rest of the eyewall or other mechanisms discussed by other researchers, such as importing angular momentum from outside the eyewall.

APPENDIX

This appendix lists the 269 TRMM tropical cyclone overflights during the first nine years of the mission (1998 to 2006) that were used in chapter 3 of the dissertation. The overflights are listed twice. First, they are listed in four categories depending on whether or not the tropical cyclone is intensifying at the time of the overflight and whether or not the TRMM Precipitation Radar observes a tall cell ($20 \text{ dBZ} \geq 14.5 \text{ km}$) in the eyewall of the tropical cyclone. Second, the overflights are listed in reverse chronological order. The columns of the tables have the following definitions:

+I	Whether or not the tropical cyclone was intensifying at the time of observations: "y" for yes or "n" for no. The intensification is based on interpolating best track 6 hourly wind estimates to the time of the TRMM overflight plus 6 hours and minus six hours.
Area	The area of eyewall cells (km^2) that have a 20 dBZ signal at least 14.5 km high. This area was calculated by multiplying the number of tall TRMM Precipitation Radar pixels by 20 km^2 , which is the horizontal area of the 5 km across pixels.
yymmdd	The date of the TRMM satellite overflight of the tropical cyclone eyewall.
orbit	The TRMM orbit number of the overflight.
v	The TRMM preprocessing version of the file being used.
#basin	The number of the storm in the basin that year and the name of the small basin. The following abbreviations are used for the small basin: West Pacific (W), South Pacific (P), North Atlantic (L), South Indian (S), East Pacific (E), North Central Pacific (C), Bay of Bengal (B), and Arabian Sea (A).
name	The common name for the tropical cyclone.
Basin	The large basin that the storm is in: West Pacific (Wpac), South Pacific (Spac), Atlantic (Atl), and North Indian (Ind).
lat N	The location of the tropical cyclone's storm center at the time of the overflight in degrees north latitude.
lon E	The location of the tropical cyclone's storm center at the time of the overflight in degrees east longitude.

hhmm UT	The time of the overflight in hours and minutes universal time.
Wind kt	The tropical cyclone wind intensity in knots interpolated from the two closest 6 hour reporting periods in the best track estimate from the National Hurricane Center or the Joint Typhoon Warning Center, depending on the ocean basin. The format is aa+bb where aa is the wind intensity at the time of the overflight and bb is the 12 hour change in the wind intensity centered on the overflight time.
h=20Z km	The maximum height of the 20 dBZ radar reflectivity in the tropical cyclone's eyewall as observed by the TRMM Precipitation Radar. Height is calculated by equation 3.4.
Ice 85 PCT	The minimum 85 GHz polarization corrected brightness temperature (PCT) (K) observed by the TRMM Microwave Imager (TMI) in the tropical cyclone's eyewall. <i>Spencer et al.</i> [1989] were the first to define 85 GHz PCT as $1.818 \text{ Tb(V)} - 0.818 \text{ Tb(H)}$. See also <i>Cecil et al.</i> [2002, part I, p. 774].
L. Ice 37 PCT	The minimum 37 GHz PCT (K) observed by the TRMM Microwave Imager (TMI) in the tropical cyclone's eyewall. <i>Cecil et al.</i> [2002, part I, p. 774] define the 37 GHz PCT as $2.20 \text{ Tb(V)} - 1.20 \text{ Tb(H)}$.
LIS fl.	The number of lightning flashes observed in the eyewall by the TRMM Lightning Imaging Sensor (LIS).
Cld 11 mu	The third lowest 11 micron cloud-top temperature (K) observed by the TRMM Visible and Infrared Scanner (VIRS) in the eyewall. The third lowest value is reported because the VIRS has 3 km pixels with area of approximately 7 km^2 , which is one third the area of the TRMM Precipitation Radar's 5 km pixels (a 20 km^2 area).
Obs	The three observed indicators of tropical cyclone intensification are identified in this column if they occurred in this tropical cyclone overflight, as discussed in chapter 3. The three indicators are tall eyewall cells (T), i.e., tall eyewall cells with 20 dBZ height $\geq 14.5 \text{ km}$; significant 85 GHz ice scattering with 85 GHz PCT $\leq 200 \text{ K}$ (I); and high clouds with 11 micron Tb $\leq 193 \text{ K}$ (C).

TRMM Tropical Cyclone Overflights Sorted by Intensity Change and Horizontal Area of the Radar-observed Tall Eyewall Cells

Intensifying Tropical Cyclones with Tall Eyewall Cells

+I	Area km2	Overflight date and storm yymmdd.orbit.v.#basin.name	Basin	lat N	lon E	hhmm UT	Wind kt	h=20Z km	Ice 85PCT	L.Ice 37PCT	LIS fl.	Cld 11mu	Obs
y	820	020302.24494.5A.02W.MITAG	Wpac	8.07	140.81	1214	90+24	17.65	112	234	1	174	TIC
y	780	980321.1793.5.29P.YALI	Spac	-17.25	166.68	1432	82+10	17.57	132	242	6	177	TIC
y	680	030907.33133.5A.15W.MAEMI	Wpac	19.40	134.67	1841	65+09	17.20	93	214	0	180	TIC
y	620	980822.4224.5.02L.BONNIE	Atl	23.18	-70.48	1806	85+14	17.16	101	243	0	189	TIC
y	540	041014.39407.6.27W.TOKAGE	Wpac	14.25	137.41	0711	80+10	17.65	103	242	1	183	TIC
y	540	990305.7298.5.25S.DAVINA	Spac	-14.31	81.36	1558	83+26	16.77	106	239	0	181	TIC
y	500	000916.16137.6.10L.FLORENCE	Atl	32.00	-66.16	0456	65+00	15.72	79	192	8	186	TIC
y	400	040922.39071.6.25W.MEARI	Wpac	16.61	138.21	1747	65+09	16.96	125	246	0	182	TIC
y	380	060914.50316.6.14W.SHANSHAN	Wpac	20.40	125.77	0444	82+10	16.75	111	234	0	186	TIC
y	360	020704.26432.5A.08W.CHATAAN	Wpac	13.46	145.27	2020	91+06	17.12	130	240	0	179	TIC
y	340	000916.16146.5.25W.SONAMU	Wpac	29.24	141.45	1851	70+00	16.23	120	244	0	188	TIC
y	320	041022.39529.6.28W.NOCK-TEN	Wpac	15.50	136.32	0301	97+05	15.07	98	234	0	189	TIC
y	300	980925.4760.5.11L.KARL	Atl	30.22	-52.86	1733	69+10	16.14	84	207	6	191	TIC
y	280	990620.8975.5.01E.ADRIAN	Epac	16.76	-106.72	0034	65+10	16.26	149	260	0	181	TIC
y	240	060427.48140.6.02B.MALA	Ind	13.18	90.64	1433	74+17	16.66	151	259	1	180	TIC
y	220	000620.14753.5.03E.CARLOTTA	Epac	14.67	-101.01	1055	73+19	15.91	122	247	0	183	TIC
y	200	030227.30138.5A.19S.JAPHET	Spac	-22.13	38.58	1406	66+13	16.68	120	240	0	183	TIC
y	180	020118.23818.5A.10S.DINA	Spac	-12.87	70.17	0230	67+14	15.95	156	252	0	181	TIC
y	140	060807.49720.6.08W.SAOMAI	Wpac	17.75	139.56	2259	75+12	15.43	164	258	0	185	TIC
y	140	030830.33006.5A.14W.DUJUAN	Wpac	17.94	132.86	1439	77+05	17.32	178	265	0	183	TIC
y	120	040803.38283.6.01L.ALEX	Atl	32.80	-77.56	0413	67+23	15.64	108	234	0	195	TI-
y	100	980321.1799.5.29P.YALI	Spac	-17.72	167.53	2238	88+06	15.85	134	238	2	185	TIC
y	80	050408.42159.6.26S.ADELINE	Spac	-16.58	72.34	2102	105+22	17.23	128	238	0	179	TIC
y	80	041018.39477.6.28W.NOCK-TEN	Wpac	9.98	149.78	1822	80+05	15.75	145	248	0	185	TIC
y	80	040816.38483.6.04L.DANIELLE	Atl	15.82	-34.64	0021	90+04	15.51	113	234	0	188	TIC
y	80	031021.33815.5A.20W.KETSANA	Wpac	16.83	131.14	1222	125+09	15.99	118	239	0	182	TIC
y	80	030824.32905.5A.12W.KROVANH	Wpac	18.83	113.82	0337	78+10	15.93	140	245	0	189	TIC
y	80	990821.9967.5.03L.BRET	Atl	24.63	-94.97	2245	113+36	15.17	150	248	2	197	TI-
y	80	990426.8116.5.04W.KATE	Wpac	21.50	135.36	1314	67+12	16.20	175	265	0	181	TIC
y	60	010827.21584.5A.07E.FLOSSIE	Epac	19.73	-113.86	1844	65+08	14.97	168	259	0	195	TI-
y	40	050909.44546.6.15W.KHANUN	Wpac	19.14	130.53	2351	94+14	15.23	183	262	0	189	TIC
y	40	050822.44266.6.08E.HILARY	Epac	17.25	-108.78	0042	90+13	15.72	154	251	0	188	TIC
y	40	020529.25863.5A.01E.ALMA	Epac	13.09	-114.73	0813	76+10	15.45	140	246	0	182	TIC
y	20	060930.50569.6.09L.ISAAC	Atl	30.37	-58.10	1025	63+08	14.92	144	249	0	191	TIC
y	20	050815.44160.6.09L.IRENE	Atl	35.61	-68.76	0543	74+05	14.63	164	253	0	193	TI-
y	20	050812.44114.6.06E.FERNANDA	Epac	17.89	-122.90	0638	75+04	14.58	187	262	0	188	TIC
y	20	050706.43547.6.04L.DENNIS	Atl	16.01	-72.37	2131	65+17	14.99	164	253	0	187	TIC
y	20	040830.38708.6.06L.FRANCES	Atl	19.20	-57.73	1020	100+05	15.40	173	246	0	191	TIC
y	20	040408.36461.6.03W.SUDAL	Wpac	8.90	139.79	0720	115+10	14.54	163	253	0	186	TIC
y	20	030829.32992.5A.10E.JIMENA	Epac	16.78	-136.70	1736	74+20	14.62	171	262	0	194	TI-
y	20	030607.31690.5A.29P.GINA	Spac	-16.13	162.69	0358	81+16	14.58	185	254	0	192	TI-
y	20	030417.30905.5A.02W.KUJIRA	Wpac	13.45	131.06	1959	108+13	14.87	133	241	0	185	TIC
y	20	030412.30828.5A.02W.KUJIRA	Wpac	10.16	151.10	2125	65+04	14.90	159	255	0	185	TIC
y	20	030228.30148.5A.19S.JAPHET	Spac	-22.96	37.80	0638	76+11	14.57	171	257	0	185	TIC
y	20	981207.5907.5.06S.THELMA	Spac	-10.20	130.97	1054	98+27	15.00	194	262	0	182	TIC
y	20	980608.3030.5.03A.03A	Ind	18.01	67.62	0056	95+08	14.74	183	257	0	184	TIC

Intensifying Tropical Cyclones without Tall Eyewall Cells

+I	Area km2	Overflight date and storm yymmdd.orbit.v.#basin.name	Basin	lat N	lon E	hhmm UT	Wind kt	h=20Z km	Ice 85PCT	L.Ice 37PCT	LIS fl.	Cld 11mu	Obs
y	0	060922.50448.6.08L.HELENE	Atl	34.65	-54.23	1613	70+03	10.49	186	255	0	205	-I-
y	0	060917.50371.6.07L.GORDON	Atl	33.86	-52.92	1735	70+05	11.73	160	249	0	201	-I-
y	0	060913.50309.6.07L.GORDON	Atl	26.44	-57.75	1800	95+25	13.28	143	255	0	198	-I-
y	0	060821.49952.6.01C.IOKE	Wpac	13.05	-166.46	2045	106+28	13.23	146	256	0	196	-I-
y	0	060719.49431.6.05E.DANIEL	Epac	11.80	-118.94	1029	78+10	14.34	177	256	0	189	-IC
y	0	060422.48063.6.23P.MONICA	Spac	-11.79	138.55	1610	128+11	13.00	138	234	6	183	-IC
y	0	051202.45868.6.29L.EPSILON	Atl	33.96	-47.78	1941	65+03	7.93	223	265	0	219	---
y	0	051202.45869.6.29L.EPSILON	Atl	34.07	-47.44	2119	65+02	11.17	162	255	0	212	-I-

y	0	051122.45699.6.03S.BERTIE	Spac	-10.85	91.16	2359	114+10	13.94	170	262	0	185	-IC
y	0	051122.45706.6.03S.BERTIE	Spac	-11.72	90.59	0950	86+19	12.32	195	262	0	195	-I-
y	0	051012.45065.6.21W.KIROGI	Wpac	20.66	132.29	0702	93+19	10.79	210	265	0	194	---
y	0	050919.44710.6.10E.JOVA	Epac	15.13	-142.22	1222	100+10	12.21	182	251	0	192	-I-
y	0	050918.44694.6.11E.KENNETH	Epac	14.16	-129.12	1143	114+05	11.06	179	260	0	191	-IC
y	0	050910.44566.6.15W.KHANUN	Wpac	24.36	125.06	0704	105+14	12.56	192	263	0	193	-I-
y	0	050813.44128.6.09L.IRENE	Atl	29.48	-68.06	0419	60+01	10.22	192	262	0	197	-I-
y	0	050719.43747.6.05L.EMILY	Atl	24.14	-95.02	1735	84+28	12.68	177	257	0	196	-I-
y	0	050716.43696.6.05W.HAITANG	Wpac	20.73	127.75	1128	139+05	11.93	167	252	2	190	-IC
y	0	050709.43594.6.04L.DENNIS	Atl	25.81	-84.80	2159	103+33	11.18	212	264	0	196	---
y	0	050424.42399.6.03W.SONCA	Wpac	14.11	130.85	0623	110+23	13.06	181	262	0	191	-IC
y	0	050406.42119.6.26S.ADELINE	Spac	-13.09	87.35	0627	105+04	12.66	142	238	7	190	-IC
y	0	041006.39280.6.26W.MA-ON	Wpac	20.53	132.71	0306	60+17	12.49	192	265	0	188	-IC
y	0	040902.38756.6.11E.HOWARD	Epac	17.83	-113.31	1214	120+19	11.70	155	253	0	193	-I-
y	0	040828.38677.6.06L.FRANCES	Atl	17.02	-51.46	1034	103+12	12.93	169	257	0	191	-IC
y	0	040824.38613.6.20W.AERE	Wpac	25.42	123.37	0827	82+07	13.00	197	259	0	197	-I-
y	0	040726.38169.6.13W.NAMTHEUN	Wpac	27.34	146.29	2100	115+02	11.31	181	257	0	199	-I-
y	0	040628.37723.6.10W.MINDULLE	Wpac	18.41	125.62	0603	115+14	13.31	142	249	0	191	-IC
y	0	040608.37418.6.07W.CONSON	Wpac	20.32	120.54	1625	88+07	11.75	193	256	0	192	-I-
y	0	040412.36522.6.03W.SUDAL	Wpac	15.68	130.99	0513	115+04	11.49	196	259	0	201	-I-
y	0	040412.36532.6.03W.SUDAL	Wpac	16.72	131.44	2006	120+01	11.70	184	255	0	187	-IC
y	0	040306.35947.6.16S.GAFILO	Spac	-14.67	53.05	0802	140+03	12.97	124	243	1	194	-I-
y	0	040203.35458.6.10S.FRANK	Spac	-18.20	70.62	2306	112+16	11.87	188	261	0	190	-IC
y	0	040130.35382.6.10S.FRANK	Spac	-16.05	62.34	0203	91+06	14.05	167	259	0	187	-IC
y	0	031113.34175.5A.02A.02A	Ind	6.05	57.40	1518	67+10	13.06	177	263	0	191	-IC
y	0	031029.33937.5A.21W.PARMA	Wpac	24.22	149.11	0818	111+14	11.46	164	259	0	190	-IC
y	0	031024.33861.5A.21W.PARMA	Wpac	30.68	158.44	1121	129+06	13.72	112	236	0	186	-IC
y	0	030927.33444.5A.15L.JUAN	Atl	35.44	-63.24	1720	88+15	13.45	155	250	0	206	-I-
y	0	030926.33430.5A.15L.JUAN	Atl	32.80	-62.07	1953	71+08	12.31	174	254	0	201	-I-
y	0	030926.33428.5A.15L.JUAN	Atl	32.21	-62.06	1638	68+10	11.23	203	260	0	211	---
y	0	030921.33343.5A.16W.CHOI-WAN	Wpac	31.15	137.24	0453	98+13	14.46	137	244	0	188	-IC
y	0	030910.33182.5A.13L.ISABEL	Atl	21.17	-51.99	2142	123+06	13.49	142	251	0	193	-I-
y	0	030830.33011.5A.14W.DUJUAN	Wpac	18.97	131.33	2250	80+09	14.00	200	266	0	190	--C
y	0	030307.30268.5A.23S.KALUNDE	Spac	-13.74	71.05	2320	127+34	12.22	139	252	1	195	-I-
y	0	030128.29669.5A.12P.BENI	Spac	-15.50	161.21	1259	94+35	13.25	205	260	0	184	--C
y	0	020902.27357.5A.02C.ELE	Wpac	22.39	174.89	0413	107+13	12.01	162	253	0	197	-I-
y	0	020831.27338.5A.10E.HERNAN	Epac	16.33	-108.53	2252	112+30	11.50	181	260	0	199	-I-
y	0	020827.27271.5A.21W.RUSA	Wpac	24.41	138.33	1609	93+00	8.67	244	270	0	195	---
y	0	020710.26518.5A.10W.HALONG	Wpac	12.29	143.74	0812	95+03	13.49	170	262	0	186	-IC
y	0	020307.24575.5A.18S.HARY	Spac	-11.37	56.52	1707	73+36	13.47	157	255	0	184	-IC
y	0	020203.24077.5A.12S.FRANCESCA	Spac	-14.87	78.21	1718	69+14	13.98	166	256	0	183	-IC
y	0	011220.23379.5A.33W.FAXAI	Spac	9.02	158.36	2317	73+23	13.41	193	260	0	189	-IC
y	0	011024.22478.5A.26W.PODUL	Wpac	16.84	156.97	0351	138+05	11.60	195	263	0	211	-I-
y	0	011007.22213.5A.11L.IRIS	Atl	16.79	-74.72	0346	75+03	11.85	171	260	0	189	-IC
y	0	010925.22032.5A.23W.LEKIMA	Wpac	21.22	121.73	1235	90+09	13.21	177	259	0	184	-IC
y	0	010919.21941.5A.21W.VIPA	Wpac	32.53	139.48	1635	65+03	11.36	196	259	0	199	-I-
y	0	010915.21868.5A.20W.NARI	Wpac	26.38	124.31	1230	75+10	10.55	225	265	0	206	---
y	0	010829.21604.5A.07E.FLOSSIE	Epac	19.87	-115.22	0159	76+10	9.74	193	258	0	193	-I-
y	0	010726.21070.5.09W.KONG-REY	Wpac	29.28	140.83	0057	80+00	11.85	197	263	0	198	-I-
y	0	010528.20140.5.01E.ADOLPH	Epac	13.93	-99.90	0142	97+25	12.49	155	237	0	199	-I-
y	0	010111.17989.5.05S.BINDU	Spac	-16.93	70.17	1612	68+08	11.25	236	264	0	192	---
y	0	010109.17958.5.05S.BINDU	Spac	-16.16	72.60	1700	90+00	13.38	184	259	0	186	-IC
y	0	001029.16822.5.30W.XANGSANE	Wpac	16.08	118.15	1519	60+23	13.46	200	261	0	181	--C
y	0	000818.15690.6.03L.ALBERTO	Atl	34.59	-48.18	2045	69+14	12.48	169	259	0	201	-I-
y	0	000818.15689.6.03L.ALBERTO	Atl	34.63	-48.19	1909	66+15	11.96	185	258	0	203	-I-
y	0	000810.15565.5.03L.ALBERTO	Atl	29.54	-57.68	2221	68+08	8.49	224	268	0	204	---
y	0	000802.15432.5.13W.JELAWAT	Wpac	22.50	147.65	1151	115+00	12.75	151	250	3	199	-I-
y	0	000217.12794.5.11S.LEON-ELINE	Spac	-19.96	50.42	0438	76+15	10.68	183	258	0	191	-IC
y	0	991116.11335.5.16L.LENNY	Atl	15.33	-69.50	1619	85+13	10.55	139	242	0	186	-IC
y	0	990922.10463.5.24W.BART	Wpac	26.06	127.13	0017	130+10	12.59	163	251	1	206	-I-
y	0	990920.10432.5.24W.BART	Wpac	23.96	125.51	1004	78+21	11.72	216	265	0	189	--C
y	0	990915.10355.5.21W.YORK	Wpac	21.44	115.33	1252	65+09	12.92	165	251	9	186	-IC
y	0	990828.10070.5.04L.CINDY	Atl	29.77	-58.10	1112	119+07	11.19	173	258	0	198	-I-
y	0	990731.9629.5.11W.OLGA	Wpac	23.28	130.49	1157	64+09	10.97	220	268	0	191	--C
y	0	990330.7683.5.31S.FREDERIC	Spac	-16.88	98.52	0157	115+10	14.17	159	257	0	188	-IC
y	0	990116.6538.6.11P.DANI	Spac	-16.22	163.93	1113	88+33	12.31	143	247	0	184	-IC
y	0	981022.5178.5.14E.LESTER	Epac	16.77	-108.70	0536	94+09	10.45	189	260	0	203	-I-
y	0	981017.5100.5.14E.LESTER	Epac	14.42	-95.21	0652	80+09	12.66	196	261	0	192	-I-
y	0	980927.4780.5.07L.GEORGES	Atl	26.96	-86.32	0016	95+04	13.43	215	260	0	189	--C
y	0	980919.4656.5.07L.GEORGES	Atl	14.10	-49.97	0339	93+14	12.04	162	252	0	199	-I-
y	0	980824.4252.5.09E.HOWARD	Epac	16.09	-114.83	1215	110+00	12.73	170	249	0	195	-I-
y	0	980210.1171.5.20S.ANACELLE	Spac	-15.50	59.61	0254	84+15	10.75	201	262	0	187	--C

Non-Intensifying Tropical Cyclones with Tall Eyewall Cells

Area	Overflight date and storm	lat	lon	hhmm	Wind	h=20Z	Ice L	Ice LIS	Cld
------	---------------------------	-----	-----	------	------	-------	-------	---------	-----

+I	km2	yymmdd.orbit.v.#basin.name	Basin	N	E	UT	kt	km	85PCT	37PCT	fl.	11mu	Obs
n	680	050603.43019.6.04W.NESAT	Wpac	12.32	134.34	0029	105-04	17.00	93	215	1	181	TIC
n	680	030831.33023.5A.10E.JIMENA	Epac	18.12	-149.43	1719	76-19	16.49	101	240	0	186	TIC
n	660	990126.6689.5.15S.DAMIEN	Spac	-14.88	94.61	0203	65-10	17.25	124	239	1	179	TIC
n	420	980918.4647.5.10W.TODD	Wpac	29.76	128.44	1349	65-05	17.98	104	221	6	185	TIC
n	340	040914.38944.6.13E.JAVIER	Epac	16.67	-107.64	1412	125-00	16.49	104	230	10	186	TIC
n	340	020311.24637.5A.18S.HARY	Spac	-21.98	51.91	1640	102-11	16.99	117	253	0	181	TIC
n	300	980927.4790.5.10L.JEANNE	Atl	26.41	-41.61	1509	70-00	16.22	119	240	1	193	TI-
n	280	040817.38513.6.04L.DANIELLE	Atl	25.72	-40.34	2227	77-18	15.45	119	230	4	189	TIC
n	200	060912.50290.6.14W.SHANSHAN	Wpac	19.93	130.66	1309	90-00	16.26	124	240	0	178	TIC
n	200	060807.49725.6.08W.SAOMAI	Wpac	18.97	137.75	0711	75-00	16.73	138	250	0	185	TIC
n	160	050604.43040.6.04W.NESAT	Wpac	15.60	130.94	0923	125-05	16.78	152	230	12	182	TIC
n	160	030405.30709.5A.26S.INIGO	Spac	-14.45	113.19	0624	125-05	15.24	133	224	14	189	TIC
n	140	060721.49466.6.06W.KAEMI	Wpac	16.64	131.12	1621	75-02	16.09	172	256	0	182	TIC
n	120	000302.13023.5.16S.NORMAN	Spac	-19.35	109.75	1710	266-20	16.30	158	254	0	181	TIC
n	60	050605.43055.6.04W.NESAT	Wpac	18.46	131.11	0828	95-10	16.73	131	254	0	185	TIC
n	60	050425.42414.6.03W.SONCA	Wpac	16.51	131.59	0528	115-04	16.48	119	239	2	184	TIC
n	60	041020.39508.6.28W.NOCK-TEN	Wpac	12.69	141.74	1808	95-00	15.97	140	245	0	176	TIC
n	60	020723.26721.5A.12W.FENGSHEN	Wpac	27.01	145.29	0915	101-25	16.24	157	262	0	189	TIC
n	40	990809.9763.5.08E.EUGENE	Epac	14.87	-129.38	2350	95-04	15.06	165	246	0	193	TI-
n	20	050812.44119.6.06E.FERNANDA	Epac	18.23	-123.99	1450	75-00	14.92	214	264	0	189	T-C
n	20	050605.43050.6.04W.NESAT	Wpac	17.51	130.63	0015	104-15	14.73	178	256	0	184	TIC
n	20	040922.39063.6.12L.KARL	Atl	24.63	-49.45	0523	95-10	14.50	197	263	0	191	TIC
n	20	010915.21872.5A.07L.FELIX	Atl	31.68	-40.96	0619	90-00	14.58	200	262	0	193	T--

Non-Intensifying Tropical Cyclones without Tall Eyewall Cells

+I	Area km2	Overflight date and storm yymmdd.orbit.v.#basin.name	Basin	lat N	lon E	h UT	Wind kt	h=20Z km	Ice 85PCT	L.Ice 37PCT	LIS fl.	Cld 11mu	Obs
n	0	061014.50789.6.21W.SOULIK	Wpac	25.63	140.85	1306	79-13	11.46	202	263	0	206	---
n	0	061001.50585.6.09L.ISAAC	Atl	33.40	-60.26	1107	70-05	11.23	166	259	0	199	-I-
n	0	060924.50470.6.16W.YAGI	Wpac	34.44	147.56	0206	75-10	12.91	196	258	0	203	-I-
n	0	060916.50347.6.14W.SHANSHAN	Wpac	25.71	124.65	0431	116-08	11.49	196	258	0	205	-I-
n	0	060915.50340.6.07L.GORDON	Atl	31.01	-53.72	1748	80-10	11.72	210	262	0	197	---
n	0	060911.50280.6.06L.FLORENCE	Atl	34.44	-64.48	2128	72-07	12.20	210	266	0	199	---
n	0	060910.50264.6.06L.FLORENCE	Atl	29.89	-66.13	2045	80-01	13.36	169	253	0	192	-I-
n	0	060902.50136.6.01C.IOKE	Wpac	24.19	155.24	1557	110-06	11.45	220	262	0	202	---
n	0	060830.50090.6.01C.IOKE	Wpac	17.98	169.04	1711	135-00	11.23	166	247	0	194	-I-
n	0	060830.50085.6.01C.IOKE	Wpac	17.32	170.07	0859	137-05	12.32	158	251	0	195	-I-
n	0	060827.50044.6.01C.IOKE	Wpac	16.82	178.30	1822	139-05	11.91	181	258	0	192	-IC
n	0	060825.50013.6.01C.IOKE	Wpac	19.20	-175.21	1838	138-10	12.39	179	251	0	193	-I-
n	0	060724.49508.6.05E.DANIEL	Epac	16.03	-139.60	0902	82-12	13.65	172	259	0	195	-I-
n	0	060707.49252.6.04W.EWINIAR	Wpac	23.09	126.58	2244	85-01	10.50	214	263	0	194	---
n	0	051207.45943.6.29L.EPSILON	Atl	29.13	-37.48	1505	62-10	9.25	207	260	0	218	---
n	0	051206.45928.6.29L.EPSILON	Atl	31.77	-33.84	1601	65-00	9.40	217	264	0	211	---
n	0	051203.45884.6.29L.EPSILON	Atl	34.42	-43.12	2024	65-00	9.65	204	262	0	216	---
n	0	050929.44871.6.19W.LONGWANG	Wpac	22.21	132.53	2045	125-02	10.14	180	255	3	195	-I-
n	0	050922.44758.6.18L.RITA	Atl	25.31	-88.58	1443	133-25	13.37	138	245	3	195	-I-
n	0	050906.44511.6.14L.MARIA	Atl	33.68	-54.73	1815	74-14	9.81	205	258	0	204	---
n	0	050813.44131.6.09L.IRENE	Atl	30.02	-68.84	0912	60-00	8.50	212	262	0	199	---
n	0	050717.43707.6.05W.HAITANG	Wpac	22.07	125.09	0359	130-21	12.36	158	256	0	194	-I-
n	0	050608.43100.6.04W.NESAT	Wpac	25.31	134.57	0541	80-14	11.09	197	255	0	202	-I-
n	0	050607.43085.6.04W.NESAT	Wpac	23.47	133.98	0636	99-14	10.99	212	262	0	201	---
n	0	050411.42206.6.26S.ADELINE	Spac	-26.51	64.89	2130	61-22	9.21	223	260	0	221	---
n	0	050218.41391.6.19P.OLAF	Spac	-23.78	-161.16	1430	95-18	12.98	172	249	0	192	-I-
n	0	041018.39479.6.27W.TOKAGE	Wpac	24.37	127.21	2135	84-12	10.82	226	263	0	191	--C
n	0	040928.39159.6.25W.MEARI	Wpac	29.35	127.38	0853	75-07	10.95	217	262	0	201	---
n	0	040927.39147.6.25W.MEARI	Wpac	26.90	125.67	1442	85-18	10.49	202	259	0	207	---
n	0	040923.39079.6.11L.JEANNE	Atl	25.45	-69.27	0601	84-05	11.48	190	262	0	194	-I-
n	0	040921.39045.6.11L.JEANNE	Atl	27.37	-70.65	0120	75-00	14.21	133	252	0	190	-IC
n	0	040921.39059.6.12L.KARL	Atl	23.10	-48.52	2251	100-11	10.05	214	264	0	194	---
n	0	040915.38954.6.09L.IVAN	Atl	25.41	-87.49	0510	120-04	11.07	178	247	0	195	-I-
n	0	040906.38811.6.22W.SONGDA	Wpac	28.63	127.10	0119	98-10	11.02	206	262	0	198	---
n	0	040904.38792.6.22W.SONGDA	Wpac	25.40	129.53	1943	122-10	13.55	164	260	0	190	-IC
n	0	040902.38750.6.22W.SONGDA	Wpac	21.45	140.24	0327	117-07	11.49	177	255	0	199	-I-
n	0	040902.38761.6.11E.HOWARD	Epac	18.37	-114.11	2025	117-11	12.74	162	246	0	200	-I-
n	0	040828.38670.6.19W.CHABA	Wpac	27.13	133.90	2353	105-05	11.91	209	261	0	196	---
n	0	040826.38639.6.19W.CHABA	Wpac	23.57	136.25	0006	129-19	12.93	169	257	0	198	-I-
n	0	040806.38333.6.14W.MERANTI	Wpac	29.85	169.41	0907	90-12	10.14	213	263	0	202	---
n	0	040729.38212.6.05E.DARBY	Epac	17.51	-127.89	1516	97-18	13.00	195	261	0	192	-I-
n	0	040727.38184.6.13W.NAMTHEUN	Wpac	30.61	142.86	2003	90-09	9.97	229	264	0	198	---
n	0	040630.37757.6.11W.TINGTING	Wpac	26.26	142.54	1048	65-01	11.98	198	262	0	196	-I-
n	0	040520.37116.6.04W.NIDA	Wpac	27.35	135.47	0745	73-12	11.46	191	256	0	192	-I-
n	0	040204.35464.6.10S.FRANK	Spac	-18.51	70.34	0717	113-06	10.48	202	264	0	200	---

n	0	031006.33581.5A.16L.KATE	Atl	35.20	-55.89	1217	74-10	11.70	146	248	0	201	-I-
n	0	031005.33566.5A.14E.NORA	Epac	18.86	-113.33	1257	84-09	14.18	174	252	0	188	-IC
n	0	030916.33275.5A.13L.ISABEL	Atl	27.91	-71.35	2058	95-00	11.69	220	264	0	205	---
n	0	030915.33248.5A.13L.ISABEL	Atl	24.36	-68.50	0344	126-11	10.18	199	257	0	195	-I-
n	0	030914.33244.5A.13L.ISABEL	Atl	24.16	-67.39	2112	134-10	11.22	179	254	0	204	-I-
n	0	030912.33202.5A.13L.ISABEL	Atl	21.69	-56.36	0456	140-00	11.97	147	240	0	199	-I-
n	0	030906.33109.5A.10L.FABIAN	Atl	34.68	-63.89	0533	100-00	10.90	204	258	0	195	---
n	0	030906.33108.5A.10L.FABIAN	Atl	34.32	-64.17	0355	100-01	10.75	197	258	0	195	-I-
n	0	030807.32644.5A.11W.ETAU	Wpac	28.12	129.18	0937	110-03	13.76	178	261	0	194	-I-
n	0	030525.31498.5A.04W.CHAN-HOM	Wpac	27.60	157.91	2059	65-17	10.73	228	265	0	211	---
n	0	030524.31479.5A.04W.CHAN-HOM	Wpac	20.65	153.55	1521	115-00	11.42	202	262	0	193	---
n	0	030416.30884.5A.02W.KUJIRA	Wpac	13.68	135.34	1105	130-17	14.00	139	252	0	187	-IC
n	0	030212.29902.5A.17S.HAPE	Spac	-16.63	69.10	1146	80-00	11.63	163	238	0	193	-I-
n	0	030114.29455.5A.10P.AMI	Spac	-25.72	-172.50	1933	97-18	11.55	220	260	0	198	---
n	0	021228.29180.5A.06P.ZOE	Spac	-12.41	169.53	0359	155-06	11.50	170	253	4	210	-I-
n	0	021227.29170.5A.05S.CRYSTAL	Spac	-21.77	60.00	1240	89-05	12.27	176	254	2	192	-I-
n	0	020903.27378.5A.22W.SINLAKU	Wpac	25.33	133.08	1255	90-00	11.26	209	264	0	197	---
n	0	020902.27369.5A.10E.HERNAN	Epac	18.65	-117.11	2239	97-15	9.49	240	268	0	206	---
n	0	020830.27314.5A.21W.RUSA	Wpac	30.41	127.63	1005	76-08	10.03	220	264	0	199	---
n	0	020825.27237.5A.08E.FAUSTO	Epac	17.74	-126.49	1153	95-20	8.50	224	265	0	208	---
n	0	020817.27115.5A.19W.PHANFONE	Wpac	29.88	137.31	1538	111-08	10.00	235	265	0	198	---
n	0	020725.26758.5A.06E.ELIDA	Epac	14.93	-112.51	1747	115-25	12.39	157	245	2	201	-I-
n	0	020717.26624.5A.12W.FENGSHEN	Wpac	14.59	167.41	0326	125-00	13.65	181	243	2	196	-I-
n	0	020307.24570.5A.02W.MITAG	Wpac	18.08	133.97	0911	69-24	6.21	261	268	0	200	---
n	0	020208.24147.5A.12S.FRANCESCA	Spac	-19.58	83.46	0607	94-05	11.60	205	258	0	197	---
n	0	010927.22057.5A.11E.JULIETTE	Epac	19.69	-110.41	0304	92-10	7.99	253	272	0	198	---
n	0	010924.22012.6.10L.HUMBERTO	Atl	33.79	-66.82	0602	74-14	13.76	160	256	0	194	-I-
n	0	010924.22016.5A.11E.JULIETTE	Epac	15.05	-103.74	1225	99-17	9.20	228	262	0	194	---
n	0	010924.22011.5A.10L.HUMBERTO	Atl	33.62	-66.97	0424	77-12	14.49	149	250	0	193	-I-
n	0	010917.21904.6.07L.FELIX	Atl	34.94	-31.74	0745	63-09	9.43	211	259	0	216	---
n	0	010917.21903.5A.07L.FELIX	Atl	34.90	-31.65	0607	64-10	11.00	201	259	0	212	---
n	0	010916.21889.5A.07L.FELIX	Atl	32.98	-33.70	0840	77-10	9.31	215	258	0	214	---
n	0	010910.21798.5A.06L.ERIN	Atl	34.91	-64.74	2140	83-13	9.61	221	263	0	213	---
n	0	010908.21761.5A.20W.NARI	Wpac	26.93	127.00	0340	66-05	12.24	210	264	0	198	---
n	0	010907.21757.5A.19W.DANAS	Wpac	28.32	144.06	2112	100-00	11.97	182	261	0	203	-I-
n	0	010805.21240.5.12W.MAN-YI	Wpac	25.95	144.23	1944	102-13	10.50	214	266	0	200	---
n	0	010727.21085.5.09W.KONG-REY	Wpac	31.13	143.51	2346	65-10	12.66	184	262	0	197	-I-
n	0	010727.21098.5.09W.KONG-REY	Wpac	32.44	147.51	1921	68-13	10.00	232	267	0	198	---
n	0	010727.21100.5.09W.KONG-REY	Wpac	32.91	148.09	2234	66-11	11.90	223	268	0	205	---
n	0	010705.20743.5.06W.UTOR	Wpac	20.97	117.53	0656	65-04	7.31	263	277	0	202	---
n	0	010530.20171.5.01E.ADOLPH	Epac	15.91	-106.31	0052	108-15	10.24	200	258	0	203	---
n	0	000929.16353.5.13L.ISAAC	Atl	33.76	-55.68	2143	86-13	13.73	175	264	0	193	-I-
n	0	000929.16353.5.13L.ISAAC	Atl	33.63	-55.58	2143	86-13	13.73	175	252	0	193	-I-
n	0	000915.16129.5.22W.SAOMAI	Wpac	33.63	128.14	1647	65-08	10.39	211	260	0	200	---
n	0	000911.16066.5.22W.SAOMAI	Wpac	25.71	129.69	1648	111-07	10.91	190	259	0	206	-I-
n	0	000815.15635.5.15W.EWINIAR	Wpac	35.29	149.84	0901	75-00	13.08	200	262	0	199	---
n	0	000807.15514.5.13W.JELAWAT	Wpac	26.78	128.44	1701	85-06	7.92	243	264	0	222	---
n	0	000805.15483.5.13W.JELAWAT	Wpac	25.93	132.66	1751	90-00	10.46	204	260	0	199	---
n	0	000729.15367.5.06E.DANIEL	Epac	18.66	-143.71	0854	65-07	12.22	193	259	0	202	-I-
n	0	000622.14784.5.03E.CARLOTTA	Epac	16.52	-106.89	1006	100-04	10.49	205	264	0	191	-C
n	0	000329.13451.5.21S.HUDAH	Spac	-16.91	69.11	2136	90-05	13.97	163	244	0	186	-IC
n	0	000215.12763.5.11S.LEON-ELINE	Spac	-18.68	56.20	0528	65-05	14.24	199	265	0	196	-I-
n	0	000214.12757.5.11S.LEON-ELINE	Spac	-18.39	57.56	2123	70-02	9.15	220	263	0	197	---
n	0	000128.12479.5.08S.CONNIE	Spac	-16.64	57.03	0616	110-09	11.83	167	262	0	203	-I-
n	0	991008.10710.5.26W.DAN	Wpac	21.82	118.12	0110	90-00	9.98	200	262	0	192	---
n	0	990922.10458.5.09L.GERT	Atl	34.55	-61.13	0153	75-05	10.49	199	260	0	193	-I-
n	0	990922.10457.5.09L.GERT	Atl	34.26	-61.51	0917	72-07	10.89	227	269	0	203	---
n	0	990916.10367.5.09L.GERT	Atl	18.09	-51.90	0736	128-06	13.33	181	256	0	190	-IC
n	0	990913.10321.5.08L.FLOYD	Atl	23.90	-70.85	0932	135-01	12.25	125	245	0	199	-I-
n	0	990830.10102.5.04L.CINDY	Atl	34.88	-54.21	1201	80-10	8.71	211	263	0	196	---
n	0	990829.10086.5.04L.CINDY	Atl	32.78	-58.15	1136	101-20	12.65	210	262	0	201	---
n	0	990822.9975.5.04L.CINDY	Atl	14.47	-33.27	1028	65-03	8.98	225	262	0	195	---
n	0	990713.9346.5.02E.BEATRIZ	Epac	15.04	-122.26	1311	104-05	10.92	178	257	0	200	-I-
n	0	990501.8194.5.05W.LEO	Wpac	21.18	115.84	1157	70-20	9.23	241	260	0	197	---
n	0	990331.7708.5.31S.FREDERIC	Spac	-17.43	91.19	1659	140-01	13.81	153	251	0	191	-IC
n	0	990311.7386.5.25S.DAVINA	Spac	-22.87	52.80	0658	75-00	13.06	161	244	0	196	-I-
n	0	981209.5931.5.06S.THELMA	Spac	-11.90	128.35	0022	130-04	13.94	120	227	8	190	-IC
n	0	980902.4391.6.04L.DANIELLE	Atl	34.90	-66.98	0801	73-08	14.00	161	250	0	200	-I-
n	0	980830.4353.5.06W.REX	Wpac	31.13	142.74	2221	90-00	14.22	192	260	0	195	-I-
n	0	980827.4299.5.09E.HOWARD	Epac	18.41	-124.94	1149	70-15	9.02	230	265	0	211	---
n	0	980826.4283.5.02L.BONNIE	Atl	32.59	-77.74	1137	100-00	8.75	228	268	0	206	---
n	0	980824.4251.5.02L.BONNIE	Atl	25.47	-72.35	1050	100-00	11.60	225	265	0	192	---
n	0	980727.3805.5.05E.DARBY	Epac	16.50	-128.47	0356	100-00	11.50	172	258	0	209	-I-
n	0	980324.1840.5.29P.YALI	Spac	-24.43	163.10	1409	60-01	12.00	211	262	0	209	---
n	0	980211.1196.5.20S.ANACELLE	Spac	-21.59	59.18	1800	115-10	12.11	181	249	0	192	-I-

TRMM Tropical Cyclone Overflights in Reverse Chronological Order

2006

Area +I	km2	Overflight date and storm yyymmdd.orbit.v.#basin.name	Basin	lat N	lon E	hhmm UT	Wind kt	h=20Z km	Ice 85PCT	L.Ice 37PCT	LIS fl.	Cld 11mu	Obs
n	0	061014.50789.6.21W.SOULIK	Wpac	25.63	140.85	1306	79-13	11.46	202	263	0	206	---
n	0	061001.50585.6.09L.ISAAC	Atl	33.40	-60.26	1107	70-05	11.23	166	259	0	199	-I-
y	20	060930.50569.6.09L.ISAAC	Atl	30.37	-58.10	1025	63+08	14.92	144	249	0	191	TIC
n	0	060924.50470.6.16W.YAGI	Wpac	34.44	147.56	0206	75-10	12.91	196	258	0	203	-I-
y	0	060922.50448.6.08L.HELENE	Atl	34.65	-54.23	1613	70+03	10.49	186	255	0	205	-I-
y	0	060917.50371.6.07L.GORDON	Atl	33.86	-52.92	1735	70+05	11.73	160	249	0	201	-I-
n	0	060916.50347.6.14W.SHANSHAN	Wpac	25.71	124.65	0431	116-08	11.49	196	258	0	205	-I-
n	0	060915.50340.6.07L.GORDON	Atl	31.01	-53.72	1748	80-10	11.72	210	262	0	197	---
y	380	060914.50316.6.14W.SHANSHAN	Wpac	20.40	125.77	0444	82+10	16.75	111	234	0	186	TIC
y	0	060913.50309.6.07L.GORDON	Atl	26.44	-57.75	1800	95+25	13.28	143	255	0	198	-I-
n	200	060912.50290.6.14W.SHANSHAN	Wpac	19.93	130.66	1309	90-00	16.26	124	240	0	178	TIC
n	0	060911.50280.6.06L.FLORENCE	Atl	34.44	-64.48	2128	72-07	12.20	210	266	0	199	---
n	0	060910.50264.6.06L.FLORENCE	Atl	29.89	-66.13	2045	80-01	13.36	169	253	0	192	-I-
n	0	060902.50136.6.01C.IOKE	Wpac	24.19	155.24	1557	110-06	11.45	220	262	0	202	---
n	0	060830.50090.6.01C.IOKE	Wpac	17.98	169.04	1711	135-00	11.23	166	247	0	194	-I-
n	0	060830.50085.6.01C.IOKE	Wpac	17.32	170.07	0859	137-05	12.32	158	251	0	195	-I-
n	0	060827.50044.6.01C.IOKE	Wpac	16.82	178.30	1822	139-05	11.91	181	258	0	192	-IC
n	0	060825.50013.6.01C.IOKE	Wpac	19.20	-175.21	1838	138-10	12.39	179	251	0	193	-I-
y	0	060821.49952.6.01C.IOKE	Wpac	13.05	-166.46	2045	106+28	13.23	146	256	0	196	-I-
n	200	060807.49725.6.08W.SAOMAI	Wpac	18.97	137.75	0711	75-00	16.73	138	250	0	185	TIC
y	140	060807.49720.6.08W.SAOMAI	Wpac	17.75	139.56	2259	75+12	15.43	164	258	0	185	TIC
n	0	060724.49508.6.05E.DANIEL	Epac	16.03	-139.60	0902	82-12	13.65	172	259	0	195	-I-
n	140	060721.49466.6.06W.KAEMI	Wpac	16.64	131.12	1621	75-02	16.09	172	256	0	182	TIC
y	0	060719.49431.6.05E.DANIEL	Epac	11.80	-118.94	1029	78+10	14.34	177	256	0	189	-IC
n	0	060707.49252.6.04W.EWINIAR	Wpac	23.09	126.58	2244	85-01	10.50	214	263	0	194	---
y	240	060427.48140.6.02B.MALA	Ind	13.18	90.64	1433	74+17	16.66	151	259	1	180	TIC
y	0	060422.48063.6.23P.MONICA	Spac	-11.79	138.55	1610	128+11	13.00	138	234	6	183	-IC

2005

Area +I	km2	Overflight date and storm yyymmdd.orbit.v.#basin.name	Basin	lat N	lon E	hhmm UT	Wind kt	h=20Z km	Ice 85PCT	L.Ice 37PCT	LIS fl.	Cld 11mu	Obs
n	0	051207.45943.6.29L.EPSILON	Atl	29.13	-37.48	1505	62-10	9.25	207	260	0	218	---
n	0	051206.45928.6.29L.EPSILON	Atl	31.77	-33.84	1601	65-00	9.40	217	264	0	211	---
n	0	051203.45884.6.29L.EPSILON	Atl	34.42	-43.12	2024	65-00	9.65	204	262	0	216	---
y	0	051202.45869.6.29L.EPSILON	Atl	34.07	-47.44	2119	65+02	11.17	162	255	0	212	-I-
y	0	051202.45868.6.29L.EPSILON	Atl	33.96	-47.78	1941	65+03	7.93	223	265	0	219	---
y	0	051122.45699.6.03S.BERTIE	Spac	-10.85	91.16	2359	114+10	13.94	170	262	0	185	-IC
y	0	051122.45706.6.03S.BERTIE	Spac	-11.72	90.59	0950	86+19	12.32	195	262	0	195	-I-
y	0	051012.45065.6.21W.KIROGI	Wpac	20.66	132.29	0702	93+19	10.79	210	265	0	194	---
n	0	050929.44871.6.19W.LONGWANG	Wpac	22.21	132.53	2045	125-02	10.14	180	255	3	195	-I-
n	0	050922.44758.6.18L.RITA	Atl	25.31	-88.58	1443	133-25	13.37	138	245	3	195	-I-
y	0	050919.44710.6.10E.JOVA	Epac	15.13	-142.22	1222	100+10	12.21	182	251	0	192	-I-
y	0	050918.44694.6.11E.KENNETH	Epac	14.16	-129.12	1143	114+05	11.06	179	260	0	191	-IC
y	0	050910.44566.6.15W.KHANUN	Wpac	24.36	125.06	0704	105+14	12.56	192	263	0	193	-I-
y	40	050909.44546.6.15W.KHANUN	Wpac	19.14	130.53	2351	94+14	15.23	183	262	0	189	TIC
n	0	050906.44511.6.14L.MARIA	Atl	33.68	-54.73	1815	74-14	9.81	205	258	0	204	---
y	40	050822.44266.6.08E.HILARY	Epac	17.25	-108.78	0042	90+13	15.72	154	251	0	188	TIC
y	20	050815.44160.6.09L.IRENE	Atl	35.61	-68.76	0543	74+05	14.63	164	253	0	193	TI-
n	0	050813.44131.6.09L.IRENE	Atl	30.02	-68.84	0912	60-00	8.50	212	262	0	199	---
y	0	050813.44128.6.09L.IRENE	Atl	29.48	-68.06	0419	60+01	10.22	192	262	0	197	-I-
n	20	050812.44119.6.06E.FERNANDA	Epac	18.23	-123.99	1450	75-00	14.92	214	264	0	189	T-C
y	20	050812.44114.6.06E.FERNANDA	Epac	17.89	-122.90	0638	75+04	14.58	187	262	0	188	TIC
y	0	050719.43747.6.05L.EMILY	Atl	24.14	-95.02	1735	84+28	12.68	177	257	0	196	-I-
n	0	050717.43707.6.05W.HAITANG	Wpac	22.07	125.09	0359	130-21	12.36	158	256	0	194	-I-
y	0	050716.43696.6.05W.HAITANG	Wpac	20.73	127.75	1128	139+05	11.93	167	252	2	190	-IC
y	0	050709.43594.6.04L.DENNIS	Atl	25.81	-84.80	2159	103+33	11.18	212	264	0	196	---
y	20	050706.43547.6.04L.DENNIS	Atl	16.01	-72.37	2131	65+17	14.99	164	253	0	187	TIC
n	0	050608.43100.6.04W.NESAT	Wpac	25.31	134.57	0541	80-14	11.09	197	255	0	202	-I-
n	0	050607.43085.6.04W.NESAT	Wpac	23.47	133.98	0636	99-14	10.99	212	262	0	201	---

n	60	050605.43055.6.04W.NESAT	Wpac	18.46	131.11	0828	95-10	16.73	131	254	0	185	TIC
n	20	050605.43050.6.04W.NESAT	Wpac	17.51	130.63	0015	104-15	14.73	178	256	0	184	TIC
n	160	050604.43040.6.04W.NESAT	Wpac	15.60	130.94	0923	125-05	16.78	152	230	12	182	TIC
n	680	050603.43019.6.04W.NESAT	Wpac	12.32	134.34	0029	105-04	17.00	93	215	1	181	TIC
n	60	050425.42414.6.03W.SONCA	Wpac	16.51	131.59	0528	115-04	16.48	119	239	2	184	TIC
y	0	050424.42399.6.03W.SONCA	Wpac	14.11	130.85	0623	110+23	13.06	181	262	0	191	-IC
n	0	050411.42206.6.26S.ADELINE	Spac	-26.51	64.89	2130	61-22	9.21	223	260	0	221	---
y	80	050408.42159.6.26S.ADELINE	Spac	-16.58	72.34	2102	105+22	17.23	128	238	0	179	TIC
y	0	050406.42119.6.26S.ADELINE	Spac	-13.09	87.35	0627	105+04	12.66	142	238	7	190	-IC
n	0	050218.41391.6.19P.OLAF	Spac	-23.78	-161.16	1430	95-18	12.98	172	249	0	192	-I-

2004

	Area +I km2	Overflight date and storm yymmdd.orbit.v.#basin.name Basin	lat N	lon E	hhmm UT	Wind kt	h=20Z km	Ice 85PCT	L.Ice 37PCT	LIS fl.	Cld 11mu	Obs	
y	320	041022.39529.6.28W.NOCK-TEN	Wpac	15.50	136.32	0301	97+05	15.07	98	234	0	189	TIC
n	60	041020.39508.6.28W.NOCK-TEN	Wpac	12.69	141.74	1808	95-00	15.97	140	245	0	176	TIC
n	0	041018.39479.6.27W.TOKAGE	Wpac	24.37	127.21	2135	84-12	10.82	226	263	0	191	--C
y	80	041018.39477.6.28W.NOCK-TEN	Wpac	9.98	149.78	1822	80+05	15.75	145	248	0	185	TIC
y	540	041014.39407.6.27W.TOKAGE	Wpac	14.25	137.41	0711	80+10	17.65	103	242	1	183	TIC
y	0	041006.39280.6.26W.MA-ON	Wpac	20.53	132.71	0306	60+17	12.49	192	265	0	188	-IC
n	0	040928.39159.6.25W.MEARI	Wpac	29.35	127.38	0853	75-07	10.95	217	262	0	201	---
n	0	040927.39147.6.25W.MEARI	Wpac	26.90	125.67	1442	85-18	10.49	202	259	0	207	---
n	0	040923.39079.6.11L.JEANNE	Atl	25.45	-69.27	0601	84-05	11.48	190	262	0	194	-I-
n	20	040922.39063.6.12L.KARL	Atl	24.63	-49.45	0523	95-10	14.50	197	263	0	191	TIC
y	400	040922.39071.6.25W.MEARI	Wpac	16.61	138.21	1747	65+09	16.96	125	246	0	182	TIC
n	0	040921.39059.6.12L.KARL	Atl	23.10	-48.52	2251	100-11	10.05	214	264	0	194	---
n	0	040921.39045.6.11L.JEANNE	Atl	27.37	-70.65	0120	75-00	14.21	133	252	0	190	-IC
n	0	040915.38954.6.09L.IVAN	Atl	25.41	-87.49	0510	120-04	11.07	178	247	0	195	-I-
n	340	040914.38944.6.13E.JAVIER	Epac	16.67	-107.64	1412	125-00	16.49	104	230	10	186	TIC
n	0	040906.38811.6.22W.SONGDA	Wpac	28.63	127.10	0119	98-10	11.02	206	262	0	198	---
n	0	040904.38792.6.22W.SONGDA	Wpac	25.40	129.53	1943	122-10	13.55	164	260	0	190	-IC
n	0	040902.38761.6.11E.HOWARD	Epac	18.37	-114.11	2025	117-11	12.74	162	246	0	200	-I-
y	0	040902.38756.6.11E.HOWARD	Epac	17.83	-113.31	1214	120+19	11.70	155	253	0	193	-I-
n	0	040902.38750.6.22W.SONGDA	Wpac	21.45	140.24	0327	117-07	11.49	177	255	0	199	-I-
y	20	040830.38708.6.06L.FRANCES	Atl	19.20	-57.73	1020	100+05	15.40	173	246	0	191	TIC
n	0	040828.38670.6.19W.CHABA	Wpac	27.13	133.90	2353	105-05	11.91	209	261	0	196	---
y	0	040828.38677.6.06L.FRANCES	Atl	17.02	-51.46	1034	103+12	12.93	169	257	0	191	-IC
n	0	040826.38639.6.19W.CHABA	Wpac	23.57	136.25	0006	129-19	12.93	169	257	0	198	-I-
y	0	040824.38613.6.20W.AERE	Wpac	25.42	123.37	0827	82+07	13.00	197	259	0	197	-I-
n	280	040817.38513.6.04L.DANIELLE	Atl	25.72	-40.34	2227	77-18	15.45	119	230	4	189	TIC
y	80	040816.38483.6.04L.DANIELLE	Atl	15.82	-34.64	0021	90+04	15.51	113	234	0	188	TIC
n	0	040806.38333.6.14W.MERANTI	Wpac	29.85	169.41	0907	90-12	10.14	213	263	0	202	---
y	120	040803.38283.6.01L.ALEX	Atl	32.80	-77.56	0413	67+23	15.64	108	234	0	195	TIC
n	0	040729.38212.6.05E.DARBY	Epac	17.51	-127.89	1516	97-18	13.00	195	261	0	192	-I-
n	0	040727.38184.6.13W.NAMTHEUN	Wpac	30.61	142.86	2003	90-09	9.97	229	264	0	198	---
y	0	040726.38169.6.13W.NAMTHEUN	Wpac	27.34	146.29	2100	115+02	11.31	181	257	0	199	-I-
n	0	040630.37757.6.11W.TINGTING	Wpac	26.26	142.54	1048	65-01	11.98	198	262	0	196	-I-
y	0	040628.37723.6.10W.MINDULLE	Wpac	18.41	125.62	0603	115+14	13.31	142	249	0	191	-IC
y	0	040608.37418.6.07W.CONSON	Wpac	20.32	120.54	1625	88+07	11.75	193	256	0	192	-I-
n	0	040520.37116.6.04W.NIDA	Wpac	27.35	135.47	0745	73-12	11.46	191	256	0	192	-I-
y	0	040412.36522.6.03W.SUDAL	Wpac	15.68	130.99	0513	115+04	11.49	196	259	0	201	-I-
y	0	040412.36532.6.03W.SUDAL	Wpac	16.72	131.44	2006	120+01	11.70	184	255	0	187	-IC
y	20	040408.36461.6.03W.SUDAL	Wpac	8.90	139.79	0720	115+10	14.54	163	253	0	186	TIC
y	0	040306.35947.6.16S.GAFILO	Spac	-14.67	53.05	0802	140+03	12.97	124	243	1	194	-I-
n	0	040204.35464.6.10S.FRANK	Spac	-18.51	70.34	0717	113-06	10.48	202	264	0	200	---
y	0	040203.35458.6.10S.FRANK	Spac	-18.20	70.62	2306	112+16	11.87	188	261	0	190	-IC
y	0	040130.35382.6.10S.FRANK	Spac	-16.05	62.34	0203	91+06	14.05	167	259	0	187	-IC

2003

	Area +I km2	Overflight date and storm yymmdd.orbit.v.#basin.name Basin	lat N	lon E	hhmm UT	Wind kt	h=20Z km	Ice 85PCT	L.Ice 37PCT	LIS fl.	Cld 11mu	Obs	
y	0	031113.34175.5A.02A.02A	Ind	6.05	57.40	1518	67+10	13.06	177	263	0	191	-IC
y	0	031029.33937.5A.21W.PARMA	Wpac	24.22	149.11	0818	111+14	11.46	164	259	0	190	-IC
y	0	031024.33861.5A.21W.PARMA	Wpac	30.68	158.44	1121	129+06	13.72	112	236	0	186	-IC
y	80	031021.33815.5A.20W.KETSANA	Wpac	16.83	131.14	1222	125+09	15.99	118	239	0	182	TIC
n	0	031006.33581.5A.16L.KATE	Atl	35.20	-55.89	1217	74-10	11.70	146	248	0	201	-I-
n	0	031005.33566.5A.14E.NORA	Epac	18.86	-113.33	1257	84-09	14.18	174	252	0	188	-IC
y	0	030927.33444.5A.15L.JUAN	Atl	35.44	-63.24	1720	88+15	13.45	155	250	0	206	-I-
y	0	030926.33430.5A.15L.JUAN	Atl	32.80	-62.07	1953	71+08	12.31	174	254	0	201	-I-
y	0	030926.33428.5A.15L.JUAN	Atl	32.21	-62.06	1638	68+10	11.23	203	260	0	211	---

y	0	030921.33343.5A.16W.CHOI-WAN	Wpac	31.15	137.24	0453	98+13	14.46	137	244	0	188	-IC
n	0	030916.33275.5A.13L.ISABEL	Atl	27.91	-71.35	2058	95-00	11.69	220	264	0	205	---
n	0	030915.33248.5A.13L.ISABEL	Atl	24.36	-68.50	0344	126-11	10.18	199	257	0	195	-I-
n	0	030914.33244.5A.13L.ISABEL	Atl	24.16	-67.39	2112	134-10	11.22	179	254	0	204	-I-
n	0	030912.33202.5A.13L.ISABEL	Atl	21.69	-56.36	0456	140-00	11.97	147	240	0	199	-I-
y	0	030910.33182.5A.13L.ISABEL	Atl	21.17	-51.99	2142	123+06	13.49	142	251	0	193	-I-
y	680	030907.33133.5A.15W.MAEMI	Wpac	19.40	134.67	1841	65+09	17.20	93	214	0	180	TIC
n	0	030906.33109.5A.10L.FABIAN	Atl	34.68	-63.89	0533	100-00	10.90	204	258	0	195	---
n	0	030906.33108.5A.10L.FABIAN	Atl	34.32	-64.17	0355	100-01	10.75	197	258	0	195	-I-
n	680	030831.33023.5A.10E.JIMENA	Epac	18.12	-149.43	1719	76-19	16.49	101	240	0	186	TIC
y	140	030830.33006.5A.14W.DUJUAN	Wpac	17.94	132.86	1439	77+05	17.32	178	265	0	183	TIC
y	0	030830.33011.5A.14W.DUJUAN	Wpac	18.97	131.33	2250	80+09	14.00	200	266	0	190	--C
y	20	030829.32992.5A.10E.JIMENA	Epac	16.78	-136.70	1736	74+20	14.62	171	262	0	194	TI-
y	80	030824.32905.5A.12W.KROVANH	Wpac	18.83	113.82	0337	78+10	15.93	140	245	0	189	TIC
n	0	030807.32644.5A.11W.ETAU	Wpac	28.12	129.18	0937	110-03	13.76	178	261	0	194	-I-
y	20	030607.31690.5A.29P.GINA	Spac	-16.13	162.69	0358	81+16	14.58	185	254	0	192	TI-
n	0	030525.31498.5A.04W.CHAN-HOM	Wpac	27.60	157.91	2059	65-17	10.73	228	265	0	211	---
n	0	030524.31479.5A.04W.CHAN-HOM	Wpac	20.65	153.55	1521	115-00	11.42	202	262	0	193	---
y	20	030417.30905.5A.02W.KUJIRA	Wpac	13.45	131.06	1959	108+13	14.87	133	241	0	185	TIC
n	0	030416.30884.5A.02W.KUJIRA	Wpac	13.68	135.34	1105	130-17	14.00	139	252	0	187	-IC
y	20	030412.30828.5A.02W.KUJIRA	Wpac	10.16	151.10	2125	65+04	14.90	159	255	0	185	TIC
n	160	030405.30709.5A.26S.INIGO	Spac	-14.45	113.19	0624	125-05	15.24	133	224	14	189	TIC
y	0	030307.30268.5A.23S.KALUNDE	Spac	-13.74	71.05	2320	127+34	12.22	139	252	1	195	-I-
y	20	030228.30148.5A.19S.JAPHET	Spac	-22.96	37.80	0638	76+11	14.57	171	257	0	185	TIC
y	200	030227.30138.5A.19S.JAPHET	Spac	-22.13	38.58	1406	66+13	16.68	120	240	0	183	TIC
n	0	030212.29902.5A.17S.HAPE	Spac	-16.63	69.10	1146	80-00	11.63	163	238	0	193	-I-
y	0	030128.29669.5A.12P.BENI	Spac	-15.50	161.21	1259	94+35	13.25	205	260	0	184	--C
n	0	030114.29455.5A.10P.AMI	Spac	-25.72	-172.50	1933	97-18	11.55	220	260	0	198	---

2002

Area	Overflight date and storm	lat	lon	hhmm	Wind	h=20Z	Ice	L.Ice	LIS	Cld			
+I km2	yyymmdd.orbit.v.#basin.name Basin	N	E	UT	kt	km	85PCT	37PCT	fl.	11mu Obs			
n	0	021228.29180.5A.06P.ZOE	Spac	-12.41	169.53	0359	155-06	11.50	170	253	4	210	-I-
n	0	021227.29170.5A.05S.CRYSTAL	Spac	-21.77	60.00	1240	89-05	12.27	176	254	2	192	-I-
n	0	020903.27378.5A.22W.SINLAKU	Wpac	25.33	133.08	1255	90-00	11.26	209	264	0	197	---
y	0	020902.27357.5A.02C.ELE	Wpac	22.39	174.89	0413	107+13	12.01	162	253	0	197	-I-
n	0	020902.27369.5A.10E.HERNAN	Epac	18.65	-117.11	2239	97-15	9.49	240	268	0	206	---
y	0	020831.27338.5A.10E.HERNAN	Epac	16.33	-108.53	2252	112+30	11.50	181	260	0	199	-I-
n	0	020830.27314.5A.21W.RUSA	Wpac	30.41	127.63	1005	76-08	10.03	220	264	0	199	---
y	0	020827.27271.5A.21W.RUSA	Wpac	24.41	138.33	1609	93+00	8.67	244	270	0	195	---
n	0	020825.27237.5A.08E.FAUSTO	Epac	17.74	-126.49	1153	95-20	8.50	224	265	0	208	---
n	0	020817.27115.5A.19W.PHANFONE	Wpac	29.88	137.31	1538	111-08	10.00	235	265	0	198	---
n	0	020725.26758.5A.06E.ELIDA	Epac	14.93	-112.51	1747	115-25	12.39	157	245	2	201	-I-
n	60	020723.26721.5A.12W.FENGSHEN	Wpac	27.01	145.29	0915	101-25	16.24	157	262	0	189	TIC
n	0	020717.26624.5A.12W.FENGSHEN	Wpac	14.59	167.41	0326	125-00	13.65	181	243	2	196	-I-
y	0	020710.26518.5A.10W.HALONG	Wpac	12.29	143.74	0812	95+03	13.49	170	262	0	186	-IC
y	360	020704.26432.5A.08W.CHATAAN	Wpac	13.46	145.27	2020	91+06	17.12	130	240	0	179	TIC
y	40	020529.25863.5A.01E.ALMA	Epac	13.09	-114.73	0813	76+10	15.45	140	246	0	182	TIC
n	340	020311.24637.5A.18S.HARY	Spac	-21.98	51.91	1640	102-11	16.99	117	253	0	181	TIC
n	0	020307.24570.5A.02W.MITAG	Wpac	18.08	133.97	0911	69-24	6.21	261	268	0	200	---
y	0	020307.24575.5A.18S.HARY	Spac	-11.37	56.52	1707	73+36	13.47	157	255	0	184	-IC
y	820	020302.24494.5A.02W.MITAG	Wpac	8.07	140.81	1214	90+24	17.65	112	234	1	174	TIC
n	0	020208.24147.5A.12S.FRANCESCA	Spac	-19.58	83.46	0607	94-05	11.60	205	258	0	197	---
y	0	020203.24077.5A.12S.FRANCESCA	Spac	-14.87	78.21	1718	69+14	13.98	166	256	0	183	-IC
y	180	020118.23818.5A.10S.DINA	Spac	-12.87	70.17	0230	67+14	15.95	156	252	0	181	TIC

2001

Area	Overflight date and storm	lat	lon	hhmm	Wind	h=20Z	Ice	L.Ice	LIS	Cld			
+I km2	yyymmdd.orbit.v.#basin.name Basin	N	E	UT	kt	km	85PCT	37PCT	fl.	11mu Obs			
y	0	011220.23379.5A.33W.FAXAI	Wpac	9.02	158.36	2317	73+23	13.41	193	260	0	189	-IC
y	0	011024.22478.5A.26W.PODUL	Wpac	16.84	156.97	0351	138+05	11.60	195	263	0	211	-I-
y	0	011007.22213.5A.11L.IRIS	Atl	16.79	-74.72	0346	75+03	11.85	171	260	0	189	-IC
n	0	010927.22057.5A.11E.JULIETTE	Epac	19.69	-110.41	0304	92-10	7.99	253	272	0	198	---
y	0	010925.22032.5A.23W.LEKIMA	Wpac	21.22	121.73	1235	90+09	13.21	177	259	0	184	-IC
n	0	010924.22011.5A.10L.HUMBERTO	Atl	33.62	-66.97	0424	77-12	14.49	149	250	0	193	-I-
n	0	010924.22012.6.10L.HUMBERTO	Atl	33.79	-66.82	0602	74-14	13.76	160	256	0	194	-I-
n	0	010924.22016.5A.11E.JULIETTE	Epac	15.05	-103.74	1225	99-17	9.20	228	262	0	194	---
y	0	010919.21941.5A.21W.VIPA	Wpac	32.53	139.48	1635	65+03	11.36	196	259	0	199	-I-
n	0	010917.21903.5A.07L.FELIX	Atl	34.90	-31.65	0607	64-10	11.00	201	259	0	212	---
n	0	010917.21904.6.07L.FELIX	Atl	34.94	-31.74	0745	63-09	9.43	211	259	0	216	---

n	0	010916.21889.5A.07L.FELIX	Atl	32.98	-33.70	0840	77-10	9.31	215	258	0	214	---
n	20	010915.21872.5A.07L.FELIX	Atl	31.68	-40.96	0619	90-00	14.58	200	262	0	193	T--
y	0	010915.21868.5A.20W.NARI	Wpac	26.38	124.31	1230	75+10	10.55	225	265	0	206	---
n	0	010910.21798.5A.06L.ERIN	Atl	34.91	-64.74	2140	83-13	9.61	221	263	0	213	---
n	0	010908.21761.5A.20W.NARI	Wpac	26.93	127.00	0340	66-05	12.24	210	264	0	198	---
n	0	010907.21757.5A.19W.DANAS	Wpac	28.32	144.06	2112	100-00	11.97	182	261	0	203	-I-
y	0	010829.21604.5A.07E.FLOSSIE	Epac	19.87	-115.22	0159	76+10	9.74	193	258	0	193	-I-
y	60	010827.21584.5A.07E.FLOSSIE	Epac	19.73	-113.86	1844	65+08	14.97	168	259	0	195	TI-
n	0	010805.21240.5.12W.MAN-YI	Wpac	25.95	144.23	1944	102-13	10.50	214	266	0	200	---
n	0	010727.21100.5.09W.KONG-REY	Wpac	32.91	148.09	2234	66-11	11.90	223	268	0	205	---
n	0	010727.21085.5.09W.KONG-REY	Wpac	31.13	143.51	2346	65-10	12.66	184	262	0	197	-I-
n	0	010727.21098.5.09W.KONG-REY	Wpac	32.44	147.51	1921	68-13	10.00	232	267	0	198	---
y	0	010726.21070.5.09W.KONG-REY	Wpac	29.28	140.83	0057	80+00	11.85	197	263	0	198	-I-
n	0	010705.20743.5.06W.UTOR	Wpac	20.97	117.53	0656	65-04	7.31	263	277	0	202	---
n	0	010530.20171.5.01E.ADOLPH	Epac	15.91	-106.31	0052	108-15	10.24	200	258	0	203	---
y	0	010528.20140.5.01E.ADOLPH	Epac	13.93	-99.90	0142	97+25	12.49	155	237	0	199	-I-
y	0	010111.17989.5.05S.BINDU	Spac	-16.93	70.17	1612	68+08	11.25	236	264	0	192	---
y	0	010109.17958.5.05S.BINDU	Spac	-16.16	72.60	1700	90+00	13.38	184	259	0	186	-IC

2000

Area +I	km2	Overflight date and storm yyymmdd.orbit.v.#basin.name	Basin	lat N	lon E	hhmm UT	Wind kt	h=20Z km	Ice 85PCT	L.Ice 37PCT	LIS fl.	Cld 11mu	Obs
y	0	001029.16822.5.30W.XANGSANE	Wpac	16.08	118.15	1519	60+23	13.46	200	261	0	181	--C
n	0	000929.16353.5.13L.ISAAC	Atl	33.76	-55.68	2143	86-13	13.73	175	264	0	193	-I-
n	0	000929.16353.5.13L.ISAAC	Atl	33.63	-55.58	2143	86-13	13.73	175	252	0	193	-I-
y	340	000916.16146.5.25W.SONAMU	Wpac	29.24	141.45	1851	70+00	16.23	120	244	0	188	TIC
y	500	000916.16137.6.10L.FLORENCE	Atl	32.00	-66.16	0456	65+00	15.72	79	192	8	186	TIC
n	0	000915.16129.5.22W.SAOMAI	Wpac	33.63	128.14	1647	65-08	10.39	211	260	0	200	---
n	0	000911.16066.5.22W.SAOMAI	Wpac	25.71	129.69	1648	111-07	10.91	190	259	0	206	-I-
y	0	000818.15690.6.03L.ALBERTO	Atl	34.59	-48.18	2045	69+14	12.48	169	259	0	201	-I-
y	0	000818.15689.6.03L.ALBERTO	Atl	34.63	-48.19	1909	66+15	11.96	185	258	0	203	-I-
n	0	000815.15635.5.15W.EWINIAR	Wpac	35.29	149.84	0901	75-00	13.08	200	262	0	199	---
y	0	000810.15565.5.03L.ALBERTO	Atl	29.54	-57.68	2221	68+08	8.49	224	268	0	204	---
n	0	000807.15514.5.13W.JELAWAT	Wpac	26.78	128.44	1701	85-06	7.92	243	264	0	222	---
n	0	000805.15483.5.13W.JELAWAT	Wpac	25.93	132.66	1751	90-00	10.46	204	260	0	199	---
y	0	000802.15432.5.13W.JELAWAT	Wpac	22.50	147.65	1151	115+00	12.75	151	250	3	199	-I-
n	0	000729.15367.5.06E.DANIEL	Epac	18.66	-143.71	0854	65-07	12.22	193	259	0	202	-I-
n	0	000622.14784.5.03E.CARLOTTA	Epac	16.52	-106.89	1006	100-04	10.49	205	264	0	191	--C
y	220	000620.14753.5.03E.CARLOTTA	Epac	14.67	-101.01	1055	73+19	15.91	122	247	0	183	TIC
n	0	000329.13451.5.21S.HUDAH	Spac	-16.91	69.11	2136	90-05	13.97	163	244	0	186	-IC
n	120	000302.13023.5.16S.NORMAN	Spac	-19.35	109.75	1710	266-20	16.30	158	254	0	181	TIC
y	0	000217.12794.5.11S.LEON-ELINE	Spac	-19.96	50.42	0438	76+15	10.68	183	258	0	191	-IC
n	0	000215.12763.5.11S.LEON-ELINE	Spac	-18.68	56.20	0528	65-05	14.24	199	265	0	196	-I-
n	0	000214.12757.5.11S.LEON-ELINE	Spac	-18.39	57.56	2123	70-02	9.15	220	263	0	197	---
n	0	000128.12479.5.08S.CONNIE	Spac	-16.64	57.03	0616	110-09	11.83	167	262	0	203	-I-

1999

Area +I	km2	Overflight date and storm yyymmdd.orbit.v.#basin.name	Basin	lat N	lon E	hhmm UT	Wind kt	h=20Z km	Ice 85PCT	L.Ice 37PCT	LIS fl.	Cld 11mu	Obs
y	0	991116.11335.5.16L.LENNY	Atl	15.33	-69.50	1619	85+13	10.55	139	242	0	186	-IC
n	0	991008.10710.5.26W.DAN	Wpac	21.82	118.12	0110	90-00	9.98	200	262	0	192	---
n	0	990922.10458.5.09L.GERT	Atl	34.55	-61.13	0153	75-05	10.49	199	260	0	193	-I-
y	0	990922.10463.5.24W.BART	Wpac	26.06	127.13	0017	130+10	12.59	163	251	1	206	-I-
n	0	990922.10457.5.09L.GERT	Atl	34.26	-61.51	0917	72-07	10.89	227	269	0	203	---
y	0	990920.10432.5.24W.BART	Wpac	23.96	125.51	1004	78+21	11.72	216	265	0	189	--C
n	0	990916.10367.5.09L.GERT	Atl	18.09	-51.90	0736	128-06	13.33	181	256	0	190	-IC
y	0	990915.10355.5.21W.YORK	Wpac	21.44	115.33	1252	65+09	12.92	165	251	9	186	-IC
n	0	990913.10321.5.08L.FLOYD	Atl	23.90	-70.85	0932	135-01	12.25	125	245	0	199	-I-
n	0	990830.10102.5.04L.CINDY	Atl	34.88	-54.21	1201	80-10	8.71	211	263	0	196	---
n	0	990829.10086.5.04L.CINDY	Atl	32.78	-58.15	1136	101-20	12.65	210	262	0	201	---
y	0	990828.10070.5.04L.CINDY	Atl	29.77	-58.10	1112	119+07	11.19	173	258	0	198	-I-
n	0	990822.9975.5.04L.CINDY	Atl	14.47	-33.27	1028	65-03	8.98	225	262	0	195	---
y	80	990821.9967.5.03L.BRET	Atl	24.63	-94.97	2245	113+36	15.17	150	248	2	197	TI-
n	40	990809.9763.5.08E.EUGENE	Epac	14.87	-129.38	2350	95-04	15.06	165	246	0	193	TI-
y	0	990731.9629.5.11W.OLGA	Wpac	23.28	130.49	1157	64+09	10.97	220	268	0	191	--C
n	0	990713.9346.5.02E.BEATRIZ	Epac	15.04	-122.26	1311	104-05	10.92	178	257	0	200	-I-
y	280	990620.8975.5.01E.ADRIAN	Epac	16.76	-106.72	0034	65+10	16.26	149	260	0	181	TIC
n	0	990501.8194.5.05W.LEO	Wpac	21.18	115.84	1157	70-20	9.23	241	260	0	197	---
y	80	990426.8116.5.04W.KATE	Wpac	21.50	135.36	1314	67+12	16.20	175	265	0	181	TIC
n	0	990331.7708.5.31S.FREDERIC	Spac	-17.43	91.19	1659	140-01	13.81	153	251	0	191	-IC

y	0	990330.7683.5.31S.FREDERIC	Spac	-16.88	98.52	0157	115+10	14.17	159	257	0	188	-IC
n	0	990311.7386.5.25S.DAVINA	Spac	-22.87	52.80	0658	75-00	13.06	161	244	0	196	-I-
y	540	990305.7298.5.25S.DAVINA	Spac	-14.31	81.36	1558	83+26	16.77	106	239	0	181	TIC
n	660	990126.6689.5.15S.DAMIEN	Spac	-14.88	94.61	0203	65-10	17.25	124	239	1	179	TIC

1998

	Area +I km2	Overflight date and storm yymmdd.orbit.v.#basin.name Basin	lat N	lon E	hhmm UT	Wind kt	h=20Z km	Ice 85PCT	L.Ice 37PCT	LIS fl.	Cld 11mu	Obs	
y	0	990116.6538.6.11P.DANI	Spac	-16.22	163.93	1113	88+33	12.31	143	247	0	184	-IC
n	0	981209.5931.5.06S.THELMA	Spac	-11.90	128.35	0022	130-04	13.94	120	227	8	190	-IC
y	20	981207.5907.5.06S.THELMA	Spac	-10.20	130.97	1054	98+27	15.00	194	262	0	182	TIC
y	0	981022.5178.5.14E.LESTER	Epac	16.77	-108.70	0536	94+09	10.45	189	260	0	203	-I-
y	0	981017.5100.5.14E.LESTER	Epac	14.42	-95.21	0652	80+09	12.66	196	261	0	192	-I-
y	0	980927.4780.5.07L.GEORGES	Atl	26.96	-86.32	0016	95+04	13.43	215	260	0	189	--C
n	300	980927.4790.5.10L.JEANNE	Atl	26.41	-41.61	1509	70-00	16.22	119	240	1	193	TI-
y	300	980925.4760.5.11L.KARL	Atl	30.22	-52.86	1733	69+10	16.14	84	207	6	191	TIC
y	0	980919.4656.5.07L.GEORGES	Atl	14.10	-49.97	0339	93+14	12.04	162	252	0	199	-I-
n	420	980918.4647.5.10W.TODD	Wpac	29.76	128.44	1349	65-05	17.98	104	221	6	185	TIC
n	0	980902.4391.6.04L.DANIELLE	Atl	34.90	-66.98	0801	73-08	14.00	161	250	0	200	-I-
n	0	980830.4353.5.06W.REX	Wpac	31.13	142.74	2221	90-00	14.22	192	260	0	195	-I-
n	0	980827.4299.5.09E.HOWARD	Epac	18.41	-124.94	1149	70-15	9.02	230	265	0	211	---
n	0	980826.4283.5.02L.BONNIE	Atl	32.59	-77.74	1137	100-00	8.75	228	268	0	206	---
n	0	980824.4251.5.02L.BONNIE	Atl	25.47	-72.35	1050	100-00	11.60	225	265	0	192	---
y	0	980824.4252.5.09E.HOWARD	Epac	16.09	-114.83	1215	110+00	12.73	170	249	0	195	-I-
y	620	980822.4224.5.02L.BONNIE	Atl	23.18	-70.48	1806	85+14	17.16	101	243	0	189	TIC
n	0	980727.3805.5.05E.DARBY	Epac	16.50	-128.47	0356	100-00	11.50	172	258	0	209	-I-
y	20	980608.3030.5.03A.03A	Ind	18.01	67.62	0056	95+08	14.74	183	257	0	184	TIC
n	0	980324.1840.5.29P.YALI	Spac	-24.43	163.10	1409	60-01	12.00	211	262	0	209	---
y	780	980321.1793.5.29P.YALI	Spac	-17.25	166.68	1432	82+10	17.57	132	242	6	177	TIC
y	100	980321.1799.5.29P.YALI	Spac	-17.72	167.53	2238	88+06	15.85	134	238	2	185	TIC
n	0	980211.1196.5.20S.ANACELLE	Spac	-21.59	59.18	1800	115-10	12.11	181	249	0	192	-I-
y	0	980210.1171.5.20S.ANACELLE	Spac	-15.50	59.61	0254	84+15	10.75	201	262	0	187	--C

REFERENCES

REFERENCES

- Aberson, S. D., M. Montgomery, M. L. Black, and M. Bell (2004), A record wind measurement in Hurricane Isabel: direct evidence of an eyewall mesocyclone, *26th Conference on Hurricanes and Tropical Meteorology*, AMS, preprint paper 5D6.
- Alcala, C. M., and A. E. Dessler (2002), Observations of deep convection in the tropics using the tropical rainfall measuring mission (TRMM) precipitation radar, *J. Geophysical Research*, 107 (D24), 4792, doi:2002JD002457.
- AMS (2000), *Glossary of Meteorology*, 2nd edition, AMS, Boston, 855 pp.
- Anagnostou, E. N., C. A. Morales, and T. Dinku (2001), The use of TRMM Precipitation Radar observations in determining ground radar calibration biases, *J. of Atmos. and Oceanic Tech.*, 18, 616–628.
- Andreas, E. L., and K. A. Emanuel (2001), Effects of sea spray on tropical cyclone intensity, *J. of the Atmospheric Sciences*, 58, 3741–3751.
- Anthes, R. A. (1982), *Tropical Cyclones: Their Evolution Structure, and Effects*, Meteorological Monographs, vol. 19, AMS, Boston, 208 pp.
- Anthes, R. A. (2003), Hot towers and hurricanes: early observations, theories, and models, chapter 10 of *Cloud Systems, Hurricanes, and the TRMM*, Meteorological Monographs, vol. 29, AMS, Boston, 139–148.
- As-Salek, J. A. (1998), Coastal trapping and funneling effects on the storm surges in the Meghna Estuary in relation to cyclones hitting Noakhali-Cox's Bazar coast of Bangladesh, *J. of Physical Oceanography*, 28, 227–249.
- Astheimer, R. W., R. DeWaard, and E. A. Jackson (1961), Infrared radiometric instruments on TIROS II, *Applied Optics*, 51, 1386–1393.
- Atkinson, G. D., and C. R. Holliday (1977), Tropical cyclone minimum sea level pressure/maximum sustained wind relationship for the western north Pacific, *Monthly Weather Review*, 105, 421–427.

- Atlas, D. (1963), Radar analysis of severe storms, *Meteorological Monographs*, vol. 5, 177–223, AMS, Boston. In particular, see Figure 28 on page 199.
- Backeus, S., P. Wikstrom, and T. Lamas (2005), A model for regional analysis of carbon sequestration and timber production, *Forest Ecology and Management*, 216, 28–40.
- Bandeem, W. R., B. J. Conrath, W. Nordberg, and H. P. Thompson (1963), *A Radiation View of Hurricane Anna from the TIROS III Meteorological Satellite*, NASA Technical Note D-1713. Downloaded from the NASA Technical Report Server, www.nttrs.nasa.gov.
- Bandeem, W. R., R. A. Hanel, J. Light, R. A. Stampfl, and W. G. Stroud (1961), Infrared and reflected solar radiation measurements from the TIROS II Meteorological Satellite, *J. of Geophysical Research*, 66, 3169–3185.
- Bankert, R. L., and P. M. Tag (2002), An automated method to estimate tropical cyclone intensity using SSM/I imagery, *J. of Applied Meteorology*, 41, 461–472.
- Barnes, R. A., W. L. Barnes, C. Lyu, and J. M. Gales (2000), An overview of the Visible and Infrared Scanner radiometric calibration algorithm, *J. of Atmospheric and Oceanic Technology*, 17, 395–405.
- Barth, S. C. (2002), *Estimating Real-time Ocean Temperature Profiles from Satellite Altimetry for use in a Coupled Model of Hurricane Intensification*, Ph.D. dissertation, University of Colorado. 103 pp.
- Battan, L. J. (1973), *Radar Observation of the Atmosphere*, University of Chicago Press, Chicago, 324 pp.
- Bevington, P. R., and D. K. Robinson (1992), *Data Reduction and Error Analysis for the Physical Sciences*, 2nd edition, McGraw-Hill, New York, 328 pp.
- Bhattacharyya, G. K., and R. A. Johnson (1977), *Statistical Concepts and Methods*, John Wiley & Sons, New York, 639 pp.
- Bilanow, S., and S. Slojkowski (2006), TRMM on-orbit performance reassessed after control change, *25th International Symposium on Space Technology and Science*, JAXA, June 4–11, 2006, Japan, preprint paper ISTS 2006-d-35.
- Bister M. (2001), Effect of peripheral convective on tropical cyclone formation, *J. of the Atmospheric Sciences*, 58, 3463–3476.
- Bister, M., and K. A. Emanuel (1998), Dissipative heating and hurricane intensity, *Meteorology and Atmospheric Physics*, 65, 233–240.

- Black, M. L., R. W. Burpee, and F. D. Marks (1996), Vertical motion characteristics of tropical cyclones determined with airborne Doppler radial velocities, *J. of the Atmospheric Sciences*, *53*, 1887–1909.
- Black, P. G., E. A. D'Asaro, W. M. Drennan, J. R. French, P. P. Niiler, T. B. Sanford, E. J. Terrill, E. J. Walsh, and J. A. Zhang (2007), Air-sea exchange in hurricanes: synthesis of observations from the Coupled Boundary Layer Air-Sea Transfer Experiment, *Bulletin of the AMS*, March 2007, 357–374.
- Black, R. A. (1990), Radar reflectivity-ice water content relationships for use above the melting level in hurricanes, *J. of Applied Meteorology*, *29*, 955–961.
- Black, R. A., and J. Hallett (1986), Observations of the distribution of ice in hurricanes, *J. of the Atmospheric Sciences*, *43*, 802–822. Most rain drops in the eyewall freeze by the time they ascent to the -5 C level.
- Black, R. A., and J. Hallett (1999), Electrification of the hurricane, *J. of the Atmospheric Sciences*, *56*, 2004–2028.
- Black, R. A., G. M. Heymsfield, and J. Hallett (2003), Extra large particle images at 12 km in a hurricane eyewall: evidence of high-altitude supercooled water? *Geophysical Research Letters*, *30*, 2003GL017864. Hydrometeors were observed to be not fully frozen in a vigorous eyewall cell at -35 C to -42 C, i.e., a 12 km altitude.
- Black, R. A., H. B. Bluestein, and M. L. Black (1994), Unusually strong vertical motions in a Caribbean hurricane, *Monthly Weather Review*, *122*, 2722–2738.
- Boccippio, D. J., and S. J. Goodman (2000), Regional differences in tropical lightning distributions, *J. of Applied Meteorology*, *39*, 2231–2248.
- Bogner, P. B., G. M. Barnes, and J. L. Franklin (2000), Conditional instability and shear for six hurricanes over the Atlantic Ocean, *Weather and Forecasting*, *15*, 192–207.
- Bohm, H. P (1989), A general equation for the terminal fall speed of solid hydrometeors, *J. of the Atmospheric Sciences*, *46*, 2419–2427.
- Bohren, C. F., and B. A. Albrecht (1998), *Atmospheric Thermodynamics*, Oxford University Press, New York, 402 pp.
- Bolton, D. (1980), The computation of equivalent potential temperature, *Monthly Weather Review*, *108*, 1046–1053.
- Bosart, L F., and D. B. Dean (1991), The Agnes rainstorm of June 1972: surface feature evolution culminating in inland storm redevelopment, *Weather and Forecasting*, *6*, 515–537.

- Braun, S. A. (2002), A cloud-resolving simulation of Hurricane Bob (1991): storm structure and eyewall buoyancy, *Monthly Weather Review*, 130, 1573–1592. "A tongue of higher θ_e air extends outward from the eye into the eyewall updraft and is nearly coincident with the low-level outflow above the boundary layer... giving the impression that the storm is drawing air out of the eye and into the updraft ." [p. 1584]
- Braun, S. A. (2006), High-resolution simulation of Hurricane Bonnie (1998), Part II: water budget, *J. of the Atmospheric Sciences*, 63, 43–64.
- Braun, S. A., M. T. Montgomery, and Z. Pu (2006), High-resolution simulation of Hurricane Bonnie (1998), Part I: the organization of eyewall vertical motion, *J. of the Atmospheric Sciences*, 63, 19–42.
- Bretherton, C. S., and P. K. Smolarkiewicz (1989), Gravity waves, compensating subsidence, and detrainment around cumulus clouds, *J. of the Atmospheric Sciences*, 46, 740–759.
- Brown, R. A., V. T. Wood, and D. Sirmans (2000), Improved WSR-88D scanning strategies for convective storms, *Weather and Forecasting*, 15, 208–220.
- Brueske, K. F., and C. S. Velden (2003), Satellite-based tropical cyclone intensity estimation using the NOAA-KML series Advanced Microwave Sounding Unit (AMSU), *Monthly Weather Review*, 131, 687–697.
- Byers H. R., and R. R. Braham (1948), Thunderstorm structure and circulation, *J. of Meteorology*, 5, 71–86.
- Camp, J. P., and M. T. Montgomery (2001), Hurricane maximum intensity: past and present, *Monthly Weather Review*, 129, 1704–1717.
- Cecil, D. J., E. J. Zipser, and S. W. Nesbitt (2002), Reflectivity, ice scattering, and lightening characteristics of tropical cyclone eyewalls and rainbands, Part II: intercomparison of observations, *Monthly Weather Review*, 130, 785–801.
- Cecil, D. J., E. J. Zipser, and S. W. Nesbitt (2002), Reflectivity, ice scattering, and lightening characteristics of tropical cyclone eyewalls and rainbands, Part I: quantitative description, *Monthly Weather Review*, 130, 769–784.
- Chapman, R. (1969), *TIROS-NIMBUS Administrative, Political, and Technological Problems of Developing U.S. Weather Satellites*, Limited advanced edition, Inter-University Case Programs, Inc., New York, 129 pp.

- Chelton, D. B., F. J. Wentz, C. L. Gentemann, R. A. de Szoeke, and M. G. Schlax (2000), Satellite microwave SST observations of transequatorial tropical instability waves, *Geophysical Research Letters*, 27 (9), 1999GL011047, 1239–1242.
- Chen, S. S., and W. M. Frank (1993), A numerical study of the genesis of extratropical convective mesovortices, Part I: evolution and dynamics, *J. of the Atmospheric Sciences*, 50, 2401–2426.
- Chen, Y., Brunet, G., and M. K. Yau (2003), Spiral bands in a simulated hurricane, Part II: wave activity diagnostics, *J. of the Atmospheric Sciences*, 60, 1239–1256.
- Chiu, L. S., A. T. C. Chang, and J. Janowiak (1993), Comparison of monthly rain rates derived from GPI and SSM/I using probability distribution functions, *J. of Applied Meteorology*, 32, 323–334.
- Chow, U. T., editor (1964), *Handbook of Applied Hydrology*, McGraw Hill Book Company, New York.
- Christian, H. J. (2000), *Algorithm Theoretical Basis Document (ATBD) for the Lightning Imaging Sensor (LIS)*, NASA Marshall Space Flight Center, Huntsville, Alabama, first published in 1994, revised version published in 2000.
- Chu, J.-W., C. R. Sampson, A. S. Levine, and E. Fukada (2002), *The Joint Typhoon Warning Center Tropical Cyclone Best-Tracks, 1945–2000*, NRL Memorandum Report, NRL/ML/7540-02-16, August 2002. Downloaded on 2007/09/02 from https://metocph.nmci.navy.mil/jtwc/best_tracks/.
- Cotton, W. R., and R. A. Anthes (1989), *Storm and Cloud Dynamics*, Academic Press, 883 pp.
- Craig, G. C., and S. L. Gray (1996), CISK or WISHE as the mechanism for tropical cyclone intensification, *J. of the Atmospheric Sciences*, 53, 3528–3540.
- Cram, T. A., J. Persing, M. T. Montgomery, and S. A. Braun (2007), A Lagrangian trajectory view on transport and mixing processes between the eye, eyewall, and environment using a high-resolution simulation of Hurricane Bonnie (1998), *J. of the Atmospheric Sciences*, 64, 1836–1856.
- CRC (1991), *CRC Standard Mathematical Tables and Formulas*, 29th edition, CRC Press, Boca Raton, 609 pp.
- CRC (2004), *CRC Handbook of Chemistry and Physics*, 85th edition, CRC Press, Boca Raton.

- Crum, T., and S. Smith (2007), Update on the NWS WSR-88D level II data collection and distribution network and plans for change, *Conference on Interactive Information Processing Systems*, AMS, preprint paper 5B2.
- Cummins, K. L., M. J. Murphy, E. A. Bardo, W. L. Hiscox, R. B. Pyle, and A. E. Pifer (1998), A combined TOA/MDF technology upgrade of the U. S. National Lightning Detection Network, *J. of Geophysical Research*, *103* (D8), 9035–9044.
- DeMaria, M. (1996), The effect of vertical shear on tropical cyclone intensity change, *J. of the Atmospheric Sciences*, *53*, 2076–2086.
- DeMaria, M., and J. Kaplan (1999), An updated statistical tropical cyclone intensity prediction scheme (SHIPS) for the Atlantic and Eastern North Pacific. *Wea. Forecasting*, *14*, 326–37.
- DeMaria, M., and J. M. Gross (2003), Evolution of prediction models, chapter 4 of *Hurricane! Coping with Disaster*, American Geophysical Union, Washington D.C., 103–126.
- DeMaria, M., J. Baik, and J. Kaplan (1993), Upper-level eddy angular momentum fluxes and tropical cyclone intensity change, *J. of the Atmospheric Sciences*, *50*, 1133–1147.
- DeMaria, M., M. Mainelli, L. K. Shay, J. A. Knaff, and J. Kaplan (2005), Further improvements to the Statistical Hurricane Intensity Prediction Scheme (SHIPS), *Weather and Forecasting*, *20*, 531–543.
- Dessler, A. E., S. P. Palm, and J. D. Spinhirne (2006), Tropical cloud-top height distributions revealed by the ice, cloud, and land elevation satellite (ICESat)/geoscience laser altimeter system (GLAS), *J. of Geophysical Research*, *111*, D12215, doi:10.1029/2005JD006705.
- Djuric, D. (1994), *Weather Analysis*, Prentice Hall, Upper Saddle River, NJ, 304 pp.
- Dong, X. Q., B. K. Xi, and P. Minnis (2006), Observational evidence of changes in water vapor, clouds, and radiation at the ARM SGP site, *Geophysical Research Letters*, *33*, L19818.
- Dorst, N. M. (2007), The National Hurricane Research Project: 50 years of research, rough rides, and name changes, *Bulletin of the AMS*, October 2007, 1566–1588.
- Doswell, C. A. (2001), Severe convective storms, chapter 1 of *Severe Convective Storms*, Meteorological Monographs, vol. 28, AMS, Boston.
- Doviak, R. J., and D. S. Zrnic (1993), *Doppler Radar and Weather Observations*, 2nd edition, Academic Press, San Diego, 562 pp.

- Drusch, M., and P. Viterbo (2007), Assimilation of screen-level variables in ECMWF's integrated forecast system: a study on the impact on the forecast quality and analyzed soil moisture, *Monthly Weather Review*, *135*, 300–314.
- Dutton, J. A. (1986), *Dynamics of Atmospheric Motion*, Dover Publication, Inc., New York, 617 pp.
- Dvorak, V. F. (1975), Tropical cyclone intensity analysis and forecasting from satellite imagery, *Monthly Weather Review*, *103*, 420–430.
- Eastin, M. D., W. M. Gray, and P. G. Black (2005), Buoyancy of convective vertical motions in the inner core of intense hurricanes, Part I: general statistics, *Monthly Weather Review*, *133*, 188–208.
- Eastin, M. D., W. M. Gray, and P. G. Black (2005), Buoyancy of convective vertical motions in the inner core of intense hurricanes, Part 2: case studies, *Monthly Weather Review*, *133*, 209–227.
- Ebert, E. E., and G. J. Holland (1992), Observations of record cold cloud-top temperatures in Tropical Cyclone Hilda (1990), *Monthly Weather Review*, *120*, 2240–2251.
- Elsner, J. B., and A. B. Kara (1999), *Hurricanes of the North Atlantic*, Oxford University Press, New York, 488 pp.
- Emanuel, K. A. (1986), An air-sea interaction theory for tropical cyclones, Part I: steady-state maintenance, *J. of the Atmospheric Sciences*, *43*, 585–604. This paper finds that the hurricane is limited to Carnot efficiency solely based on the assumption that the hurricanes is in gradient wind balance, not assuming that the secondary circulation is a closed circuit.
- Emanuel, K. A. (1987), The dependence of hurricane intensity on climate, *Nature*, *326*, 483–485.
- Emanuel, K. A. (1988), The maximum intensity of tropical cyclones, *J. of the Atmospheric Sciences*, *45*, 1143–1155. A more clear explanation of the Carnot Engine analogy applied to the tropical cyclone can be found on Emanuel's website, "Tropical cyclone Potential Intensity Theory", last updated in 1996. There is a typo however in equation (4) of this web page. A factor of " T_s " is erroneously included in the definition of V_s^2 . Only if Emanuel were doing the derivation in terms of entropy, then the T_s term would belong, but this web page is doing the derivation in terms of enthalpy.
- Emanuel, K. A. (1988), Toward a general theory of hurricanes, *American Scientist*, July-August 1988, 371–379.

- Emanuel, K. A. (1994), *Atmospheric Convection*, Oxford University Press, 580 pp.
- Emanuel, K. A. (1995), Sensitivity of tropical cyclones to surface exchange coefficients and a revised steady-state model incorporating eye dynamics, *J. of the Atmospheric Sciences*, 52, 3969–3976. This paper uses enthalpy, as does this dissertation, instead of entropy, as is done in *Emanuel* [1997].
- Emanuel, K. A. (1997), Some aspects of hurricane inner-core dynamics and energetics, *J. of the Atmospheric Sciences*, 54, 1014–1026.
- Emanuel, K. A. (1998), The power of a hurricane: an example of reckless driving on the information superhighway, *Weather*, 54, 107–108.
- Emanuel, K. A. (1999), Thermodynamic control of hurricane intensity, *Nature*, 401, 665–669.
- Emanuel, K. A. (2000), A statistical analysis of tropical cyclone intensity, *Monthly Weather Review*, 128, 1139–1152.
- Emanuel, K. A. (2003), A similarity hypothesis for air-sea exchange at extreme wind speeds, *J. of the Atmospheric Sciences*, 60, 1420–1428.
- Emanuel, K. A. (2003), Tropical cyclones, *Annual Review of Earth and Planetary Science*, 31, 75–104.
- Emanuel, K. A., C. DesAutels, C. Holloway, and R. Korty (2004), Environmental control of tropical cyclone intensity, *J. of the Atmospheric Sciences*, 61, 843–858.
- Federal Coordinator for Meteorological Services and Supporting Research (1990), *Doppler Radar Meteorological Observations*, Handbook No. 11, Parts A through D, FCM-H11B-1990, Washington DC.
- Ferrier, B. S., and R. A. Houze (1989), One-dimensional time-dependent modeling of GATE cumulonimbus convection, *J. of the Atmospheric Sciences*, 46, 330–352.
- Ferrier, B. S., J. Simpson, and W. Tao (1996), Factors responsible for precipitation efficiencies in midlatitude and tropical squall simulations, *Monthly Weather Review*, 124, 2100–2125.
- Folkens, I. (2002), Origin of lapse rate changes in the upper tropical troposphere, *J. of the Atmospheric Sciences*, 59, 992–1005.
- Fovell, R. G., and P.-H. Tan (1998), The temporal behavior of numerically simulated multicell-type storms, Part II: the convective cell life cycle and cell regeneration, *Monthly Weather Review*, 126, 551–577.

- Fovell, R. G., G. L. Mullendore, and S.-H. Kim (2006), Discrete propagation in numerically simulation of nocturnal squall lines, *Monthly Weather Review*, *134*, 3735–3752.
- Franklin, C. N., G. J. Holland, and P. T. May (2006), Mechanisms for generation of mesoscale vorticity features in tropical cyclone rainbands, *Monthly Weather Review*, *134*, 2649–2669.
- Franklin, J. L. (2005), *2004 National Hurricane Center Forecast Verification Report*, NOAA, <http://www.nhc.noaa.gov/verification/pdfs/2004.pdf>.
- Franklin, J. L. (2007), *2006 National Hurricane Center Forecast Verification Report*, NOAA.
- Franklin, J. L., C. J. McAdie, and M. B. Laurence (2003), Trends in track forecasting for tropical cyclones threatening the United States, 1970–2001, *Bulletin of the AMS*, September 2003, 1197–1203.
- Franklin, J. L., M. L. Black, and K. Valde (2003), GPS dropwindsonde wind profiles in hurricanes and their operational implications, *Weather and Forecasting*, *18*, 32–44.
- Franklin, J. L., S. J. Lord, and F. D. Marks (1988), Dropwindsonde and radar observations of the eye of Hurricane Gloria (1985), *Monthly Weather Review*, *116*, 1237–1244.
- Free, M., M. Bister, and K. Emanuel (2004), Potential intensity of tropical cyclones: comparison of results from radiosonde and reanalysis data, *J. of Climate*, *17*, 1722–1727.
- Fujita, T., and J. Arnold (1963), *The Decaying Stage of Hurricane Anna of July 1961 as Portrayed by TIROS Cloud Photographs and Infra-red Radiation from the Top of the Storm*, Research paper #28, Dept. of the Geophysical Sciences, University of Chicago. Downloaded from the NASA Technical Report Server, www.ntrs.nasa.gov.
- Gangoiti, G., J. Sancho, G. Ibarra, L. Alonso, J. A. Garcia, M. Navazo, N. Durana, and J. L. Ilardia (1997), Rise of moist plumes from tall stacks in turbulent and stratified atmospheres, *Atmospheric Environment*, *31*, 253–269.
- Geerts, B., G. M. Heymsfield, L. Tian, J. B. Halverson, A. Guillory, and M. I. Mejia (2000), Hurricane Georges's landfall in the Dominican Republic: detailed airborne doppler radar imagery, *Bulletin of the AMS*, *81*, 999–1018.
- Gill, A. E. (1982), *Atmosphere-Ocean Dynamics*, Academic Press, San Diego, 662 pp.

- Gilmore, M. S., and L. J. Wicker (2002), Influences of the local environment on supercell cloud-to-ground lightning, radar characteristics, and severe weather on 2 June 1995, *Monthly Weather Review*, *130*, 2349–2372.
- Goody, R. (2003), On the mechanical efficiency of deep, tropical convection, *J. of the Atmospheric Sciences*, *60*, 2827–2832.
- Gratz, J. B. (2005), Unlocking the treasure chest of level-II radar data: lessons in technology transfer policy for the atmospheric sciences, *First Symposium on Policy Research*, AMS, Atlantic, Georgia, preprint paper P1.6.
- Gray, W. M. (1998), The formation of tropical cyclones, *Meteorological and Atmospheric Physics*, *67*, 37–69.
- Greenstone, R. (1996), Second Joint TRMM Science Team Meeting, *The Earth Observer*, NASA Goddard, Greenbelt, Maryland, March / April, 8, no. 2.
- Griffin, J. S., R. W. Burpee, F. D. Marks, and J. L. Franklin (1992), Real-time airborne analysis of aircraft data supporting operational tropical cyclone forecasting, *Computer Techniques*, *7*, 480–490.
- Guinn, T. A., and W. H. Schubert (1993), Hurricane spiral bands, *J. of the Atmospheric Sciences*, *58*, 3380–4502.
- Hack, J. J., and W. H. Schubert (1986), Nonlinear response of atmospheric vortices to heating by organized cumulus convection, *J. of the Atmospheric Sciences*, *43* (15), 1559–1573.
- Haltiner, G. J., and F. L. Martin (1957), *Dynamical and Physical Meteorology*, McGraw-Hill, New York, 470 pp.
- Haltiner, G. J., and R. T. Williams (1980), *Numerical Prediction and Dynamic Meteorology*, Wiley, N.Y., 477 pp.
- Halverson, J. B., J. Simpson, G. Heymsfield, H. Pierce, T. Hock, and L. Ritchie (2006), Warm core structure of Hurricane Erin diagnosed from high altitude dropsondes during CAMEX 4, *J. of the Atmospheric Sciences*, *63*, 309–324.
- Halverson, J., M. Black, S. Braun, D. Cecil, M. Goodman, A. Heymsfield, G. Heymsfield, R. Hood, T. Krishnamurti, G. McFarquhar, M. J. Mahoney, J. Molinari, R. Rogers, J. Turk, C. Velden, D. L. Zhang, E. Zipser, and R. Kakar (2007), Investigating tropical cyclogenesis and hurricane intensity change, *Bulletin of the AMS*, June 2007, 867–882.

- Harasti, P. R., C. J. McAdie, P. P. Dodge, W. Lee, J. Tuttle, S. T. Murillo, and F. D. Marks (2004), Real-time implementation of single-doppler radar analysis methods for tropical cyclones: algorithm improvements and use with WSR-88D display data, *Weather and Forecasting*, *19*, 219–239.
- Harries, J. E. (1997), Atmospheric radiation and atmospheric humidity, *Quarterly J. of the Royal Meteorological Society*, *123*, 2173–2186.
- Hawkins, H. F., and D. T. Rubsam (1968), Hurricane Hilda (1964), *Monthly Weather Review*, *96*, 617–636.
- Hawkins, H. F., and S. M. Imbembo (1976), The structure of a small, intense hurricane—Inez 1966, *Monthly Weather Review*, *104*, 418–442.
- Hawkins, J. D., M. Helvston, T. F. Lee, F. J. Turk, K. Richardson, C. Sampson, J. Kent, and R. Wade (2006), Tropical cyclone multiple eyewall configurations, *27th Conference on Hurricanes and Tropical Meteorology*, AMS, Monterey, California, preprint paper 6B.1.
- Hawkins, J. D., T. F. Lee, J. Turk, C. Sampson, J. Kent, and K. Richardson (2001), Real-time internet distribution of satellite products for tropical cyclone reconnaissance, *Bulletin of the AMS*, *82*, 567–578.
- Hayes, J. M., and G. L. Stephens (2007), Tropical ocean cloudiness and the incidence of precipitation: early results from CloudSat, *Geophysical Research Letters*, *34*, 2007GL029355.
- Hayes, P. H., and M. E. McIntyre (1987), On the evolution of vorticity and potential vorticity in the presence of diabatic heating and frictional or other forces, *J. of the Atmospheric Sciences*, *44*, 828–841.
- Heiss, W. H., and D. L. McGrew (1990), Nexrad: Next Generation Weather Radar (WSR-88D), *Microwave Journal*, January 1990, 79–98.
- Hendricks, E. A., M. T. Montgomery, and C. A. Davis (2004), The role of "vortical hot towers" in the formation of Tropical Cyclone Diana (1984), *J. of the Atmospheric Sciences*, *61*, 1210–1232.
- Hennon, P. A. (2006), *The Role of the Ocean in Convective Burst Initiation: Implications for Tropical Cyclone Intensification*, Ph.D. Dissertation, Ohio State University, 2006.
- Hess, S. L. (1959), *Introduction to Theoretical Meteorology*, Holt, New York, 362 pp.

- Heymsfield, G. M., B. Geerts, and L. Tian (2000), TRMM Precipitation Radar reflectivity profiles as compared with high-resolution airborne and ground-based radar measurements, *J. of Applied Meteorology*, *39*, 2080–2102.
- Heymsfield, G. M., J. B. Halverson, J. Simpson, L. Tian, and T. P. Bui (2001), ER-2 doppler radar investigation of the eyewall of Hurricane Bonnie during the convection and moisture experiment-3. *J. Appl. Meteor.*, *40*, 1310–30.
- Highwood E. J., and B. J. Hoskins (1998), The tropical tropopause, *Quarterly J. of the Royal Meteorological Society*, *124*, 1579–1604.
- Hoinka, K. P. (1999), Temperature, humidity, and wind at the global tropopause, *Monthly Weather Review*, *127*, 2248–2265.
- Holland, G. (1980), An analytic model of the wind and pressure profiles in hurricanes, *Monthly Weather Review*, *108*, 1212–1218.
- Holland, G. J. (1997), The maximum potential intensity of tropical cyclones, *J. of the Atmospheric Sciences*, *54*, 2519–2541.
- Holland, G. J., T. D. Keenan, and G. D. Crane (1984), Observations of a phenomenal temperature perturbation in Tropical Cyclone Kerry (1979), *Monthly Weather Review*, *112*, 1074–1082.
- Holton, J. R. (1992), *An Introduction to Dynamic Meteorology*, 3rd edition, Academic Press, 511 pp.
- Hoskins, B. J., M. E. McIntyre, and A. W. Robertson (1985), On the use and significance of isentropic potential vorticity maps, *Quarterly J. of the Royal Meteorological Society*, *111*, 877–946.
- Hou, A. Y. (2006), The Global Precipitation Measurement (GPM) mission: an overview, *2006 EUMETSAT Meteorological Satellite Conference*, Helsinki, Finland, PowerPoint presentation available from the GPM web site: <http://gpm.gsfc.nasa.gov/>.
- Houghton, J. (2004), *Global Warming: The Complete Briefing*, 3rd edition, Cambridge University Press, Cambridge, 351 pp.
- Houghton, J. T. (1986), *The Physics of Atmospheres*, 2nd edition, Cambridge University Press, Cambridge, 271 pp.
- Houston, S. H., W. A. Shaffer, and M. D. Powell (1999), Comparisons of HRD and SLOSH surface wind fields in hurricanes: implications for storm surge modeling, *Weather and Forecasting*, *14*, 671–686.

- Houze, R. A. (1993), *Cloud Dynamics*, Academic Press, 573 pp.
- Howard, K. W., J. J. Gourley, and R. A. Maddox (1997), Uncertainties in WSR-88D measurements and their impact on monitoring life cycles, *Weather and Forecasting*, 12, 166–174.
- Hudlow, M. D., and V. L. Patterson (1979), *Gate Radar Rainfall Atlas*, NOAA Special Report.
- Iguchi, T., R. Meneghini, J. Awaka, T. Kozu, and K. Okamoto (2000), Rain profiling algorithm for TRMM Precipitation Radar data, *Advances in Space Research*, 25, 973–976.
- Iguchi, T., T. Kozu, R. Meneghini, J. Awaka, and K. Okamoto (2000), Rain-profiling algorithm for the TRMM Precipitation Radar, *J. of Applied Meteorology*, 39, 2038–2052.
- Im, E., C. Wu, and S. L. Durden (2005), Cloud profiling radar for the CloudSat mission, *IEEE A&E Systems Magazine*, October 2005, 15–18.
- Jackson, G. S. (2005), Passive millimeter-wave signatures of ice particles in Hurricane Erin, IGARSS, preprint paper.
- Jakes, J. (1966), *TIROS: Weather Eye in Space*, Julian Messner, 192 pp.
- Janssen, M. A., Editor (1993), *Atmospheric Remote Sensing by Microwave Radiometry*, Wiley, NY, 572 pp.
- Jarvinen, B. R., C. J. Neumann, and M. A. S. Davis (1984), *A Tropical Cyclone Data Tape for the North Atlantic Basin, 1886–1983: Contents, Limitations, and Uses*, NOAA Technical Memorandum, NWS NHC 22, March 1984. Downloaded on 2007/09/02 from <http://www.nhc.noaa.gov/pastall.shtml> .
- Jennings, A. H. (1950), World's greatest observed point rainfalls, *Monthly Weather Review*, 78, 4–5.
- Jensen, M. P., and A. D. Del Genio (2006), Factors limiting convective cloud-top height at the ARM Nauru Island climate research facility, *J. Climate*, 19, 2105–2117.
- Johansen, B. E. (2002), *The Global Warming Desk Reference*, Greenwood Press, Westport, Connecticut, 355 pp. As stated on p. 355, Johansen is a professor of communication and Native American studies.
- Jordan, C. L., D. A. Hurt, and C. A. Lowrey (1959), On the structure of Hurricane Daisy on 27 August 1958, *Proceedings of the First Conference on Cumulus Convection*, Pergamon Press, 65–84.

- Jorgensen, D. P., E. J. Zipser, and M. A. LeMone (1985), Vertical motions in intense hurricanes, *J. of the Atmospheric Sciences*, *42*, 839–856.
- Kakar, R., M. Goodman, R. Hood, and A. Guillory (2006), Overview of the Convection and Moisture Experiment (CAMEX), *J. of the Atmospheric Sciences*, *63*, 5–18.
- Kalnay, E., M. Kanamitsu, R. Kistler, W. Collins, D. Deaven, L. Gandin, M. Iredell, S. Saha, G. White, J. Woollen, Y. Zhu, M. Chelliah, W. Ebisuzaki, W. Higgins, J. Janowiah, K. C. Mo, C. Ropelewski, J. Wang, A. Leetmaa, R. Reynolds, R. Jenne, and D. Joseph (1996), The NCEP/NCAR 40-year reanalysis project, *Bulletin of the AMS*, March 1996, p. 437–471.
- Kaplan, J., and M. DeMaria (2003), Large-scale characteristics of rapidly intensifying tropical cyclones in the North Atlantic basin, *Weather and Forecasting*, *18*, 1093–1108.
- Kelley, O. A., and J. Stout (2004), Convective towers in eyewalls of tropical cyclones observed by the TRMM Precipitation Radar in 1998–2001, *20th Conference on Weather Analysis and Forecasting*, AMS, Seattle, Washington, preprint paper P1.43.
- Kelley, O. A., J. Stout, and J. B. Halverson (2004), Tall precipitation cells in tropical cyclone eyewalls are associated with tropical cyclone intensification, *Geophysical Research Letters*, *31*, L24112, doi:10.1029/2004GL021616.
- Kelley, O. A., J. Stout, and J. B. Halverson (2005), Tropical cyclone intensification detected by continuously monitoring tall precipitation in the eyewall, *Geophysical Research Letters*, *32*, L20819, doi:10.1029/2005GL023583.
- Kiladis, G. N., K. H. Straub, G. C. Reid, and K. S. Gage (2001), *Quarterly J. of the Royal Meteorological Society*, *127*, 1961–1983.
- Klotzbach, P. J (2006), Trends in global tropical cyclone activity over the past twenty years (1986–2005), *Geophysical Research Letters*, *33*, 2006GL025881.
- Knight, C. A., and N. C. Knight (2001), Hailstorms, chapter 6 of *Severe Convective Storms*, Meteorological Monographs, vol. 28, 223–248, AMS, Boston.
- Kollias, P., E. E. Clothiaux, M. A. Miller, B. A. Albrecht, G. L. Stephens, and T. P. Ackerman (2007), Millimeter-wavelength radars: new frontier in atmospheric cloud and precipitation research, *Bulletin of the AMS*, 2007, October 2007, 1608–1624.
- Kozu, T. (1991), *Estimation of Raindrop Size Distribution from Spaceborne Radar Measurements*, Ph.D. Dissertation, Kyoto University.

- Kozu, T., T. Kawanishi, H. Kuroiwa, M. Kojima, K. Oikawa, H. Kumagai, K. Okamoto, M. Okumura, H. Nakatsuka, and K. Nishikawa (2001), Development of Precipitation Radar on board the TRMM satellite, *IEEE Transactions in Geoscience and Remote Sensing*, 39, 102–116.
- Krishnamurti, T. N., J. Sanjay, T. S. Kumar, A. J. O'Shay, and R. J. Pasch (2005), On the weakening of Hurricane Lili, October, 2002, *Tellus*, 57A, 65–83.
- Krishnamurti, T. N., S. Pattnaik, L. Stefanova, T. S. Kumar, B. P. Mackey, and A. J. O'Shay (2005), The tropical cyclone intensity issue, *Monthly Weather Review*, 133, 1886–1912.
- Kuang, Z., and C. S. Bretherton (2006), A mass-flux scheme view of a high-resolution simulation of a transition from shallow to deep cumulus convection, *J. of the Atmospheric Sciences*, 63, 1895–1909. The abstract states: "contrary to the assumption made in many cumulus schemes, nearly undilute air parcels are too infrequent to be relevant to any stage of the simulated convection."
- Kummerow, C., W. Barnes, T. Kozu, J. Shiue, and J. Simpson (1998), The TRMM sensor package, *J. Atmos. and Oceanic Tech.*, 15, 809–817.
- Kummerow, C., Y. Hong, W. S. Olson, S. Yang, R. F. Adler, J. McCollum, R. Ferraro, G. Petty, D. B. Shin, and T. T. Wilheit (2001), The evolution of the Goddard Profiling Algorithm (GPROF) for rainfall estimation from passive microwave sensors, *J. Applied Meteorology*, 40, 1801–1820.
- La Seur, N. E., and H. F. Hawkins (1963), An analysis of Hurricane Cleo (1958) based on data from research reconnaissance aircraft, *Monthly Weather Review*, October-December, 1963, 694–709.
- Lamb, D. (2001), Rain production in convective storms, chapter 8 of *Severe Convective Storms*, Meteorological Monographs, vol. 28, AMS, Boston.
- Landsea, C. W., B. A. Harper, K. Hoarau, and J. A. Knaff (2006), Can we detect trends in extreme tropical cyclones? *Science*, 313, 28 July 2006, 452–454. Page 453 states: "Operational changes at the various tropical cyclone warning centers probably also contributed to discontinuities in tropical cyclone intensity estimates and to more frequent identification of extreme tropical cyclones (along with a shift to stronger maximum sustained surface wind in general) by 1990."
- Lane, T. P., and M. J. Reeder (2001), Convectively generated gravity waves and their effect on the cloud environment, *J. of the Atmospheric Sciences*, 58, 2427–2440.

- Lane, T. P., M. J. Reeder, and T. L. Clark (2001), Numerical modeling of gravity wave generation by deep tropical convection, *J. of the Atmospheric Sciences*, 58, 1249–1274.
- Langley, R. B. (1999), *A Few Facts Concerning GMT, UT, and the RGO*, web site, downloaded 06 Sep 2007 from <http://www.apparent-wind.com/gmt-explained.html>.
- Law, K. T. (2006), *A Statistical Model to Forecast Short-term Atlantic Hurricane Intensity*, Ph.D. Dissertation, Ohio State University.
- Lee, W., B. J. Jou, P. Chang, and S. Deng (1999), Tropical cyclone kinematic structure retrieved from single-doppler radar observations, Part I: interpretation of doppler velocity patterns and GBVTD technique, *Monthly Weather Review*, 127, 2419–2439.
- Leipper, D. F., and D. Volgenau (1972), Hurricane heat potential in the Gulf of Mexico, *J. of Physical Oceanography*, 2, 218–224. This paper defines the concept of ocean heat content as it relates to a hurricane's potential wind intensity.
- Leutbecher, M. (2005), On ensemble prediction using singular vectors started from forecasts, *Monthly Weather Review*, 133, 3038–3046.
- Liu, C., and E. J. Zipser (2005), Global distribution of convection penetrating the tropical tropopause, *J. of Geophysical Research*, 110, D23104, doi:10.1029/2005JD006063.
- Lonfat, M., F. D. Marks, and S. S. Chen (2004), Precipitation distribution in tropical cyclones using the TRMM Microwave Imager: a global perspective, *Monthly Weather Review*, 132, 1465–1660.
- Lyons, W. A., and C. S. Keen (1994), Observations of lightning in convective supercells within tropical storms and hurricanes, *Monthly Weather Review*, 122, 1897–1916.
- Lyu, C.-H., and W. L. Barnes (2003), Four years of TRMM / VIRS on-orbit calibrations and characterization using lunar models and data from Terra / MODIS, *J. of Atmospheric and Ocean Technology*, 20, 333–347.
- Malkus, J. S. (1958), On the structure and maintenance of the mature hurricane eye, *J. of Meteorology*, 15, 337–349.
- Malkus, J. S. (1959), Recent developments in studies of penetrative convection and application to tropical cyclone cumulonimbus towers, *Proceedings of the First Conference on Cumulus Convection*, Pergamon Press, 65–84.
- Malkus, J. S., and H. Riehl (1964), *Cloud Structure and Distributions of the Tropical Pacific Ocean*, University of California Press, 229 pp.

- Malkus, J. S., and H. Riehl (1960), On the dynamics and energy transformations in steady-state hurricanes, *Tellus*, 12, 1–20.
- Mapes, B. E. (2001), Water's two height scales: the moist adiabat and the radiative troposphere, *Quarterly J. of the Royal Meteorological Society*, 127, 2353–2366.
- Mapes, B. E., P. E. Ciesielski, and R. H. Johnson (2003), Sampling errors in rawinsonde-array budgets, *J. of the Atmospheric Sciences*, 60, 2697–2714.
- Marks, F. D., R. A. Houze, and J. F. Gamache (1992), Dual-aircraft investigation of the inner core of Hurricane Norbert, Part I: kinematic structure, *J. of the Atmospheric Sciences*, 49, 919–942.
- Markson, R. (2007), The global circuit intensity: its measurement and variation over the last 50 years, *Bulletin of the AMS*, February 2007, 223–241.
- Marshall, J. S., R. C. Langille, and W. M. Palmer (1947), Measurement of rainfall by radar, *J. of Meteorology*, 4, 186–192.
- Mass, C. F. (2003), IFPS and the future of the National Weather Service, *Weather and Forecasting*, 18, 75–79.
- May, P. T., and G. J. Holland (1999), The role of potential vorticity generation in tropical cyclone rainbands, *J. of the Atmospheric Sciences*, 56, 1224–1228.
- McCaul, E. W., D. E. Buechler, S. J. Goodman, and M. Kamarhati (2004), Doppler radar and lightning network observations of a severe outbreak of tropical cyclone tornadoes, *Monthly Weather Review*, 132, 1747–1763.
- McGregor, G. R., and S. Nieuwolt (1998), *Tropical Climatology*, 2nd edition, Wiley, 339 pp.
- Meneghini, R., and T. Kozu (1990), *Spaceborne Weather Radar*, Artech House, Boston, 199 pp.
- Meneghini, R., L. Liao, and L. Tian (2005a), A feasibility study of simultaneous estimates of water vapor and precipitation parameters using a three-frequency radar, *J. of Applied Meteorology*, 44, 1511–1525.
- Meneghini, R., L. Liao, and L. Tian (2005b), The potential for water vapor and precipitation estimation with a differential frequency radar, *32nd Conference on Radar Meteorology*, preprint paper 5R5.

- Meneghini, R., T. Iguchi, T. Kozu, L. Liao, K. Okamoto, J. A. Jones, and J. Kwiatkowski (2000), Use of the surface reference technique for path attenuation estimates from the TRMM Precipitation Radar, *J. of Applied Meteorology*, 39, 2053–2070.
- Miller, R. G. (1985), *Beyond Anova*, John Wiley & Sons, Inc., 317 pp.
- Molinari, J. P. Moore, and V. Idone (1999), Convective structure of hurricanes as revealed by lightning locations, *Monthly Weather Review*, 127, 520–534.
- Monni, S., S. Syri, and I. Savolainen (2004), Uncertainties in the Finnish greenhouse gas emission inventory, *Environmental Science and Policy*, 7, 87–98.
- Montgomery, D. C., and G. C. Runger (2003), *Applied Statistics and Probability for Engineers*, 3rd edition, Wiley, 706 pp.
- Montgomery, M. T., and J. Enagonio (1998), Tropical cyclogenesis via convectively forced vortex Rossby waves in a three-dimensional quasigeostrophic model, *J. of the Atmospheric Sciences*, 55, 3176–3207.
- Montgomery, M. T., and R. J. Kallenbach (1997), A theory of vortex Rossby waves and its application to spiral bands and intensity change in hurricanes, *Quarterly J. of the Royal Meteorological Society*, 123, 435–465.
- Montgomery, M. T., M. E. Nicholls, T. A. Cram, and A. B. Sanders (2006), A vortical hot tower route to tropical cyclogenesis, *J. of the Atmospheric Sciences*, 63, 355–386.
- Montgomery, M. T., M. M. Bell, S. D. Aberson, and M. L. Black (2006), Hurricane Isabel (2003): new insights into the physics of intense storms, Part 1: mean vortex structure and maximum intensity estimates, *Bulletin of the AMS*, October 2006, 1335–1347.
- Nappo, C. J. (2002), *An Introduction to Atmospheric Gravity Waves*, Academic Press: Amsterdam, 276 pp.
- NASA (1962), *Final Report on the TIROS I Meteorological Satellite System*, Technical Report R-131, U. S. Government Printing Office, NASA TR R-131. 258 pp.
- NASA (1964), *The Early Years: Goddard Space Flight Center, Historical Origins and Activities through December 1962*, U. S. Government Printing Office, 273 pp.
- NASA (2000), New satellite-generated rain maps provide an improved look at tropical rainfall, Press Release #00-148. Robert Adler is quoted as saying that "scientists are using TRMM as a flying rain gauge."
- NASA (2005), NASA's tropical cloud systems and processes mission in Costa Rica – update 4, released on July 19, 2005, on the NASA Hurricane Resource Web Site

http://www.nasa.gov/vision/earth/lookingatearth/tcsp_updates.html . Quoting the news story: "The ER-2 plane overflew Hurricane Emily on July 17 around 4 a.m. EDT, heading west-northwest at 17–18 knots (19–20 mph). ... Emily is an extremely powerful storm, rated a borderline Category 4–5 The flight was the first in which the ER-2 has collected data in such an intense tropical system. Flying twice over the eye of the hurricane at 65,000 feet, the plane encountered pronounced turbulence — an unusual occurrence.... The eye-wall clouds powering Emily were extremely energetic and deep. Large amounts of lightning were detected by ER-2 instrumentation, as well as thunderclouds that towered to at least 60,000 feet. NASA instruments recorded unprecedented detail of the hurricane's vertical structure and precipitation levels."

NASA Goddard (1970), *Encyclopedia, Satellites and Sounding Rockets of Goddard Space Flight Center: 1959–1969*, NASA, 328 pp.

National Research Council (2004), *Assessment of the Benefits of Extending the Tropical Rainfall Measuring Mission, Interim Report*, National Academies Press, Washington, D.C. 39 pp. [<http://www.nap.edu>]. Page 18 states that the TRMM satellite is projected to have sufficient fuel to remain in orbit until 2011, which would cause TRMM to have 14 years in space since the satellite was launched in November of 1997.

Negri, A. J., N. Burkardt, J. H. Golden, J. B. Halverson, G. J. Huffman, M. C. Larsen, J. A. McGinley, R. G. Updike, J. P. Verdin, and G. F. Wiecek (2005), Hurricane–flood–landslide continuum, *Bulletin of the AMS*, September 2005, 1241–1247.

NICT (2004), *NICT Newsletter*, issue 1, fall and winter, 2004. On page 8, it states: "The National Institute of Information and Communications Technology (referred to as NICT, below) was established in April 2004, through the integration of the Communications Research Laboratory (CRL) and the Telecommunications Advancement Organization of Japan (TAO)."

NOAA (1977), *Five- to 60-minute Precipitation Frequency for the Eastern and Central United States*, NOAA Technical memorandum NWS HYDRO-35, Silver Spring, Maryland, June 1977, 34 pp. This document can be downloaded from the National Weather Service at [<http://www.nws.noaa.gov>], and is referred to "Tech Memo 35." For some portions of the United States, Tech Memo 35 has been replaced by the 2003 on-line publication of "NOAA Atlas 14". As of 2007, the Gulf Coast and Southeast Coast of the United States has not yet been described in NOAA Atlas 14.

NOAA (2007), *Doppler Radar Meteorological Observations*, Federal Meteorological Handbook No. 11, parts A, B, C, and D.

NOAA (2007), *Interagency Strategic Research Plan for Tropical Cyclones: The Way Ahead*, report # FCM-P36-2007. available from <http://www.ofcm.gov/> and

- <http://www.ofcm.gov/p36-isrtc/fcm-p36.htm> . page 111 (i.e., page 3–39, section 3.4.3) mentioned role of human forecaster. page 145 (i.e., page 4–7, section 4.2.5) mentions the Global Precipitation Measuring (GPM) Mission satellite.
- Nolan, D. S., Y. Moon, and D. P. Stern (2007), Tropical cyclone intensification from asymmetric convection: energetics and efficiency, *Journal of the Atmospheric Sciences*, *64*, 3377–3405.
- Nunez, E. (1981), *Tropical Cyclone Structure and Intensity Change*, Ph.D. Dissertation, Colorado State University.
- Nyberg, J., B. A. Malmgren, A. Winter, M. R. Jury, K. H. Kilbourne, and T. M. Quinn (2007), Low Atlantic hurricane activity in the 1970s and 1980s compared to the past 270 years, *Nature*, *447*, 7 June 2007, 698–702.
- Okamoto, K. (2003), A short history of the TRMM precipitation radar, chapter 16 of *Cloud Systems, Hurricanes, and the Tropical Rainfall Measuring Mission (TRMM)*, Meteorological Monographs, vol. 51, AMS, Boston.
- Palmen, E., and C. W. Newton (1969), *Atmospheric Circulation Systems*, Academic Press, NY, 603 pp.
- Parker, M. D., and R. H. Johnson (2004), Simulated convective lines with leading precipitation, Part 1: governing dynamics, *J. of the Atmospheric Sciences*, *61*, 1637–1655.
- Paulhus, J. L. H. (1965), Indian Ocean and Taiwan rainfalls set new records, *Monthly Weather Review*, *93*, 331–335.
- Pauluis, O., and I. M. Held (2002), Entropy budget of an atmosphere in radiative-convective equilibrium, Part I: maximum work and frictional dissipation, *J. of the Atmospheric Sciences*, *59*, 125–139.
- Pauluis, O., V. Balaji, and I. M. Held (2000), Frictional dissipation in a precipitating atmosphere, *J. of the Atmospheric Sciences*, *57*, 989–994.
- Pedlosky, J. (1979), *Geophysical Fluid Dynamics*, Springer-Verlag, 624 pp.
- Persing, J., and M. T. Montgomery (2003), Hurricane superintensity, *J. of the Atmospheric Science*, *60*, 2349–2371. "a beneficial interaction between the eyewall and the warm, moist air in the low-level eye permits modeling storm intensities that greatly exceed [Emanuel's Maximum Potential Intensity] E-MPI [p. 2355]." "What remains is to establish the means by which the introduction of air with high entropy from the eye into the eyewall produces a stronger storm [p. 2359]." "Although in reality MPI is rarely exceeded (*Emanuel* 2000), this mechanism may play a role in

- boosting the intensity of observed hurricanes that are subject to adverse conditions [p. 2362]."
- Persing, J., and M. T. Montgomery (2005), Is environmental CAPE important in the determination of maximum potential hurricane intensity, *J. of the Atmospheric Sciences*, 62, 542–550.
- Petty, G. W. (1994), Physical retrievals of over-ocean rain rate from multichannel microwave imagery, Part I: theoretical characteristics of normalized polarization and scattering indices, *Meteorol. Atmos. Phys.*, 54, 79–99.
- Pielke, R. A., and C. W. Landsea (1998), Normalized hurricane damages in the United States: 1925–95, *Weather and Forecasting*, 13, 621–631.
- Powell, M. D., P. J. Vickery, and T. A. Reinhold (2003), Reduced drag coefficient for high wind speeds in tropical cyclones, *Nature*, 422, 279–283.
- Powell, M. D., S. H. Houston, and T. A. Reinhold (1996), Hurricane Andrew's landfall in South Florida, Part I: Standardizing measurements for documentation of surface wind fields, *Weather and Forecasting*, 11, 304–328.
- Pryor, S. P. (1978), *Measurement of Thunderstorm Cloud-Top Parameters Using High-Frequency Satellite Imagery*, Master's Thesis, Colorado State University, Fort Collins. On page 1: "With the advent of the Applications Technology Satellites (ATS) in the late 60's meteorologists were given an essentially stationary platform from which to study earth's weather.... Even though the ATS series observed the earth only in the visible, it was possible to gain new insights... [T]he introduction of an infrared sensor on the Synchronous Meteorological and Geostationary Operational Environmental Satellites (SMS/GOES) have further expanded the possibilities..."
- Quante, M., and V. Matthias (2006), Water in the Earth's atmosphere, *J. De Physique IV*, 139, 37–61.
- Rakov V. A., and M. A. Uman (2003), *Lightning: Physics and Effects*, Cambridge, England, 687 pp.
- Rappaport, E. N. (2000), Loss of life in the United States associated with recent Atlantic tropical cyclones, *Bulletin of the AMS*, September 2006, 2065–2073.
- Rasmussen, E. A. (2003), *Polar Lows: Mesoscale Weather Systems in the Polar Regions*, Cambridge University Press, Cambridge, 612 pp.
- Ray, P. S., editor (1986), *Mesoscale Meteorology and Forecasting*, AMS, Boston, 793 pp.

- Raymond, D. J., and H. Jiang (1990), Theory of long-lived mesoscale convective systems, *J. of the Atmospheric Sciences*, 47, 3067–3077.
- Reasor, P. D., M. T. Montgomery, F. D. Marks, and J. F. Gamache (2000), Low-wavenumber structure and evolution of the hurricane inner core observed by airborne dual-doppler radar, *Monthly Weather Review*, 128, 1653–1680.
- Riehl, H. (1954), *Tropical Meteorology*, McGraw-Hill Book Co., NY, chapter 11.
- Riehl, H., and J. S. Malkus (1958), On the heat balance in the equatorial trough zone, *Geophysica*, 6, 503–538.
- Rinehart, R. E. (1997), *Radar for Meteorologists*, Rinehart Publications, Columbus, Montana, 428 pp.
- Ritchie, E. A., and R. L. Elsberry (2001), Simulations of the transformation stage of the extratropical transition of tropical cyclones, *Monthly Weather Review*, 129, 1462–1480.
- Ritchie, E. A., J. Simpson, W. T. Liu, J. Halverson, C. Velden, K. F. Brueske, and H. Pierce (2003), Present day satellite technology for hurricane research: a closer look at formation and intensification, chapter 12 of *Hurricane! Coping with Disaster*, American Geophysical Union, Washington, D.C., pp. 249–290.
- Rodgers, E. B., W. S. Olson, V. M. Karyampudi, and H. F. Pierce (1998), Satellite-derived latent heating distribution and environmental influences in Hurricane Opal (1995), *Monthly Weather Review*, 126, 1229–1247.
- Rodgers, E., W. Olson, J. Halverson, J. Simpson, and H. Pierce (2000), Environmental forcing of Supertyphoon Paka's (1997) latent heat structure, *J. Applied Meteorology*, 39, 1983–2006.
- Roebber, P. J., and L. F. Bosart (1996), The contributions of education and experience to forecast skill, *Weather and Forecasting*, 11, 21–40.
- Rogers R. F., and J. M. Fritsch (2001), Cyclogenesis from convectively driven amplification of midlevel mesoscale convective vortices, *Monthly Weather Review*, 129, 605–637.
- Rogers, R., S. Aberson, J. Kaplan, and S. Goldenberg (2002), A pronounced upper-tropospheric warm anomaly encountered by the NOAA G-IV aircraft in the vicinity of deep convection, *Monthly Weather Review*, 130, 180–187.
- Rogers, R., S. Aberson, M. Black, P. Black, J. Cione, P. Dodge, J. Dunion, J. Gamache, J. Kaplan, M. Powell, N. Shay, N. Surgi, and E. Uhlhorn (2006), The intensity

- forecasting experiment: a NOAA multiyear field program for improving tropical cyclone intensity forecasts, *Bulletin of the AMS*, November 2006, 1523–1537.
- Rolle, K. C. (2005), *Thermodynamics and Heat Power*, 6th edition, Prentice Hall, 611 pp.
- Ruckstuhl, C., R. Philipona, J. Morland, and A. Ohmura (2007), Observed relationship between surface specific humidity, integrated water vapor, and longwave downward radiation at different altitudes, *J. of Geophysical Research—Atmospheres*, *11* (D3), D03302.
- Rumsey, D. (2007), *Intermediate Statistics for Dummies*, Wiley Publishing, Inc., 362 pp.
- Schubert W. H., M. T. Montgomery, R. K. Taft, T. A. Guinn, S. R. Fulton, J. P. Kossin, and J. P. Edwards (1999), Polygonal eyewalls, asymmetric eye contractions and potential vorticity mixing in hurricanes, *J. of the Atmospheric Sciences*, *56*, 1197–1223.
- Schubert, W. H., C. M. Rozoff, J. L. Vigh, B. D. McNoldy, and J. P. Kossin (2007), On the distribution of subsidence in the hurricane eye, *Quarterly J. of the Royal Meteorological Society*, *133*, 595–605.
- Schubert, W. H., M. T. Montgomery, R. K. Taft, T. A. Guinn, S. R. Fulton, J. P. Kossin, and J. P. Edwards (1999), Polygonal eyewalls, asymmetric eye contraction, and potential vorticity mixing in hurricanes, *J. of the Atmospheric Sciences*, *56*, 1198–1223.
- Schumacher, C., and R. A. Houze (2000), Comparison of radar data from the TRMM satellite and Kwajalein oceanic validation site, *J. of Applied Meteorology*, *39*, 2151–2164.
- Scorer, R. S., and F. H. Ludlam (1953), Bubble theory of penetrative convection, *Quarterly J. of the Royal Meteor. Society*, *79*, 94–103.
- Seeber, G. (1993), *Satellite Geodesy*, deGruyter, Berlin, 531 pp.
- Serway, R. A., and J. W. Jewett (2004), *Physics for Scientists and Engineers*, 6th edition, vol. 1, Thomson, p. 68 and chapter 7.
- Shay, L. K., G. J. Goni, and P. G. Black (2000), Effects of a warm oceanic feature on Hurricane Opal, *Monthly Weather Review*, *128*, 1366–1383. The paper discusses the concept of ocean heat content.
- Sherwood, S. C., P. Minnis, and M. McGill (2004), Deep convective cloud-top heights and their thermodynamic control during CRYSTAL-FACE, *J. of Geophysical Research*, *109*, 2004JD004811.

- Simpson, J., J. B. Halverson, B. S. Ferrier, W. A. Petersen, R. H. Simpson, R. Blakeslee, and S. L. Durden (1998), On the role of “hot towers” in tropical cyclone formation, *Meteor. Atmos. Phys.*, *67*, 15–35.
- Simpson, R. (1974), The hurricane disaster–potential scale, *Weatherwise*, August 1974, pp. 169 and 186.
- Simpson, R., editor, (2003), *Hurricane! Coping with Disaster*, American Geophysical Union, Washington, D.C., 360 pp.
- Sippel, J. A., and J. W. Nielsen-Gammon (2006), The multiple-vortex nature of tropical cyclogenesis, *Monthly Weather Review*, *134*, 1796–1814.
- Smith, E. A., X. Xiang, A. Mugnai, R. E. Hood, and R. W. Spencer (1994), Behavior of an inversion-based precipitation retrieval algorithm with high-resolution AMPR measurements including a low-frequency 10.7 GHz channel, *J. of Atmospheric and Oceanic Technology*, *11*, 858–873. "Although scattering signatures at 37 and 85 GHz are quite common in satellite measurements, footprint size precludes observing strong scattering at 19 GHz" [p. 863].
- Smith, J. A., M. L. Baeck, and Y. Zhang (2001), Extreme rainfall and flooding from supercell thunderstorms, *J. of Hydrometeorology*, *2*, 469–489.
- Smith, R. K. (2000), The role of cumulus convection in tropical cyclones and its representation in tropical cyclone models, *Review of Geophysics*, *38*, 465–489.
- Sparks, P. R. (2003), Wind speeds in tropical cyclones and associated insurance losses, *J. Wind Engineering and Industrial Aerodynamics*, *91*, 1731–1751.
- Spencer, R. W., H. M. Goodman, and R. E. Hood (1989), Precipitation retrieval over land and ocean with the SSM/I: identification and characteristics of the scattering signal, *J. Atmos. and Oceanic Tech.*, *6*, 254–273.
- Spokas, K., J. Bogner, J. P. Chanton, M. Morcet, C. Aran, M.-L. Graff, Y. Golvan, and I. Hebe (2006), Methane mass balance at three landfill sites: What is the efficiency of capture by gas collection systems? *Waste Management*, *26*, 516–525.
- Stear, J. R. (1965), Sounding in the eye of Hurricane Arlene to 108,760 feet, *Monthly Weather Review*, *93*, 380–382.
- Steranka, J., E. B. Rodgers, and R. C. Gentry (1986), The relationship between satellite measured convective bursts and tropical cyclone intensification, *Monthly Weather Review*, *114*, 1539–1546.

- Stern, D. P., and S. D. Aberson (2006), Extreme vertical winds measured by dropwindsondes in hurricanes, *AMS 27th Conference on Hurricanes and Tropical Meteorology*, preprint paper 16B.8.
- Stuart, N. A., P. S. Market, B. Telfeyan, G. M. Lackmann, K. Carey, H. E. Brooks, D. Nietfeld, B. C. Motta, and K. Reeves (2006), The future of humans in an increasingly automated forecast process, *Bulletin of the AMS*, November 2006, 1498–1502.
- Takahashi, N., and T. Iguchi (2004), Estimation and correction of beam mismatch of the precipitation radar after an orbit boost of the Tropical Rainfall Measuring Mission satellite, *IEEE Transactions on Geoscience and Remote Sensing*, 42, 2362–2369.
- Takahashi, N., H. Kuroiwa, and T. Kawanishi (2003), Four-year result of external calibration for precipitation radar (PR) of the TRMM satellite, *IEEE Transactions on Geoscience and Remote Sensing*, 41, 2398–2403.
- Tao, W., E. A. Smith, R. F. Adler, Z. S. Haddad, A. Y. Hou, T. Iguchi, R. Kakar, T. N. Krishnamurti, C. D. Kummerow, S. Lang, R. Meneghini, K. Nakamura, T. Nakazawa, K. Okamoto, W. S. Olson, S. Satoh, S. Shige, J. Simpson, Y. Takayabu, G. J. Tripoli, and S. Yang (2006), Retrieval of latent heating from TRMM measurements, *Bulletin of the AMS*, November 2006, 1555–1572.
- Tao, W.-K., and R. Adler (editors) (2003), *Cloud Systems, Hurricanes, and the Tropical Rainfall Measuring Mission (TRMM)*, Meteorological Monographs, vol. 51, AMS, Boston, 234 pp.
- Tepper, M. (1963), A solution in search of a problem, *Bulletin of the AMS*, 44, 543–548. Downloaded from the NASA Technical Report Server, www.ntrs.nasa.gov. A discussion of the usefulness of the TIROS meteorological satellite series.
- Thomas, G. E., and K. Stamnes (1999), *Radiative Transfer in the Atmosphere and Ocean*, Cambridge University Press, Cambridge, 517 pp.
- Thuburn J., and G. C. Craig (1997), GCM tests of theories for the height of the tropopause, *J. of the Atmospheric Sciences*, 54, 869–882.
- Thurai, M., E. Deguchi, T. Iguchi, and K. Okamoto (2003), Freezing height distribution in the Tropics, *International J. of Satellite Communication and Networking*, 21, 533–545.
- Toracinta, E. R., D. J. Cecil, E. J. Zipser, and S. W. Nesbitt (2002), Radar, passive microwave, and lightning characteristics of precipitating systems in the tropics, *Monthly Weather Review*, 130, 802–824.

- Tory, K. J., M. T. Montgomery, N. E. Davidson, and J. D. Kepert (2006), Prediction and diagnosis of tropical cyclone formation in a NWP system, Part II: a diagnosis of Tropical Cyclone Chris formation, *J. of the Atmospheric Sciences*, 63, 3091–3113.
- TRMM Precipitation Radar Team (2005), *Tropical Rainfall Measuring Mission (TRMM) Precipitation Radar Algorithm Instruction Manual Version 6*, Japan Aerospace Exploration Agency (JAXA), 175 pp.
- TRMM Project Office (1996), *Flight Operations Plan (FOP) for the TRMM*, NASA Goddard, Greenbelt, Maryland, document TRMM-490-076. Section 8.1.1. titled "orbit determination" states that the definitive orbit requirement is an accuracy of "1 km along and across track and 100 meters radially" [p. 8–1].
- TRMM Science Data and Information System (TSDIS) (2005), *File Specifications for TRMM Products – Level 1*, Volume 3 of the *Interface Control Specification Between TSDIS and the TSDIS Science User (TSU)*, NASA, Greenbelt, Maryland, 116 pp. Updated periodically and available for download from the TSDIS homepage: <http://www-tdis.gsfc.nasa.gov/>.
- TRMM Science Data and Information System (TSDIS) (2006), *File Specifications for TRMM Products – Level 2 and 3*, Volume 4 of the *Interface Control Specification Between TSDIS and the TSDIS Science User (TSU)*, NASA, Greenbelt, Maryland, 95 pp. Updated periodically and available for download from the TSDIS homepage: <http://www-tdis.gsfc.nasa.gov/>.
- Tulich, S. N., D. A. Randall, and B. E. Mapes (2007), Vertical-mode and cloud decomposition of large-scale convectively coupled gravity waves in a two-dimensional cloud-resolving model, *J. of the Atmospheric Sciences*, 64, 1210–1229.
- Tunc, G. I., S. Turut-Asik, and E. Akbostanci (2006), CO₂ emissions vs. CO₂ responsibility: An input-output approach for the Turkish economy, *Energy Policy*, 35, 855–868.
- Turner, J. S. (1962), The starting plume in neutral surroundings, *J. Fluid Mechanics*, 13, 356–368. Cited on page 235 of Houze [1993].
- U. S. Weather Research Program (2000), Implementation Plan—Tropical cyclone Landfall. p. 25. http://box.mmm.ucar.edu/USWRP/implementation/download/usrp-docs/USWRP_IMPLEMENTATION_PLAN_912.pdf.
- Uno, S., and T. Iwasaki (2006), A cascade-type global energy conversion diagram based on wave-mean flow interactions, *J. of the Atmospheric Sciences*, 63, 3277–3295.

- Ushio, T., S. J. Heckman, D. J. Boccippio, and H. J. Christian (2001), A survey of thunderstorm flash rates compared to cloud top height using TRMM satellite data, *J. of Geophysical Research*, 106 (D20), 24089–24095.
- Vasquez, T. (2003), *Weather Map Handbook*, Weather Graphics Technologies, Austin, Texas, 167 pp. See www.weathergraphics.com. A text for mid-latitude weather forecasting from weather maps. Page 148 defines CAPE in terms of a altitude change, not a pressure change. CAPE under 300 J/kg is classified as "mostly stable, little or no convection." CAPE over 2500 J/kg is classified a "very unstable, severe thunderstorms, possible tornadoes."
- Velden, C., B. Harper, F. Wells, J. L. Beven, R. Zehr, T. Olander, M. Mayfield, C. Guard, M. Lander, R. Edson, L. Avila, A. Burton, M. Turk, A. Kikuchi, A. Christian, P. Caroff, and P. McCrone (2006), The Dvorak tropical cyclone intensity estimation technique: a satellite-based method that has endured for over 30 years, *Bulletin of the AMS*, September 2006, 1195–1210. See also the supplement to this article, pages S6–S10.
- Wallace, J. M., and P. V. Hobbs (2006), *Atmospheric Science*, 2nd edition, Academic Press, Amsterdam, 483 pp.
- Walpole, R. E., and R. H. Myers (1985), *Probability and Statistics for Engineers and Scientists*, 3rd edition, McMillan Publishing Company, New York, 639 pp.
- Wang, Y., and C. Wu (2004), Current understanding of tropical cyclone structure and intensity changes—a review, *Meteorology and Atmospheric Physics*, 87, 257–278.
- Wentz, F. J., C. Gentemann, D. Smith, and D. Chelton (2000), Satellite measurements of sea surface temperature through clouds, *Science*, 288, 847–850.
- Wessa, P. (2007), Free Statistics Software, Office for Research and Development and Education, <http://www.wessa.net/>.
- West, D. A. (1998), *The Use of Satellite Microwave Rainfall Measurements to Predict Eastern North Pacific Tropical Cyclone Intensity*, Ph.D. Dissertation, Ohio State University, 1998.
- Williams, E. R. (2001), The electrification of severe storms, chapter 13 of *Severe Convective Storms*, Meteorological Monographs, vol. 28, AMS, Boston, 527–561.
- Willoughby H. E., and M. E. Rahn (2004), Parametric representation of the primary hurricane vortex, Part I: observations and evaluation of the Holland (1980) model, *Monthly Weather Review*, 132, 3034–3048.

- Willoughby, H. E. (1998), Tropical cyclone eye thermodynamics, *Monthly Weather Review*, 126, 3053–3067.
- Wimmers, A. J., and C. S. Velden (2007), MIMIC, a new approach to visualizing satellite microwave imagery of tropical cyclones, *Bulletin of the AMS*, August 2007, 1187–1196.
- World Meteorological Organization (WMO) (1963), *Reduction and Use of Data Obtained by TIROS Meteorological Satellites*, Technical note no. 49, WMO-No.11.TP.58, 58 pp.
- Yang, B., Y. Wang, and B. Wang (2007), The effect of internally generated inner-core asymmetries on tropical cyclone potential intensity, *J. of the Atmospheric Sciences*, 64, 1165–1188.
- Yau, M. K., Y. Liu, D. L. Zhang, and Y. Chen (2004), A multi-scale numerical study of Hurricane Andrew (1992), Part IV: small-scale inner-core structures and wind streaks, *Monthly Weather Review*, 132, 1410–1433.
- Younger, M. S. (1979), *A Handbook for Linear Regression*, Duxbury Press, North Scituate, Massachusetts, 570 pp.
- Zehr, R. (2004), The objective Dvorak technique – historical perspective, *26th Conference on Hurricanes and Tropical Meteorology*, AMS, Miami, Florida, preprint paper 8A.3.
- Zeng, X. (2005), An equation for moist entropy in a precipitating and icy atmosphere, *J. of the Atmospheric Sciences*, 62, 4293–4309.
- Zhang, C., and M.-D. Chou (1999), Variability of water vapor, infrared radiative cooling, and atmospheric instability for deep convection in the equatorial western Pacific, *J. of the Atmospheric Sciences*, 56, 711–723.
- Zhang, D.-L., and C. Q. Kieu (2006), Potential vorticity diagnosis of a simulated hurricane, Part II: quasi-balanced contributions to forced secondary circulations, *J. of the Atmospheric Sciences*, 63, 2898–2914.
- Zhu, T., and D.-L. Zhang (2002), Impact of the Advanced Microwave Sounding Unit measurements on hurricane prediction, *Monthly Weather Review*, 130, 2416–2432.
- Zhu, T., D.-L. Zhang, and F. Weng (2004), Numerical simulation of Hurricane Bonnie (1998), Part I: eyewall evolution and intensity changes, *Monthly Weather Review*, 132, 225–241.

Zipser, E. J. (2003), Some view on "hot towers" after 50 years of tropical field programs and two years of TRMM data, chapter 5 of *Cloud Systems, Hurricanes, and the TRMM*, Meteorological Monographs, vol. 51, AMS.

Zipser, E. J., D. J. Cecil, C. Liu, S. W. Nesbitt, and D. P. Yorty (2006), Where are the most intense thunderstorms on Earth? *Bulletin of the AMS*, August 2006, 1057–1070.

Zipser, E. J., R. J. Meitin, and M. A. LeMone (1981), Mesoscale motion fields associated with a slowly moving GATE convective band, *J. of the Atmospheric Sciences*, 38, 1725–1750.

CURRICULUM VITAE

Owen Kelley uses space-based and ground-based instruments to study changes in tropical cyclone structure that occur in periods of hours or days. He has published two papers in *Geophysical Research Letters* describing how radar data can be used to forecast increases in a tropical cyclone's wind intensity. In his research, Kelley is still trying to discover why "Hot Towers", tall rain clouds often just ten kilometers across, are so intimately connected with what happens on a much larger scale to a tropical cyclone that is hundreds of kilometers across. Kelley also develops visualization software for the Tropical Rainfall Measuring Mission (TRMM) satellite launched in 1997 and the Global Precipitation Measuring (GPM) Mission satellite that is scheduled to be launched in 2013. Kelley feels that this is an exciting time to be a tropical cyclone researcher because many discoveries are about to be made through frequent high-resolution observations. Kelley has been interviewed about his research for the "Hyper-Hurricane" episode of the *Naked Science* series on the National Geographic Channel (2007), for the Earth & Sky radio program (2006), and by *Galveston County Daily News* (2004).

Kelley has been a researcher at NASA Goddard since 1997. That year, he earned a masters degree in Applied Physics from George Mason University. In 1993, he earned his bachelors degree from St. John's College, Annapolis, the "Great Books" college.